IR/UV Double-Resonance Spectroscopy of Reactive Hydrocarbon Species and their Reaction Products in Cold Molecular Jets

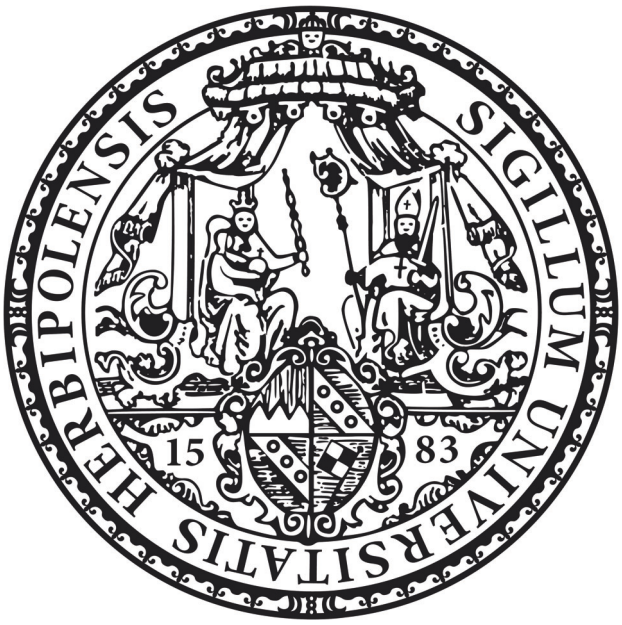

Dissertation zur Erlangung des naturwissenschaftlichen Doktorgrades der Julius-Maximilians-Universität Würzburg

vorgelegt von

Florian Hirsch
aus Aschaffenburg

Würzburg, 2021

Eingereicht bei der Fakultät für Chemie und Pharmazie am .....

Gutachter der schriftlichen Arbeit:

1. Gutachter: .....
2. Gutachter: .....

Prüfer des öffentlichen Promotionskolloquiums:

1. Prüfer: .....
2. Prüfer: .....
3. Prüfer: .....

Datum des öffentlichen Promotionskolloquiums: .....

Doktorurkunde ausgehändigt am .....

"If a cluttered desk is a sign of a cluttered mind, of what, then, is an empty desk a sign?"

- Albert Einstein

Contents

0.1 Abbreviations

1,4-CAF	1,4-cycloaddition/fragmentation
AC	alternating current
DC	direct current
DFT	density functional theory
DIB	diffuse interstellar band
DPI	dissociative photoionization
ESI	electrospray ionization
FAB	fast atom bombardment
FEL	free-electron laser
FWHM	full width at half maximum
HACA	hydrogen-abstraction/ C_2H_2-addition
Hz	hertz
IDS	ion dip spectroscopy
IE	ionization energy
IP	ionization potential
IR	infrared
ISM	interstellar medium
MAC	methyl-addition/cyclization
MALDI	matrix-assisted laser desorption/ionization
MPI	multi-photon ionization
MS	mass spectrum
NRMPI	non-resonant multi-photon ionization
PAC	phenyl-addition/cyclization
PAH	polycyclic aromatic hydrocarbon
PI	photoionization
PIMS	photoionization mass spectrometry
REMPI	resonance enhanced multi-photon ionization
ROS	reactive oxygen species
RSR	resonance-stabilized radical
SHG	second harmonic generation
SiC	silicon carbide
SPI	single-photon ionization
THG	third harmonic generation
TOF	time-of-flight
TPES	threshold photoelectron spectroscopy
UV	ultraviolet
VUV	vacuum ultraviolet

0.2 List of Publications

Most contents of this thesis have been published as articles in peer-reviewed journals and are listed below:

- F. Hirsch, K. Pachner, I. Fischer, K. Issler, J. Peterson, R. Mitric, S. Bakels and Anouk Rijs, Do Xylylenes Isomerize in Pyrolysis?, *ChemPhysChem*, **2020**, 21, 14, 1515-1518
- F. Hirsch, M. Flock, I. Fischer, S. Bakels and Anouk Rijs, The Gas-Phase Infrared Spectra of Xylyl Radicals, *J. Phys. Chem. A*, **2019**, 123, 44, 9573-9578
- F. Hirsch, E. Reusch, P. Constantinidis, I. Fischer, S. Bakels, A. Rijs and P. Hemberger, Self-Reaction of ortho-Benzyne at High Temperatures Investigated by Infrared and Photoelectron Spectroscopy, *J. Phys. Chem. A*, **2018**, 122, 49, 9563-9571
- F. Hirsch, P. Constantinidis, I. Fischer, S. Bakels and A. Rijs, Dimerization of the Benzyl Radical in a High-Temperature Pyrolysis Reactor Investigated by IR/UV Ion Dip Spectroscopy, *Chem. Eur. J.* , **2018**, 24, 7647

Further publications not discussed in this thesis:

- K. H. Eckstein, F. Hirsch, R. Martel and T. Hertel, Infrared Study of Charge Carrier Confinement in Doped (6,5) Carbon Nanotubes, *J. Phys. Chem. C*, **2021**, 125, 10, 5700-5707
- J. Ramler, J. Poater, F. Hirsch, B. Ritschel, I. Fischer, F. M. Bickelhaupt and C. Lichtenberg, Carbon monoxide insertion at a heavy p-block element: unprecedented formation of a cationic bismuth carbamoyl, *Chem. Sci.*, **2019**, 10, 4169-4176
- B. Hupp, J. Nitsch, T. Schmitt, R. Bertermann, K. Edkins, F. Hirsch, M. Auth, A. Sperlich and A. Steffen, Stimulus-Triggered Formation of an Anion-Cation Exciplex in Copper(I) Complexes as a Mechanism for Mechanochromic Phosphorescence, *Angew. Chem. Int. Ed.*, **2018**, 57, 41, 13671-13675

- B. Ahmed, S. Kumar, A. K. Ojha, F. Hirsch, S. Riese, I. Fischer, Facile synthesis and photophysics of graphene quantum dots, *J. Photochem. Photobiol. A*, **2018**, 364, 671-678

- K. Issler, A. Röder, F. Hirsch, L. Poisson, I. Fischer, R. Mitric and J. Peterson, Excited state dynamics and time-resolved photoelectron spectroscopy of para-xylylene, *Faraday Discuss.*, **2018**, 212, 83-100

- B. Ahmed, A. K Ojha, A. Singh, F. Hirsch, I. Fischer, P. Donfack and A. Materny, Well-controlled in-situ growth of 2D WO3 rectangular sheets on reduced graphene oxide with strong photocatalytic and antibacterial properties, *J. Hazard. Mater.*, **2018**, 347, 266-278

- B. Ahmed, A. K. Ojha, F. Hirsch, I. Fischer, P. Donfack and A. Materny, Tailoring of enhanced interfacial polarization in WO3 nanorods grown over reduced graphene oxide synthesized by a one-step hydrothermal method, *RSC Adv.*, **2017**, 7, 13985-13996

- P. Constantinidis, F. Hirsch, I. Fischer, A. Dey and A. M. Rijs, Products of the Propargyl Self-Reaction at High Temperatures Investigated by IR/UV Ion Dip Spectroscopy, *J. Phys. Chem. A*, **2017**, 121, 1, 181-191

Chapter 1

Introduction

Reactive species like radicals, biradicals, and carbenes are important groups of molecules present in numerous areas of chemistry. Students are usually introduced to this field during their undergraduate studies by several well known representatives. Basic concepts of the electronic structures of these molecules are illustrated by important examples like the hydroxyl radical or triplet oxygen. Rare cases of very stable radicals are also presented in the form of the simple nitric oxide radical or commercially available organic compounds like (2,2,6,6-tetramethylpiperidin-1-yl)oxyl (TEMPO). Apart from that, reactive species are omnipresent in many reaction mechanisms in organic and inorganic chemistry, where they often represent key short-lived intermediates in synthesis.

Radicals are particularly important in the field of polymer chemistry. Here, radicals are produced by various methods like photolysis, thermal decompositions, or most often radical initiators.[1] The radicals then undergo radical chain polymerization, which enables the growth of long polymer chains until termination.[2] The compounds produced with this technique are essential for modern life, produced on a gigaton scale every year. They include common materials like polyethylene (PE), polypropylene (PP), and polyvinyl chloride (PVC).[3] Hence, a profound understanding of the underlying radical chemistry is essential for optimizing these processes, as this market is highly competitive and lowering production costs can provide a significant advantage.

Other areas, in which radicals are prominent, are biological systems and medicine. Here, the term free radicals is usually connected to reactive oxygen species (ROS), which can be harmful to living organisms. Those can damage various important biological systems like proteins, lipids, or DNA and are supposedly directly linked to human diseases like cancer, Parkinson's disease, and Alzheimer's disease.[4–6] Thus, the human body has adapted to those ROS with various defense mechanisms like

antioxidants and enzymes to reduce oxidative stress.[7] Nevertheless, radicals are also essential for the proper function of organisms. Here, they play an important role in cell maturation,[8] defense against diseases,[9,10] and signal processing.[11–14]

These species are open-shell molecules, where electrons singly occupy one or more orbitals. They themselves are usually thermodynamically stable but exhibit a high reactivity towards bimolecular reactions. This is based on the low to absent reaction barrier these species show, which leads to a high reaction probability upon collision with another reaction partner. Consequently, radicals, biradicals, and carbenes are very difficult to study under normal conditions as their lifetime in chemical reactions is usually only a fraction of a second.

Over the last decades, several techniques have been developed to avoid these problems. They allow to generate and study reactive species in more detail. These include matrix isolation,[15,16] flame studies,[17,18] shock tubes[19,20], and molecular beams.[21,22] All these methodologies utilize the principle of isolation to separate the reactive species from potential reaction partners. This is then usually coupled with spectroscopic or spectrometric detection methods for analysis.

In the current thesis, hydrocarbon radicals, biradicals, and their reaction products were studied utilizing molecular beam techniques and structure-sensitive IR/UV double resonance spectroscopy. These reactive species and the polycyclic aromatic hydrocarbons they produce are of high importance in areas where they either occur in high concentration or are stable under the respective environmental conditions; most notably, in the fields of combustion, atmospheric and interstellar chemistry.

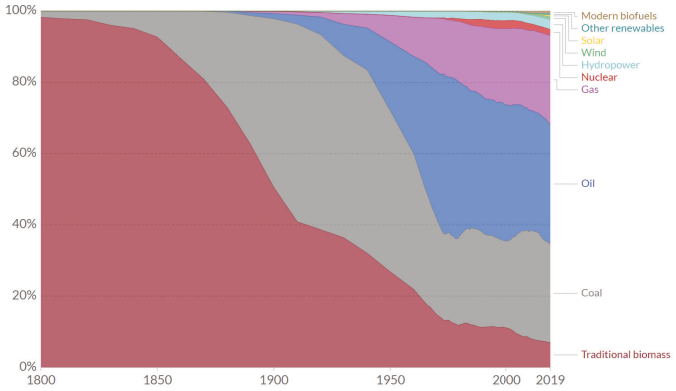

Figure 1.1: Evolution of the world's energy consumption by source since 1800. The majority is still coming from non-renewable energy sources like coal, oil, or gas.[23]

The importance of hydrocarbon radicals and PAHs in **combustion** processes is evident. Despite a push in the development and implementation of emission-free energy sources over the last two decades, renewable energy sources like wind, solar, and hydropower only make up less than 5% of the global energy production (c.f. Fig. 1.1). The vast majority of energy generated still relies on the combustion of fossil fuels, mainly coal, gas, and oil.

The negative implications of such an energy composition on the environment are widely known, especially regarding climate change. These problems are further enhanced considering the growth in global energy consumption. The world's need for energy, especially electricity, has risen annually since the mid-'60s, only somewhat stabilizing for first-world areas. The increase in energy consumption in up-and-coming industrial countries, however, is enormous. The Asia Pacific region, especially, more than doubled its annual energy consumption since the 2000's to over 70000 TWh; this is more than North America and Europe combined. Considering that most of this energy is produced in oil, gas, and coal power plants, it is evident that a fundamental understanding of the basic chemical and physical processes of the combustion of fossil fuels is more important than ever.[23,25,26]

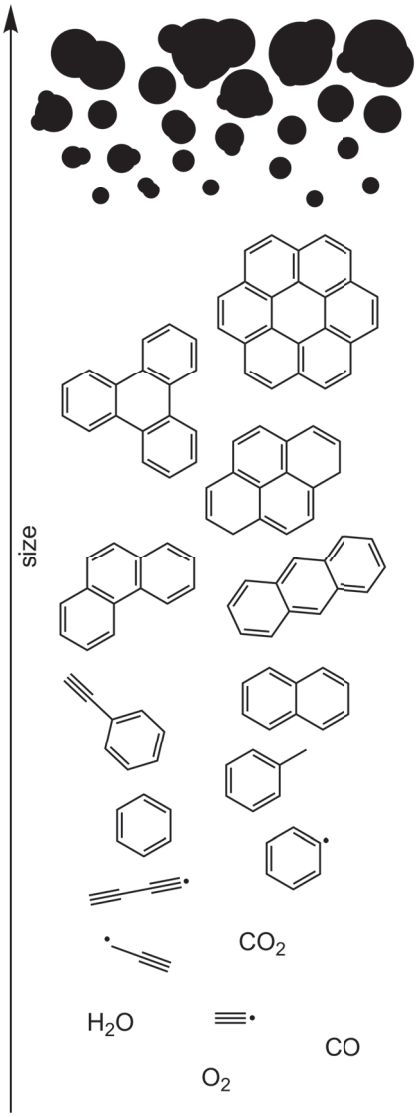

Figure 1.2: Molecular growth from small molecules to PAHs and particular matter.[24]

The combustion of hydrocarbons can be highly complex. The simple notion that hydrocarbons burn in an oxygen environment to water and carbon dioxide, which is often already taught in school, is more than idealistic. In reality, combustion is often incomplete. This depends on the molecular structure of the fuel, the availability of oxygen, and important physical variables like temperature and pressure.[27,28] This leads to many side reactions and the production of undesired secondary combustion products. These include toxic species like carbon monoxide or PAHs and soot, which are mutagens linked to cardiopulmonary disease and lung cancer.[29–35] Especially the latter ones gained more attention in recent years with the introduction of stricter monitoring and labor protection limits for particulate matter in the European Union.[36,37]

PAHs and, consequently, soot are generally formed from small hydrocarbon radicals. Such are produced in the combustion of hydrocarbons under fuel-rich conditions via oxidation with oxygen or thermal fragmentation.[38] The concentration of these radicals is usually high enough to then form heavier molecules in radical-radical reactions. This is especially the case in combustion engines, where high pressures are utilized to initiate the combustion process. Since the initial radicals are very small, consecutive growth reactions are required to form larger PAHs (c.f. Fig. 1.2). Here, the formation of the first aromatic ring, usually benzene, is considered the first important step in PAH growth. The first attempt to develop a coherent theory resulted in the hydrogen-abstraction/ C_2H_2-addition mechanism (HACA).[39,40] Within the HACA mechanism, benzene is formed by the two-fold addition of acetylene to the ethynyl radical, forming phenyl upon final cyclization. This mechanism was particularly sound, as high concentrations of acetylene are very common in hot flames. Although the HACA mechanism can generally explain further PAH growth, e.g., to naphthalene or phenanthrene, it was rapidly noticed that this mechanism is too slow to explain the extensive formation of PAHs in combustion processes.[41–43] Thus, further mechanisms were suggested to expand the theory of PAH formation like phenyl addition/cyclization (PAC),[44,45] methyl addition/cyclization (MAC),[46] 1,4-cycloaddition/fragmentation (1,4-CAF)[47], and many more.[43,48–53] This exemplifies that the formations of PAHs in hot flames are highly complicated due to the complex nature of these systems and the large number of species present. This not only makes studies on this topic very difficult but is also a challenge for computational simulations.[54–56] In general, up to this day, the theory of PAH formation is still not complete and fully understood.[57] Therefore, it is highly advised to simplify and break down specific radical reactions to better understand important underlying partial reactions. Once the PAHs grow large enough (>300 amu) in size, the transition from molecular size to three-dimensional particles occurs through the aforementioned mechanisms. Here, the PAHs start coagulating to form primary soot particles. These then increase their size via surface growth to soot particles of various dimensions and shapes.[38]

PAHs are not only a problem in the direct vicinity where they are produced. Ultimately, most PAHs will be dumped into the atmosphere where they are distributed. Hence, a profound understanding of PAHs and their role in **atmospheric chemistry** is highly desirable. Sources of atmospheric PAHs include anthropogenic emissions from residential combustion, transportation, metal production, and others. But also natural origins like volcanic activities, wildfires, and evaporation from the earth's surface contribute to the total PAH concentration in the atmosphere.[58] The global PAH emissions reached their height in the '90s and are fortunately on

a decline due to more stringent emission regulations. Nowadays, the annual emissions of the 16 most important PAHs (according to the Environmental Protection Agency[58]) are around 500 kT, where newly industrialized countries like China, India, and Brazil are the major contributors.[59]

The main interest in atmospheric PAHs is based on the aforementioned health risks. Here, especially secondary reaction products of PAHs in the atmosphere are of particular concern. PAHs can form derivatives by the reaction with reactive atmospheric gases like OH, O_2, or NO_3. The most common of these species belong to the group of nitrated (NPAHs), oxygenated (OPAHs), and hydroxylated (OHPAHs) PAHs and might pose additional hazards.[61–67] Although PAHs and their derivatives concentrations can be very localized to some areas, these species can disperse globally depending on the population and industrial activity. Particularly, an accumulation at the polar regions through long-range transport has been observed.[58,68,69]

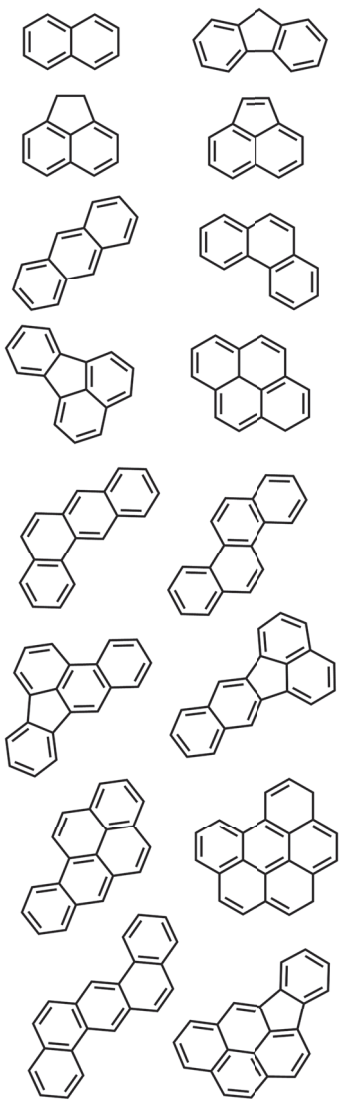

Figure 1.3: List of 16 important PAH pollutants acc. to the Environmental Protection Agency.[60]

Removal of these species mainly occurs via wet or dry deposition as well as photochemical degradation.[68] The predominant mechanism for PAHs is dry deposition, where particles in the air adsorb the molecules. These are then directly deposited on the earth's surface or washed out from the atmosphere by precipitation. However, the PAH derivatives often possess a higher polarity and hydrophilic properties which allows for wet deposition. Here, the species are directly dissolved in clouds into raindrops and consequently removed from the atmosphere by wash- or rain-out.[58,65,68,70,71]

The third field where small hydrocarbon radicals and PAHs play an important role is in **interstellar chemistry**. When most people think about space, they usually picture a vast emptiness, maybe with a planet and a star here in there. Although this notion is not entirely incorrect, the interstellar medium (ISM) is much more diverse in reality. Large accumulations of molecular matter are located in the ISM in the form of clouds and nebulae. The composition of these structures range

from simple, mostly bimolecular, molecules in diffuse clouds and dark nebulae to large complex molecules in dark clouds.[72] The physical environment in these clouds can vary greatly in terms of temperature and particle density which directly influences the chemical processes in these structures and the utilized detection methods.

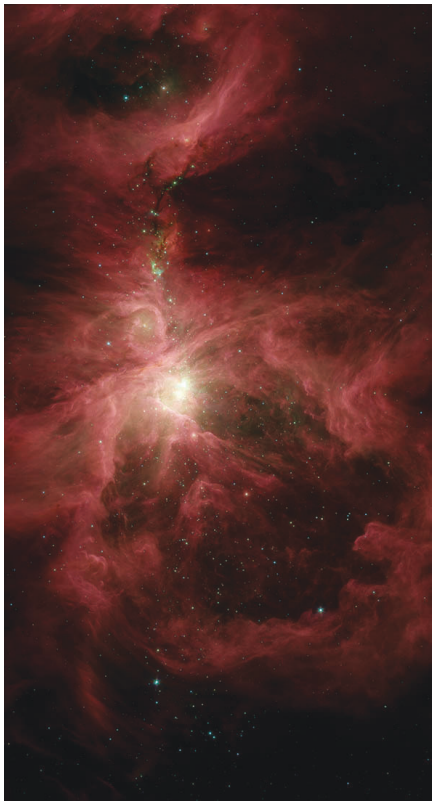

Figure 1.4: The mid-IR emission of the Orion nebula as captured by the Spitzer Space Telescope. The cloud is illuminated by young stars formed within this region of space.[73]

In general, the ISM is one of the few environments in which radicals are actually relatively stable. The low particle densities (compared to terrestrial conditions) deprive radicals of potential reaction partners resulting in radical lifetimes on a much larger timescale. Furthermore, radicals are steadily produced in the ISM from their neutral species by cosmic radiation. Hence, it is plausible that radicals represent a considerable amount of the molecules in interstellar clouds. In fact, the first two molecules ever detected in the ISM were radicals: methylidyne CH and cyanogen CN, and their respective ions.[72,74,75] These were identified in the late '30s by optical absorption studies, preceding the development of radio astronomy over the following decades. But not only the mere presence of radicals in the ISM is very interesting; they supposedly play an important role in the formation of larger molecules. Many new species have been identified within the last 70 years due to progress in telescope technology. This brings up the question of how these molecules are formed.

The physical environmental conditions in the ISM are not particularly beneficial for chemical reactions. In dark clouds, for example, which are clusters of particularly complex molecules, particle densities of 10^4-10^7 per cm^3 are observed, and temperatures often range between 20-150 K.[72] Here, the temperature is the main critical parameter. Under such cool conditions, chemical reactions have to be exothermic and basically activation energy free.[72] This concludes that only certain kinds of chemical reactions are possible, i.e., ion, radical, and surface catalyzed reactions. Hence, the formation of many species in the ISM might be based on radical reactions.

The presence of many heavier molecules in the ISM has been discussed over the years, especially concerning the diffuse interstellar bands (DIBs). Up to this day, the origins of the DIBs are not well understood, but larger carbon species like aliphatic chains and PAHs are often discussed as major sources.[76–79] This was originally based on their high photodissociation resistance in the ISM, the high carbon abundance in interstellar clouds, and their strong electronic transitions in the visible and near-infrared range.[80] The first unambiguous identification of a PAH carrier in the DIBs, however, was only achieved recently. Maier et al. measured the gas-phase absorption of C_{60}^+ under suitable laboratory conditions and were able to assign it to the DIBs at 9632 Å and 9577 Å.[81] This illustrates how valuable experimental comparative data is in the identification of molecules in the ISM.

Most indications of PAHs in the ISM nowadays originate from infrared data.[82] Since the Infrared Space Observatory and the Spitzer Space Observatory installation, large data sets of IR emission spectra became available. Especially, the emission in the mid-IR region is plentiful and corresponds to a variety of CH and CC modes. It has been suggested that these emitters contain roughly around 50 C atoms, as these species must have a low enough heat capacity for efficient mid-IR emission after UV absorption.[83] Consequently, PAHs represent excellent candidates for the origin of many of these mid-IR emission features.[84,85] The data further indicates that PAHs are omnipresent in the ISM, and high concentrations up to 10^{-7}, in relation to hydrogen, are suggested.[83] The knowledge of the presence of PAHs in the ISM has extensive consequences. It is assumed that they play a major role in the photoelectric heating of gases, UV screening, and ionization processes.[86] This means that PAHs might be profoundly responsible for specific environmental conditions important for many chemical and physical phenomena in the ISM. Furthermore, PAH features are particularly pronounced in regions of young stars and are thus presumed to be indicators of star formation in the universe.[83]

The following thesis covers several hydrocarbon radicals and biradicals, as well as their high-temperature reaction products. These species are studied utilizing combined mass spectrometric and infrared spectroscopic methods. In Chapter 2, necessary basic principles will be presented, including theoretical basics, experimental basics, and the utilized experimental setups. The following chapter features the results and discussions of the IR/UV experiments on ortho-benzyne (Section 3.1), benzyl (Section 3.2), xylyl (Section 3.3), xylylene (Section 3.4), and fulvenallenyl (Section 3.5). Finally, the major conclusions of this thesis are summarized in Chapter 4.

Chapter 2

Basic Principles

2.1 Molecular Beam Techniques

Radicals and biradicals usually exhibit a high reactivity towards intermolecular reactions, although they are thermodynamically stable. Consequently, it is difficult to study these species under normal conditions and requires experiments to be performed in isolation. A good way to achieve this is to utilize molecular beam techniques. Here, the reactive molecules can be isolated within a molecular beam, which can be combined with many different analyzing methods. Furthermore, the unique properties of supersonic jets are beneficial for spectroscopic applications as they can greatly improve the quality of spectroscopic measurements.

2.1.1 Properties of Molecular Beams

Figure 2.1 illustrates the basic principle of molecular beam generation. Consider an ensemble of molecules within a reservoir with a small hole leading to a low-pressure source chamber. The velocity of such an ensemble will be represented by a Maxwell-Boltzmann distribution at a given temperature.[87,88] If the pressure in the reservoir is high enough, molecules will expand into the vacuum of the source chamber via supersonic expansion. During this process, the molecules leaving the reservoir collide with each other, exchanging energy. This leads to a transfer of internal vibrational and rotational energy into the longitudinal velocity of the particles; the molecules cool down drastically. This process endures as long as the particle density is high enough and stops once no more collisions are possible, the molecules are isolated and reach their terminal velocity v_t:[89]

$$v_t = \sqrt{\frac{2k_b(T_0 - T_1)}{m_{mol}} \frac{\gamma}{\gamma - 1}}, \text{with } T_0 >> T_1 \tag{2.1}$$

Equation 2.1 can be derived from classical thermodynamics for an ideal gas, with the initial T_0 and final T_1 temperatures, the molecular mass m_{mol} and the specific heat ratio γ. It nicely illustrates the connection between the translational temperature cooling and the terminal velocity.[89] Finally, the central part of the jet is selected by a skimmer[90–92] to remove particles with an appreciable transversal velocity component. The molecular beam entering the detection chamber now solely consists of cold molecules moving in the z-direction.

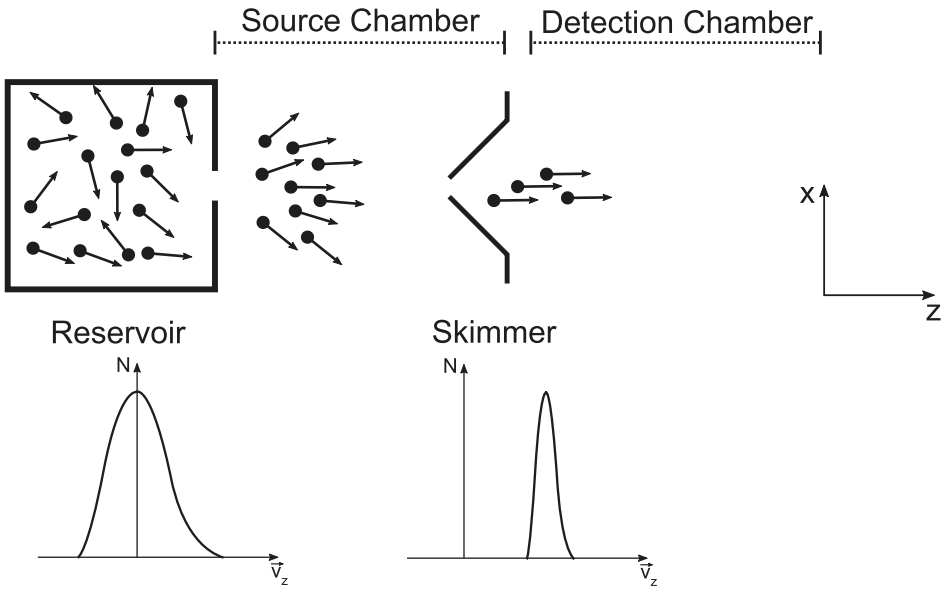

Figure 2.1: Cooling effect occurring in molecular beams via adiabatic expansion.

The resulting jet properties can provide notable advantages in spectroscopic applications. The low temperature of the molecules can result in high-resolution spectra, as the population of excited vibrational and rotational states is significantly lowered.[88,93–95] The high directionality along the z-axis can furthermore minimize the effect of Doppler broadening.[96,97] Also, low temperatures might allow studying systems, which otherwise would not be accessible at elevated temperatures, like weakly bound or van der Waals complexes.[98–101]

In this thesis, the samples were seeded in a noble gas (He or Ar). This allows higher pressures in the reservoir and increases the number of collisions during expansion, both improving cooling. Furthermore, if the carrier gas is added in excess, it dilutes the sample significantly (improving isolating properties) and allows for higher terminal velocities.[87] Furthermore, a solenoid valve was employed to generate a pulsed molecular beam. This provides additional cooling as the pressure

gradient increases and reduces the gas load on the source chamber.[89] The valves can also be equipped with a variety of different nozzles which can heavily influence the beam characteristics[102,103] and the terminal translational temperature parallel to the trajectory according to Eq. 2.2:[88]

$$T_1^{||} \propto T_0 \times (P_0 d)^{-6\frac{\gamma-1}{\gamma+2}} \tag{2.2}$$

With these techniques, translational and rotational temperatures in the sub 10 K region can be achieved.[104] For the experiments conducted in this thesis, these temperatures were estimated to be in the region between 50 - 150 K.

If an experiment requires additional cooling, molecular beam techniques can be extended utilizing novel cooling solutions like Stark-[105,106], Zeeman-[107,108] or optical-[109,110] decelerators.[111] With these methods, temperatures in the low mK regime can be achieved. Furthermore, other isolation techniques in the liquid (He-nanodroplets)[112,113] and solid phase[114] (matrix-isolation) are also available and are often coupled with molecular beam sources.

2.1.2 Time of Flight Mass Spectrometry

Time of flight mass spectrometry (TOF-MS) is a detection method to determine the mass of ions in gas phase applications. Nowadays, it provides high mass resolution of a nearly unlimited mass range. Due to its high flexibility, it can be combined with various ionization methods (MALDI,[115] ESI,[116] PI,[117] etc.) to study many systems from atoms[118] to biomolecules.[119] These spectrometers can be set up in several configurations depending on the application.[120,121] In this thesis, an orthogonal reflectron TOF-MS setup was utilized for the main part of the IR/UV experiments. A schematic of such is displayed in Fig. 2.2.

A molecular beam enters the detection chamber of the spectrometer, and the neutral molecules are ionized via photoionization by an external laser. This ionization takes place within the ion optics of the spectrometer. Here, an electromagnetic field is applied at two electrostatic plates (repeller/extractor), which accelerates ions into the orthogonal flight tube. A third plate downstream (ground) and additional shielding within the flight tube provide a field-free environment afterwards, the ions are reflected at the end of the flight tube by an ion reflector. This deceleration compensates for the energy spread of ions with the same mass and extends the drift path length, both enhancing mass resolution.[122,123] Finally, the ions are focused on a microchannel plate (MCP) detector to record the ion flight time. TOF-spectrometers are operated under vacuum, usually in the range between 10^{-5}-10^{-8} mbar, and thus multiple flanges are available for turbomolecular pumps, pressure

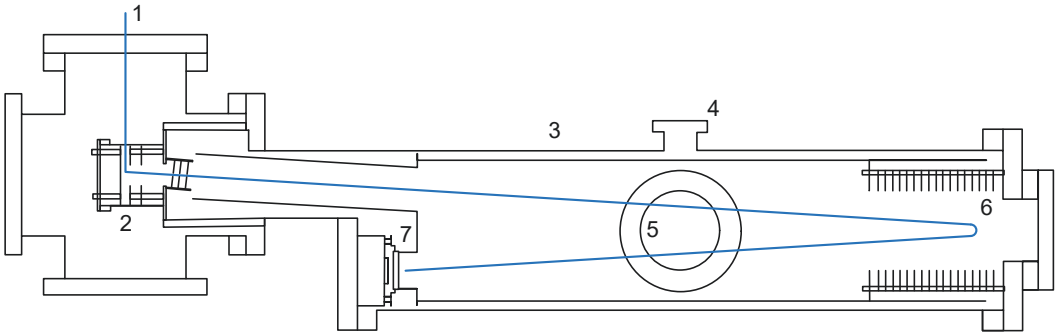

Figure 2.2: Schematic of the reflectron time of flight mass spectrometer as utilized for the IR/UV-IDS experiments in the *FELIX Laboratory*. The molecular trajectory is depicted as the blue line.

gauges, electrical feedthroughs, windows, etc.

For such a setup, the ion mass m can be obtained from the ion drift flight time t_{drift} according to:[121]

$$t_{drift} \approx 1.4 x_{drift} \sqrt{\frac{m}{2ezU}} \tag{2.3}$$

or

$$m \approx \left(\frac{2ezUt_{drift}^2}{1.4 x_{drift}^2} \right) \tag{2.4}$$

with the drift length x_{drift}, elementary charge e, ion charge number z, and the voltage of the acceleration field U.

In practice, the drift time t_{drift} is not well defined, as the start of the drift can not be accurately determined. If so, the masses are identified using two-point calibration with two known masses $\frac{m_1}{t_{drift,1}}$ and $\frac{m_2}{t_{drift,2}}$.

2.1.3 Molecular Beam Source

The precursor molecules for flash pyrolysis are seeded within a noble gas utilizing a molecular beam source according to Fig. 2.3. The noble gas is connected at **1** to a 6 mm stainless steel tube **2** (*Swagelok*). For additional stiffness and easier handling, the tube is welded inside a bigger stainless steel tube **3** of similar length. The tube is guided through a KF-160 flange **6** to attach the source to a vacuum chamber. This assembly is secured by a feed-through nut with an o-ring seal, press-fitting the tube to the flange and providing an air-tight connection. An additional rail **5** on the vacuum side of the source provides additional stability and prevents the source from undesired movement. The central tube is then connected to the sample container **7** (stainless steel T-filter, SS-4TF-LE *Swagelok*). Here, precursor molecules are picked up by the noble gas and seeded within the molecular beam. Finally, a pulsed molecular jet is produced by a solenoid valve (*Parker, Series 9*).

The precursor can either be placed directly into the bottom part of the sample container or be placed in an open glass vial with a sample holder. Both approaches work well, but a direct insertion of a compound provides a larger surface area, whereas placing the precursor into a vial significantly facilitates the cleaning of the sample container. For samples that require additional heating (up to 200°C) to improve the gas phase concentration, a heating wire can be attached to the sample container. The wire is embedded into a steel collar **d** for easy handling and can be attached to the lower part of the sample container. The sample temperature can then be monitored with a type K thermocouple (*Testa Sensor GmbH*) mounted on the top of the main body **c**.

For all parts on the vacuum side that require electric wiring, several vacuum feed-throughs are distributed on the flange. Here, all wires are soldered on the vacuum side of the feed-throughs and are then connected to outside devices via BNC connectors. This is usually required for the flash pyrolysis unit (DC power supply), sample heater (DC power supply), thermocouple (temperature monitor), and solenoid valve (pulse driver). Note that heat-resistant cable sheathing should be utilized for wires which are in close proximity to heated elements.

Since the source consists of several detachable parts, the air-tightness should be checked before installing the source in a vacuum chamber. Hereby, high pressure is applied to the gas inlet, and all crucial connections are covered with soapy water. Potential leaks can then be easily identified by bubble formation, and the connec-

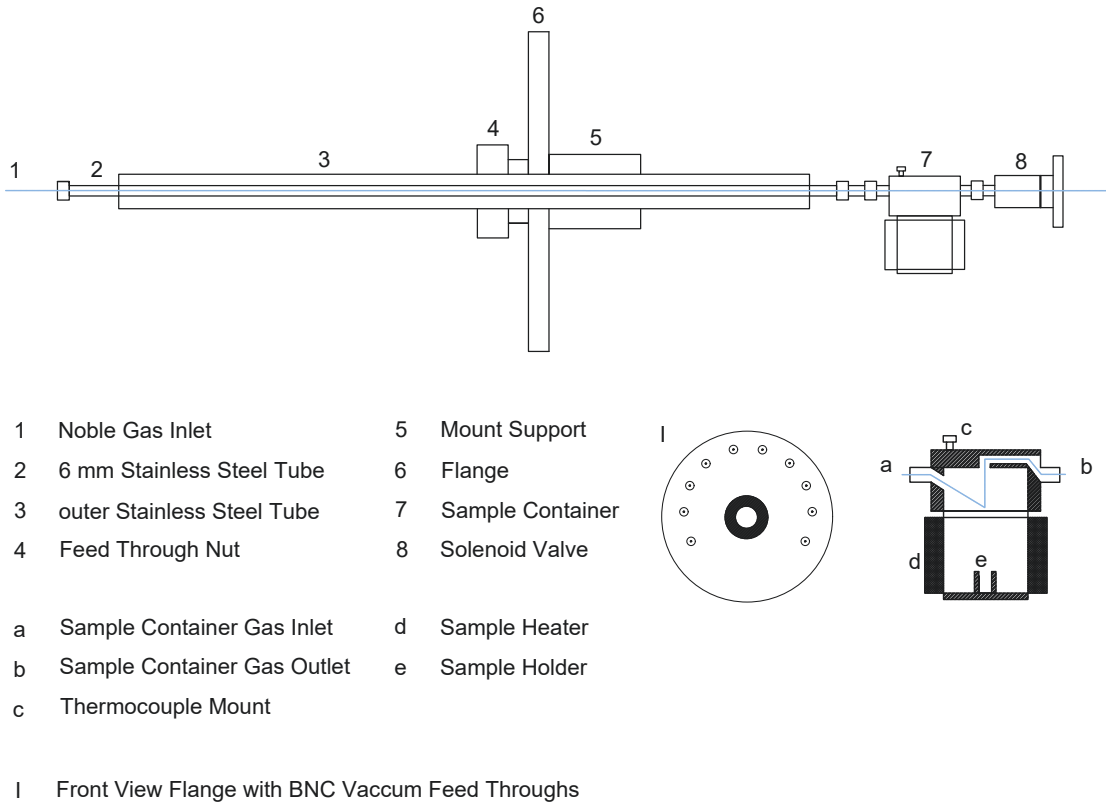

Figure 2.3: Schematic of a molecular beam source, which was utilized to produce a pulsed molecular beam for all experiments in this thesis.

tions can be retightened until the bubbling stops. It is also advisable to check all electric connections by measuring the electrical resistance between the outside feed-throughs and the respective devices.

A big advantage of this design is its high flexibility as all major connections are industry standard sized and o-ring sealed. This allows a source to be attached to a variety of vacuum chambers and devices. Usually, only the distance between the source and skimmer has to be adjusted. This can easily be achieved by altering the mounting position of the tube with respect to the flange via nut **4**.

2.1.4 Generation of Reactive Species

A crucial step in researching highly reactive species like radicals is the initial generation of the molecules. The vast majority of these are not stable under normal ambient conditions and have to be produced from a suitable precursor. Several methods for this have been developed over the last decades.

Electrical discharges have been utilized to generate reactive species in the field of atmospheric-[124,125] and astrochemistry.[126–128] It is based on the creation of a cold plasma to decompose a precursor into smaller fragments. Experimentally, this is accomplished by a high voltage and a ground electrode separated by a non-conductive spacer within a vacuum environment. A precursor, often seeded in a noble gas jet, is guided through those electrodes, and an electrical discharge is triggered. This fragmentation process is rather harsh and non-selective, leading to a variety of different products. Like other generation methods, it can be combined with many molecular beam techniques, e.g., pulsed beams, for efficient cooling.[129] Due to many decomposition products in discharge sources, a structure-sensitive detection method is highly desirable, as solely mass spectrometry-based methods might not be able to identify all species. In this regard, electrical discharge has recently been successfully combined with IR/UV ion dip spectroscopy allowing for precise identification of molecular beam composition by mass-selected IR spectroscopy.[130]

Alternatively, reactive species can be generated with a chemical reactor. Here, **fluorine abstraction** represents the most utilized method.[131–133] Fluorine atoms are capable of abstracting a variety of atoms from molecules to produce radicals.[134] However, this methodology is mainly applied to hydrogen-containing systems, as the formation of HF is highly efficient and energetically driven ($D_{e(HF)} = 593$ kJ mol^{-1}).[135] If the precursor is small and contains only a single hydrogen or all hydrogen atoms are equivalent, the radical generation can be quite specific. For most hydrocarbon precursors, which contain many different hydrogen atoms, however, a large number of different species are generated from the reaction with multiple fluorine atoms. In this case, a structure-sensitive detection method is essential.[136] A disadvantage of chemical reactors is that they are usually utilized in effusive beam experiments and can not benefit from the advantages of a supersonic jet.

Probably the most selective and widely used method to produce radicals is **photolysis**. Here, the reactive species is generated by photo-excitation of a suitable precursor into a dissociative electronic state. The subsequent dissociation results in the formation of the radical and the counter fragment.[137] Photolysis can be

combined with a variety of molecular beam techniques, especially pulsed jets. The laser excitation is performed directly after the nozzle of the molecular beam source or in an attached quartz tube.[137] The (potentially) small excess energy transferred during photolysis, combined with supersonic cooling, allows for the generation of particularly cold molecules compared to other methods. Furthermore, many precursors are available for photolysis, as many bromides and iodides show dissociative states at common wavelength like 266 nm (Nd:YAG 4th harmonic) or 193 nm (ArF excimer).[138–140] However, the usually low conversion coefficient can be challenging for some experiments to produce sufficient radical density in the gas phase, compared to other methods.

In this thesis, **pyrolysis** was used to generate the reactive species. This method is based on the thermal decomposition of a suitable precursor. A molecule with an appropriate leaving group entering a heated reactor is homolytically split to create radicals. Due to the high conversion efficiency, a high radical density can be achieved. This methodology has first been utilized in effusive beam experiments at low vapor pressures. However, the high molecule concentration in such a setup promotes undesired radical-radical recombination and secondary reaction products.[137] Pyrolysis was tremendously improved by the introduction of flash pyrolysis. The pyrolysis could now be combined with pulsed molecular beam sources at high pressure. This lessens the dwell time within the pyrolysis tube to less than 100 µs to reduce the aforementioned unwanted processes and makes cooling via supersonic expansion possible.[141] The vast pool of suitable pyrolysis precursors enables the generation of many reactive species, some not available with other methods. In general, the high flexibility of pyrolysis sources led to their implementation into many experiments with various detection methods, e.g., millimeter-wave spectroscopy[142], electronic UV spectroscopy[143,144], matrix-isolation[145], femtosecond time-resolved photoionization[146], and many more.

2.1.4.1 Flash Pyrolysis Unit

The flash pyrolysis unit employed in this thesis is constructed following the design of Kohn and Chen,[147] often referred to as *Chen Nozzle*. It consists of a silicon carbide (SiC) tube and two identical stainless steel electrodes. Applying a current to the electrodes heats the SiC tube in the heating region to temperatures between 600 - 1800 K. Molecules are then pyrolyzed upon injection into the SiC tube from a solenoid valve.

The SiC tube (*Saint Gobain Keramik, Hexoloy Se*) has a length between 20-40 mm with an inner diameter of 1 mm. It is connected to the nozzle of a solenoid valve (*general valve, parker*) via a ceramic tube mount (MACOR) attached to the

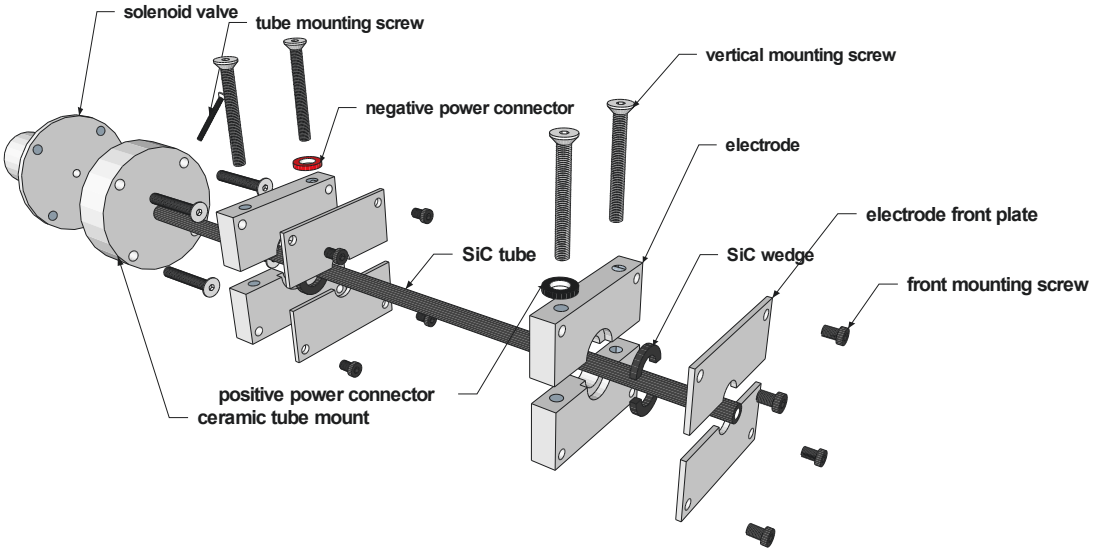

Figure 2.4: Exploded view drawing of a flash pyrolysis unit.

faceplate of the valve. The tube is held in place by insertion into the central borehole of the tube mount and secured via press-fit with a screw. The tube mount also serves as a thermal insulator resisting temperatures up to 1000 K.[87] The electrodes are then attached downstream. The last electrode is usually placed flush with the end of the SiC tube. An electrode consists of an upper/lower main electrode body, a SiC wedge, and an electrode front plate. The SiC wedge is placed into the cavity of the main body and press-fit into place by the front plate with two screws. The electrode is then attached to the SiC tube by assembling the upper and lower part with two vertical mounting screws. This also determines the mounting pressure and should be performed carefully to prevent damaging the tube. The inner diameter of the SiC wedges matches the outer circumference of the SiC tube, ensuring contact between the SiC tube and the electrode. This furthermore prevents cracking of the SiC tube from thermal expansion of the electrode during operation. The electrodes are connected to a DC power supply using two power connectors (metal washers) jammed between the electrode and a vertical mounting screw. Typically, a power between 0 - 80 W is applied for heating. It can be increased above this threshold for a certain period of time, but the risk of tube burn out is then increased as well. The placement of the upstream electrode defines the heating region of the pyrolysis unit. Typical heating lengths are in the range between 5-10 mm. Here, shorter heating lengths efficiently produce decomposition products from the precursor. However, if secondary reaction products of the reactive species are of interest, longer heating

regions can promote bimolecular reactions. The SiC tube can then additionally serve as a chemical flow reactor. For trouble-free operation of the flash pyrolysis, the resistance between the electrodes has to be adjusted properly, usually in the range between 30-100 Ω. This can be achieved by varying the distance between the electrodes or by removing parts of the outer graphite layer of the SiC tube with sandpaper.

A big advantage of this design is its simplicity and low manufacturing cost. This allows to stock multiple spare parts for fast repair or even have multiple flash pyrolysis units on hand to completely swap the flash pyrolysis during an experiment if it malfunctions.

2.1.4.2 Selection of Pyrolysis Precursors

For the controlled generation of specific reactive species, a proper selection of suitable precursors is as important as the experimental setup. The pool of potential precursors for flash pyrolysis is large and a few examples are displayed in Fig. 2.5. In general, pyrolysis precursors should have the following properties:

- good leaving group
- high vapor pressure
- thermal stability

Pyrolysis is based on homolytically breaking the weakest bond in a molecule. For this to happen, a weakest bond has to exist, and thus a good leaving group is critical. In general, the easier it is to cleave a precursor, the better, because the pyrolysis can be operated at lower temperatures which prevents undesired secondary reactions and decomposition. A simple approach is to employ halides, e.g., bromides or iodides. The carbon-halide bond is the weakest in a molecule for many hydrocarbon compounds and hence serves as a predetermined breaking point for pyrolysis. In this case, selecting the proper precursor is rather simple, as the halide is located directly next to the radical center to produce. A further practical advantage of these precursors is the wide commercial availability of halide compounds, as they are common reactants in chemical synthesis. Other precursors often employed include nitrites, azo or highly-strained compounds. These are often very efficient in producing reactive species at low temperatures. Especially, highly-strained dimers (cf. Fig. 2.6 II) have been proven to provide high gas-phase concentrations without the formation of additional fragments.[148]

In some cases, the influence of the leaving group on the experiment has to be considered as well. For example, consider the generation of methylcyclopentadienyl

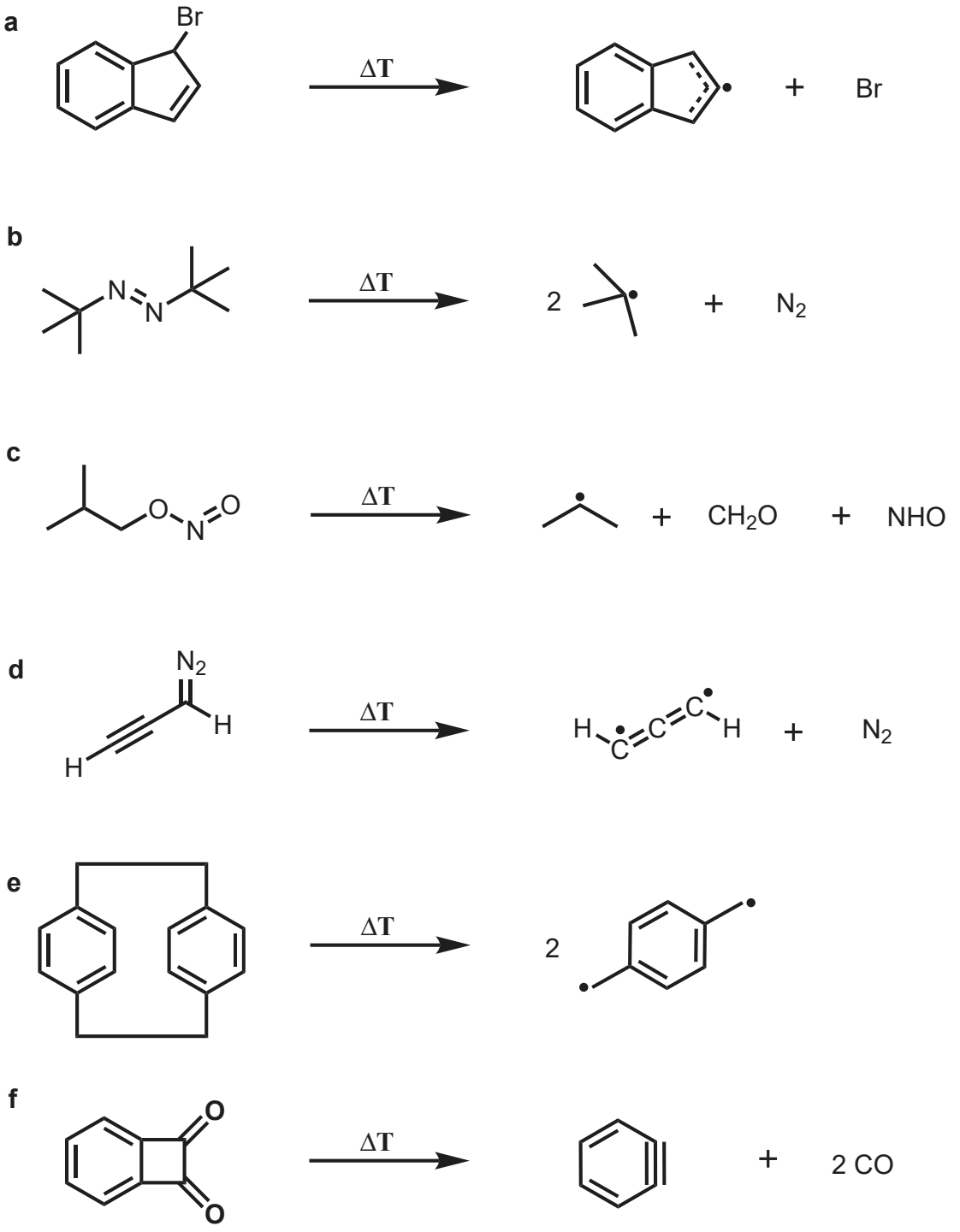

Figure 2.5: Overview of some good examples for pyrolysis precursors: a) indenyl bromide,[149]b) azo-tert-butane,[150]c) i-butyl nitrite,[150]d) diazopropyne,[151] e) [2.2]paracyclophane,[148],f) benzocyclobutenedione.[152]

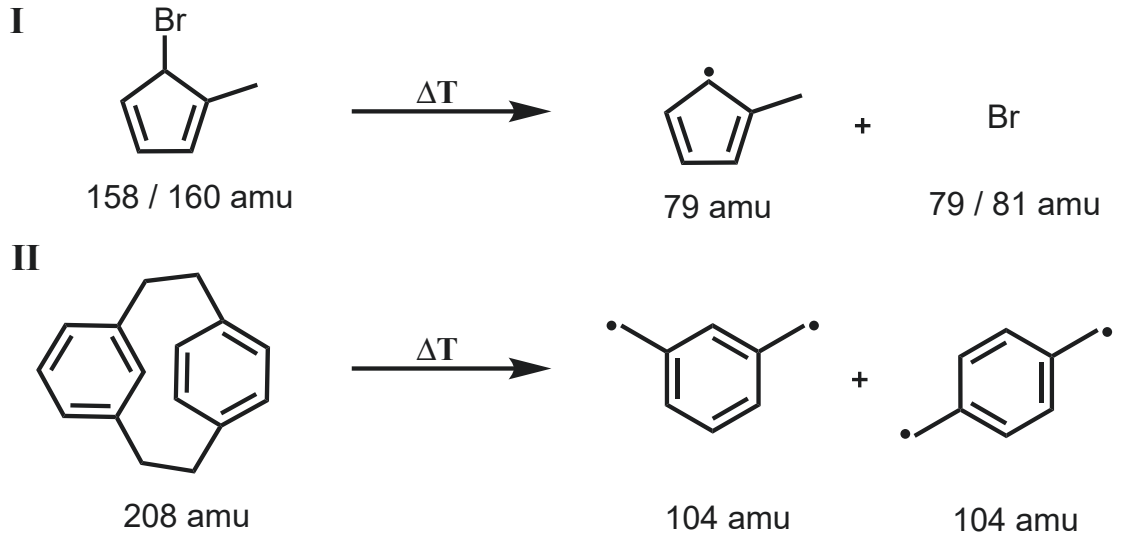

Figure 2.6: Examples of two potential problematic pyrolysis precursors. I) Decomposition of 5-bromo-1-methyl-1,3-cyclopentadiene to methylcyclopentadienyl and bromine. II) Decomposition of [2.2]metaparacyclophane to meta- and paraxylylene.

from its respective bromide precursor in Fig. 2.6 I. The mass of the radical and the bromine both have the same mass of 79 amu. If the experiment is based on mass spectrometry and both species can be ionized, this might pose a problem. Additionally, consider the pyrolysis product of [2.2]metaparacyclophane in Fig. 2.6 II. Here, two isomers are produced which can not be distinguished with non-selective detection methods, and might lead to false conclusions regarding isomerization. Thus, the potential influence of a leaving group should always be thoroughly considered.

Besides the pyrolysis characteristics, the physical properties of the precursor are also very important, especially the vapor pressure and thermal stability. Many gas-phase experiments require a certain molecule density for proper detection. This can be achieved if the vapor pressure of the precursor is sufficient to seed a considerable amount of molecules into the carrier gas. This, however, is often not the case. Accordingly, it is common practice to heat up the precursor to increase gas phase concentration. In this regard, sample temperatures up to 200 °C are not uncommon. In cases like this, the precursor must be thermally stable to at least the heating temperature. Otherwise, decomposition of the precursor might inhibit proper measurements or even lead to false results. Furthermore, since halides are often employed as precursors in pyrolysis experiments, the formation of potentially corrosive substances should also be considered. HCl and HBr are often produced as

secondary pyrolysis products, which can degrade metallic parts and tubing material. If that is the case, regular service of susceptible components is highly advised.

2.2 Ionization Schemes

The detection of neutral species with mass spectroscopic methods requires ionization of the molecules for detection. Nowadays, many ionization methods are available for different applications, e.g., EI, ESI, MALDI, FAB, etc. In this thesis, single-photon ionization (SPI) and resonance-enhanced multi-photon ionization (REMPI) were utilized. Both methods are purely laser-based and adaptable to a variety of different experiments. Furthermore, SPI and REMPI are rather mild ionization techniques that prevent undesired fragmentation and allow for a precise determination of the energy delivered during ionization.[153] In the following section, the basic principles of those photoionization methods will be discussed briefly.

2.2.1 Single Photon Ionization and VUV Generation

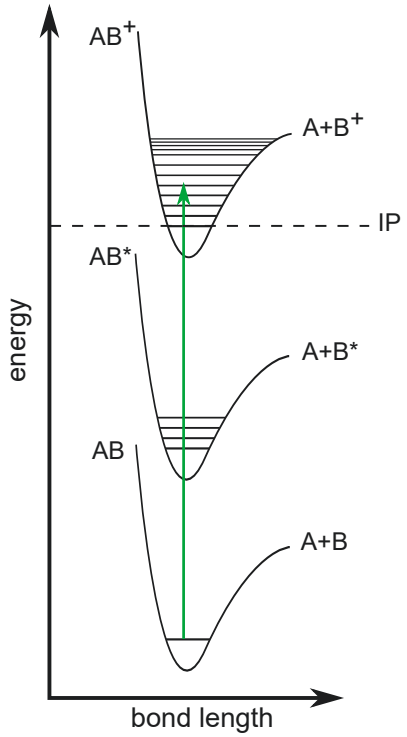

Figure 2.7: Ionization process of a molecule AB with a single photon.

Ionization of a molecule with one photon is referred to as single-photon ionization (SPI). Here, a photon with enough energy to overcome the ionization potential (IP) of a molecule AB is absorbed, resulting in the removal of an electron and ionization of the molecule to AB^+. This process is schematically displayed in Fig. 2.7. The number of ions produced with this technique depends on the SPI cross section σ_{SPI}, the laser intensity I, and the number of the neutral species N_0:[154]

$$N_{ion} = \sigma_{SPI}(\lambda) I N_0 \tag{2.5}$$

A big advantage of SPI is that the ionization mainly depends on the ionization cross section σ_{SPI} and the IP of the molecules. Potential wavelength-dependent absorption cross sections of excited states are irrelevant. Hence, this ionization scheme can be applied to molecular beams, which consist of a large variety of different molecular species as long as the photon energy exceeds the IP of the molecules. Furthermore, ionization cross sections for molecules with related characteristics and weights are often similar. For example, PAH like indene, naphthalene, phenanthrene, etc.,

exhibit σ_{SPI} (10.5 eV) within an order of magnitude between 10 and 100 Mb.[155–163] This allows not only to identify molecules via their mass but also to get a rough estimation of the relative abundance of each species via their respective signal intensity.

Ionization via SPI is usually performed with high-energy photons in the VUV region. Typical high-quality light sources for this spectral range include synchrotrons and FELs. However, these are usually only available at larger research facilities. In this thesis, VUV radiation of 10.5 eV was produced by frequency-tripling in a noble gas cell, as regular energy conversion of laser radiation with nonlinear optical crystals is not possible for < 190 nm. This photon energy is widely applicable as most organic and hydrocarbon molecules have ionization energies below 10 eV.[153,164] The process for a Xe cell utilized in this thesis is depicted in Fig. 2.8.

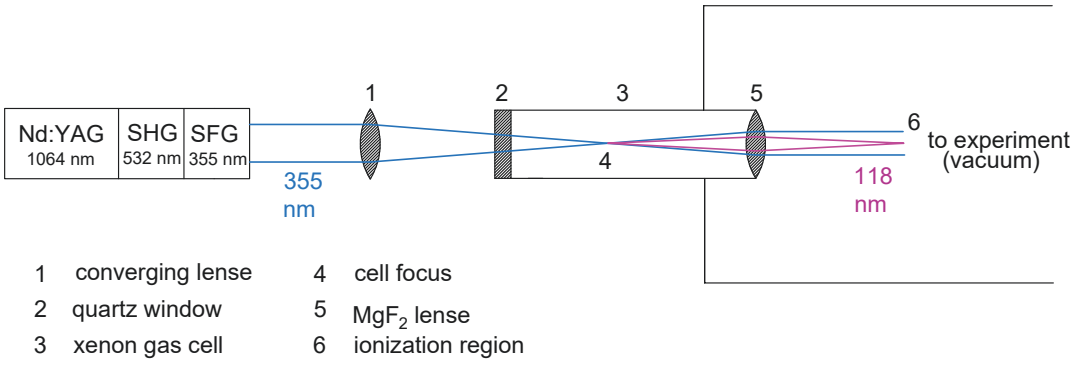

Figure 2.8: Schematic of the VUV generation utilizing a Xe gas cell and radiation produced by a ns Nd:YAG laser setup. The 355 nm beam path is depicted in blue and the tripled 118 nm radiation in purple.

A Nd:YAG laser produces radiation of 1064 nm, which is subsequently converted to 532 nm by second harmonic generation (SHG) and then to 355 nm by sum-frequency generation (SFG). The laser beam ($\approx$ 18 mJ) is then focused into a Xe filled gas cell ($p \approx 17$ torr) where 118 nm (10.5 eV) light is produced by four-wave-mixing. Finally, the VUV radiation is focused in the ionization region of the experiment.

Frequency-Tripling is a third-order non-linear process that requires high intensities for appreciable results. The intensity of third harmonic generation for a Gaussian beam is:[154]

$$I_{3v} \approx N^2 |\chi^{(3)}|^2 I(v)^3 F(b\Delta k) \tag{2.6}$$

with the confocal parameter b and the beam waist ω_0

$$b = 2\pi v c^{-1} \omega_0^2 \tag{2.7}$$

and wave vector difference Δk

$$\Delta k = k_{3v} - 3k_{3v} = 2\pi v c^{-1}(n_{3v} - n_v) \tag{2.8}$$

Equation 2.6 shows that the intensity of the third harmonic I_{3v} depends on the number of density N, the third-order electric susceptibility $\chi^{(3)}$, the intensity of the incident laser radiation $I(v)$ and the geometrical phase-matching condition $F(b\Delta k)$.

The phase matching is a critical parameter for the up-conversion to work. Considering Eq. 2.7 and 2.8, this is mainly dependent on the difference of the wave vectors k_{3v} and k_v. Under normal circumstances, the mismatch of Δk has to be zero so that destructive interference is minimized over the interaction length (see Fig. 2.9). This is true if the refractive index of the tripling medium $n(v)$ is identical for v and $3v$.[165]

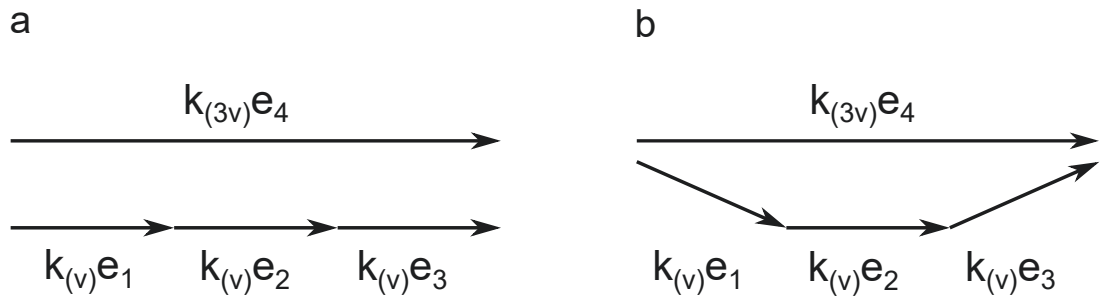

Figure 2.9: Wave vector phase matching condition for four-wave-mixing. **a** describes the regular case and **b** is valid for strong fields.

However, for high photon densities like in this thesis, the situation changes for applications that require focusing. Intense focusing induces a phase-slip between the incident and produced radiation, and changes the direction of the unit vector e slightly (see Fig. 2.9, b).[165,166] Here, the wave vector momentum

$$k_{3v}e_4 = k_v e_1 + k_v e_2 + k_v e_3 \tag{2.9}$$

as well as the energy $E(3v) = 3E(v)$ have to be conserved. Consequently, $k(3v) < 3k(v)$ has to be fulfilled, which is the case for $\Delta k < 0$. A negative Δk can be achieved in media that have a negative dispersion with $n(3v) < n(v)$.[165] This is why VUV third-harmonic generation is often performed in noble gases, which have regions of negative dispersion on the high energy side of resonances with suitable energies and are furthermore easy to handle. Many refractive indices for noble gases have been compiled in the literature over the years.[167–170] Xe, for the 118 nm generation, for example, is negatively dispersive in the range from 117.2 - 119.0 nm corresponding to the $5d^3P_1$ transition.[154,171]

The conversion efficiency in such noble gas cells is usually very small due to the low value of the third-order susceptibility.[154] Hence, according to Eq. 2.5, N and $F(bk)$ must be carefully optimized for sufficient THG. The obvious solution to this is to raise the noble gas pressure in the cell to increase N.[165] However, this is only applicable up to a certain pressure, as the negative dispersion is pressure dependant. In some cases, where higher conversion efficiencies are required, an additional gas with positive dispersion can be added to the cell to artificially increase N and the intensity of the third harmonic generation.

2.2.2 Multi-Photon Ionization

Neutral molecules can also be ionized with more than one photon. This method is referred to as multi-photon ionization (MPI). This methodology can be divided into non-resonance multi-photon ionization (NRMPI) and resonance-enhanced multi-photon ionization (REMPI), as depicted in Fig. 2.10.[172]

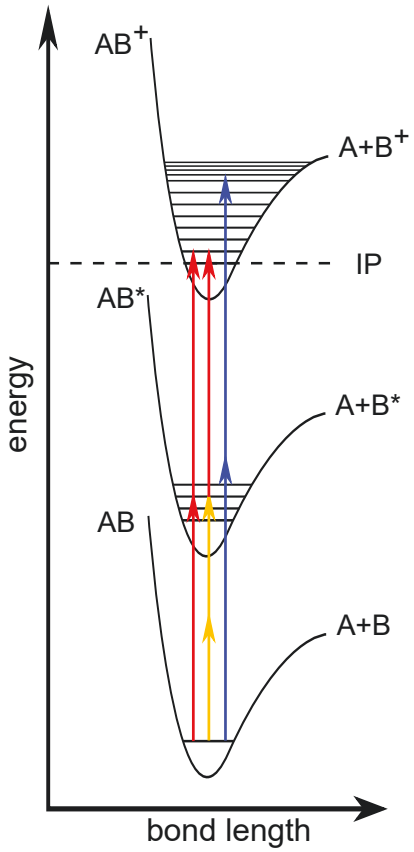

Figure 2.10: Examples of different resonance enhanced ionization schemes: [1+1]-REMPI (left), [2+1']-REMPI (center), and NRMPI (right).

In a non-resonance ionization, the molecule is excited to a virtual state with one or multiple photons and then immediately ionized. In the case of REMPI, a neutral molecule is excited to a real electronic excited state by one or multiple photons. This excited molecule can then be ionized within the lifetime of the excited state by one or more additional photons. Here, the signals produced by REMPI are usually far superior to the ones produced by NRMPI due to the resonance enhancement and the larger transition dipole moments of the excited states.[150,173] Note that for very short laser pulses (fs and below), this advantage becomes negligible.[174] The number of ions N_{ion} generated via a REMPI process can be approximately described by Eq. 2.10:[175–177]

$$N_{ion} \approx \frac{1}{2}\sigma_1(\lambda)\sigma_2(\lambda)I^2N_0 \qquad (2.10)$$

With the absorption cross sections from the ground σ_1 and excited state σ_2, the laser intensity I and the number of density of neutral molecules N_0. REMPI also produces larger signals than SPI because absorption cross sections are usually significantly larger than ionization cross sections (compare Eq. 2.5 and Eq. 2.10).

To classify the large amount of possible REMPI schemes, naming follows a certain terminology, e.g. [1+1], [2+1'], [2+2], etc. Here, the first number indicates the number of photons required for excitation into an electronic state. The second number then specifies the number of photons used for ionization. The addition of a prime ' indicates that a photon of a different wavelength is used in the respective process.

The ionization utilized in this thesis for all IR/UV experiments follows a [1+1]-REMPI scheme. This was mainly chosen for the good signal intensity and the capability to detect trace species.[178] Although REMPI usually is a very selective ionization method, as the photon energy has to match the excited state of the respective molecules, it can be applied to the simultaneous detection of most PAHs. The majority of polycyclic aromatic hydrocarbons have chromophores with broad absorption bands in the range of 230-300 nm.[179] Nanosecond dye lasers can easily provide this radiation as excited state lifetimes for PAHs are typically on a ns scale.[179,180] Additionally, most PAHs have an IE below 9 eV, making a [1+1]-REMPI scheme within the absorption spectrum viable.[180] For example, an [1+1] ionization from frequency-doubled Coumarin 153 fits within the absorption range and provides 9.36 eV at 265 nm for ionization.

2.2.3 Dissociative Photoionization

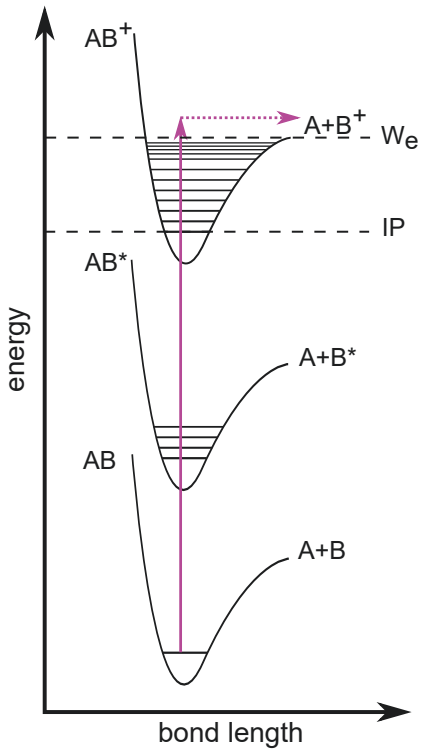

Figure 2.11: Dissociative photoionization of a molecule AB induced by a SPI.

In the experimental section of this thesis, the term dissociative photoionization (DPI) appears on several occasions. It describes the process of photoionization induced fragmentation of a molecule AB into a neutral fragment A, an ion B^+ and an electron. DPI occurs when the energy delivered by the ionization photon exceeds the dissociation barrier in the ionic state of a molecule. Thus, DPI is often observed in SPI experiments with VUV photons, where the ionization excess energy can be significant, but can also occur with MPI schemes if enough energy is transferred.

For a correct interpretation of experimental data, it is important to identify fragments produced by DPI. Here, a method purely based on mass spectrometry is usually insufficient as DPI fragments will just show up as additional mass signals. In the case of IR/UV ion dip spectroscopy, the inherent structural sensitivity can be utilized to identify masses produced by DPI. Since fragmentation occurs after ionization, the DPI product B^+ will appear at the mass of the fragment but will show the gas phase IR spec-

trum of the parent molecule AB. Consequently, in IR/UV ion dip experiments, it can be clearly distinguished if a mass originates from DPI or is a real reaction product of the reactive species formed in pyrolysis.

2.3 IR/UV Spectroscopy

IR/UV spectroscopy is a general term that includes a variety of different double resonant action spectroscopic methods utilizing IR and UV radiation. It is commonly based on inducing a population change within an ensemble of molecules via intense IR excitation, which will consequently be probed utilizing UV ionization. Many techniques have been developed over the years to apply this kind of spectroscopy to many scientific studies, e.g., IR/VUV spectroscopy,[181] IR/UV fluorescence depletion spectroscopy,[182] or vibrationally assisted VUV ionization.[183,184]

In this thesis, IR/UV ion dip spectroscopy (IR/UV-IDS) was employed. It provides mass-selected IR spectra of molecules that are seeded in a free jet. This method can be used to study a large variety of molecular systems like small hydrocarbon radicals,[185] biomolecules,[186,187] or weakly-bond clusters due to its high flexibility.[188,189] For the studies presented in the experimental section of this thesis, IR/UV-IDS was utilized to study the vibrational structure of reactive hydrocarbon species produced by flash pyrolysis as well as identifying potential reaction products and getting a better insight into the dynamics of their formation.

2.3.1 Principles of IR/UV Ion Dip Spectroscopy

The fundamental principle of IR/UV-IDS is depicted in Fig. 2.12. An ensemble of molecules AB produced by flash pyrolysis is in its electronic and vibrational ground state after expansion. A UV laser adjusted to an excited state AB* ionizes a number of molecules via [1+1]-REMPI, and the ions are detected by TOF-MS. This will result in a stable mass signal depending on the number of ionized molecules. Now, if the molecules are excited with IR light of suitable energy corresponding to a vibrational transition, before the ionization step, the initial vibronic population will decrease. Consequently, the UV ionization will probe fewer species from $v = 0$, which will result in a decreased mass signal because fewer molecules will be ionized. This decrease is called *dip* and appears at all vibrational transitions over the IR scan range. Scanning the IR laser over the fingerprint region from 500-1800 cm^{-1} then allows for unambiguous identification of species via their respective fingerprint IR spectrum. The number of vibrationally excited molecules N_{vib} mainly depends on the IR absorption cross section $\sigma_{ir}(\lambda)$ and the IR photon fluence Φ:

$$N_{vib} = N_0 e^{-\sigma_{ir}(\lambda)\Phi} \tag{2.11}$$

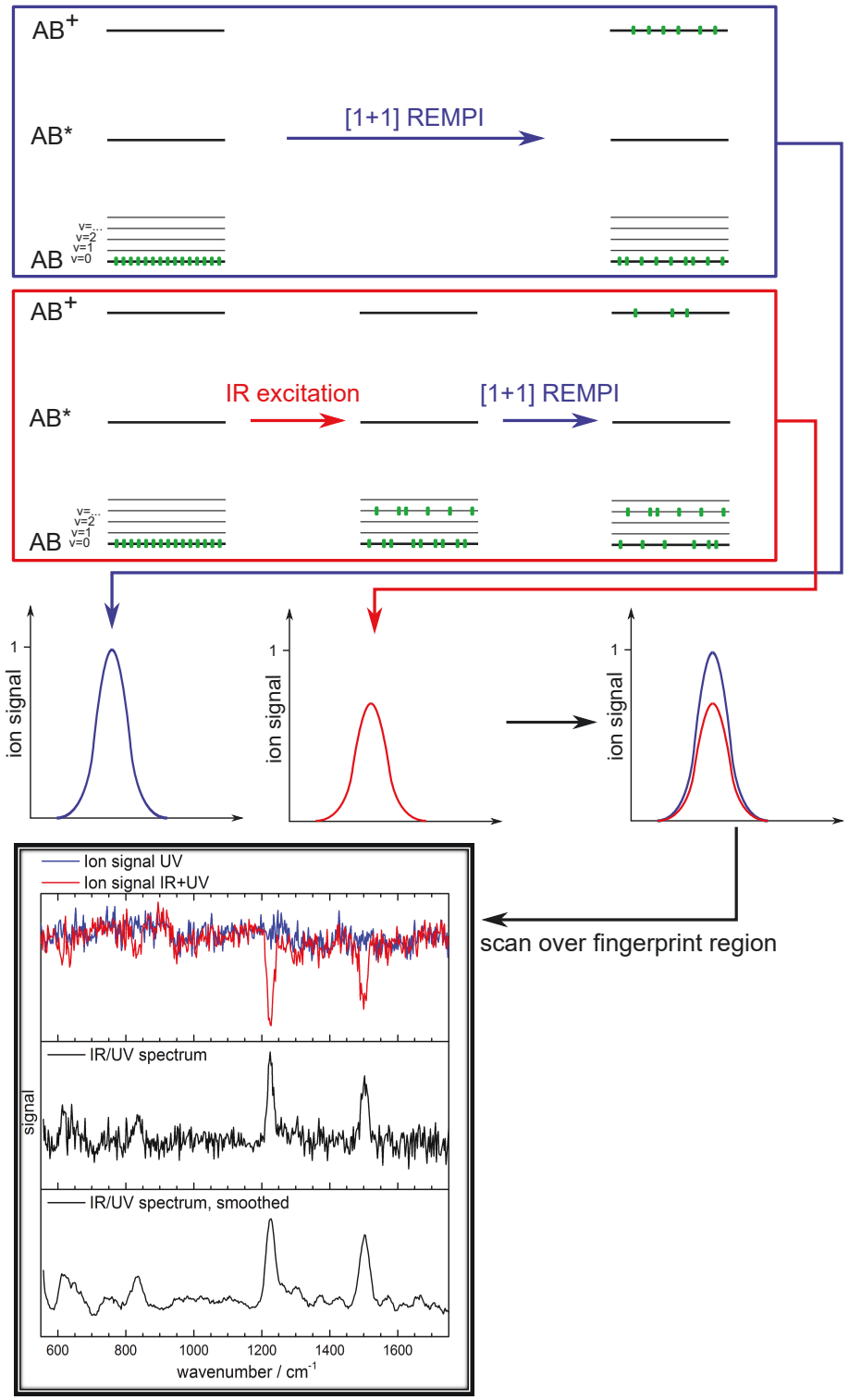

Figure 2.12: Illustration of the principle of IR/UV-IDS. Excitation schemes and populated states are depicted at the top, whereas the resulting ion signals and spectra are depicted in the center and bottom, respectively.

The depletion signal from IR/UV-IDS can sometimes exceed 50% because the system does not have to follow a Maxwell-Boltzmann distribution. The ground and vibrationally excited state is technically not an isolated two-state system. The vibrationally excited species can transfer energy to other vibrational modes via intramolecular vibrational energy redistribution (IVR), absorb additional IR photons, or undergo IR-induced fragmentation. All of this can lead to a depopulation of the vibrational excited state and cause a population inversion for the ground state, producing depletion signals over 50%.[154,190]

A big advantage of this technique is that all species visible in the mass spectrum are measured simultaneously.

2.3.2 IR/UV Data Analysis Software

The raw data of the IR/UV-IDS experiments contain mass, IR wavenumber, and signal intensity information. This information was originally measured using the proprietary measurement software at the FELIX laboratory and is saved in a 3-dimensional HDF5 file format. For easier handling, the data were dumped into a

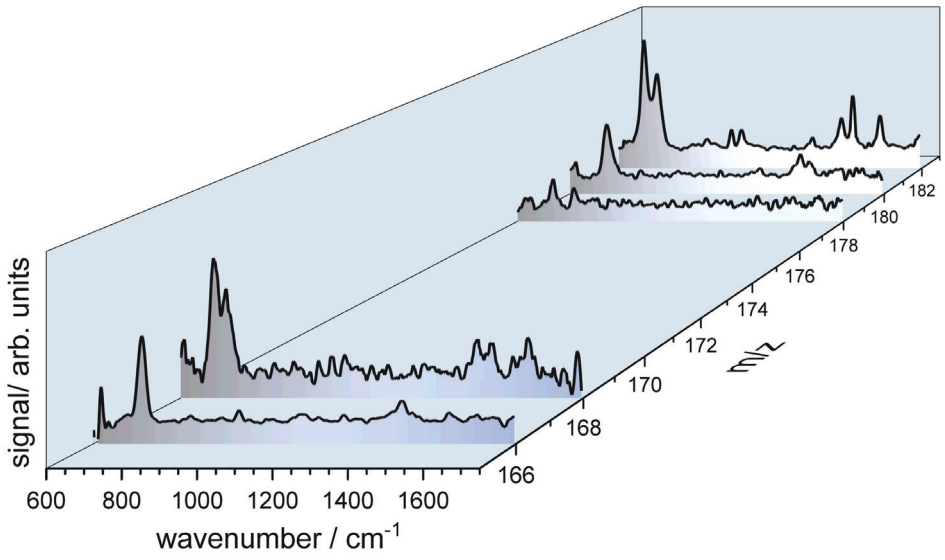

Figure 2.13: Vibrational spectra in the fingerprint region received for multiple masses in an IR/UV-IDS experiment.

2-dimensional text format with the HDF5 tool library. Then the data was further formatted, calibrated for wavelength/laser power and compiled, with the programs *ReadOut_HDF5Dump.vi*, *IRUV_Tool_v10.vi*, *FELIX_correction_6th_o_2015_09_26.vi*

and *IRUV_Average.vi* provided by Dr. Philipp Constantinidis.[154] Subsequently, general data processing was performed using the OriginPro suite.

The raw data include the signal of the traces with IR+UV intensity I_{IR+UV} and only UV intensity I_{UV}. The ion dip spectrum can then be calculated by Eq. 2.12

$$I_{IR/UV}(\tilde{\nu}) = log\left(\frac{I_{UV}(\tilde{\nu})}{I_{IR+UV}(\tilde{\nu})}\right) \tag{2.12}$$

which provides the IR spectrum for each mass observed in the experiments. This spectrum is further corrected for potential deviations in laser power and wavelength calibration. The calibration data, measured several times between measurements, is fitted with a second/third order polynomial for the wavelength calibration and a sixth-order polynomial for the power calibration. The final IR spectra of the species are then generated by averaging multiple scans of the same species to improve the quality. For better identification, the spectra are further smoothed using digital Savitzky-Golay filtering.

The vibrational DFT calculations for identification of the species were performed using the Gaussian09 suite of programs.[191] The molecule geometries were created in GaussVIEW 5.0 and the calculation were conducted on the cluster of the *Leibnitz-Rechenzentrum der Bayerischen Akademie der Wissenschaften*. The essential IR spectra were then evaluated and convolved using either GaussVIEW 5.0 or Chemcraft. Afterward, the calculated IR spectra were scaled if necessary.

2.4 Experimental Setup for IR/UV Ion Dip Spectroscopy

The experimental setup for all IR/UV-IDS experiments conducted at the FELIX laboratory is depicted in Fig. 2.14.

The molecular beam source, as described in Section 2.1.3, is mounted to the source chamber of the TOF-MS. Here, an ISO-160-KF flange adapter is used, as the original mounting port of the source chamber is incompatible with a 160-KF flange. The vertical and horizontal position of the beam source can be adjusted via screws on the adapter for alignment of the molecular beam with respect to the source chamber and the skimmer. For seeding, a PVC tube is attached to the source and connected to the in-house gas distribution system. This provides a noble gas flow (He or Ar) in the range between 0.6 - 3.0 bar absolute. Several turbomolecular pumps evacuate the entire apparatus, and pressure gauges monitor the pressure at relevant positions. The produced free jet is expanded into the vacuum of the source chamber at around 10^{-4}-10^{-6} mbar and subsequently skimmed entering the

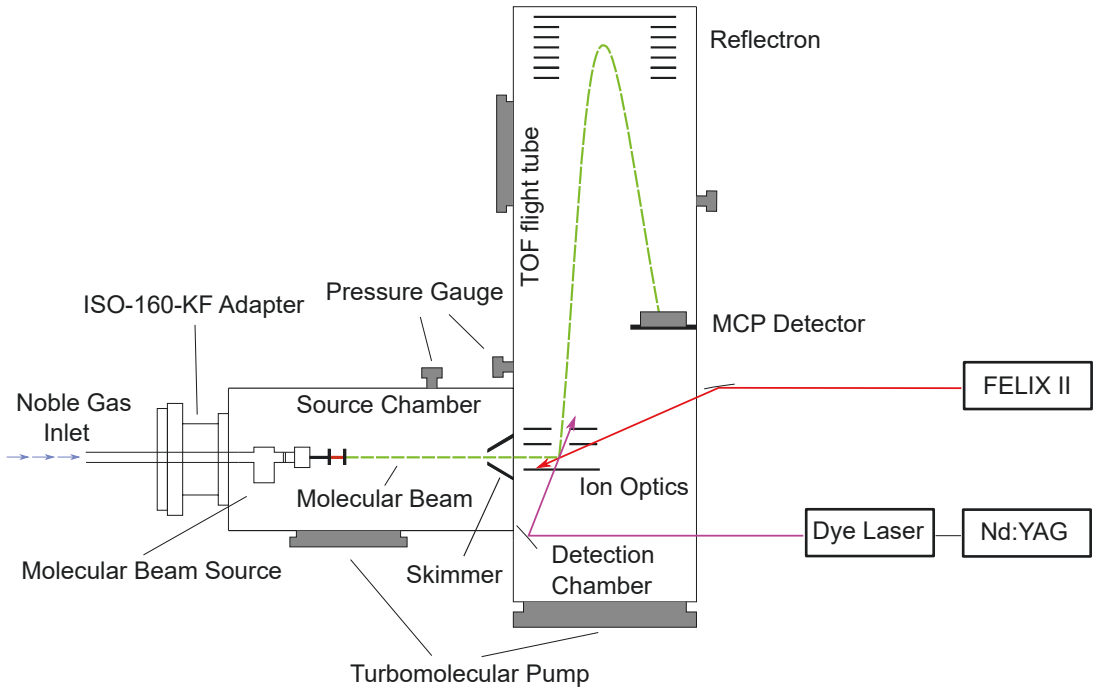

Figure 2.14: Complete schematic overview of the experimental setup utilized in the IR/UV-IDS experiments at the *FELIX Laboratory*, including molecular beam source, TOF-MS apparatus, and beam paths.

ionization region of the main chamber (10^{-6}-10^{-7} mbar). Here the molecular beam is crossed by UV and IR radiation to conduct the IR/UV-IDS experiment. Finally, the produced ions are detected via TOF-MS (*Jordan*).

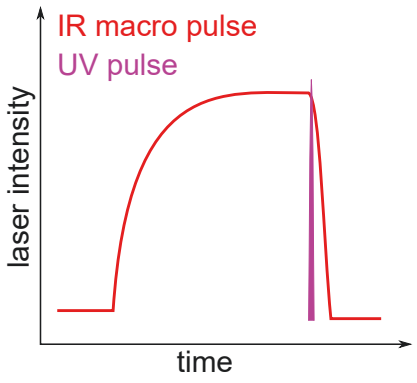

Figure 2.15: Time dependency between IR and UV radiation.

The UV radiation is provided by a Nd:YAG pumped ns dye laser. Typical laser dyes employed to study hydrocarbon radicals and PAHs produce frequency-doubled light in the range between 240-300 nm and include dyes like Coumarines, Pyridines, and Rhodamines. The scannable IR radiation for the fingerprint region is provided by the free-electron laser FELIX, as described in Section 2.5. The dye laser is usually operated at 20 or 10 Hz and FELIX at 10 or 5 Hz. This means that the irradiation of the samples alternate between IR+UV and UV, which minimizes the effect of potential changes in the characteristics of the

molecular beam or the lasers. For measurements in the fingerprint region, the FEL is scanned from ca. 500-1800 cm^{-1}. Here, a step width between 2.0-2.5 cm^{-1} has proven to be a good trade-off between resolution and measuring time. For each IR wavelength, the signal is averaged over 20-50 mass spectra to account for small fluctuations. All timings are controlled by a delay generator (*DG645, Stanford Research Systems*). The master-trigger t_0 is provided by FELIX II, and all other timings are adjusted with respect to t_0. The temporal overlap between IR and UV is chosen in a way that their maximum signal intensity overlap, as depicted in Fig. 2.15.

In earlier experiments, the IR light propargated perpendicular to the molecular beam and opposite to the UV light (see Fig. 2.16). Although this geometry works fine, it can sometimes be challenging to overlap both lasers with the molecular beam and can only be done during beam time when the FEL is running. In later experiments, the setup was changed so the IR radiation enters the detection chamber opposite the molecular beam trajectory. This approach allows aligning the IR path with a HeNe service laser without the FEL running. Thus, the laser can be aligned optically through the skimmer, which guarantees a full overlap of the IR radiation with the molecular beam. Consequently, the UV laser can readily be aligned via the TOF mass signal. Only small optimization of the IR alignment must be performed during a beam shift to optimize the depletion signal.

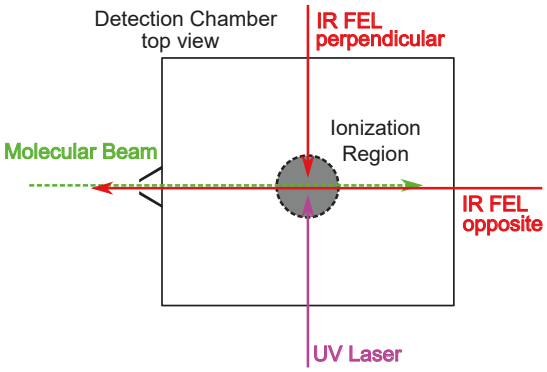

Figure 2.16: Depiction of the two beam path configurations utilized in this thesis.

2.5 Free Electron Lasers and FELIX

Free Electron Lasers (FEL) are a class of light sources that produce coherent high brilliance radiation. These devices can be operated in various configurations producing light around a narrow spectral bandwidth from the microwave to the X-ray regime. The light is generated by a beam of relativistic electrons injected into an undulator and forced on a sinusoidal trajectory by an external magnetic field. Hereby, the radiation is produced by electrons emitting bremsstrahlung in a small cone along the trajectory. Thus electrons serve in FELs as both the pump- and lasing-medium. The fundamental principle of FEL radiation was discovered by John Madey[192] in 1971, and the first FEL in the infrared region was constructed during the ´70s at Stanford University.[193–195] The increased interest in these high-power light sources, especially for the x-ray regime, led to the construction of several FELs in the last two decades.[196] For example, for the European Union, multiple FEL facilities collaborate in the *FELs of Europe* project, including IR-FELs like CLIO[197], FELBE[198], FELIX[199], and TARLA[200], as well as X-ray FELs like FERMI[201], FLASH[202], European X-FEL[203], MAX IV FEL[204], SwizzFEL[205], and PolFEL.[206] Beamtime at these facilities faces increasing demand as application numbers are growing annually. The FEL radiation is employed in a wide variety of different scientific areas in basic research. Still, FELs recently also started finding their way into different fields like medicine[207] and military applications.[208]

As mentioned above, FELs can be operated in various configurations, depending on the required characteristics of the radiation. For simplification, they can usually be classified into two groups: low-gain and high-gain FELs. Low-gain FELs utilize mirrors to produce undulator radiation within an optical resonator. The lack of highly reflective materials for shorter-wavelength light, however, prohibits the same approach, e.g., for X-ray FELs. Thus, the light amplification has to be achieved in a single undulator pass cycle, which requires a longer undulator length and comes with additional technical challenges.[195] In the following section, the fundamental operating principles of a low-gain compton FEL will be discussed briefly. These include FELIX, which was utilized in all IR/UV experiments in this thesis. For a more in-depth treatment of the physical and engineering fundamentals, refer to the cited literature.

2.5.1 Basic Operating Principles of Low-Gain Compton FELs

Figure 2.17 shows a minimal working layout of a low-gain FEL. These are often referred to as FEL oscillators, and the term *low-gain* comes from the fact that the radiation field is only amplified by a few percent per electron injection.

The initial electron beam is produced by an electron gun, usually a thermionic triode. The beam is subsequently shortened by an rf buncher before being injected into a linear accelerator (LINAC). Here the electrons are accelerated to the desired energies. Usually, traveling-wave radio-frequency LINACs are employed, which provide constant acceleration of the electrons and preserve beam characteristics. Finally, the electron beam is guided through an undulator to generate the radiation.[209]

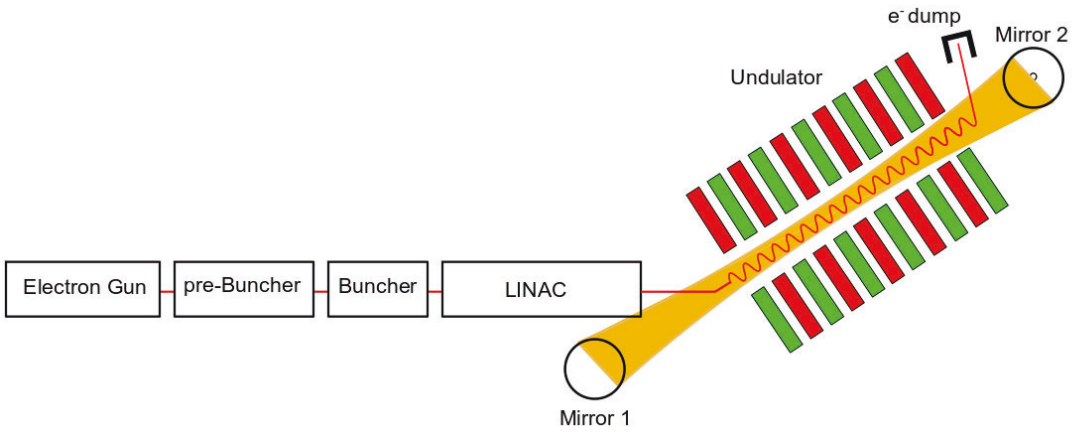

Figure 2.17: Basic illustration of a low-gain FEL with electron beam generation and undulator.

The undulator is the central piece of every FEL. It consists of two rows of permanent magnets, which generate a magnetic field between the two rows. The distance between two magnets with the same polarity within a row is defined as the undulator period λ_u. An undulator can be characterized using the undulator parameter K given in Eq. 2.13:

$$K = \frac{eB_0\lambda_u}{2\pi m_e c} = 0.934 B_0 \lambda_u \tag{2.13}$$

The undulator period is a constant parameter for any given undulator. The magnetic field B_0 can be modified by changing the distance between the two magnet rows to alter K.[209] When the electron beam enters the undulator, they are forced on

a perpendicular sinusoidal trajectory by the magnet field. Here, the electrons start to produce spontaneous emission. This radiation is initially very weak and is not coherent as the size of the electron bunches is bigger than the emission wavelength. The electrons emit the radiation at a maximum angle of Θ_{max} according to Eq. 2.14:[195]

$$\Theta_{max} \approx \left[\frac{dx}{dz}\right]_{max} = \frac{K}{\beta\gamma} \approx \frac{K}{\gamma} \tag{2.14}$$

with the Lorentz Factor γ:

$$\gamma = \frac{1}{\sqrt{1-(\frac{v}{c})^2}} \geq 1 \tag{2.15}$$

Fulfillment of $\Theta_{max} \leq \frac{1}{\gamma}$ is important to allow the emitted radiation to spatially overlap for constructive interference. This condition is fulfilled for undulators as $K \leq 1$. Furthermore, a small angle results in radiation with a small spectral bandwidth centered around a resonance wavelength. This is an important advantage of FELs as the majority of the energy is converted into nearly monochromatic light, as opposite to wigglers (K>>1) or traditional bending magnets, which produce a more continuous spectrum.[195]

The radiation produced by spontaneous emission and later the stimulated emission are both Doppler shifted by a factor of $\approx \gamma^2$ and have to fulfil the resonance condition given in Eq. 2.16:

$$n\lambda_l = \frac{\lambda_u(1+K^2)}{2\gamma^2} \tag{2.16}$$

The radiation produced so far by spontaneous emission is weak and not coherent. To produce strong and coherent laser radiation, a coherency dependency between the electrons has to be established. This procedure is called microbunching. Here, the electron bunches are sub-divided into several small microbunches, separated by one wavelength λ_l. This is accomplished by modulating the electron velocity through energy exchange with the electric field of the light within the resonator. The energy transfer is efficient when the electric field vector E_x of the light and the transverse electron velocity component v_x point in the same direction. This can easily be described for multiple configurations by considering the ponderomotive phase ϕ_0, reflecting the relative phase conditions between the light and electron trajectory at t=0 (see Fig. 2.18).[195] Case a and b show the situation when energy is exchanged between an electron and the radiation. The electron can either be slowed down (a, $\Psi_0 = 0$) by energy transfer to the light or accelerated vice versa (b, $\Psi_0 = -\pi$). This change in longitudinal electron velocity along the undulator

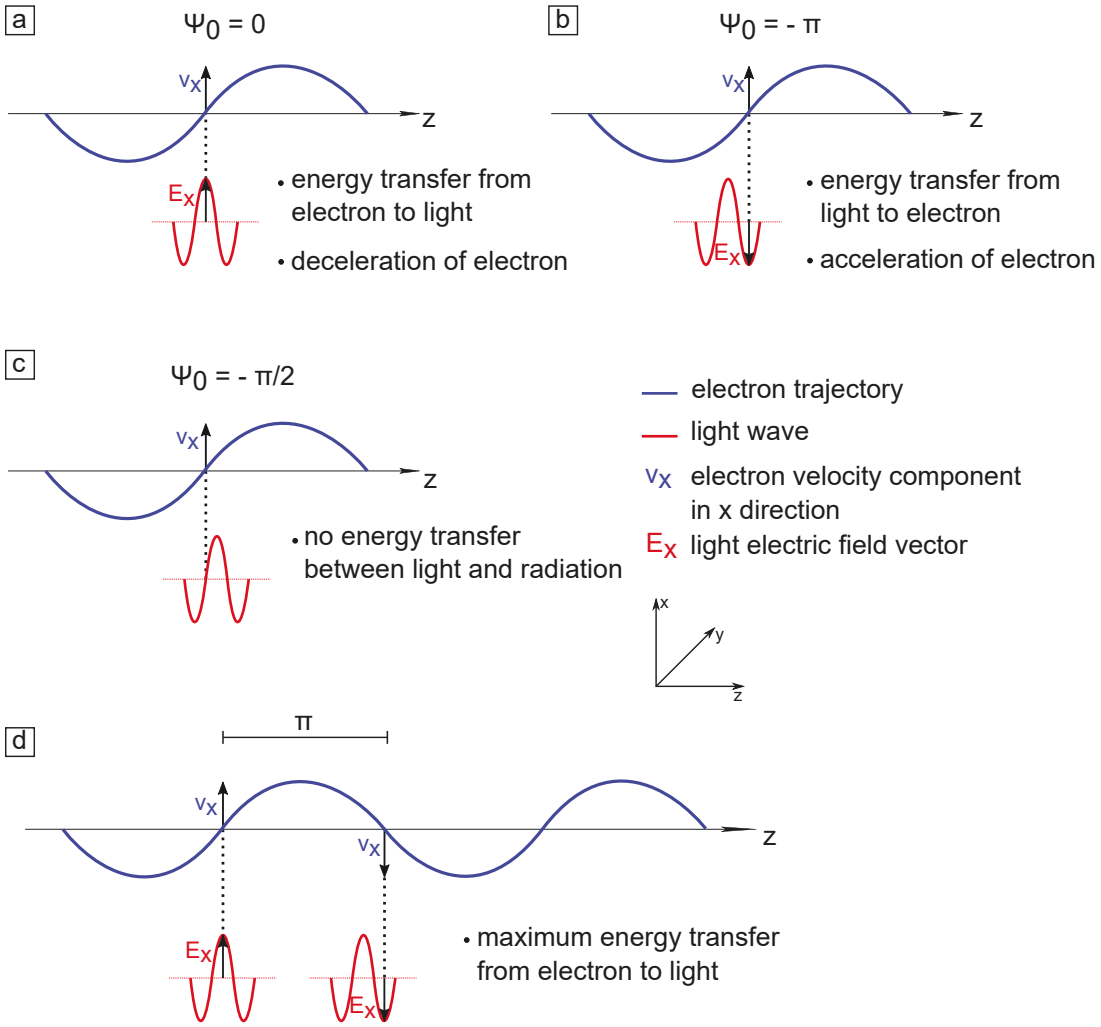

Figure 2.18: Important phase conditions between electron beam (blue) and light wave (red) in FEL light generation.

will change the electron density distribution over several undulator periods and form microbunches (see Fig. 2.19, left).

These microbunches are separated by λ_l and emit light approximately like a single particle. This effect increases the light intensity drastically and also establishes the necessary coherency for the FEL radiation. Additionally, for proper FEL operation, a certain phase correlation must be maintained for large parts of the undulator so that the light can be amplified. Otherwise, the radiation would dump energy back into the electron beam, which is obviously not desirable. As seen before, energy transfer from an electron to a light wave is achieved at $\Psi_0 = 0$ (see Fig. 2.18, a). It can easily be achieved at the beginning of the undulator (t=0) by choosing proper phase conditions. However, the longitudinal velocity of the light ($v_{l,z} \approx c$) and the electrons ($v_{e,z} < c$) are different, resulting in an inherent time dependency of the ponderomotive phase Ψ. To maintain the necessary phase for light amplification, the light wave has to *slip* by $\frac{\lambda_l}{2}$ per half electron period π during the propagation through the undulator as displayed in Fig. 2.18, d.[210] This slippage is only allowed for a certain wavelength, but luckily these have already been considered in the resonance conditions in Eq. 2.16.[195]

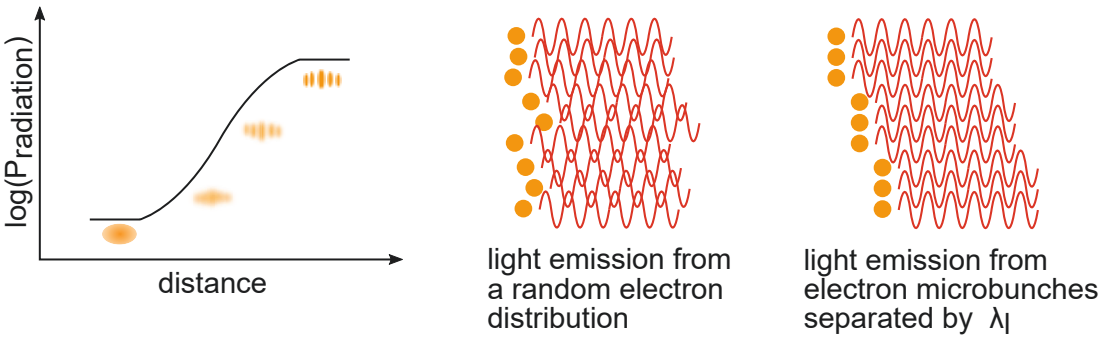

Figure 2.19: Principle of microbunching and coherent light generation. Adapted from Ref.[211]

Microbunching and effective energy transfer represent the fundamental gain-mechanism in low-gain FELs. Once these conditions are met, the intensity I of the generated radiation scales drastically with the number of injected electrons N_e; approximately $I \propto N_e^2$ compared to the intensity of the spontaneous emission $I_{sp} \propto N_e$.[196] Besides the high brilliance, the FEL radiation also has a narrow linewidth. The spectral bandwidth can be derived from the wave train produced by an electron moving through an undulator with N_u periods. The electric field of the radiation develops according to Eq. 2.17 during the time $T = \frac{N_u \lambda_l}{c}$.[195]

$$E_l(t) = \begin{cases} E_0 e^{-i\omega_l t} & \text{, if } -T/2 \leq t \leq T/2 \\ 0 & \text{, else} \end{cases} \tag{2.17}$$

The lineshape can then be obtained by Fourier transformation of the electric field according to Eq. 2.18:

$$A(\omega) = \int_{-\infty}^{\infty} E_l(t) e^{-i\omega t} dt = E_0 \int_{-T/2}^{T/2} e^{-i(\omega_l - \omega)t} dt = 2E_0 \frac{sin((\omega_l - \omega)T/2)}{\omega_l - \omega} \tag{2.18}$$

The lineshape can then be plotted with the intensity I:

$$I(\omega) \propto |A(\omega)|^2 \propto (\frac{sin\xi}{\xi})^2 \tag{2.19}$$

with

$$\xi = \frac{(\omega_l - \omega)T}{2} = \pi N_u \frac{\omega_l - \omega}{\omega_l} \tag{2.20}$$

Figure 2.20 shows that the radiation is centered around its resonance frequency ω_l with a short FWHM of

$$\Delta\omega \approx \frac{\omega_l}{N_u} \tag{2.21}$$

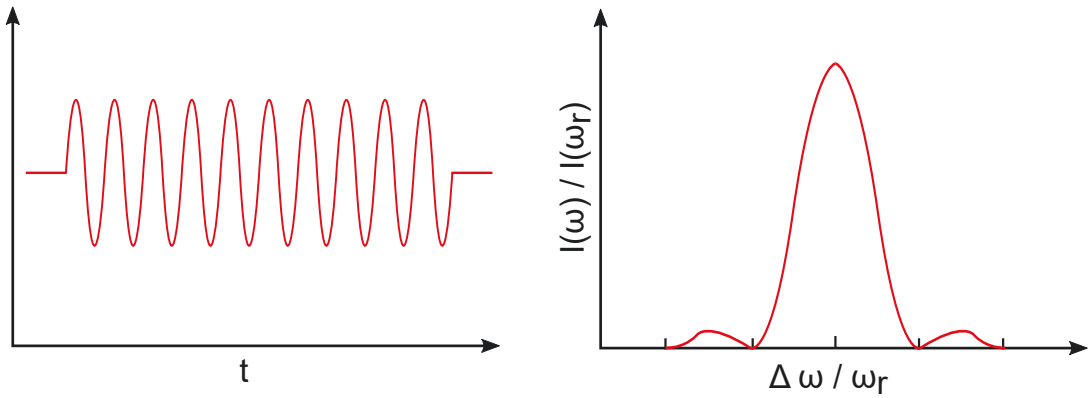

Figure 2.20: Depiction of a 10-fold wave train on the left and the resulting lineshape on the right.

For a more comprehensive treatment on FEL theory, the book *Ultraviolet and Soft X-Ray Free-Electron Lasers* by Peter Schmüser et al.[195] is recommended, as it lays out all necessary physical and mathematical fundamentals of FEL operation.

2.5.2 The Free Electron Laser FELIX

All IR/UV experiments in this thesis have been conducted utilizing the *Free Electron Laser for Infrared eXperiments* (FELIX) as a high power IR source in the mid-IR region. The FEL is located at the *FELIX Laboratory* of the *Radboud University* in Nijmegen, the Netherlands. FELIX features two undulators FELIX-1 and FELIX-2 which produce IR radiation in the range of 30-150 μm and 3-45 μm, respectively.

Table 2.1: Overview of the Beam Characteristics of the two Undulators FELIX-1 and FELIX-2.

Experimental Parameters		
Parameter	Value	Unit
Spectral Range	30 - 150	μm
(FELIX-1)	333 - 66	cm^{-1}
Spectral Range	3 - 45	μm
(FELIX-2)	3333 - 222	cm^{-1}
Repetition Rate (Micropulse)	20, 50 or 1000	MHz
Energy (Micropulse)	< 40	μJ
Repetition Rate (Macropulse)	< 10	Hz
Energy (Macropulse)	< 200	mJ
Spectral Bandwidth	0.4 - 5.0	%
Polarization	$> 95\%$ linear	

Micropulses are generated at a repetition rate of 25, 50, or 1000 MHz with up to 40 μJ of pulse energy. At 1 GHz, this translates to a macropulse energy of up to 200 mJ and a repetition rate of up to 10 Hz. The spectral bandwidth of these macropulses depends on the photon energy produced and is typically in the range of 0.4-5.0 % of the central wavelength. The resulting radiation is linear polarised (> 95 %) with respect to the undulator orientation. Finally, the light is transported to the end-user stations via an evacuated mirror-based light guidance system. Note that for samples sensitive to high power IR radiation, the light can be attenuated by several dB. This can prevent oversaturation effects such as line broadening and IR-induced molecular dissociation.

For the experiments in this thesis, FELIX was operated at either 5 Hz (10 Hz UV excitation) or 10 Hz (20 Hz UV excitation). Furthermore, FELIX-2 was employed to generate IR radiation for the scans in the fingerprint region from ca. 500-1800 cm^{-1}. Although the undulator is more than capable of covering the necessary spectral range (3-45 μm / 3333-222 cm^{-1}), it is not possible to perform

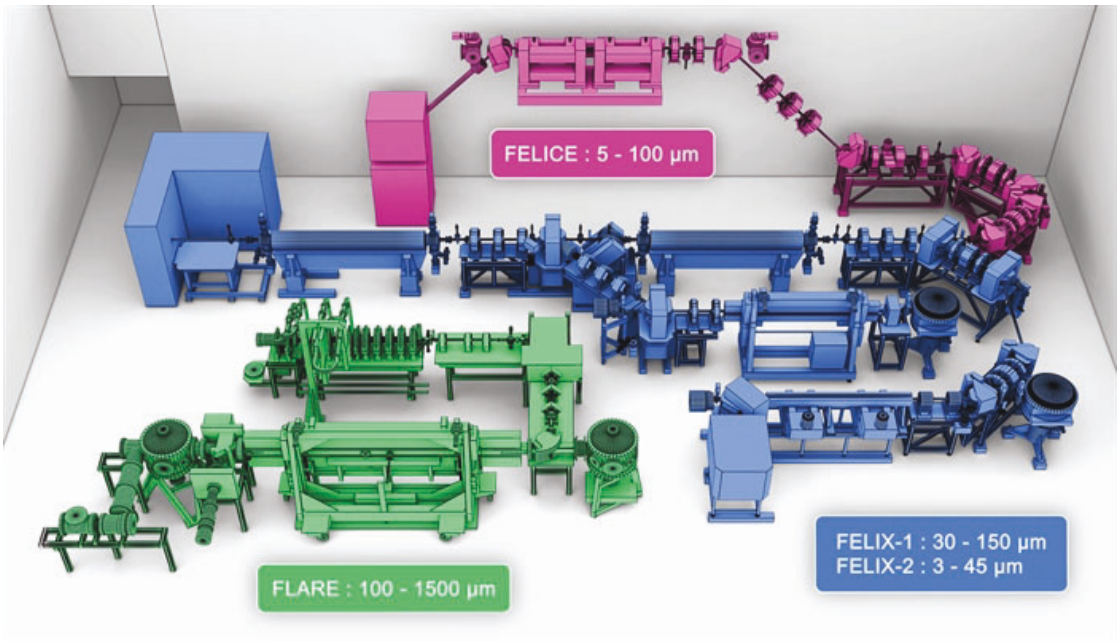

Figure 2.21: Illustration of all light sources in the *FELIX Laboratory Vault* including FLARE (green), FELICE (pink) and FELIX (blue).[212]

the fingerprint scan in a single measurement, as the undulator parameters have to be adjusted in between. Thus, the fingerprint region was usually split into two equal parts, and the whole range was scanned in two measurements. To account for drifts and inconsistencies in wavelength calibrations as well as fluctuations in output power, calibration scans of the IR radiations were performed in between measurements to correct the experimental data.

2.5.3 Technical Details FELIX

A simplified sketch of FELIX is shown in Fig. 2.22. An injector consisting of a 1 GHz thermic triode electron gun, a 1 GHz prebuncher, and a 4 GHz buncher produces a pulsed electron beam of ≈ 4 MeV. Two traveling-wave radio linear accelerators (LINAC) accelerate the electrons up to 25 MeV (for FELIX-1) or 45 MeV (for FELIX-2) before the beam is directed to the respective undulator.

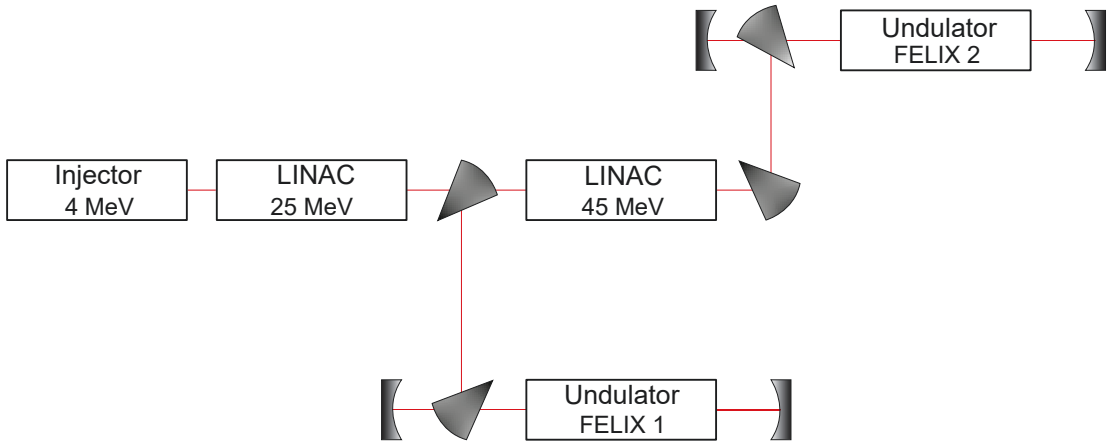

Figure 2.22: Schematic of FELIX-1 and FELIX-2 with their respective LINACs and undulators.

Both undulators are identical in construction and include 38 field periods of samarium-cobalt permanent magnets of 65 mm length. The spacing between the two magnet rows can be modified to adjust the center wavelength of the produced radiation. The undulators are located in a cavity between two gold-plated copper mirrors, forming a resonator of 6 m in length. To prevent absorption of the IR radiation by atmospheric gases and water vapor, the complete optical path is evacuated, and spaces between machines are bridged by optical beam tubes. In operation, a small part of the radiation in the cavity is coupled out via a hole in the downstream mirror and transported to the end user stations.[209]

Chapter 3

Results

3.1 Ortho-Benzyne

3.1.1 Introduction

Ortho-benzyne is a particularly interesting molecule because of its uncommon electronic structure. Using simple valence bond nomenclature, it can be represented in three forms as illustrated in Fig. 3.1: Cumulene, biradical, and Kekulé.

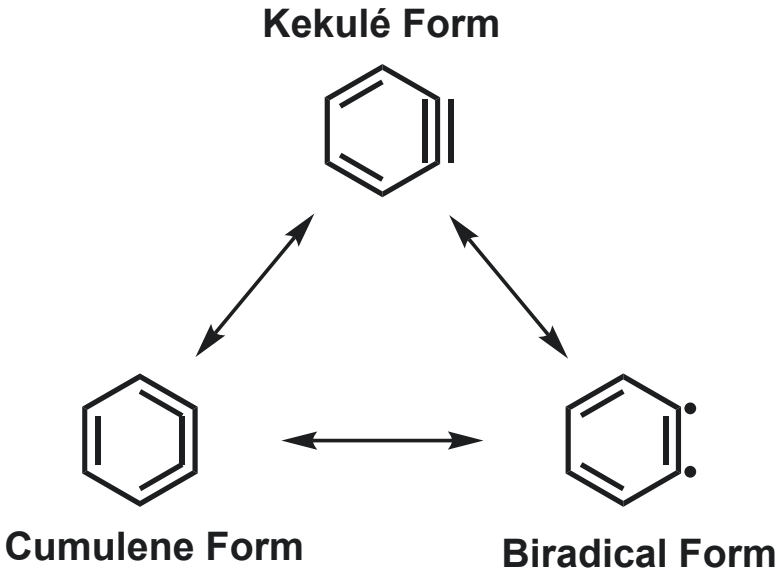

Figure 3.1: Three ways to describe the electronic structure of the ortho-benzyne: Cumulene, biradical, and Kekulé.

The cumulene form has been identified in the liquid phase utilizing molecular containers and NMR spectroscopy.[213] This is especially intriguing as ortho-benzyne has been discussed as an important reactive intermediate in the field of nucleophilic aromatic substitution.[87,214,215] Isolated, however, experiments show that o-C_6H_4 displays mainly aryne character in low-temperature environments or the gas-phase. The IR spectrum was measured in several matrix isolation studies[216–219] since the early '70s, and its gas-phase structure was determined utilizing microwave spectroscopy.[220,221] Since o-C_6H_4 can also be considered a biradicaloid, the energy difference between singlet and triplet is of particular interest. Zhang and Chen[222] measured the gap by utilizing photoelectron spectroscopy and Wenthold et al.[223] employed UV spectroscopy.[224]

Besides the interest in the characteristics of ortho-benzyne itself, o-C_6H_4 has been considered an important molecule in PAH formation. Although it is not stable

under ambient conditions, studies suggest that it can be formed via unimolecular decomposition from benzene and the phenyl radical.[225,226] Such a reaction could be induced, for example, by cosmic radiation in the interstellar medium, where the benzene precursor has already been identified in the protoplanetary nebula CRL 618.[227] However, a study by Widicus Weaver and coworkers was not able to identify ortho-benzyne in the Ku-, K- or Q-band of CRL 618.[228] This leads to the conclusion that either other spectroscopic methods have to be applied to identify o-C_6H_4 in the ISM or the potential formation of ortho-benzyne in clouds like CRL 618 has to be reconsidered.[228]

Figure 3.2: Picture of the Westbrook Nebula CRL 618 taken by the Wide Field Camera 3 of the Hubble Space Telescope. Graphic published in the public domain by NASA and ESA.

However, taking a look at other high-temperature environments, ortho-benzyne might play a very important role in the formation of PAHs in the combustion of fuels. Here it is especially important to understand the underlying mechanisms in the growth of these molecules, as these PAHs and the resulting soot are emitted in the surroundings of humans and are considered to be carcinogenic. Although modern gasoline manufacturers have strict limits for the benzene content in their blends, these fuels may still contain up to 1% benzene. Furthermore, substances introduced to replace the harmful benzene like xylene and other methylated benzene derivatives may also decompose to phenyl and consequently ortho-benzyne during combustion. Moreover, Zhang and coworkers showed in crossed molecular beam experiments that ortho-benzyne could be formed in a bimolecular reaction between the ethynyl radical (C_2H) and vinylacetylene (C_4H_4), both species commonly present in hot flame experiments.[224]

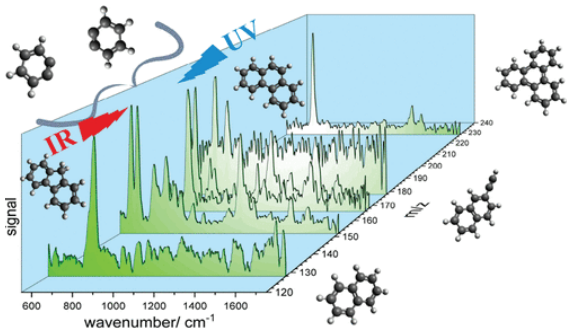

Figure 3.3: TOC graphic of the ortho-benzyne publication *Self-Reaction of ortho-Benzyne at High Temperatures Investigated by Infrared and Photoelectron Spectroscopy* as published in J. Phys. Chem. A. Adapted with permission from Ref.[229]

To better understand the involvement of ortho-benzyne in the growth of PAHs, IR/UV ion dip experiments were conducted to identify the formed reaction products via their infrared spectrum. This methodology allowed to identify the self-reaction products of ortho-benzyne up to mass 228 by comparing their gas-phase IR spectra to vibrational calculations. The results of this study are complemented with photoelectron spectroscopy experiments by Engelbert Reusch to identify smaller reaction products. Most of the following information is taken from the published article in the Journal of Physical Chemistry A.[229]

3.1.2 Experimental Parameters

Ortho-benzyne **2** was generated in a pyrolysis SiC flow reactor from benzocyclobutendione **1**. The precursor was heated to approximately 132 °C to improve vapor pressure and seeded in 1.4 bar Argon. A pulsed molecular beam (20 Hz) was produced by a solenoid valve and **1** was cleaved in the resistively heated microreactor before entering the source chamber of a TOF-mass spectrometer via adiabatic expansion.

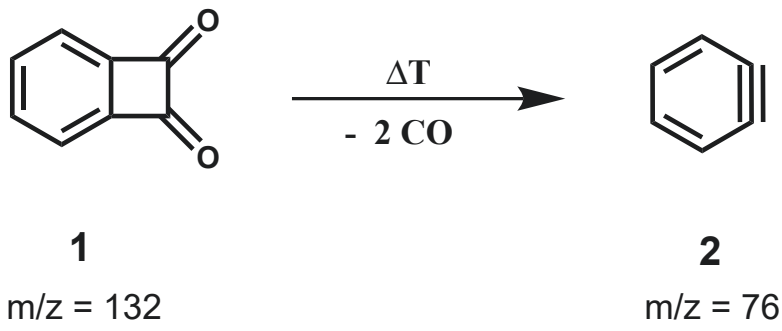

Figure 3.4: The thermal decomposition of benzocyclobutendione produces ortho-benzyne via the elimination of carbon monoxide.

Here, the cold inner part of the molecular beam is skimmed, entering the main chamber and ionization region. For the double resonant experiment, UV and IR beam were spatially overlapped in the ionization region of the ion optic. The produced ions are detected using time-of-flight mass spectrometry. Time-wise, the FEL-IR was fired 200 ns before the UV laser, which was optimized to maximize the depletion signal.

The 265 nm UV radiation was produced by a frequency-doubled Nd:YAG pumped dye laser with approx. 1 mJ of output power at a 20 Hz repetition rate. The ionization followed a [1+1]-REMPI scheme, which is suitable to de-

Table 3.1: Overview of the Experimental Parameters of the ortho-Benzyne IR/UV Experiments.

Experimental Parameters	
Parameter	Value
Precursor	$C_8H_8O_2$
UV Wavelength	265 nm
UV Energy	1 mJ
UV Delay	200 ns
Ionization Scheme	[1+1]-REMPI
UV Repetition Rate	20 Hz
IR Scan Range	550 - 1750 cm^{-1}
IR Step Width	2.5 cm^{-1}
IR Repetition Rate	10 Hz
Seeding Gas	Argon
Seeding Pressure	1.4 bar

tect a large variety of different PAHs. A free-electron laser provided the IR radiation at the *FELIX Laboratory* (*Free Electron Laser for Infrared eXperiments*, Nijmegen, the Netherlands). The FEL was scanned over the fingerprint region from 550-1750 cm^{-1} at a repetition rate of 10 Hz and step width of 2.5 cm^{-1}. The resulting ion dip spectra were corrected for IR laser power, averaged, and finally smoothed using Savitzky-Golay filtering. For identification, the mass-selected IR spectra were compared to vibrational DFT calculations at a B3LYP/6-311G** level of theory. Due to the harmonic nature of those calculations, the harmonic energies were scaled by a factor of 0.967 (m/z= 128 with 0.976) to account for an anharmonic correction, and the resulting stick spectra were convolved with a Lorentzian (FWHM = 8 cm^{-1}) for a better comparison with the experimental data.

3.1.3 Results and Discussion

3.1.3.1 Mass Spectra of the Decomposition of Benzocyclobutendione

The relative beam composition of the pyrolysis of **1** is depicted in the upper trace of Fig. 3.5 in a 118 nm SPI mass spectrum. It shows a complete conversion of the precursor (m/z = 132) and the formation of lighter and heavier reaction products.

The major decomposition product appears at m/z = 76 (C_6H_4), which is consistent with the formation of ortho-benzyne in the experiment. Further peaks at lower masses can be observed at m/z = 39 (C_3H_3), m/z = 50 (C_4H_2) and m/z = 67 (C_5H_7). These may result from further thermal decomposition during pyrolysis, DPI processes during photoionization, or fragmentation caused by strong IR excitation. Intermediate masses show peaks at m/z = 104 (C_8H_8) and m/z = 122 (C_9H_{14}). Masses that lie in between the precursor and the target molecule are often meta-stable intermediates in the precursor decomposition reaction. However, a formation via molecular growth from smaller reactive species or decomposition from heavier reaction products has to be considered as well. These heavier molecules can be seen in the MS at m/z = 148 ($C_{11}H_{16}$), m/z = 152 ($C_{12}H_8$) and m/z = 176/177 ($C_{13}H_{20}$). They are usually formed in the microreactor during pyrolysis, and mass 152 represents the dimerization product of ortho-benzyne, which at the same time constitutes the second strongest peak in the MS.

A [1+1]-REMPI mass spectrum is depicted in the lower trace of Fig 3.5. Comparing it to the 118 nm SPI spectrum, additional masses are visible as molecules with a suitable UV-chromophore (e.g., many PAHs) are efficiently ionized in a [1+1] process and can be detected in a lower concentration. Two intense bands dominate the spectrum at m/z = 152 ($C_{12}H_8$) and m/z = 228 ($C_{18}H_{12}$), both probably resulting from direct ortho-benzyne self reactions. Other signals represent typical

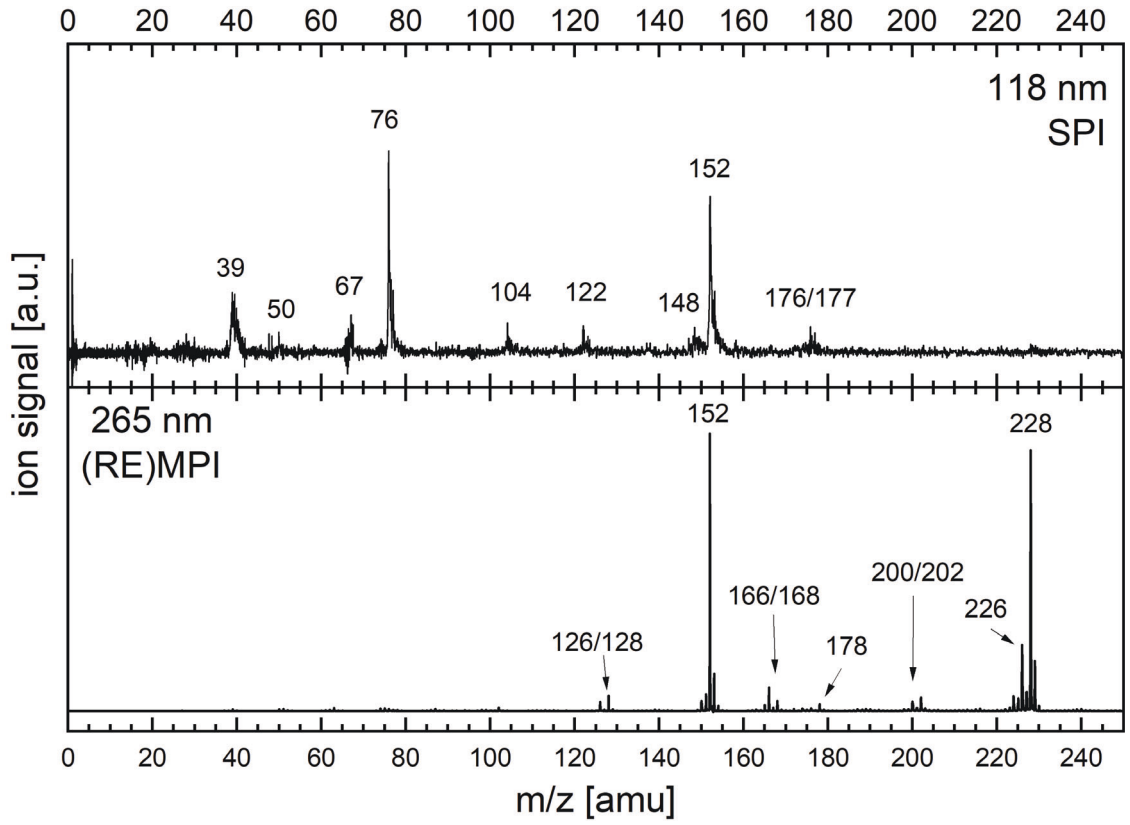

Figure 3.5: Mass spectra of pyrolytically cleaved benzocyclobutendione measured by 118 nm SPI (top trace) and 265 nm [1+1]-REMPI (bottom trace) in the range from 0 to 250 amu.

PAH masses often observed in high-temperature experiments like m/z = 126/128 ($C_{10}H_6/C_{10}H_8$), m/z = 166/168 ($C_{13}H_{10}/C_{13}H_{12}$) and m/z = 178 ($C_{14}H_{10}$). Masses 200/202 and 224/226 are dissociative photoionization products of mass 228, and their IR spectra are presented in the Appendix (Fig. A.5).

3.1.3.2 Mass 128: Naphthalene

The lightest molecule in the experiment, which can be identified by IR/UV ion dip spectroscopy, is mass 128 ($C_{10}H_8$). The gas-phase IR spectrum of this mass is depicted in Fig. 3.6 in comparison to vibrational calculations of naphthalene. Both spectra match very well, and hence the carrier of mass 128 can be identified as naphthalene. Naphthalene displays only a single strong vibrational mode at 781 cm^{-1} in the region from 550 - 1750 cm^{-1} due to its high D_{2h} symmetry. It is commonly observed in high-temperature environments, and it can be formed via

various reactions. In our case, we mainly attribute its formation to a condensation reaction Eq. 3.1 between ortho-benzyne and benzene. C_6H_4 is purposefully generated in the pyrolysis. Although a mass of 78 is not easily visible in the SPI mass spectrum, benzene was identified in the molecular beam via MS-TPES as well.[229]

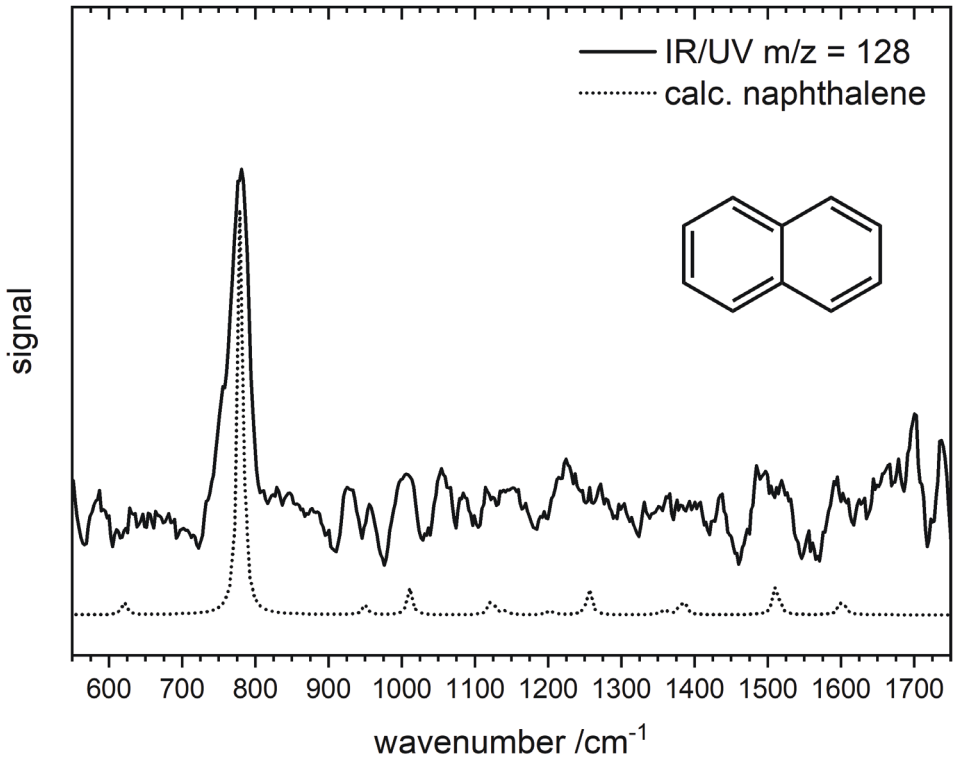

Figure 3.6: The IR/UV spectrum of m/z=128 (solid line) from the decomposition of benzocyclobutendione in comparison with vibrational DFT calculations of naphthalene (dotted line). Adapted with permission from Ref.[229]

$$o-C_6H_4 \; + \; C_6H_6 \rightarrow \; C_{10}H_8 \; + \; C_2H_2, \; \Delta_R H(0\ K) \; = \; -163\ kJ\ mol^{-1} \quad (3.1)$$

This pathway was thoroughly investigated theoretically by Comandini and Brezinsky[230]. The authors showed that in Eq. 3.1 the reactants initially form a benzobicyclo[2,2,2]octatriene (see Fig. 3.7) intermediate in a 1,4-cycloaddition (radical/π bond insertion) reaction. The barrier for this first reaction was calculated to be relatively low with 28 kJ mol^{-1}, which is readily available within a pyrolysis reactor. The subsequent dissociation to naphthalene and acetylene is furthermore energetically preferred compared to its back-reaction by 56 kJ mol^{-1}. The study

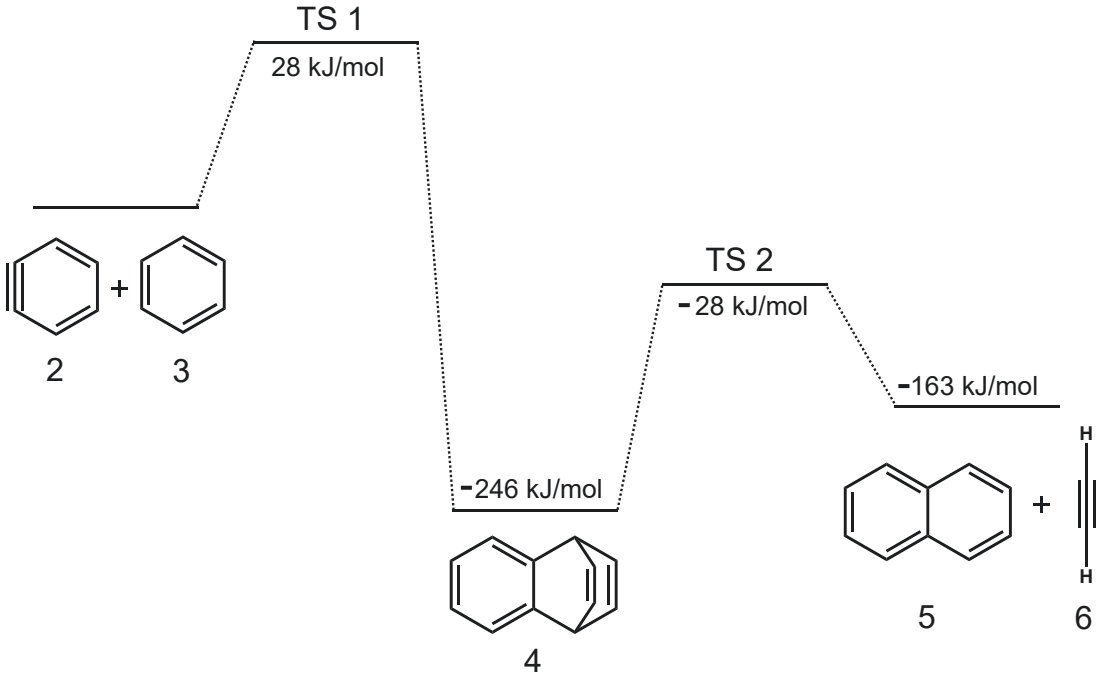

Figure 3.7: Energetics of the formation of naphthalene from ortho-benzyne and benzene. The reaction proceeds via a benzobicyclo[2,2,2]octatriene intermediate. Graphic adapted from Ref.[230]

also revealed a particularly high-temperature dependency of the rate constants for the decomposition reaction of the intermediate. This might explain why the intermediate can not accumulate significantly to be identified in the experiments at high temperatures, which would appear at m/z = 134.

3.1.3.3 Mass 152: 2-Ethynylnaphthalene and Biphenylene

Mass 152 corresponds to a hydrocarbon molecule with $C_{12}H_8$ composition and also resembles the direct dimerization product of ortho-benzyne. Reasonable carriers for this peak are 2-ethynylnaphthalene and biphenylene, both typical PAHs formed in hot flames. Their calculated IR spectra compared with the experimental IR/UV data are depicted in Fig. 3.8 (right). Here, the carrier can easily be identified as 2-ethynylnaphthalene by its very pronounced structure from 600-1000 cm^{-1}, which is very well represented in the experimental and theoretical spectrum. The vibrations in this region mainly resemble ring modes, which are particularly characteristic for 2-ethynylnaphthalene due to its low symmetry. Small deviations in signal intensity result from harmonic approximations in the calculations, as they do not account for

anharmonicity and the influence of overtones or combination bands. In fact, the vibrational mode at 1211 cm^{-1} is a combination band/overtone of the C≡C—H bending mode and can serve as a distinct probe for similar compounds with free terminal ethynyl side chains.[231–233] Its formation can be explained by a HACA type growth reaction of naphthalene and acetylene (see Eq. 3.2).

$$C_{10}H_8 \ + \ C_2H_2 \rightarrow \ C_{12}H_8 \ + \ H_2 \tag{3.2}$$

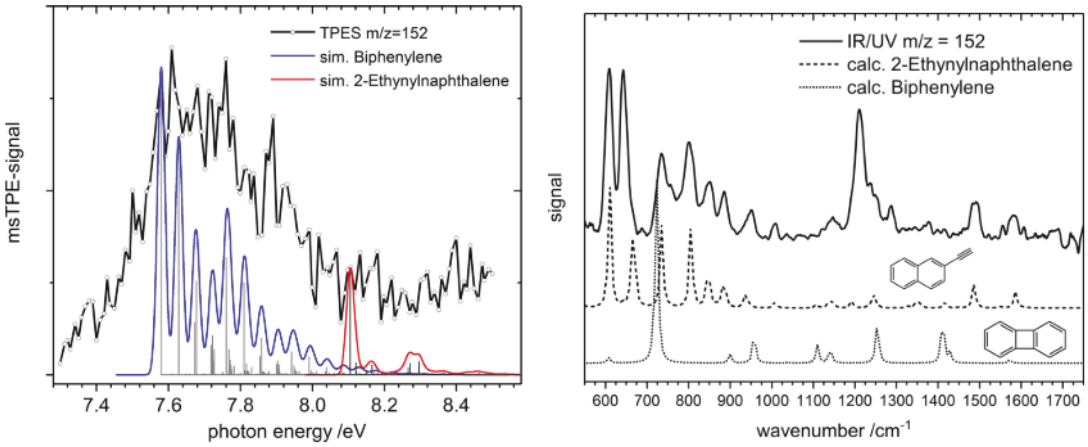

Figure 3.8: Left: MS-TPES by Engelbert Reusch of m/z=152 in comparison to simulations of biphenylene (blue) and 2-ethynylnaphthalene (red). Right: IR/UV spectrum of m/z=152 in comparison with 2-ethynylnaphthalene (dashed line) and biphenylene (dotted line). Adapted with permission from Ref.[229]

Interestingly, previous studies, e.g., by Friedrichs et al.,[234] suggest biphenylene to be the dimerization product of ortho-benzyne and hence the carrier of mass 152.[235] Indeed, biphenylene was identified in the experiment of Engelbert Reusch by its TPES and IE (see Fig. 3.8, left) in the joint study.[229] Here, the TPE and IR/UV results are complementary. The TPES shows only the presence of biphenylene when comparing the experimental data (black line) to Franck-Condon simulations (blue line). 2-ethynylnaphthalene could not be clearly observed, which would exhibit a signal at around 8.1 eV, indicated by the simulations in red. We attribute this discrepancy to the quality of the TPE spectrum on the one hand and, on the other, that biphenylene is a weak absorber at 265 nm, which was utilized in the IR/UV experiments. This also concludes that biphenylene is probably formed in higher concentrations as it was still detectable in the TPES, although the signal/noise ratio was low. The IR/UV experiment was then able to identify smaller amounts of 2-ethynylnaphthalene due to its resonance enhancement and selectivity.

3.1.3.4 Mass 166: Fluorene

The carrier of mass 166 is identified as fluorene **10** and its IR/UV spectrum is depicted in Fig. 3.9. Fluorene is the most stable isomer with $C_{13}H_{10}$ composition and is a common combustion product due to its high stability. The formation, however, is not trivial starting from ortho-benzyne. Fluorene has an odd number of carbon atoms and would also require an odd-numbered reaction partner in a condensation. Suggested growth pathways are displayed in Fig. 3.10.

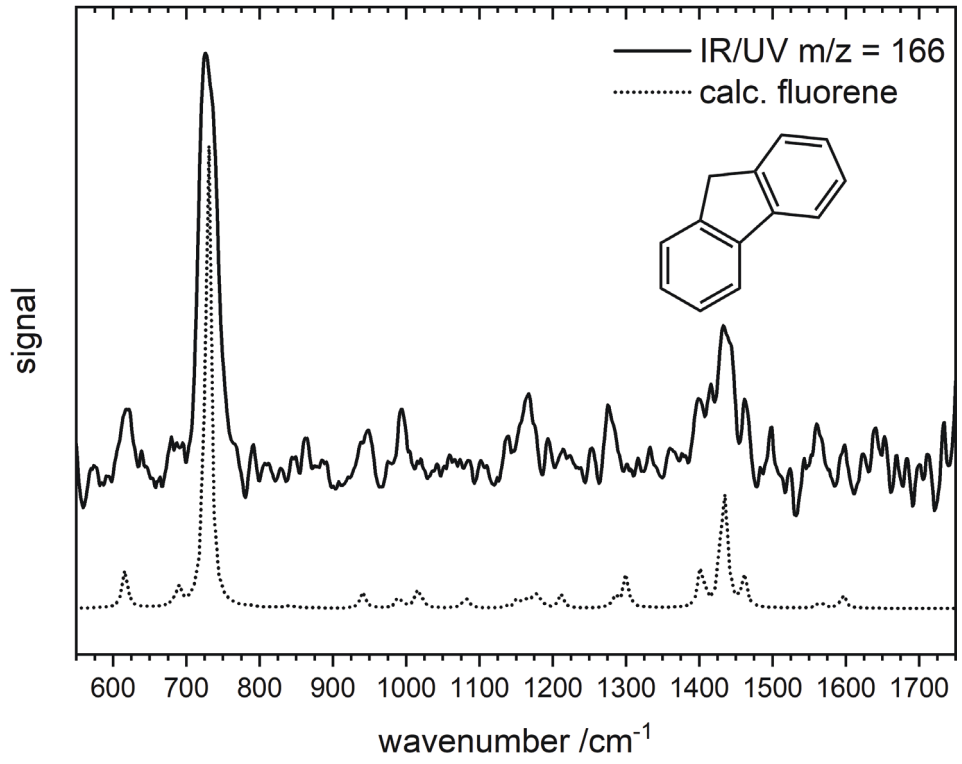

Figure 3.9: The IR/UV spectrum of m/z=166 (solid line) from the decomposition of benzocyclobutendione in comparison with vibrational DFT calculations of fluorene (dotted line). Adapted with permission from Ref.[229]

All formation pathways involve the formation of phenyl **8** as a key component. **8** forms fluorene in condensation with benzyl via a diphenylmethane intermediate followed by cyclization to **10**. Although multiple reactants necessary for the formation of phenyl are present in the current study (**3**, **6** and **7** have been identified by TPES), the key intermediates **8** and **9** were not observed. Note that **8** and **9** have been identified in the IR/UV experiments on the benzyl radical (see Section 3.1) under very comparable conditions and should therefore definitely be identifi-

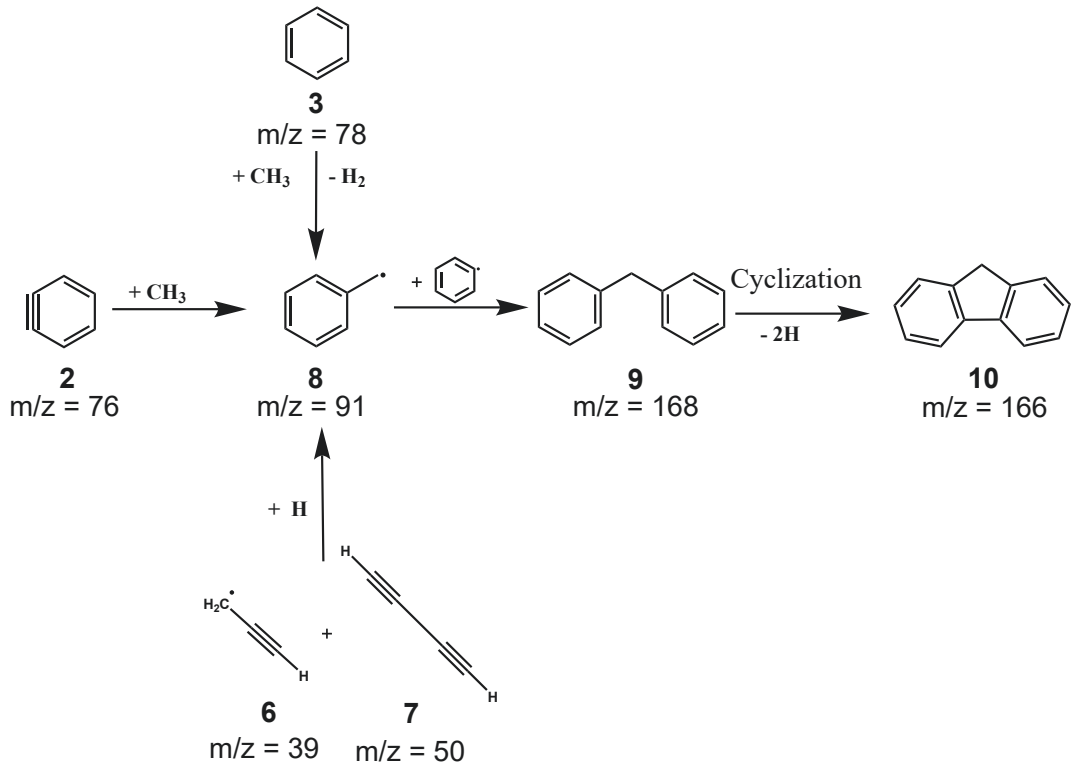

Figure 3.10: Three suggested reaction pathways for the formation of fluorene. For all reactants the formation of benzyl **8** is the first step, which further associates with phenyl to form diphenylmethane and finally fluorene.

able if formed. This concludes that fluorene might not be formed via this growth mechanism in the molecular beam. Considering the identification of biphenylene as the dimerization product of ortho-benzyne, other pathways arise according to Fig. 3.11.

The formation of fluorene could be attributed to the involvement of methyl radicals as odd-numbered C_1-units, which have also been identified by TPES in the experiment. They could either take part in the dimerization of **2** for a direct formation of fluorene or be inserted into biphenylene afterward. Both pathways are not trivial: For path 1 (solid arrow), the formation is ascribed to a simultaneous insertion of methyl during isomerization. Here, intermediate transition states can be described as biradicals, representing potential activated species for CH_3 addition, followed by cyclization to form **10**. The question is whether the formed biradical state exhibits a sufficiently long lifetime that CH_3 addition can occur. Moreover, pathway 1 would also be a 3 body reaction, making it additionally difficult in gas-phase experiments. Path 2 (dashed arrow) is very similar, but here **11** is formed

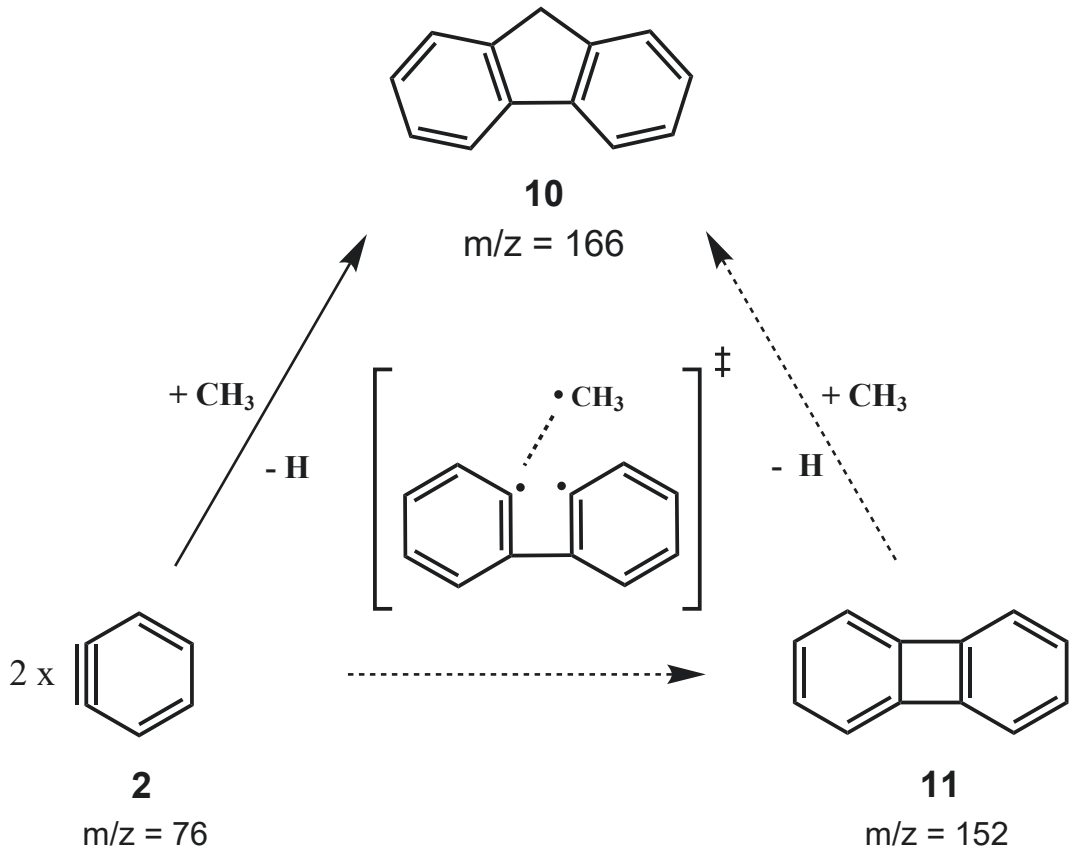

Figure 3.11: Alternative formation pathways for fluorene via biphenylene.

in a first step, and CH_3 is added in an insertion reaction afterward. The transition state would look identical to pathway 1 if the C-C bond was cleaved before CH_3 insertion. It is, however, questionable if biphenylene would undergo such a reaction due to its stability. Note that both proposed reaction pathways are speculative and only based on identifying all necessary reactants in the experiment. For a proper evaluation, elaborate quantum chemical calculations are necessary to see if these pathways are energetically accessible and chemically meaningful.

3.1.3.5 Mass 178: Phenanthrene and Anthracene

The gas-phase IR spectrum of mass 178 displays a low signal/noise ratio but exhibits three distinct features in the low energy region at 723 cm^{-1}, 796 cm^{-1}, and 864 cm^{-1}. These modes can be assigned to three ring wagging vibrations of phenanthrene, as is displayed in Fig. 3.12. Especially, the first two signals match the DFT calculations very well in energy and intensity. The third peak at 864 cm^{-1} is broadened and higher in signal intensity considering the signal strength predicted in the calculations of phenanthrene. For this reason, anthracene has also to be considered as a potential contributor. Due to its higher symmetry, anthracene has only two strong vibrations in this region. The strongest peak is energetically very similar to the corresponding vibration in phenanthrene and can consequently not be utilized to identify anthracene in an environment where phenanthrene is present. The second peak at around 866 cm^{-1} is also energetically very close to a phenanthrene vibration, but the relative signal intensity of the anthracene mode is distinctively stronger. Hence, we interpret the signal intensity of the third peak at 864 cm^{-1} as an indicator for the presence of anthracene. The formation of phenanthrene and anthracene in an ortho-benzyne environment has recently been studied by theory.[47] The authors showed that the formation of both species via a diradical cycloaddition/fragmentation reaction is energetically viable, very similar to the mechanism described before in the formation of naphthalene. As shown by the authors, the calculated potential energy surface is not trivial and involves several biradical intermediates. Both reactions are described in Eq. 3.3 and 3.4:

$$o-C_6H_4 \ + \ C_{10}H_8 \rightarrow \ C_{14}H_{10,p} \ + \ C_2H_2, \ \Delta_R H(0\ K) \ = -170\ kJ\ mol^{-1} \quad (3.3)$$

$$o-C_6H_4 \ + \ C_{10}H_8 \rightarrow \ C_{14}H_{10,a} \ + \ C_2H_2, \ \Delta_R H(0\ K) \ = -150\ kJ\ mol^{-1} \quad (3.4)$$

Both reactants for these reactions are present in the experiment as ortho-benzyne is specifically generated in the pyrolysis, and naphthalene was already identified. Moreover, both pathways represent a source of acetylene in the experiment, which was also identified by TPES. The reactions are highly exothermic with - 170 kJ mol^{-1} (phenanthrene, 3.3) and - 150 kJ mol^{-1} (anthracene, 3.4) respectively. Phenanthrene hereby is the more stable $C_{14}H_8$ isomer by about 20 kJ mol^{-1} compared to anthracene. The reaction pathway for Eq. 3.4, however, involves a maximum energy barrier which is 15 kJ mol^{-1} lower compared to the one in the formation of phenanthrene. We therefore attribute the main contribution of the m/z = 178 IR/UV spectrum to phenanthrene and acknowledge a potential influence

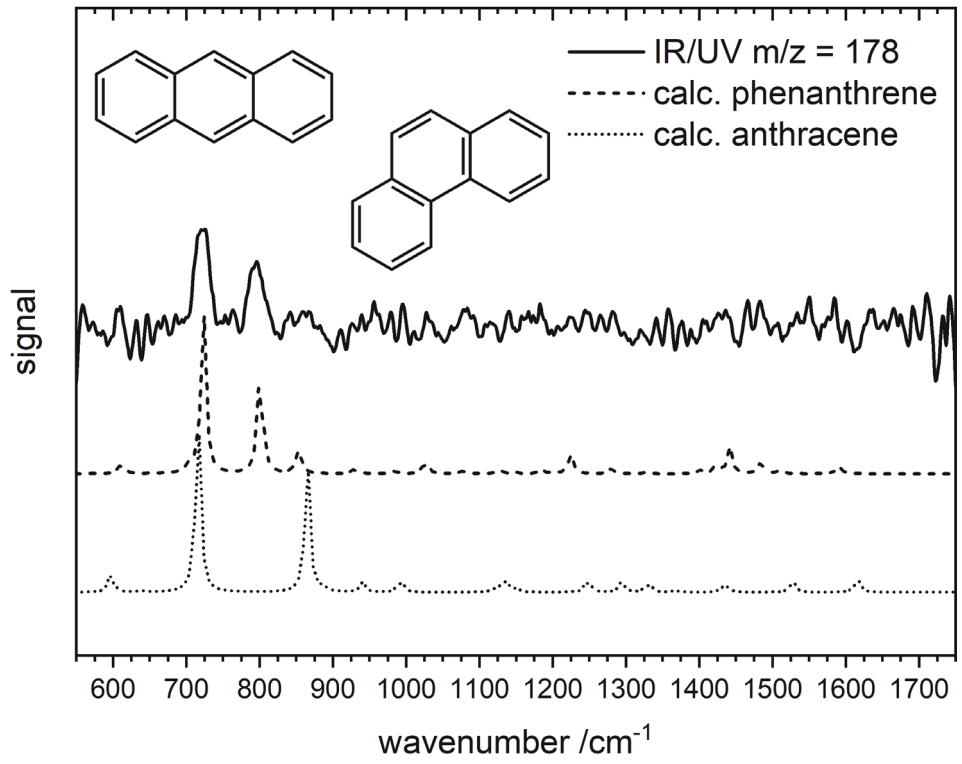

Figure 3.12: The IR/UV spectrum of m/z=178 (solid line) from the decomposition of benzocyclobutendione in comparison with vibrational DFT calculations of phenanthrene (dashed line) and anthracene (dotted line). Adapted with permission from Ref.[229]

of anthracene in lower concentrations. Note that the reactions in Eq. 3.3 and 3.4 are not the only possible ways to form phenanthrene and anthracene in hot flames. Other PAH growth mechanisms can also form these isomers in high-temperature environments and would also be a potential contributor to their formation in our experiments. Especially HACA type reactions should receive additional consideration where $C_{14}H_8$ is formed via the consecutive addition of two acetylene units to naphthalene.

3.1.3.6 Mass 228: Triphenylene

The heaviest species observable in the experiment is mass 228. Its IR/UV spectrum is depicted in Fig. 3.13. A hydrocarbon molecule of this mass corresponds to a chemical composition of $C_{18}H_{12}$ and could represent a trimerization product of ortho-benzyne. Comparing the spectrum to vibrational calculation, the carrier can be identified as triphenylene.

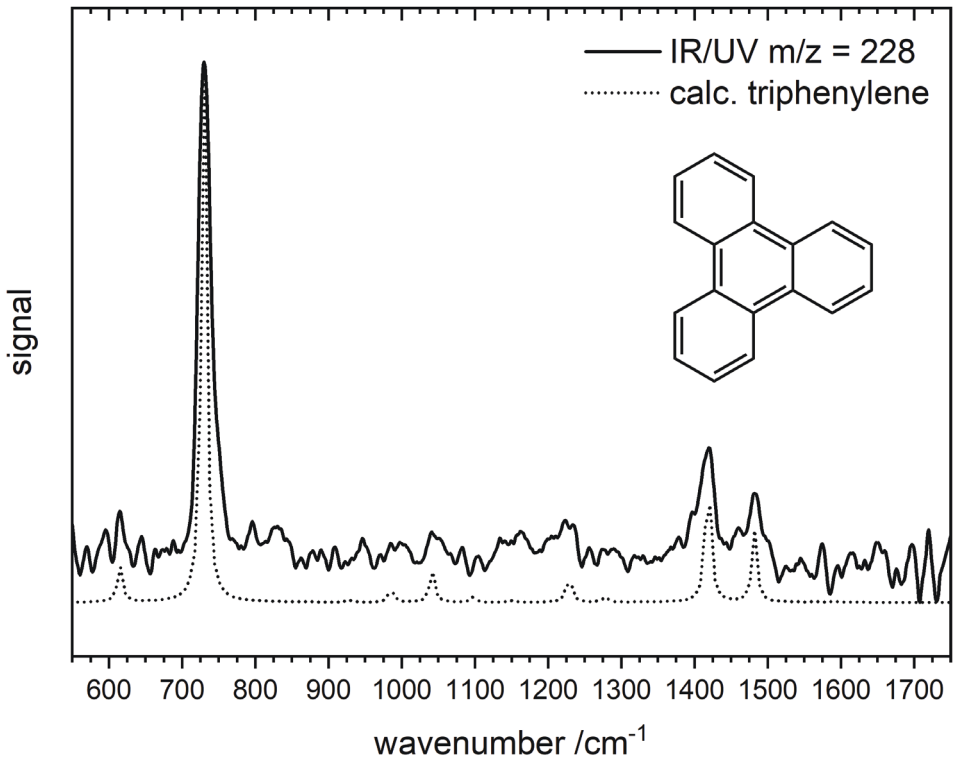

Figure 3.13: The IR/UV spectrum of m/z=228 (solid line) from the decomposition of benzocyclobutendione in comparison with vibrational DFT calculations of triphenylene (dotted line). Adapted with permission from Ref.[229]

The IR spectrum is dominated by the strong in-plane C-H wagging vibration at 731 cm^{-1} but less intense in-plane rocking modes at 1420 cm^{-1} and 1483 cm^{-1} are as well clearly observable in the experimental spectrum. Triphenylene is a well-known reaction product of ortho-benzyne in the liquid phase and can also be expected to be formed in the gas-phase.[236] In combustion chemistry, it has been suggested to be a viable PAH product of PAC-type reactions, but only a weak signal has previously been recorded in phenyl radical experiments.[45,155] Comandini and coworkers again suggest the formation via a diradical 1,4-cycloaddition/fragmentation reaction, sim-

ilar to the formation of naphthalene and phenanthrene. Here, ortho-benzyne condensates with phenanthrene to form triphenylene and acetylene according to Eq. 3.5.

$$o-C_6H_4 \ + \ C_{14}H_{10,p} \rightarrow \ C_{18}H_{12,a} \ + \ C_2H_2, \ \Delta_R H(0 \ K) \ = -161 \ kJ \ mol^{-1} \quad (3.5)$$

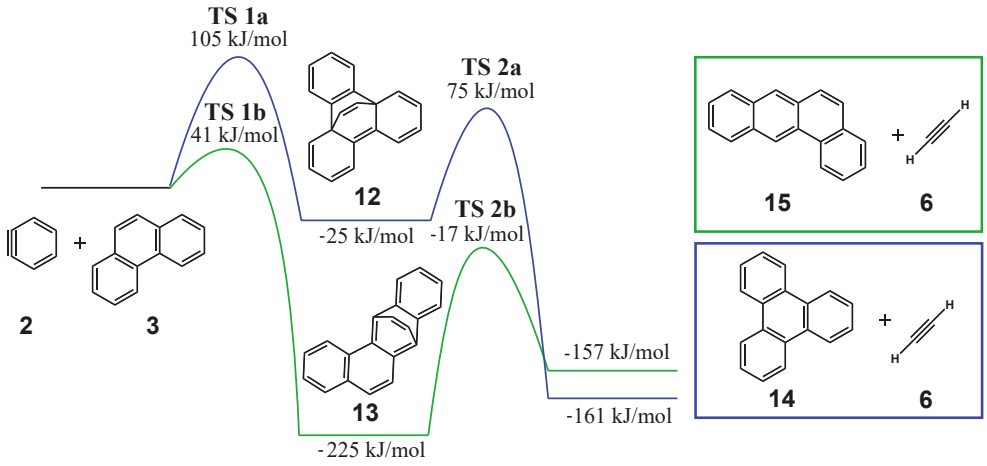

Figure 3.14: Energies, intermediates and transition states of the formation of triphenylene and benzo[a]anthracene.[47]

Again, this reaction constitutes another source of acetylene and is exothermic by -161 kJ mol^{-1}. The reaction pathway (blue trajectory) involves a maximum reaction barrier of 105 kJ mol^{-1} and involves bicyclic intermediates as depicted in Fig. 3.14. Another possible product of this reaction is the benzo[a]anthracene isomer. The overall energetics of this reaction are very similar with -157 kJ mol^{-1}, but all reaction barriers are considerably lower compared to the blue pathway. Interestingly, the experimental IR spectrum shows no indication of **15** which has a characteristic vibrational mode at around 880 cm^{-1}. This leads to the conclusion that **15** is not formed under the applied experimental conditions, and **14** is the sole carrier of mass 228 according to Eq. 3.5.

3.1.4 Summary

The reaction products of the ortho-benzyne self-reaction were investigated by IR/UV ion dip spectroscopy and augmented with TPES data by Engelbert Reusch. This project is a pristine example of how different spectroscopic methods combined can help gather extensive information about a specific system. A total overview of all identified reaction products is depicted in Fig. 3.15.

The IR experiments allowed the identification of several PAH products due to their efficient ionization at 265 nm. Naphthalene, fluorene, 2-ethynylnaphthalene, phenanthrene, and triphenylene were identified as carriers of distinct signals in the mass spectrum. This suggests that ortho-benzyne is an efficient precursor to form various common PAHs up to four aromatic rings in high-temperature environments. Suggested formation pathways for the respective molecules were discussed in the previous section.

In particular the results on naphthalene, phenanthrene, and triphenylene are very interesting, because they support recent findings, that these species can be formed via diradical 1,4-cycloaddition/fragmentation (1,4-CAF) pathways in an ortho-benzyne rich environment.[47] This Diels-Alder like mechanism seems not only to be a very efficient way to form PAHs in general, but also produces acetylene which can subsequently be available for further HACA-type reactions like the formation of 2-ethynylnaphthalene.

The identification of molecules with smaller ionization cross sections like methyl, acetylene, diacetylene, and benzene by TPES contributed immensely to the evaluation of all pathways. Particularly the identification of biphenylene as an additional carrier of mass 152, which was not present in the IR experiments, shows the advantage of combining different spectroscopic methods to analyze gas-phase reaction products.

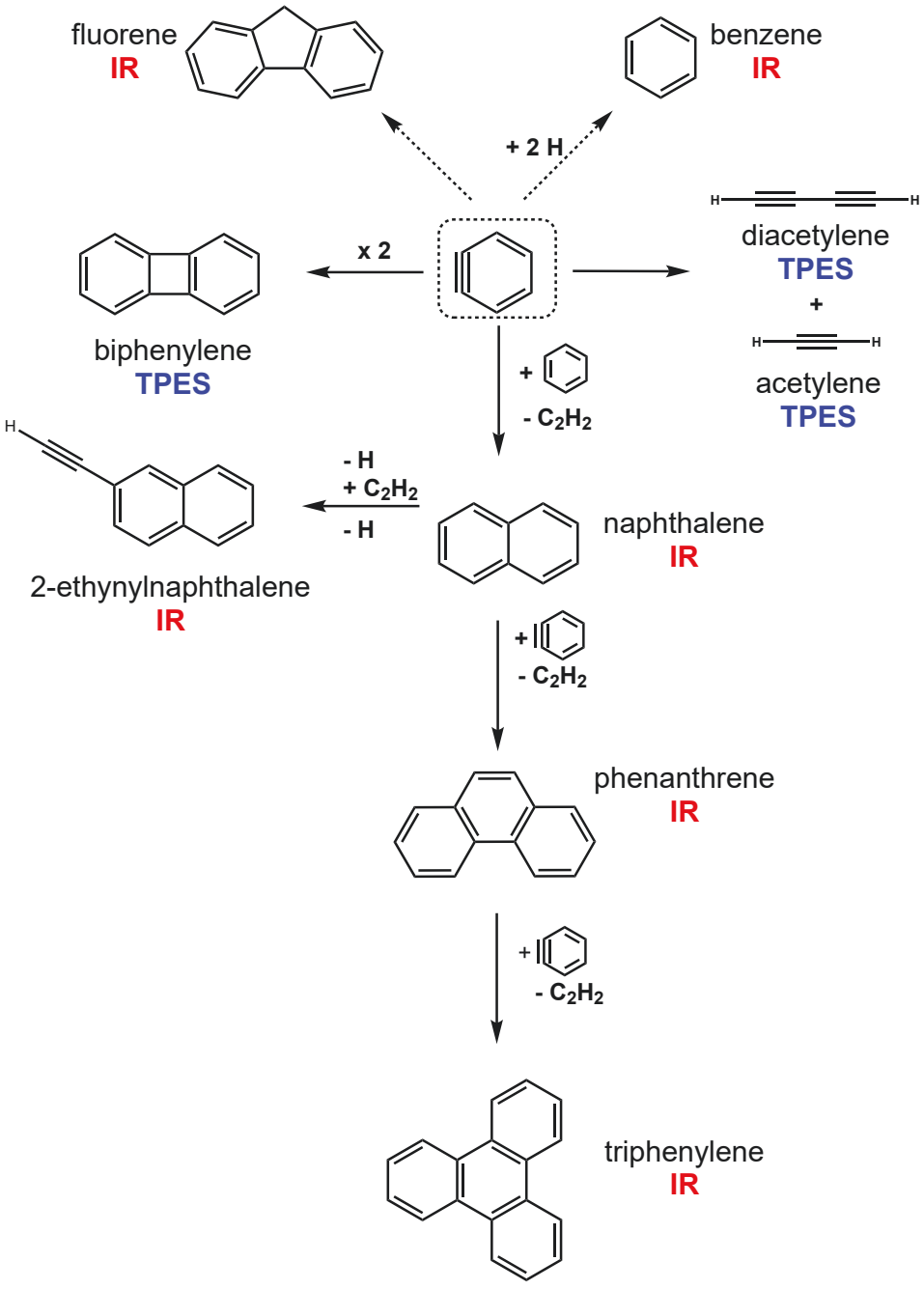

Figure 3.15: Overview of all identified reaction products of the ortho-benzyne experiments with suggested reaction pathways. Species identified via IR/UV spectroscopy are labeled red, whereas species identified in the TPES experiments are labeled blue.

3.2 The Benzyl Radical

3.2.1 Introduction

The importance of resonance-stabilized radicals (RSR) in the formation of PAHs in hot flames and combustion processes has been discussed in the literature for a long time. Due to their high stability, these molecules can form and accumulate in high-temperature environments and can subsequently be available for further reactions. The prime example of a hydrocarbon RSR with a π-electron system is the benzyl radical C_7H_7.[237] It is of high importance in combustion research, as it is strongly linked to toluene, which is a common component of modern fuels due to its high energy density and anti-knocking properties.[238,239] In hot flames, growth reactions based on radical mechanisms are widespread. Hence, a corresponding radical to a fuel component, in the present case the benzyl radical and toluene, can be regarded as an activated species.

Accordingly, there is a strong connection between benzyl and toluene research in literature.

The benzyl radical itself has been investigated thoroughly in the past decades. In this regard, pyrolytically generated radicals and their decomposition products have been studied by time-resolved UV spectroscopy[241,242], threshold photoelectron spectroscopy[243,244], IR/UV spectroscopy[245], and photofragment spectroscopy.[246,247] In this study, it was chosen to selectively generate benzyl radicals by pyrolysis of a suitable nitrite precursor instead of generating the radicals from toluene. This allows for a relatively neat generation of benzyl radicals in the molecular beam and avoids the formation of other reactive species from high-temperature toluene decomposition. Thus, it is possible to investigate the reaction products mainly formed from the benzyl radicals them-

Figure 3.16: Dimerization of the benzyl radical title cover as a hot topic article published in Chemistry A European Journal. Adapted with permission from Ref.[240]

selves. Former studies on the self-reaction products of benzyl with structural sensitivity are rather scarce and are usually discussed within toluene studies. The importance of understanding the PAH growth of benzyl becomes evident by looking at the mesomeric structure of benzyl, illustrated in Fig. 3.17. The radical

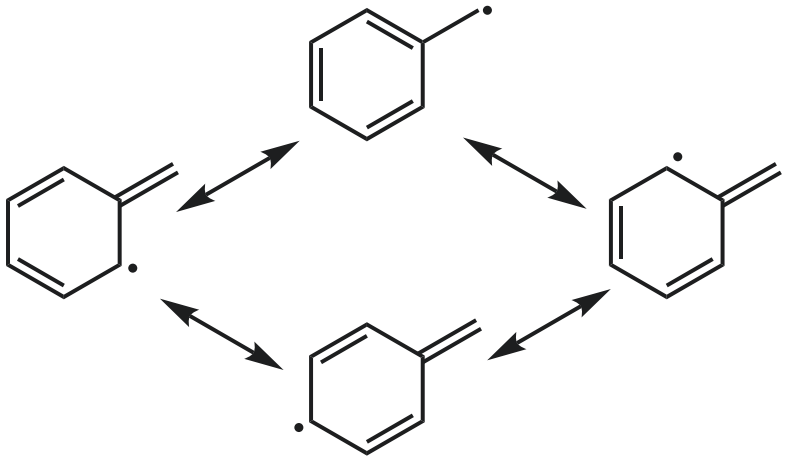

Figure 3.17: The three mesomeric stabilized structures of benzyl radicals: Benzylic-, ortho- and para- position.

center can be located in benzylic, ortho, and para position. Although the benzylic position is generally regarded as the most stable one, condensation reaction from ortho- and para- attacks may not be neglected. Structural identification of the reaction products may lead to a better understanding of the gas-phase reaction dynamics of benzyl radicals and reveal the importance of benzyl in PAH formation. Furthermore, due to the role of benzyl as an archetype RSH, it might be possible to transfer these findings to similar RSH systems to predict their role in the formation of PAHs in high-temperature environments. Therefore, IR/UV double resonance spectroscopy was employed to identify the self-reaction products of benzyl radicals in a molecular beam via their gas-phase IR spectra. Note that the findings in the following section are published in Ref.[240] and large parts of the content are taken from this publication.

3.2.2 Experimental Parameters

Benzyl radicals were pyrolytically generated from 2-phenylethyl nitrite in a resistively heated SiC flow reactor, with a length of 38 mm and an inner diameter of 1 mm. The precursor was heated to 85-95 °C to improve vapor pressure and increase molecule concentration in the seeding gas.

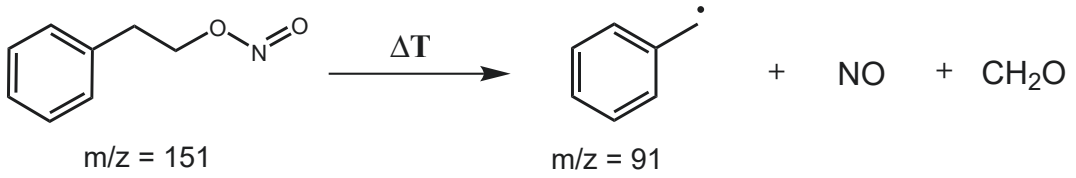

Figure 3.18: Thermal decomposition of the 2-phenylethyl nitrite precursor to generate benzyl radicals. Additional reaction products are formaldehyde and nitric oxide. Adapted with permission from Ref.[240]

Experimental parameters (e.g. backing gas, backing pressure, pyrolysis temperature, etc.) were optimized utilizing SPI-MS in regard to benzyl radical generation and the formation of heavier reaction products.

The IR/UV experiments have been conducted at the FEL beamline of the FELIX laboratory. Hereby, the precursor was seeded in 1.4 bar argon and cleaved at a pyrolysis temperature of approximately 1100 °C.

Table 3.2: Overview of the Experimental Parameters of the IR/UV Benzyl Experiments.

Experimental Parameters	
Parameter	Value
Precursor	$C_8H_9NO_2$
UV Wavelength	265 nm
UV Energy	0.65 mJ
UV Delay	200 ns
Ionization Scheme	[1+1]-REMPI
UV Repetition Rate	20 Hz
IR Scan Range	550 - 1750 cm^{-1}
IR Step Width	2.5 cm^{-1}
IR Repetition Rate	10 Hz
Seeding Gas	Argon
Seeding Pressure	1.4 bar

After expanding the molecular beam through a pulsed solenoid valve into the pre-chamber of a TOF-MS spectrometer, the beam was skimmed, entering the ionization region. For the double resonant experiment, a UV-wavelength of 265 nm with 0.65 mJ of output power at 20 Hz (Nd:YAG pumped ns-dye laser, frequency-doubled 530 nm, Coumarin 153) was employed for a [1+1]-REMPI scheme. The beams were spatially overlapped, and the IR beam was scanned over the fingerprint region from 550 - 1750 cm^{-1}, with a repetition rate of 10 Hz, output power up to 100 mJ, and step width of 2.5 cm^{-1}. Finally,

the ion signals were detected using TOF-MS, and the IR/UV spectra were received after data analyses according to Chapter 2.3 and compared to computed vibrational spectra on a B3LYP/6-311G(p,d) (DFT, harmonic, scaling factor: 0.975, Lorentzian convolution, FWHM = 8 cm^{-1}) level of theory.

3.2.3 Results and Discussion

3.2.3.1 Mass Spectra of the Thermal Decomposition of 2-Phenylethyl Nitrite

The 118 nm SPI mass spectrum of 2-phenylethyl nitrite is depicted in the upper trace of Fig. 3.19. It provides an approximate insight into the relative composition of the pyrolysis products present in the molecular beam. The MS indicates a complete conversion of the precursor (m/z = 151) into predominantly benzyl radicals at mass peak m/z = 91. The peaks to lower masses (m/z = 30, 65, 78) show side products of the precursor decomposition at m/z = 30 (NO_2 and CH_2O) and other unimolecular decomposition products like cyclopentadienyl (m/z = 65) and benzene (m/z = 78) resulting from high-temperature decomposition or DPI.

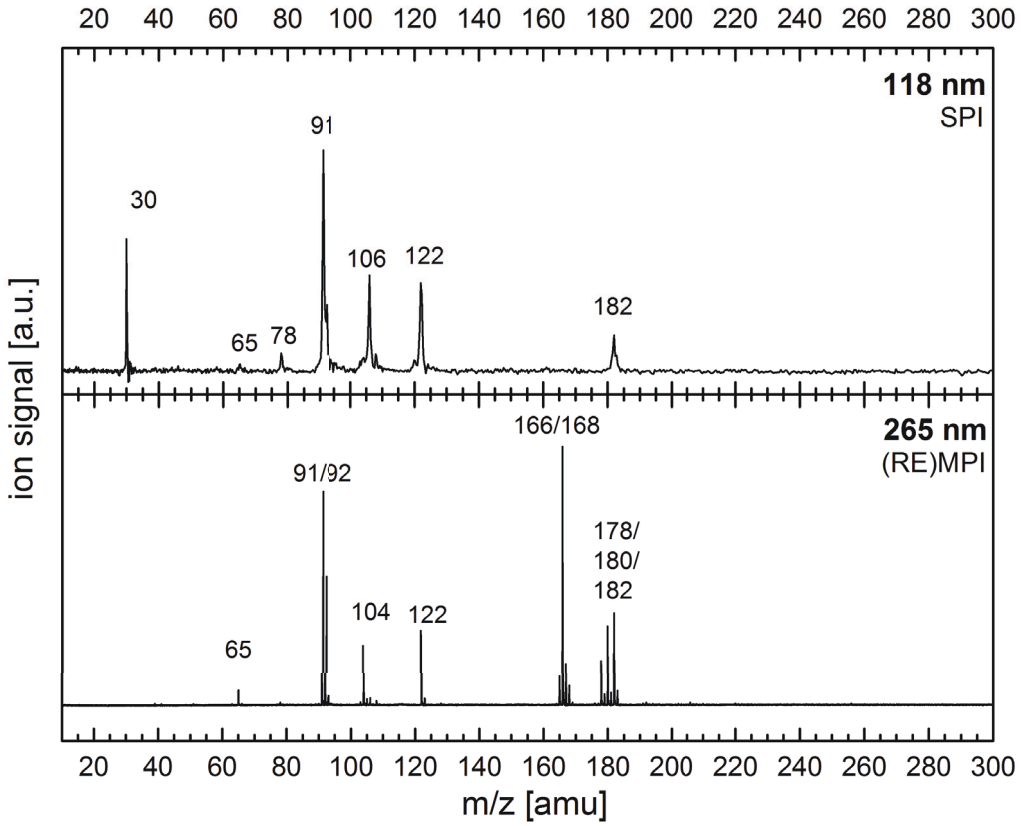

Figure 3.19: Mass spectra of the thermal decomposition of the phenylethyl nitrite precursor. **top:** single-photon ionization at 118 nm; **bottom:** [1+1]REMPI at 265 nm. Adapted with permission from Ref.[240]

The main reaction product of the generated benzyl radicals is observed at mass peak m/z = 182, which corresponds to the dimer with a composition of $C_{14}H_{12}$. The other two visible peaks at m/z = 106 and m/z = 122 correlate to phenyl ethanol (an educt of the precursor synthesis) and benzaldehyde (a possible pyrolysis decomposition product of phenyl ethanol). These are impurities of the used precursor and are not considered in the following discussion.

The [1+1]-REMPI mass spectrum at 265 nm is shown in the lower trace of Fig. 3.19. Due to the strong absorption cross-sections for PAHs in this energy region, additional masses can be observed compared to the SPI spectrum. These appear at higher masses and hence correlate to additional benzyl reaction products. Peak m/z = 168 relates to the addition of a phenyl unit (m/z = 77) to benzyl (m/z = 91) to form a species with $C_{13}H_{13}$ composition, which apparently undergoes H_2-loss to form a species with m/z = 166.

A similar process can be observed for the heaviest masses in the experiment. The dimerization product of two benzyl radicals shows a peak at m/z = 182 to form a molecule with $C_{14}H_{12}$ composition. The masses at 180 and 178 suggest a consecutive abstraction of H_2 from the dimer to form these obviously stable molecules in the molecular beam. Note that m/z = 106 is not visible in the REMPI spectrum, probably due to it being benzaldehyde, which can not be ionized with two 265 nm photons (IE = 9.36 eV).[248] Mass 104 was identified as styrene and will not be further discussed in the following section. It is probably being generated from side products and is not involved in the self-reaction of benzyl in this experiment.

3.2.3.2 Masses 166 and 168: Fluorene and Diphenylmethane

The predominant peak in the 265 nm REMPI spectrum of the decomposition of **2** is mass 168 and constitutes a molecule with $C_{13}H_{12}$ composition. It correlates to an addition of a phenyl unit (m/z = 77) to benzyl (m/z = 91), and its IR/UV spectrum (solid line) is shown in the upper trace of Fig. 3.20. The vibrational spectrum is dominated by two strong bands in the 650 - 800 cm^{-1} region and three smaller bands to higher energies between 1400 - 1650 cm^{-1}. For the energies between these regions, a meaningful assignment of signals is challenging due to small signal intensities.

Comparing the IR spectrum to calculated vibrational spectra of suitable candidates, the peak at m/z = 168 can clearly be identified as diphenylmethane, as all significant experimental peaks are present in the DFT calculations. The appearance of a mass with this molecular weight is not surprising, as it has been observed in similar experiments of toluene pyrolysis.[249] Here, the authors attribute the formation to a reaction between benzene (m/z = 78) and benzyl (m/z = 91). Looking

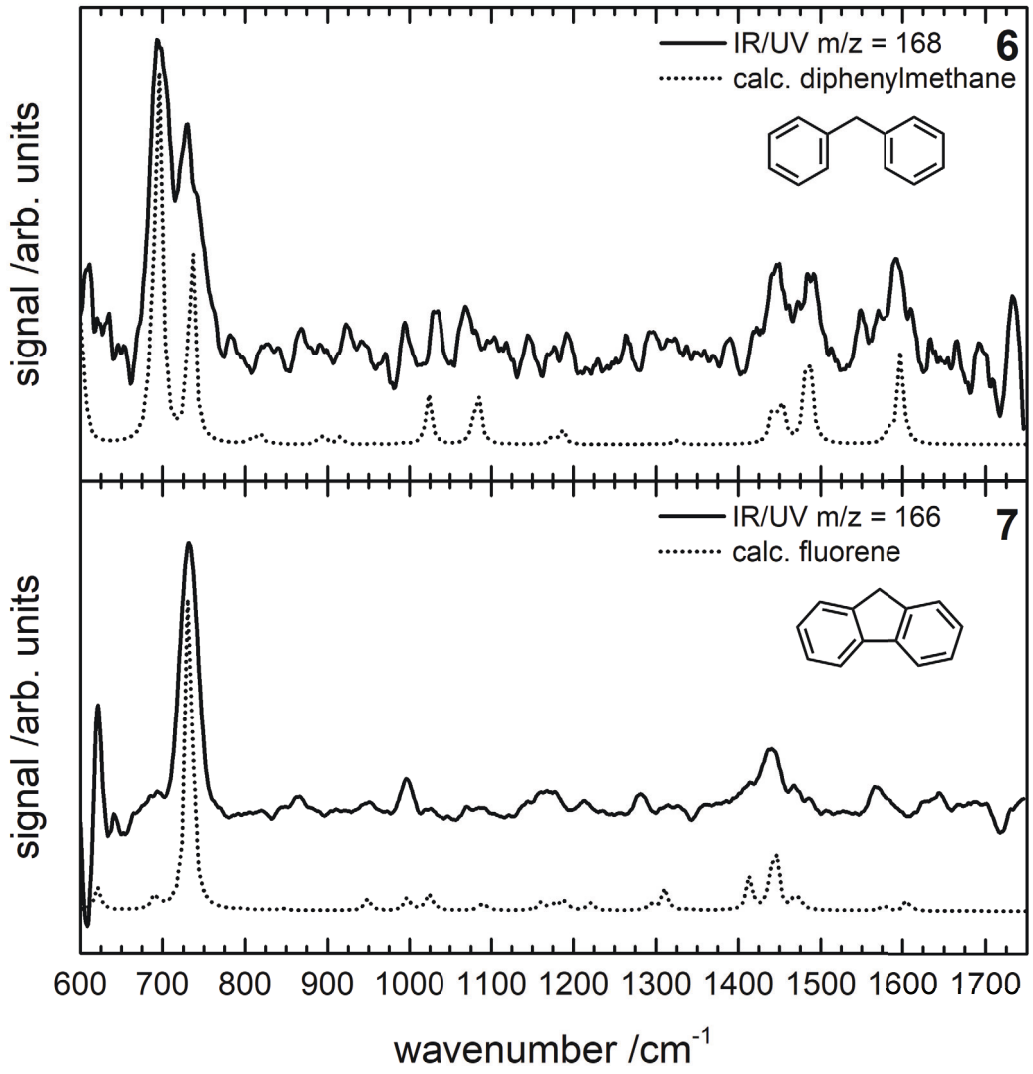

Figure 3.20: **top:** IR/UV spectrum of mass 168 (solid line) in comparison with DFT calculations of diphenylmethane (dotted line); **bottom:** IR/UV spectrum of the 166 (solid line) in comparison with DFT calculations of fluorene (dotted line). Adapted with permission from Ref.[240]

at the SPI-MS (see Fig. 3.19) of the current study, a mass corresponding to benzene can be observed as a peak at m/z = 78. Consequently, phenyl radicals should also be present in the high-temperature flow reactor. Still, they can possibly not be observed in the mass spectrum due to their high reactivity and, therefore, low concentration. Hence, we attribute the formation of diphenylmethane to the direct reaction product of benzyl with phenyl according to Fig. 3.21 (first reaction).

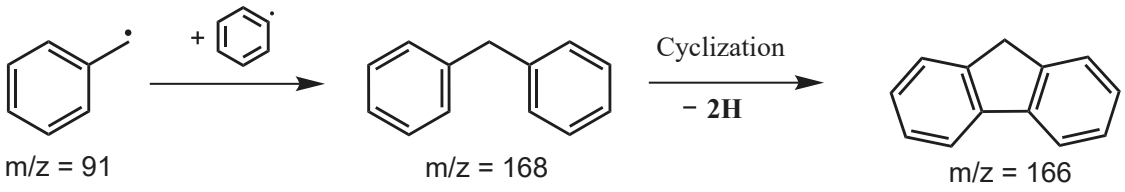

Figure 3.21: Association of benzyl and phenyl radicals to form diphenylmethane with subsequent cyclization to fluorene.

The next mass in the MS appears 2 amu lower to diphenylmethane at m/z = 166. This resembles an H_2-loss from diphenylmethane and hence suggests a strong connection in the formation between those two species. Figure 3.20 (bottom trace) shows the experimental IR/UV spectrum of mass 166 compared to the calculated vibrations of fluorene. Both spectra exhibit a major signal at 732 cm^{-1}, which is the B_1 out-of-plane vibration of the fluorene framework. Moreover, the less intense vibrations in the 1400 - 1500 cm^{-1} region are in good agreement with the calculated values.

Therefore, mass 166 can be readily identified as fluorene, and no contributions of other possible carriers are visible. Due to the previous observation, the formation of fluorene can easily be explained by H_2 elimination and ring-closing of diphenylmethane (see Fig. 3.21).[249] Fluorene has been previously discussed as the carrier of mass 166 in flame experiments. Here, the authors propose a classical HACA mechanism to account for the formation of fluorene in their experiments based on the observation of high acetylene concentrations and key intermediates.[248] Such a step-wise formation would undergo gradual addition of acetylene units to a framework starting from benzyl according to $C_7H_7 \rightarrow C_9H_8 \rightarrow C_{11}H_8 \rightarrow C_{13}H_{10}$. On the other hand, these stable intermediates are not observed and hence the formation of fluorene can be attributed to the antecedent reaction between benzyl and phenyl.[44,249]

3.2.3.3 Masses 182, 180 and 178: Phenanthrene, 9,10-Dihydrophenanthrene, and Bibenzyl

The heaviest molecules observed in the study show peaks at mass 182, 180, and 178. Again, the spacing by 2 amu suggests a strong connection in the formation of these three species. The heaviest mass of the pyrolysis is the benzyl dimerization product at m/z = 182. Although it only shows a medium peak in the REMPI spectrum, it is indeed the only PAH product with a large enough gas-phase concentration to be identified in the SPI-MS in Fig. 3.19 (top trace). Its IR/UV spectrum is depicted in the top trace of Fig. 3.22. Comparing it to quantum chemical calculations reveals the carrier of m/z = 182 to be bibenzyl (1,2-diphenylethane), as all major vibrational modes are present in the experimental and calculated spectrum. Note that two rotational isomers exist for **3**; anti and gauche. Previous studies pointed out that the energy difference between those two rotamers is insignificantly small.[250] Comparing the experimental IR spectrum to those rotamers indicates that both isomers are present in the experiment. Due to the different symmetry of the rotational isomers (C_{2h} for anti and C_2 for gauche), their IR spectra differ and can consequently be identified by their respective unique vibrations. The mode at 1334 cm^{-1} is an inimitable characteristic of the gauche isomer, and the relative intensities of the three vibrations at 1445 cm^{-1},1488 cm^{-1} and 1593 cm^{-1} are in good agreement with the anti rotamer. Moreover, the relative intensities of the two dominating bands between 700 cm^{-1} and 800 cm^{-1} suggest a contribution of both isomers. Considering earlier studies, which suggest a relative composition of 70% gauche and 30% anti, we confirm that such a mixture would adequately represent the IR spectrum measured in our study.[251] Bibenzyl is also the reasonable dimerization product from a chemist's perspective. It represents the condensation product from the most stable form of benzyl radicals, where the radical is in a benzylic position. This dimerization is barrierless and exothermic by 283.2 kJ mol^{-1}.[252] Low pressure but high temperature dependency is predicted for this reaction; at low temperatures, the dimerization is the dominant reaction, whereas the significance of the back reaction increases at higher temperatures.[248,253–260]

Nevertheless, due to the mesomeric stabilization of these radicals, products resulting from ortho- and para-attacks should also be considered, and a comparison for those is shown in Fig. A.1 - A.4 in the Appendix. However, comparing these calculations to the experimental data suggests no contribution to the IR/UV spectrum. Merely 2-benzyltoluene exhibits vibrational modes at roughly the same energies of the measured spectrum but can be discarded because of the wrong intensities of the peaks. Hence, bibenzyl is identified as the sole carrier of mass 182.

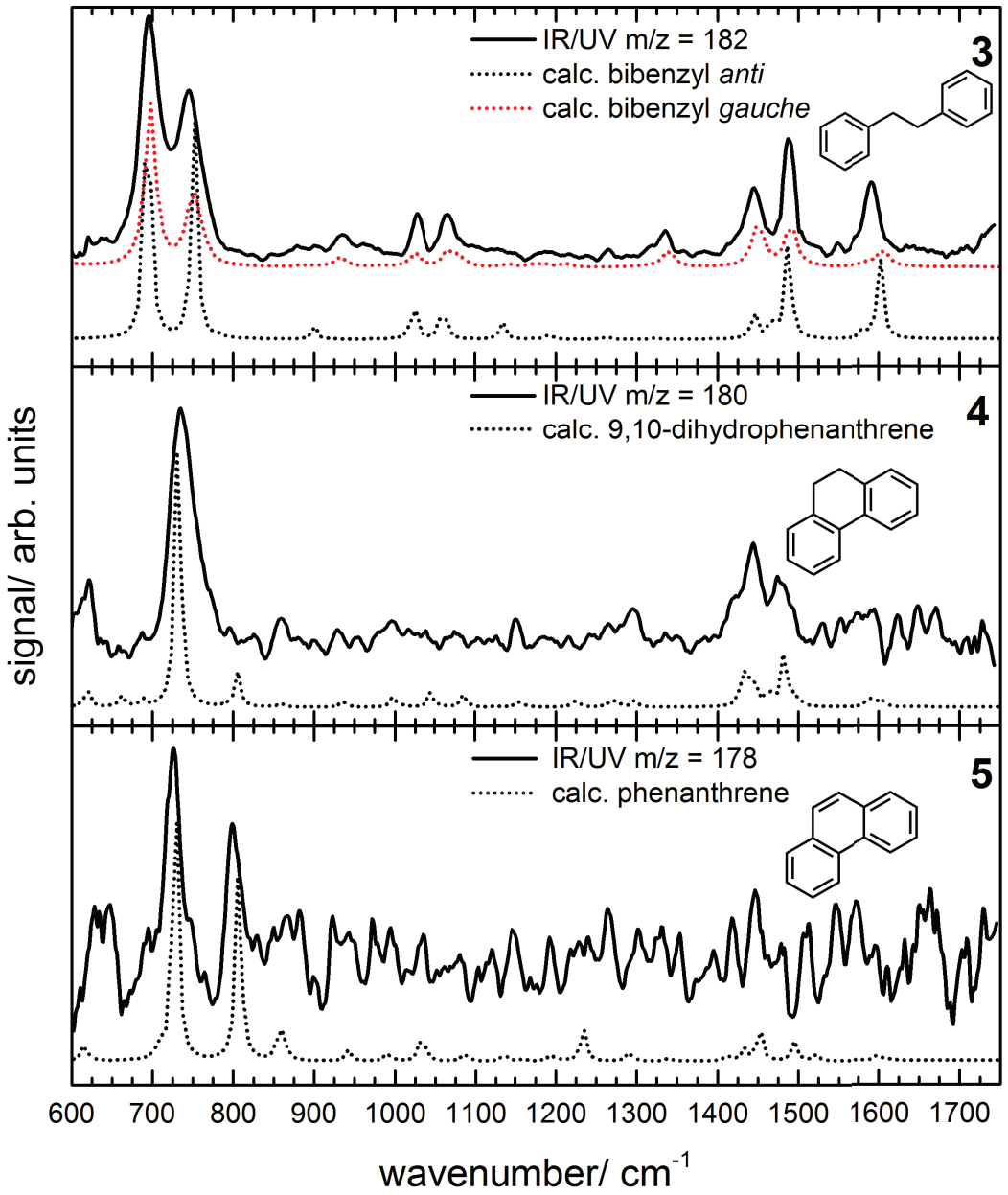

Figure 3.22: IR/UV spectra of masses 182, 180 and 178 after the decomposition of phenylethyl nitrite. **top:** IR/UV spectrum of mass 182 (solid line) in comparison with DFT calculations of the two rotamers of bibenzyl (dotted line); **center:** IR/UV spectrum of mass 180 (solid line) in comparison with DFT calculations of 9,10-dihydrophenanthrene (dotted line); **bottom:** IR/UV spectrum of mass 178 (solid line) in comparison with DFT calculations of phenanthrene (dotted line). Adapted with permission from Ref.[240]

The next two masses appear 2 amu and 4 amu below bibenzyl at m/z = 180 and m/z = 178, indicating formation via sequential H_2-loss starting from bibenzyl. The IR/UV spectrum of mass 180 is depicted in the center trace of Fig. 3.22. Its carrier can be identified as 9,10-dihydrophenanthrene. The experimental spectrum matches the computed vibrations well, displaying a dominant out-of-plane vibrational mode at 734 cm^{-1} and two further peaks in the higher energy region between 1400 - 1500 cm^{-1}. The IR spectrum of mass 178, on the other hand, is shown in the lower trace of Fig. 3.22. This spectrum's signal/noise ratio is apparently lower compared to other masses, but due to characteristic low energy bands, especially the two out-of-plane vibrations at 724 cm^{-1} and 797 cm^{-1}, the mass can be identified as phenanthrene. The observation of all three masses is in agreement with similar studies on toluene combustion. Here, phenanthrene has been identified either by mole fraction analysis or IE measurements.[248,261] In a toluene pyrolysis study by Shukla et al., the authors observed the formation of **5** and attributed it to consecutive H_2-loss from **3** as well.[249] In general, three reaction pathways are possible for the formation of phenanthrene at high temperatures (see Fig. 3.23).

Pathway **I** and **II** represent the formation via a growth mechanism. Pathway **I** shows a HACA type reaction, in which acetylene is added to biphenyl, followed by cyclization and H_2-loss. Pathway **II** displays a rather special condensation between indene and cyclopentadienyl, both common products of many flame experiments. However, both reaction pathways (**I** and **II**) can be discarded in our study, as except for a small signal at m/z = 65 (for cyclopentadienyl), none of the necessary reactants were observed in the present study, and no acetylene was added to the experiment. Pathway **IIIa** and **IIIb** (see Fig. 3.23, bottom) show the formation of phenanthrene from bibenzyl via two consecutive H_2-losses. Reaction **IIIa** hereby proceeds via initial H_2-loss and aromatization to form stilbene, followed by another H_2-loss and cyclization to phenanthrene. On the other hand, pathway **IIIb** displays the opposite sequence. Bibenzyl undergoes first a cyclization to 9-10-dihydrophenanthrene before aromatization takes place to form phenanthrene. The m/z = 180 intermediate has been detected in previous studies and was usually identified as E-stilbene, generally due to chemical intuition and simple calculations.[249] However, in the present study, the carrier of mass 180 is clearly identified as 9,10-dihydrophenanthrene, and no influence of E-stilbene on the IR spectrum can be observed. Note that stilbene should, in principle, be detectable at the employed UV energies and would show two distinct vibrational modes in the 600 - 800 cm^{-1} region. Consequently, the present study suggests the formation of phenanthrene via pathway **IIIb**. Recent CBS-QB3 calculations by Sinha and Raj support this result, which questioned the importance of stilbene in the formation of phenanthrene at high temperatures.[252]

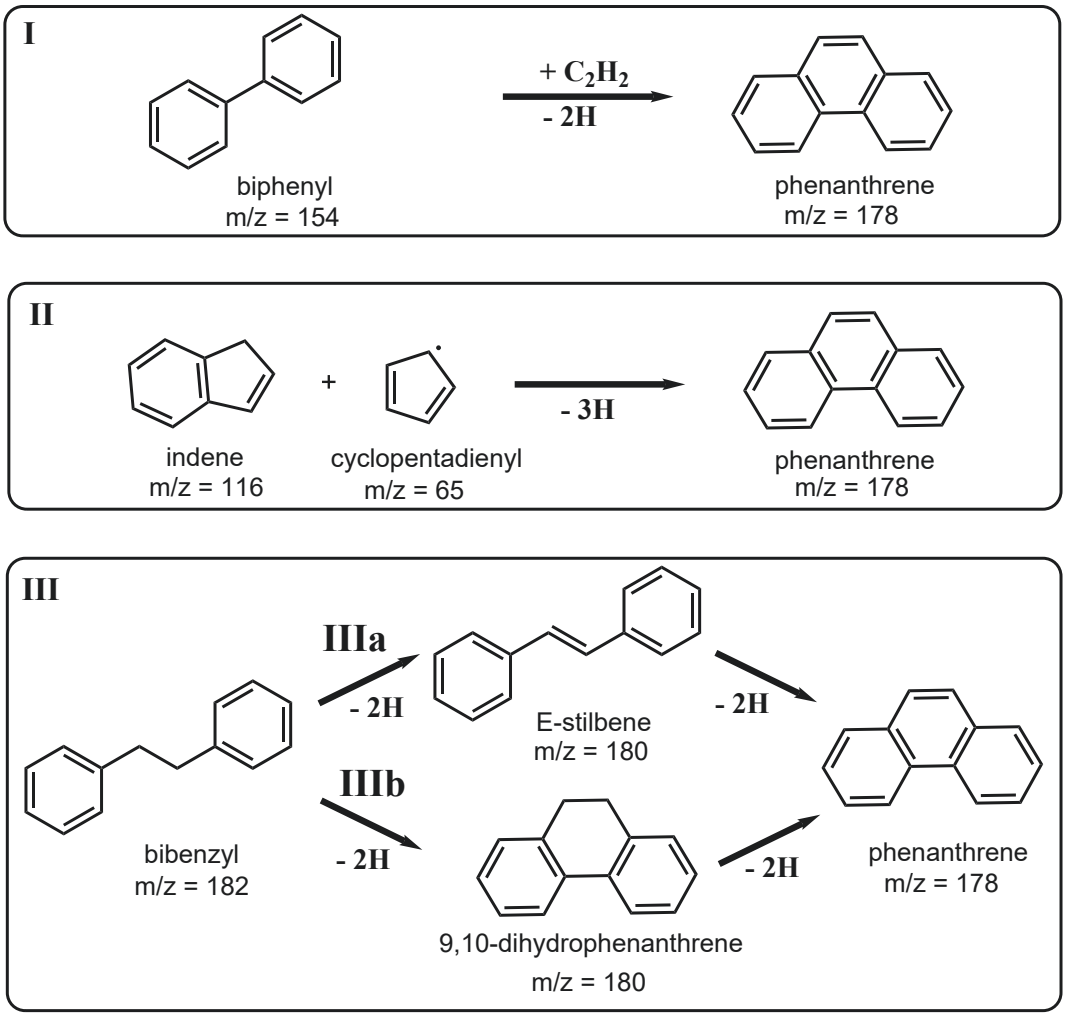

Figure 3.23: Three possible formation pathways for phenanthrene starting from (**I**) biphenyl, (**II**) indene and cyclopentadienyl or (**III**) bibenzyl.

The authors suggest that the formation of phenanthrene via **IIIb** is preferred above 1200 K. They show that the formation of 9,10-dihydrophenanthrene from bibenzyl is almost isoenergetic with an activation barrier of 70.1 kJ mol^{-1}. On the other hand, the formation of stilbene (**IIIa**) requires an activation energy of 168.8 kJ mol^{-1} and the reaction is overall endothermic by 90.2 kJ mol^{-1}.

3.2.4 Summary

The present study on the dimerization of benzyl radicals at high temperatures revealed several condensation products, which were identified by IR/UV ion dip spectroscopy in a molecular beam. The carriers of the mass signals were identified as fluorene (m/z = 166), diphenylmethane (m/z = 168), phenanthrene (m/z = 178), 9,10-dihydrophenanthrene (m/z = 180), and bibenzyl (m/z = 182) by comparison of the mass-selected gas-phase IR spectra with vibrational calculations. An overview of the observed reaction products and the proposed reaction pathways are displayed in Fig. 3.24.

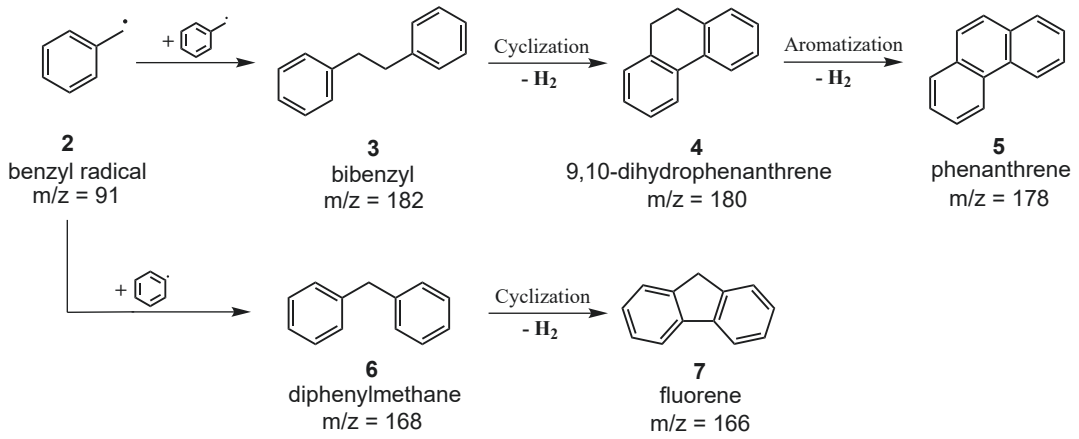

Figure 3.24: Overview of the identified mass carriers of the benzyl experiments with suggested reaction pathways.

The experiment suggests that diphenylmethane and bibenzyl are direct condensation products of benzyl radicals. Fluorene is formed via the addition of a phenyl unit, and phenanthrene being the final dimerization product. Both PAHs show subsequent H_2-loss to form other stable PAHs in a high-temperature environment. In this regard, diphenylmethane undergoes cyclization and H_2-loss to form fluorene, which is commonly found in various high-temperature and flame studies. On the other hand, bibenzyl shows the formation of phenanthrene by an initial cyclization/H_2-loss reaction to 9-10-dihydrophenanthrene and subsequent aromatization/H_2-loss to phenanthrene. Thereby, this study challenges the commonly assumed involvement of stilbene in the formation of phenanthrene and confirms recent theoretical predictions for the formation of phenanthrene from bibenzyl via the 9,10-dihydrophenanthrene pathway.

3.3 Ortho-, Meta- and Para-Xylyl Radicals

3.3.1 Introduction

Xylyl radicals are a group of resonance stabilized hydrocarbons with C_8H_9 composition. They exist in three different isomeric forms: ortho, meta, and para; which are depicted in Fig. 3.25. The interest in these molecules is closely related to the research on benzyl radicals, as presented in Chapter 3.2, and extends the molecular framework by an additional methyl unit. Xylyl radicals play an important role in combustion chemistry as they represent the major decomposition product of xylene.

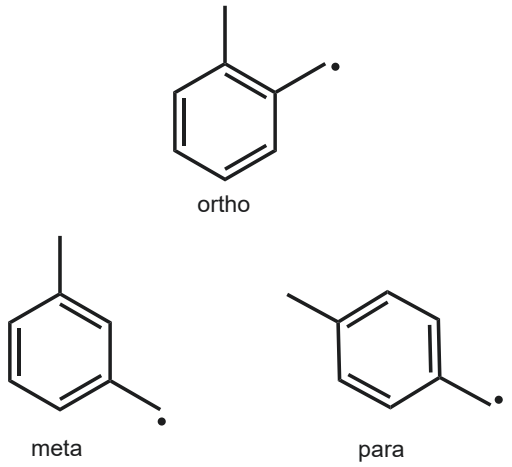

Figure 3.25: The three isomeric forms of xylyl radicals; ortho, meta, and para.

Xylenes are additives in modern gasoline blends, similar to toluene, and have replaced other harmful boosting agents in recent years.[262–264] These additives are important to improve combustion performance with their high energy density and anti-knock properties.[265] The primary decomposition of these precursors in high-temperature environments is H-abstraction at a methyl group.[224,266,267] This leads to the production of RSHs, which can accumulate in hot flames due to their high stability and low reactivity towards oxygen. Since these radicals have been considered a potential source for the formation of harmful PAHs, the scientific interest in these additives has been significant for years.[249,252] They were studied utilizing various spectroscopic methods such as IR/UV[245], UV-Vis[268,269], photofragment[247], high-resolution photoelectron[243,270,271], laser-induced fluorescence[272] and femtosecond time-resolved spectroscopy.[273]

Studies on the three isomers of xylyl are scarce, but the research is getting more momentum in recent years. The excited states and torsional parameters have been studied by emission spectroscopy.[274–280] The ionization energies have been quantified by photoelectron-photoion coincidence spectroscopy[281,282] and higher-lying electronic states have been studied by multiphoton ionization.[283,284] Research on the excited state dynamics has been conducted utilizing velocity map imaging[284] and femtosecond time-resolved spectroscopy.[273]

The question remains whether xylyl radicals can be selectively generated in the gas-phase. In the following study, we employed IR/UV ion dip spectroscopy to answer this question. This methodology enables the mass-selected measurement of gas-phase IR spectra. Accordingly, it is possible to identify whether xylyl radicals are selectively produced from suitable precursors and stable in a high-temperature environment or are susceptible to further decomposition/isomerization. Furthermore, these measurements would allow recording the gas-phase vibrational spectrum of these radicals for the first time. Note that most findings in the following section are published in Ref.[285] and are taken from this publication.

Figure 3.26: TOC image of the article *The Gas-Phase Infrared Spectra of Xylyl Radicals* as published in J. Phys. Chem. Adapted with permission from Ref.[285]

3.3.2 Experimental Parameters

All three xylyl isomers were produced by flash pyrolysis of the respective nitrite precursor according to Fig. 3.27. The nitrites were synthesized from (methylphenyl)ethyl alcohols according to literature.[284] The products were purified by distillation under reduced pressure and stored in a dark freezer. Prior to use, the precursors were distilled again to remove alcohols that accumulate in the product over time.

The precursors were placed in a heatable sample container and heated to 95-110 °C to improve vapor pressure. They were seeded in 1.5 bar He, and a pulsed molecular jet was produced by a solenoid valve operating at 20 Hz. Afterward, the jet was guided through a resistively heated SiC micro-reactor (approx. 1000 K) in order to cleave the precursor and consequently expanded into the pre-chamber of a differentially pumped vacuum apparatus. The molecular jet with the pyrolysis products is skimmed, entering the ionization region of a TOF-MS. Here, the molecular beam is crossed by IR and UV radiation, and the resulting ions were accelerated towards an MCP array for detection.

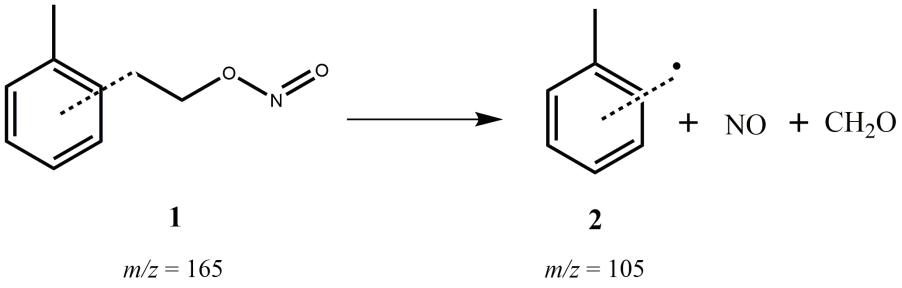

Figure 3.27: Thermal decomposition of the (methylphenyl)ethyl nitrite precursor to the respective xylyl radical. Secondary reaction products are formaldehyde and nitric oxide. Adapted with permission from Ref.[285]

A frequency-doubled Nd:YAG pumped dye laser was utilized as a UV source. For ionization via a [1+1]-REMPI process, rhodamine 101 was employed to produce radiation in the range of 309-312 nm after frequency doubling. The UV laser was set to a repetition rate of 20 Hz and delivered pulses with approx. 1.5 mJ per pulse. The UV wavelength was optimized with regards to xylyl ionization efficiency in preliminary experiments and set to 311.35 nm (ortho), 310.08 nm (meta), and 309.73 nm (para), respectively. The free-electron laser FELIX was utilized to produce the IR radiation for the double-resonance experiment. It creates IR light up to 100 mJ per macropulse at 10 Hz and the wavelength can be modified to scan the fingerprint region from 550 to 1700 cm^{-1}. The scan step width was set to 2 cm^{-1} and the line width of the IR radiation can be estimated to be 0.5% of the set wavenumber for the used parameters. The UV pulse was delayed by 200 ns with regards to the IR radiation to optimize the temporal overlap between IR excitation and ionization. After data acquisition and analysis, the spectra were compared to ab initio calculations on a B3LYP/6-311++G** level of theory as

Table 3.3: Overview of the Experimental Parameters of the Xylyl IR/UV Experiments.

Experimental Parameters	
Parameter	Value
Precursor	$C_8H_8NO_2$
UV Wavelength(o)	311.35 nm
UV Wavelength(m)	310.08 nm
UV Wavelength(p)	309.73 nm
UV Energy	1.5 mJ
UV Delay	200 ns
Ionization Scheme	[1+1]-REMPI
IR Scan Range	550 - 1700 cm^{-1}
IR Step Width	2.0 cm^{-1}
UV Repetition Rate	20 Hz
IR Repetition Rate	10 Hz
Seeding Gas	Helium
Seeding Pressure	1.5 bar

implemented in the Gaussian 09 suite. The vibrational frequencies were calculated with an anharmonic correction which was necessary for an accurate description of the xylyl radicals. Finally, the calculated spectra were convolved with a gaussian function (FWHM = 8 cm^{-1}) for better comparison with the experimental spectra.

3.3.3 Results and Discussion

3.3.3.1 Mass Spectra of the Thermal Decomposition of the Xylyl Precursors

A selection of [1+1]-REMPI mass spectra for the three xylyl precursors is depicted in Fig. 3.28. They were recorded at their respective optimized ionization wavelength around 310 nm, and masses in the range from 0 to 240 amu are displayed. As expected, all three mass spectra show very similar mass signals. The absence of a signal at m/z = 165 suggests a complete conversion of the precursors after pyrolysis. The spectra show an efficient generation of xylyl radicals, as all three spectra are dominated by strong mass peaks at m/z = 105. Furthermore, various lower masses are visible in all spectra, including a signal at m/z = 77 and a satellite at m/z = 103. These lighter masses are produced by DPI of m/z = 105 as most show the same IR spectrum as the predominant signal. All spectra also share a signal peak at m/z = 208. This represents the radical-radical dimerization product of mass 105 after H_2-loss. Finally, various signals can be observed between mass 105 and 208. Again, these signals can be explained by DPI of mass 208, as most share the same IR spectrum. Note that for some of the very small signals, the ion dip signal was insufficient to provide a meaningful IR spectrum for identification.

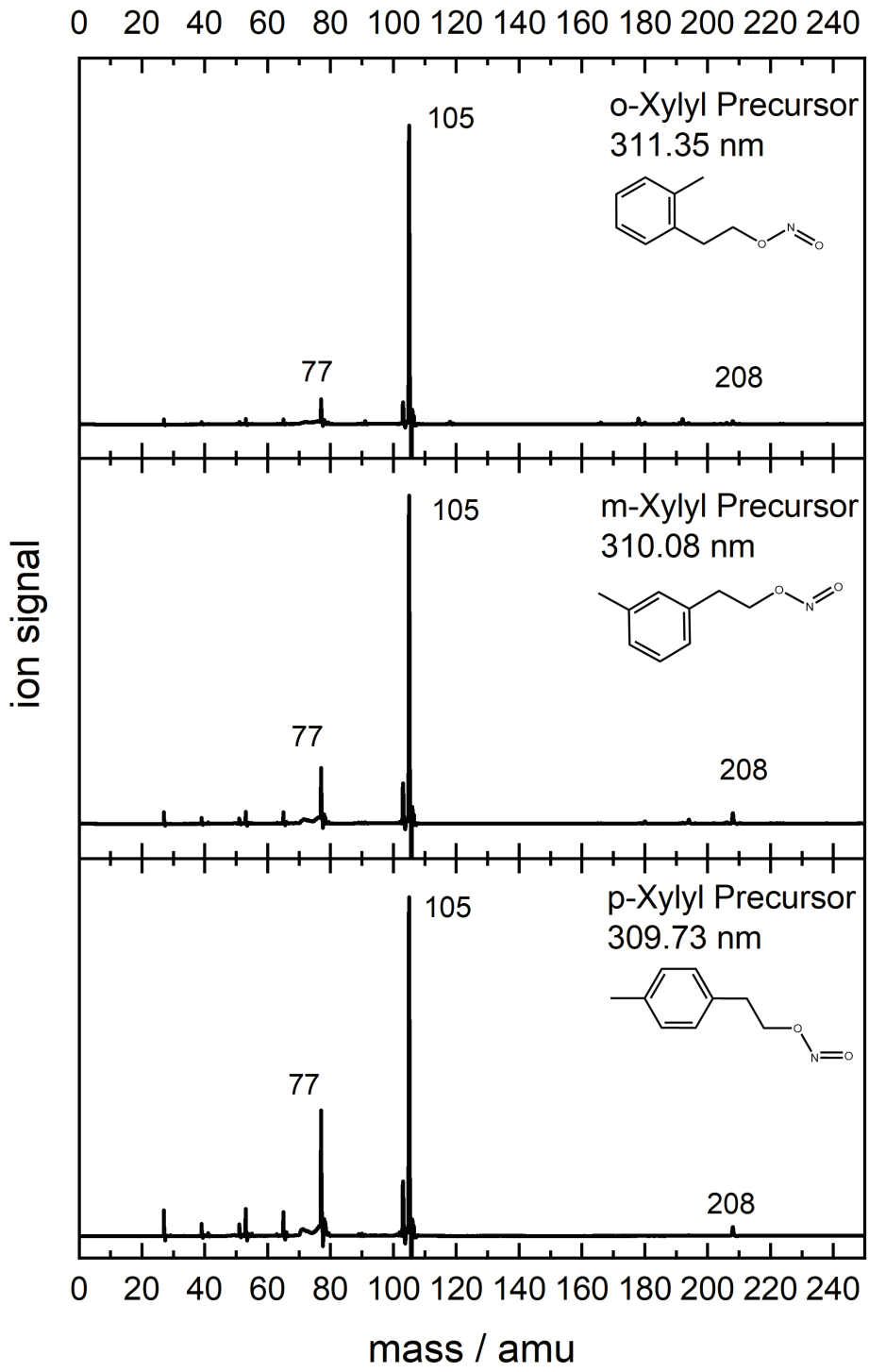

Figure 3.28: [1+1]-REMPI mass spectra of the xylyl precursors. **top**: Pyrolysis of 2-(2-methylphenyl)ethyl nitrite at 311.35 nm; **center**: Pyrolysis of 2-(3-methylphenyl)ethyl nitrite at 310.08 nm; **bottom**: Pyrolysis of 2-(4-methylphenyl)ethyl nitrite at 309.73 nm. Adapted with permission from Ref.[285]

3.3.3.2 IR Spectra of the three Xylyl Radicals

The mass-selected (m/z = 105) IR spectra of the three xylyl radical precursors are depicted in Fig. 3.29. The experimental spectra (solid line) are compared to anharmonic DFT calculation (dotted line) and were normalized for better comparison. Some low-intensity combination bands with torsional contribution were ignored as they were expected not to be accurately calculated at the chosen level of theory. Note that this did not change the overall contour of the calculated spectra. A complete list with all identified vibrational modes is shown in Table 3.4.

3.3.3.3 The IR Spectrum of the ortho-Xylyl Radical

The IR/UV spectrum of mass 105 after decomposition of 2-(2-methylphenyl)ethyl nitrite is shown in the top trace of Fig. 3.29. Comparing the experimental spectrum to DFT calculations, the carrier can clearly be identified as the ortho-xylyl radical. The spectrum shows four distinct signals, two in the lower and two in the higher energy region. The two fundamental wagging modes of ortho-xylyl appear at 689 cm^{-1} and 758 cm^{-1} and agree well with the calculated energies at 703 cm^{-1} (35_1) and 768 cm^{-1} (32_1). These two wagging vibrations are characteristic for all xylyl radicals but differ in energy and intensity slightly for the respective isomer. In this case, the energy spacing and relative intensity between the two signals are well described by theory and allows for a clear identification of the carrier. At higher energies, a peak around 1453 cm^{-1} and 1566 cm^{-1} can be observed. The first signal is broadened as it is composed of several fundamentals (12_1, 13_1, 14_1, 15_1), overtones (34_2) and combination bands (32_135_1, 34_135_1), which overlap in the experimental data. The smaller peak at 1566 cm^{-1}, however, displays a sharper contour and can be assigned to the 10_1 deformation mode calculated at 1564 cm^{-1}. The middle section of the experimental spectrum between 800 cm^{-1} and 1400 cm^{-1} shows no distinct features. This agrees with computations as only very low-intensity vibrations were calculated in this region.

Besides these identified vibrational signals, the data does not exhibit any other meaningful features. This concludes that ortho-xylyl is the sole carrier of mass 105, and no other molecules with the same mass are present. Furthermore, it shows that ortho-xylyl is stable when isolated in a noble gas and would consequently be available for other types of spectroscopic experiments.

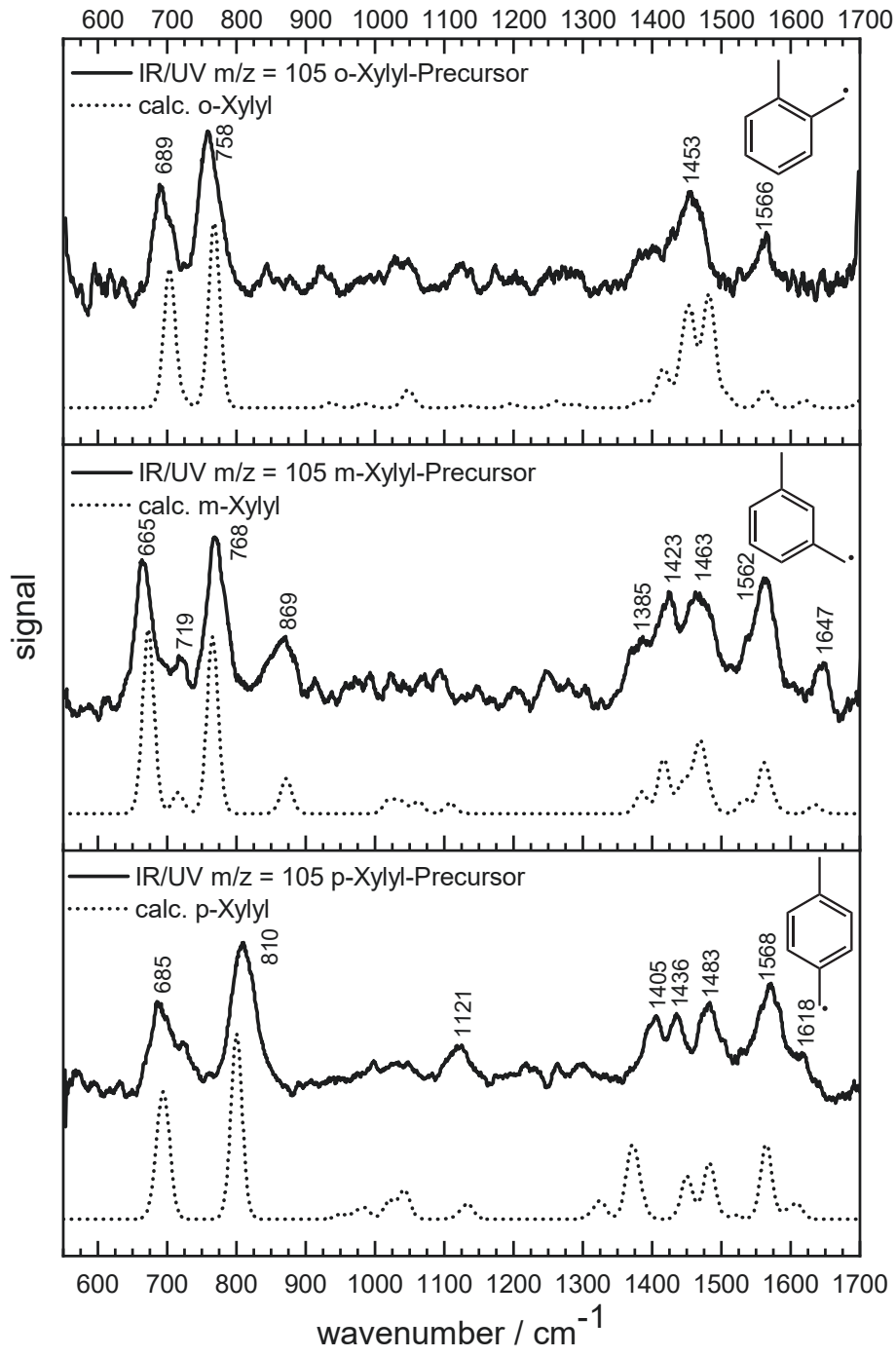

Figure 3.29: IR/UV spectra of the three xylyl radical traces (solid line) in comparison to vibrational calculations (dotted line). **top**: IR/UV from the decomposition of 2-(2-methylphenyl)ethyl nitrite in comparison to ortho-xylyl; **center**: IR/UV from the decomposition of 2-(3-methylphenyl)ethyl nitrite in comparison to meta-xylyl; **bottom**: IR/UV from the decomposition of 2-(4-methylphenyl)ethyl nitrite in comparison to para-xylyl. Adapted with permission from Ref.[285]

Note that the spectrum seems to rise to both ends of the measured range, suggesting the presence of additional signals. This, however, is due to inconsistencies of the FEL at the edges of the scannable range and is amplified in the processing of the raw data. These have been observed before and hence should be considered artifacts.

3.3.3.4 The IR Spectrum of the meta-Xylyl Radical

The mass-selected IR spectrum of the meta-xylyl precursor 2-(3-methylphenyl)ethyl nitrite is displayed in the center trace of Fig. 3.29. Again, the spectrum displays two distinct wagging vibrations in the lower energy region at 665 cm $^{-1}$ and 768 cm^{-1} which are in good agreement with the calculations at 673 cm^{-1} (35_1) and 766 cm^{-1} (32_1). In addition, theory predicts two small vibrational modes in this region; another wagging mode at 719 cm^{-1} (34_1) and a CH_2/CH_3 twist at 859 cm^{-1} (31_1). Although the predicted intensity is quite small, both signals can clearly be observed in the experimental spectrum at 719 cm^{-1} and 869 cm^{-1}. These small vibrations are unique to the meta isomer in the group of xylyl radicals and are absent in the IR spectrum of the other xylyl isomers. The middle part of the spectrum is featureless, and the calculations only predict signals with insignificant intensity. The upper energy region, however, shows five peaks above 1350 cm^{-1}. The first three signals appear at 1385 cm^{-1}, 1423 cm^{-1}, and 1463 cm^{-1}, which partially overlap above a broad base. The other two peaks are well separated at 1562 cm^{-1} and 1647 cm^{-1}. Calculations predict these signals to be composed of several fundamental, overtones and combination bands, which are listed in more detail in Table 3.4. Overall the calculated spectrum matches the experimental data very well, and thus the carrier of mass 105 can unambiguously be identified as meta-xylyl. Again, no contribution of other possible carriers can be observed in the spectrum, suggesting a neat generation of meta-xylyl in the pyrolysis.

3.3.3.5 The IR Spectrum of the para-Xylyl Radical

The lower trace in Fig. 3.29 shows the IR/UV spectrum of m/z = 105 after decomposition of 2-(4-methylphenyl)ethyl nitrite. The calculated spectrum shows two characteristic low energy bands for para-xylyl. The first consists of the modes 35_1 (688 cm^{-1}) and 34_1 (698 cm^{-1}), which overlap to a single band in the calculated spectrum. This matches the experimental data well with a peak at 685 cm^{-1} and a small shoulder to higher energies. The second peak is a wagging mode calculated at 800 cm^{-1} (31_1) and is also in good agreement with the measured peak at 810 cm^{-1}. Theory again only predicts low-intensity modes in the central section of the

fingerprint region. This time, however, a peak at 1121 cm^{-1} is clearly identifiable in this region due to a better signal/noise ratio in the measurement. It can be assigned to the 23_1 in-plane bending mode calculated at 1135 cm^{-1}. The calculated spectrum also suggests several other modes from 950 cm^{-1} - 1100cm^{-1} with similar intensities. However, it was not possible to resolve these vibrations in the experiment, and the data only show severe broadening in this area. In the higher energy region above 1400 cm^{-1} four distinct signals can be identified at 1405 cm^{-1}, 1436 cm^{-1}, 1483 cm^{-1} and 1568 cm^{-1}. The first one at 1405 cm^{-1} corresponds to the two overtones 34_2 and 35_2 and the 34_135_1 combination band. The calculated spectrum underestimates this signal noticeably by 31 cm^{-1}, showing a peak at 1374 cm^{-1}. The next signals, however, are well represented in the calculations in spacing and relative intensity. The mode at 1436 cm^{-1} is comprised of two fundamentals at 1450 cm^{-1}(14_1) and 1451 cm^{-1}(15_1). The 12_1 deformation mode appears in the experiment at 1568 cm^{-1}. Para-xylyl also exhibits a C=C aromatic stretching mode (10_1) of medium intensity in this region. It can be observed at 1568 cm^{-1} and is well separated. Finally, the attentive observer might observe a small shoulder to higher energies at 1618 cm^{-1}. In consideration of the calculated vibrations, this peak can be assigned to a combination band (31_132_1) calculated at 1609 cm^{-1}. As for the other two isomers, the carrier of mass 105 of pyrolytically cleaved 2-(4-methylphenyl)ethyl nitrite can be unambiguously identified as the respective xylyl isomer, para-xylyl.

Table 3.4: Identified Vibrational Bands of the three Xylyl Radical Isomers in Comparison with Calculated Energies. Energies given in cm^{-1}.

Experimental Parameters		
Isomer	Energy	Transition
ortho	689	$35_1(703, \omega_{CH_2,CH_3,ring})$
	758	$32_1(768, \omega_{CH_2,ring})$
	1453	$15_1(1450, \delta_{CH_3}), 14_1(1453, \delta_{IP}), 13_1(1477, \beta_{CH_2,CH_3}),$ $12_1(1485, \beta_{CH_2,CH_3}), 34_2(1441), 32_135_1(1459),$ $34_135_1(1417)$
	1566	$10_1(1564, s_{CCring})$
meta	665	$35_1(673, \omega_{CH_2,ring})$
	719	$34_1(716, \omega_{CH_2,ring})$
	768	$32_1(766, \omega_{CH_2,ring})$
	869	$31_1(859, \tau)$
	1385	$34_135_1(1385)$
	1423	$34_2(1417), 15_1(1443, \delta_{CH_3})$
	1463	$12_1(1471, \beta_{CH_2,CH_3}), 13_1(1459, \beta_{CH_2,CH_3})$
	1562	$10_1(1561, s_{CCring}), 31_134_1(1575)$
	1647	$31_132_1(1635)$
para	685	$35_1(688, \omega_{CH_2}), 34_1(698, \omega_{CH_2,CH_3})$
	810	$31_1(800, \omega_{ring})$
	1121	$23_1(1135, \beta_{ring})$
	1405	$35_2(1370), 34_2(1384), 34_135_1(1374)$
	1436	$14_1(1450, \delta_{CH_3}), 15_1(1451)$
	1483	$12_1(1483, \delta)$
	1568	$10_1(1565, s_{CCring})$
	1618	$31_132_1(1609)$

Vibrational descriptors were applied where suitable following: s = stretch, β = in plane bend, δ = deformation, ω = wagging, τ = twist

3.3.3.6 Xylyl Dimers

The experiments on the three xylyl radicals also revealed a mass signal at m/z = 208 in the mass spectra of all three precursors, as displayed in Fig. 3.28. It corresponds to the dimerization product of two xylyl radicals accompanied by loss of H_2. The IR/UV spectrum of mass 208 for the meta and para experiments are shown in Fig. 3.30 and Fig. 3.31.

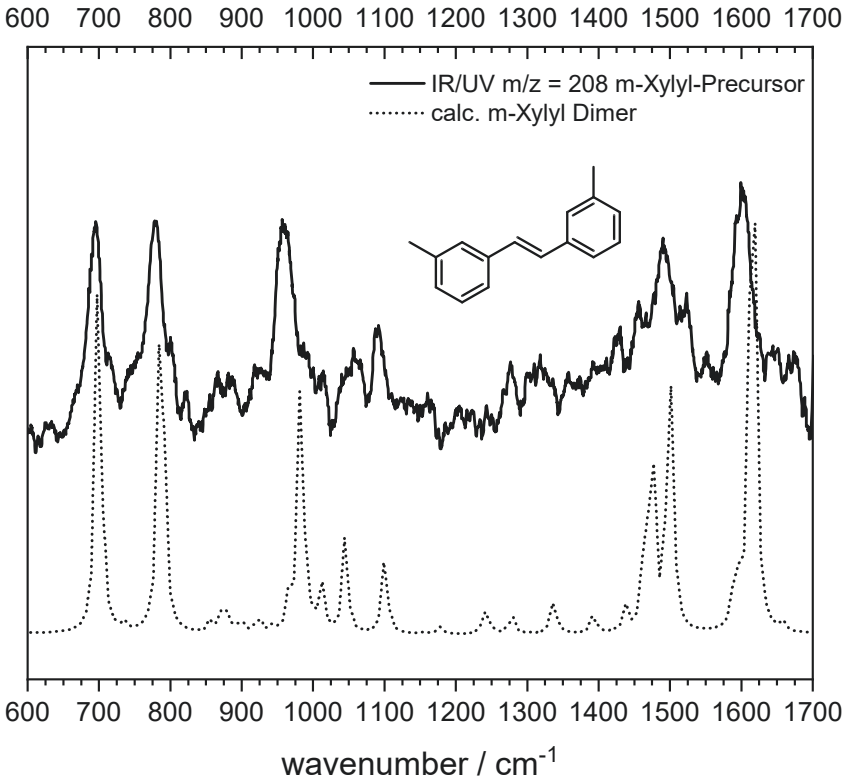

Figure 3.30: The IR/UV signal of the meta-xylyl dimerization product at mass 208 (solid line) in comparison to vibrational DFT calculations of (E)-1,2-bis(3-methylphenyl)ethene (dotted line). Adapted with permission from Ref.[285]

The respective spectrum for the ortho experiments had a too low signal/noise ratio for identification. The data in comparison with calculations revealed the dimerization product to be stilbene derivatives, (E)-1,2-bis(3-methylphenyl)ethene and (E)-1,2-bis(4-methylphenyl)ethene, respectively. This is very interesting considering the findings from previous benzyl experiments (see Section 3.2.3.3), which is a very similar system. The xylyl dimers are most likely formed under radical-radical addition and subsequent H_2-loss to form the stilbene double bond. In contrast, the benzyl dimerization and following reactions showed a preference for cycliza-

tion after initial addition to forming 9,10-dihydrophenanthrene and phenanthrene. This observation might be due to inefficient ionization of phenanthrene derivatives around 310 nm. But note further that no stilbene derivatives have been observed in the benzyl experiments under similar conditions. Consequently, it can be assumed that due to increased steric interaction, cyclization is hindered in the dimerization of xylyl radicals, which might explain the difference in dimerization characteristics compared to benzyl.

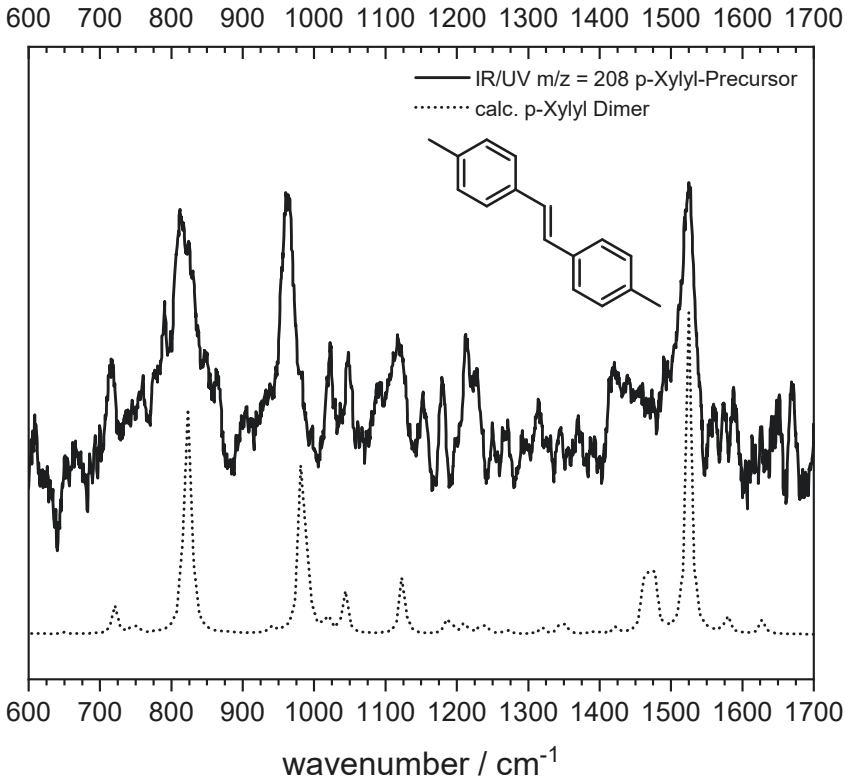

Figure 3.31: The IR/UV signal of the para-xylyl dimerization product at mass 208 (solid line) in comparison to vibrational DFT calculations of (E)-1,2-bis(4-methylphenyl)ethene (dotted line). Adapted with permission from Ref.[285]

3.3.3.7 Xylyl Radical Isomerization

An important topic when it comes to xylyl radicals is the question if they isomerize in a high-temperature environment like a heated micro-reactor. The isomerization of different C_8H_9 isomers has been studied theoretically, and the three xylyl radicals can be regarded as isoenergetic, as the difference in the heat of formation is less than 1 kJ mol^{-1}.[282] Meta-xylyl is supposed to be most susceptible to isomerization. It is the least stable isomer, and the activation energy to isomerize to ortho- or para-xylyl was calculated to be +292 kJ mol^{-1} and +289 kJ mol^{-1}, respectively. Hemberger et al. showed in a photoionization study that para-xylylene is formed in the pyrolysis of meta-xylyl bromide, demonstrating an accessible isomerization pathway from meta- to para-xylyl.[282]

Furthermore, isomerization of xylyl involving methyltropyl has been reported by Reilly and coworkers.[286] Recent experiments, however, showed that ortho- and para-xylyl H-abstraction is favored in contrast to isomerization, which leads to the formation of para-xylylene and benzocyclobutene, respectively.[284]

In the present study, no isomerization products were observed. This shows that a neat sample of a specific xylyl radical can be produced utilizing nitrite precursors under mild pyrolysis conditions, which avoids unwanted isomerization processes. The occurrence of isomerization products in other studies might originate in the use of precursors which exhibit higher leaving group binding energies, e.g., halogenides. These require higher pyrolysis temperatures for bond cleavage, which might make several isomerization pathways energetically accessible. The same concept applies to other generation methods, which inherently deploy a lot of thermal energy into the experiment, like molecular discharge sources.

This suggests that the reactor temperature is the crucial experimental parameter for xylyl radical isomerization and must be minimized when a clean radical sample is required for the experiment.

3.3.4 Summary

This study on the three isomers of xylyl radicals allowed for the first measurement of their fingerprint IR spectrum in an isolated gas-phase environment. The molecular structures and vibrational modes of the isomers are very similar. A comparison of the vibrational data revealed that all isomers could be unambiguously differentiated by their strong low energy modes. Therefore the identification of xylyl radicals is accessible via IR spectroscopy. This is a useful finding as identification via purely ionization-based methods is possibly hindered by the similarity of the d3 $\leftarrow$ d0 transition between all three isomers.

Previous studies suggest that isomerization has to be considered as a follow-up reaction when xylyl radicals are formed, especially for the less stable meta isomer. In the present study, however, it was shown that these radicals could be neatly generated under the utilized experimental parameters from their respective nitrite precursors by flash-pyrolysis. This allows for the specific generation of certain isomers for future experiments without the necessity of coupled structural sensitivity.

All structural identification was carried out with the help of DFT calculations on a B3LYP/6-311++G** level of theory as implemented in gaussian09. Here, it turned out that taking anharmonicity into account was not only beneficial but necessary for a correct simulation of the vibrational spectra. The lower energy modes of the xylyl isomers are energetically very similar in their position and require a precise theoretical description to differentiate between the isomers. Furthermore, the inclusion of overtones and combination bands from the anharmonic calculations allowed for an accurate prediction of the higher energy vibrational landscape for all isomers.

Finally, the only other masses identified besides the xylyl radicals were dimerization products originating from radical-radical association. Here, the dimers were identified as stilbene isomers, (E)-1,2-bis(3-methyl-phenyl)ethene and (E)-1,2-bis(4-methylphenyl)ethene, as it would be expected from a neat generation of the respective xylyl radicals. Other masses observable in the mass spectra were consequently all a result of dissociative photoionization from either the xylyl radicals themselves or their dimerization products.

3.4 Ortho-, Meta- and Para-Xylylene

3.4.1 Introduction

Xylylenes are a group of resonance stabilized hydrocarbons that exhibit distinct biradical character.[287,288] Although molecular hydrocarbon biradicals have been studied for years, much of this research is limited to theoretical work as experiments are difficult to perform. Due to the unstable nature of the vast majority of these molecules, experiments must be performed in isolation. The biradicals themselves have to be generated in a mild and selective manner. Consequently, gas-phase molecular beam and matrix isolation techniques combined with spectroscopic detection have been proven useful to investigate these systems in recent years.

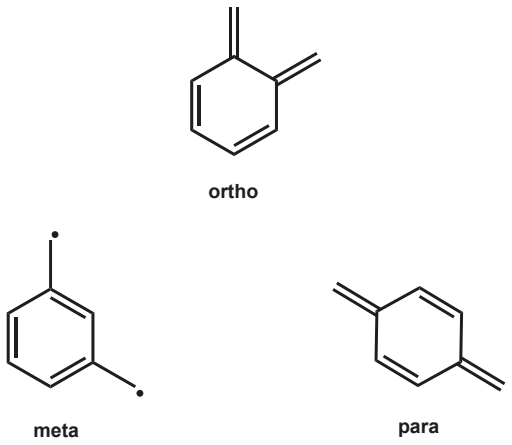

Figure 3.32: The three xylylene isomers: Ortho, meta and para.

Moreover, xylylenes represent an additional decomposition product (cf. Fig. 3.33) in the high-temperature reaction of xylene.[289,290] As mentioned in Chapter 3.3, xylene is an important anti-knock agent in gasoline blends that decompose to xylyl radicals during combustion. If another hydrogen is abstracted, xylylenes can be formed, which can contribute to the formation of PAHs and soot.

C_8H_8 is the composition of the xylylene molecules, and they appear in ortho-, meta-, and para-constitution as depicted in Fig. 3.32. Meta-xylylene is usually depicted in non-Kekulé form because it represents a true biradical. Ortho- and para-xylylene exhibit a lesser biradical character due to mesomeric stabilization and are usually depicted in a Kekulé structure. The drastic difference in biradical character combined with their simple structure makes them outstanding benchmark molecules for molecular biradicals.

Recent spectroscopic studies include matrix-isolation experiments,[291–293] threshold-photoelectron spectroscopy[281,282,294] and femtosecond time-resolved photoelectron spectroscopy.[87,295] These gave new information about their structural properties, thermochemistry, excited state dynamics, and high-temperature reactivity. For techniques that lack structural sensitivity, it is important to confirm the

formation of the desired species for a specific generation method, e.g., pyrolysis. This is especially important because it has been suggested that xylylenes exhibit a high probability to isomerize.

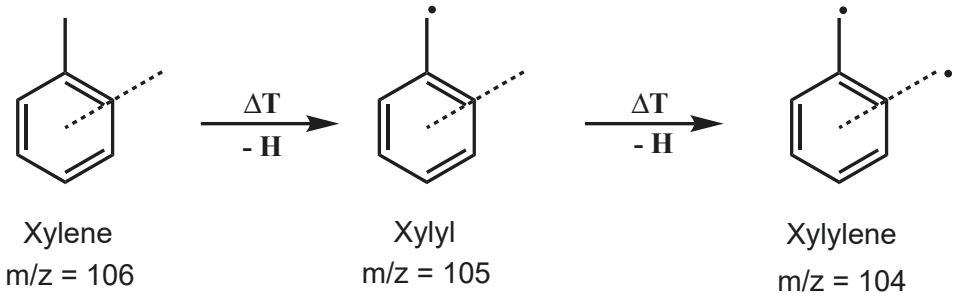

Figure 3.33: Thermal decomposition of xylene to xylyl and xylylene via sequential hydrogen elimination.

Hence, in the current study, IR/UV ion dip spectroscopy was employed to confirm the generation of pyrolytically generated xylylenes in a molecular beam environment and observe potential secondary reaction products. Identification is carried out by comparison of the mass-selected IR spectra with DFT calculations. Most of these results have been published in Ref.[148]

3.4.2 Experimental Parameters

The xylylene isomers were pyrolytically generated in a resistively heated SiC microreactor. The precursors employed were 3-isochromanone (ortho-xylylene), 1,3-bisbromomethylbenzene (meta-xylylene) and [2.2]paracyclophane (para-xylylene). The samples were placed in a sample container within a molecular beam source and heated to 80°C, 110°C, or 170°C to increase gas-phase concentration. After seeding the precursors in a noble gas (He/Ar), a solenoid valve is employed to create the pulsed free jet.

Subsequently, the beam is guided through the pyrolysis unit and expanded into a deferentially pumped vacuum apparatus. The cold central cone of the jet is skimmed, entering the ionization region of a time-of-flight spectrometer, where the beam is crossed by the incident IR and UV radiation.

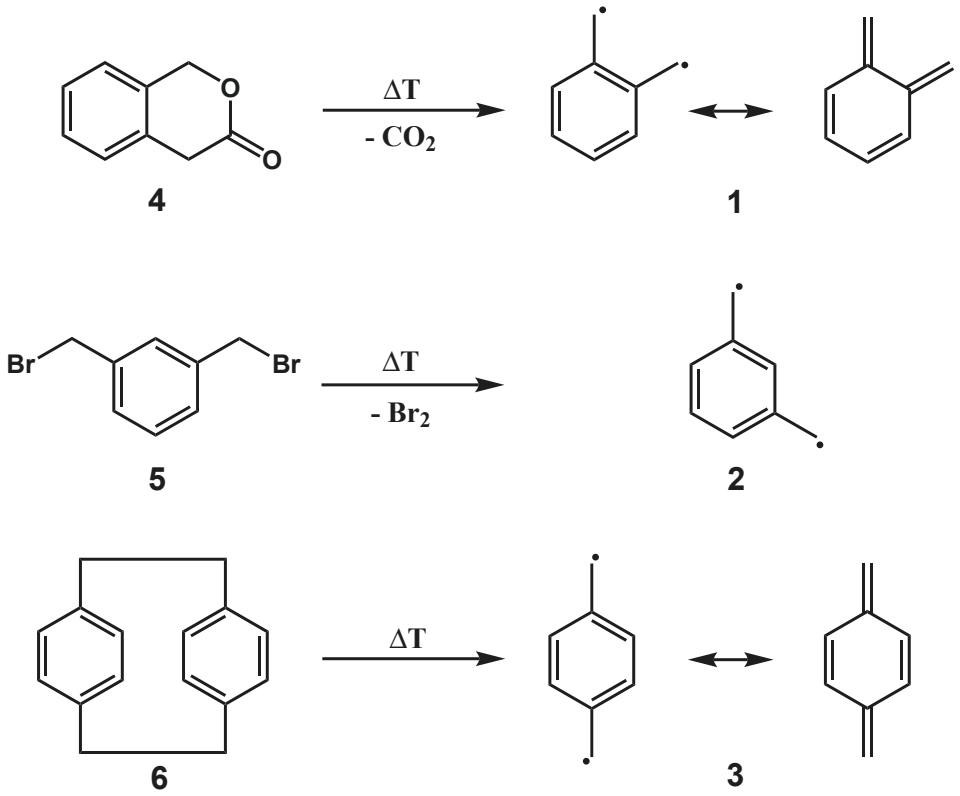

Figure 3.34: Overview of the thermal decomposition of all three xylylene precursors. **top**: Decomposition of 3-isochromanone to ortho-xylylene; **center**: Decomposition of 1,3-bisbromomethylbenzene to meta-xylylene; **bottom**: Decomposition of [2.2]paracyclophane to para-xylylene.

A dye laser pumped by a pulsed Nd:YAG (20 Hz) produced frequency-doubled UV radiation at 265 nm and 266 nm. The molecules were ionized following a [1+1]-REMPI scheme with an average laser power between 0.75 - 1.00 mJ. A free-electron laser (FELIX) provided scannable IR radiation in the fingerprint region between 550-1750 cm^{-1}.

The FEL was operated at 10 Hz with a scan step width of 2.0 cm^{-1} or 2.5 cm^{-1}, respectively. Furthermore, a delay between IR and UV of 200 ns was set to optimize the depletion signal. The experimental TOF-MS data were corrected for variations in laser power, averaged over multiple measurements, and finally smoothed using digital filtering.

Table 3.5: Overview of the Experimental Parameters of the Xylylene IR/UV Experiments.

Experimental Parameters	
Parameter	Value
Precursor (ortho)	$C_9H_8O_2$
Precursor (meta)	$C_8H_8Br_2$
Precursor (para)	$C_{16}H_{16}$
UV Wavelength(ortho)	266 nm
UV Wavelength(meta)	266 nm
UV Wavelength(para)	265 nm
UV Energy	0.75-1.00 mJ
UV Delay	200 ns
Ionization Scheme	[1+1]-REMPI
UV Repetition Rate	20 Hz
IR Scan Range	550 - 1750 cm^{-1}
IR Step Width	2.0 / 2.5 cm^{-1}
IR Repetition Rate	10 Hz
Seeding Gas (ortho/meta)	Helium
Seeding Gas (para)	Argon
Seeding Pressure (ortho/meta)	1.5 bar
Seeding Pressure (para)	1.4 bar

For identification, the resulting mass-selected IR spectra were compared to vibrational calculations at a B3LYP/6-311++G** level of theory as implemented in the Gaussian09 suite.[191] Calculations for the xylylene molecules were augmented with anharmonic corrections to provide a sufficient representation of the vibrational modes. This was not necessary for other species, and hence these were calculated in the harmonic approximation. Note that anharmonic effects on the mid-IR region of PAHs have recently been investigated in detail by Rijs and coworkers.[296]

3.4.3 Results and Discussion

3.4.3.1 The Mass Spectra of the Xylylene Precursors

The conversion of **4** (3-isochromanone), **5** (1,3-bisbromomethylbenzene) and **6** ([2.2]paracyclophane) to the respective xylylene radicals were observed via the [1+1]-REMPI mass spectra at 265 nm and 266 nm, as depicted in Fig. 3.35. The spectra were further normalized for better visual comparison.

Here, all precursors show a good conversion to carriers with m/z = 104, which are the dominant signal peaks in the mass spectra. No signal at the masses of the respective precursors can be observed, which indicates a full thermal conversion. The MS also shows peaks with lower masses and small intensities. These signals below 100 amu are probably mainly caused by dissociative photoionization and are no additional decomposition products of the precursor.

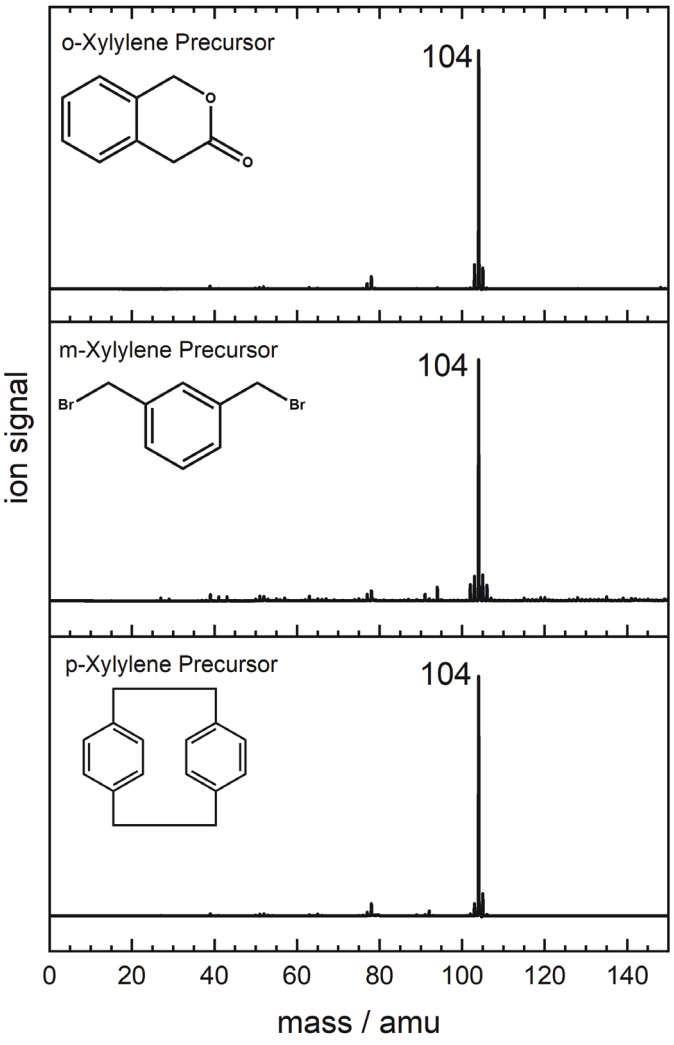

Figure 3.35: Mass spectra of the xylylene experiments. **top**: Thermal decomposition of 3-isochromanone; **center**: Thermal decomposition of 1,3-bisbromomethylbenzene; **bottom**: Thermal decomposition of [2.2]paracyclophane.

3.4.3.2 IR/UV of Mass 104 from the Decomposition of 3-Isochromanone

The IR/UV spectrum of **4** at mass 104 is depicted in Fig. 3.36. The spectrum exhibits a very good signal/noise ratio in the fingerprint region from 550-1750 cm^{-1}. Major vibrational modes are observed at 717 cm^{-1}, 783 cm^{-1}, 1197 cm^{-1} and 1455 cm^{-1}.

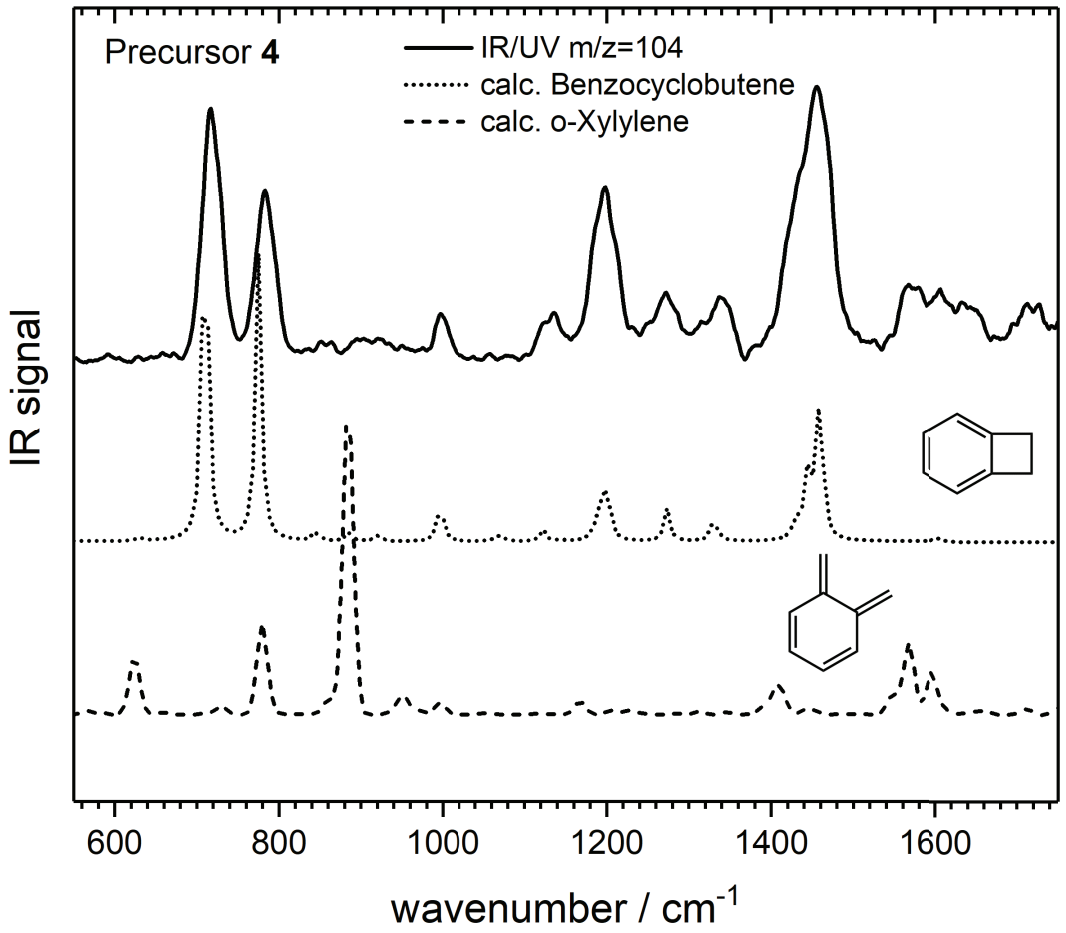

Figure 3.36: The IR/UV spectrum of mass 104 (solid line) from the decomposition of 3-isochromanone in comparison with vibrational calculations of benzocyclobutene (dotted line) and para-xylylene (dashed line).

Comparing the experimental spectrum to anharmonic vibrational calculations of ortho-xylylene (dashed line) shows no conformance. On the other hand, the experimental data matches the harmonic vibrational spectrum of benzocyclobutene

(dotted line) very well. All major modes are well represented in the simulation and experiment. Only small variations in signal intensity are observed, especially for the two strong modes in the lower energy region, which can easily be explained by inefficiencies in the harmonic approximation. Consequently, the carrier of mass 104 can clearly be identified as benzocyclobutene, and no indication of **1** is present in the experimental data.

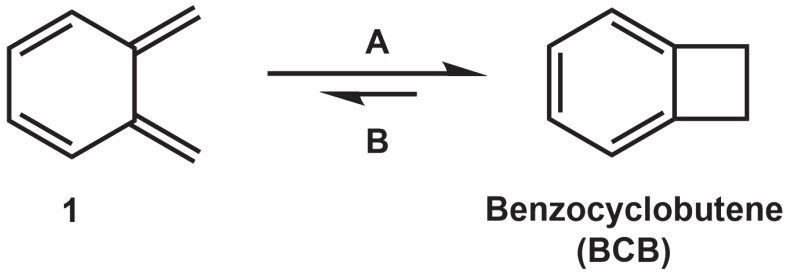

Figure 3.37: Equilibrium between para-xylylene and benzocyclobutene. The forward reaction A is energetically favoured.

This is not entirely surprising as the equilibrium between **1** and benzocyclobutene (cf. Fig. 3.37) has been a well-understood isomerization in organic synthesis for decades. In this regard, benzocyclobutene has been proven to be a very useful precursor to generate ortho-xylylene via **B** in solution upon thermal activation. The reverse isomerization **A** exhibits in the gas-phase a low reaction barrier of 0.17 eV and is exothermic by 0.48 eV.[284] These energies are readily available in a pyrolysis experiment like this, and thus this reaction could be accessible.

3.4.3.3 IR/UV of Mass 104 from the Decomposition of 1,3-Bisbromoethylbenzene

Figure 3.38 shows the IR/UV spectrum of m/z = 104. The experimental spectrum (solid line) is dominated by three strong bands in the lower energy region at 705 cm^{-1}, 780 cm^{-1}, and 910 cm^{-1}. Further bands to higher wavenumbers are also clearly distinguishable but exhibit a lower signal/noise ratio and partially overlap. The simulated vibrational spectrum of meta-xylylene (dashed line) does not match the experimental data, as major vibrational modes at 464 cm^{-1}, 763 cm^{-1}, 1254 cm^{-1}, and 1576 cm^{-1} are not observed. However, the results match the calculated spectrum of styrene (dotted line). All major bands below 1200 cm^{-1} are clearly identifiable in the experiments, and also, the vibrational landscape in the higher energy region is in good agreement between experiment and theory.

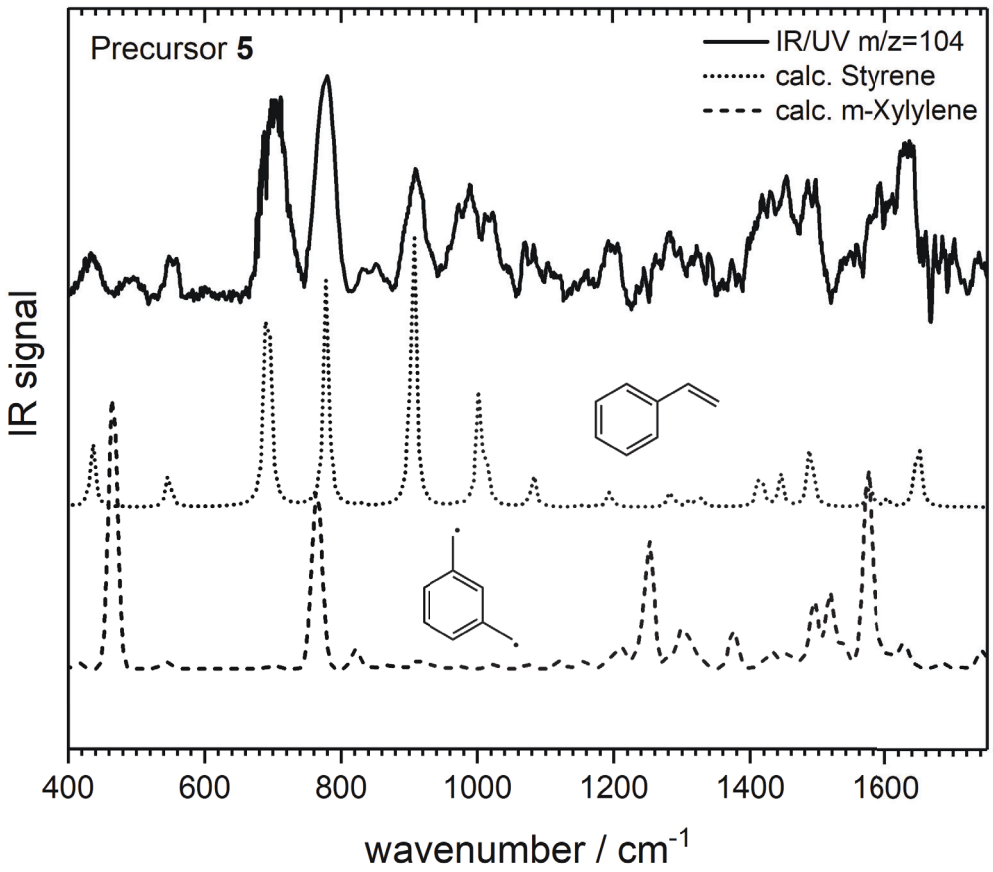

Figure 3.38: The IR/UV spectrum of mass 104 (solid line) from the decomposition of 1,3-bisbromoethylbenzene in comparison with vibrational calculations of styrene (dotted line) and meta-xylylene (dashed line).

Styrene is the most stable isomer with C_8H_8 constitution. It has been observed previously as a decomposition product of xylenes and xylyl radicals.[297] The formation has been discussed by a series of ring-closing/ring-expansion reactions involving ortho- or para-xylylene intermediates.

For meta-xylylene, this isomerization was recently studied theoretically by Reilley and coworkers.[286] They calculated the enthalpy of reaction to be highly exothermic by -183.7 kJ mol^{-1}, and the energetics of the reaction is displayed in Fig. 3.39. The initial step is the recombination reaction of **2** with a hydrogen radical to form meta-xylyl radical (**I**). Note that free hydrogen radicals are usually considered sufficiently available in a pyrolytically heated micro-reactor. The formation of **I** comes with an excess heat of 367.4 kJ mol^{-1} and the high temperatures during pyrolysis dump enough energy in the system to easily overcome all further reaction barriers (Δ_{max}H(0 K, **TSIII** − **I**) = 344.8 kJ mol^{-1}) to styrene. After the formation of **I**, the reaction proceeds via ring-expansion to form the methyltropyl radical (**V**). **V** is a rather stable radical due to its aromatic stabilization and is supposed to play an important role in the decomposition of toluene. Furthermore, Reilley et al. suggest **V** to be a common intermediate in reaction pathways of ortho- and para-xylylene, which might allow for direct isomerization between the three xylylene or xylyl isomers via a similar pathway. This, however, was not observed in the current study. Finally, styrene is formed from **V** after activation to the α-radical, ring-contraction to form the styrene molecular frame and consequently rearomatization by the elimination of hydrogen. Note that other reaction mechanisms for this isomerization have been suggested in the literature, which often include initial isomerization to other xylyl or xylylene isomers.[298,299]

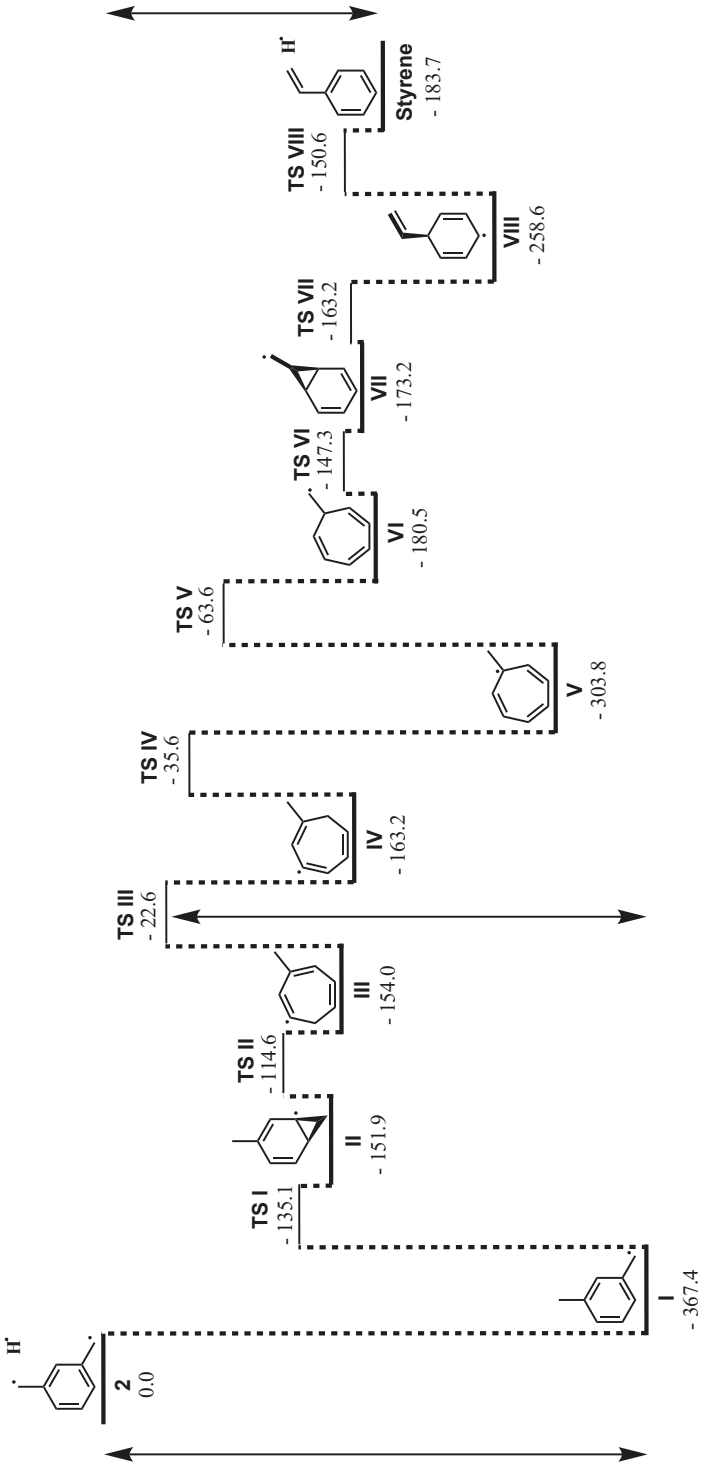

Figure 3.39: Energies and intermediates in the isomerization between meta-xylylene and styrene. Values given in kJ mol^{-1}. Figure partly adapted from Ref.[286]

3.4.3.4 IR/UV of Mass 104 from the Decomposition of [2.2]Paracyclophane

The results of the decomposition of **6** are displayed in Fig. 3.40. It shows the mass-selected (m/z = 104) IR/UV spectrum at the top (solid line) and the computed IR spectrum of para-xylylene at the bottom (dotted line). Due to its high symmetry, para-xylylene shows a quite simple IR spectrum dominated by two deformation modes at 445 cm^{-1} and 864 cm^{-1}, as well as a strong C=C bending mode at 1583 cm^{-1}.

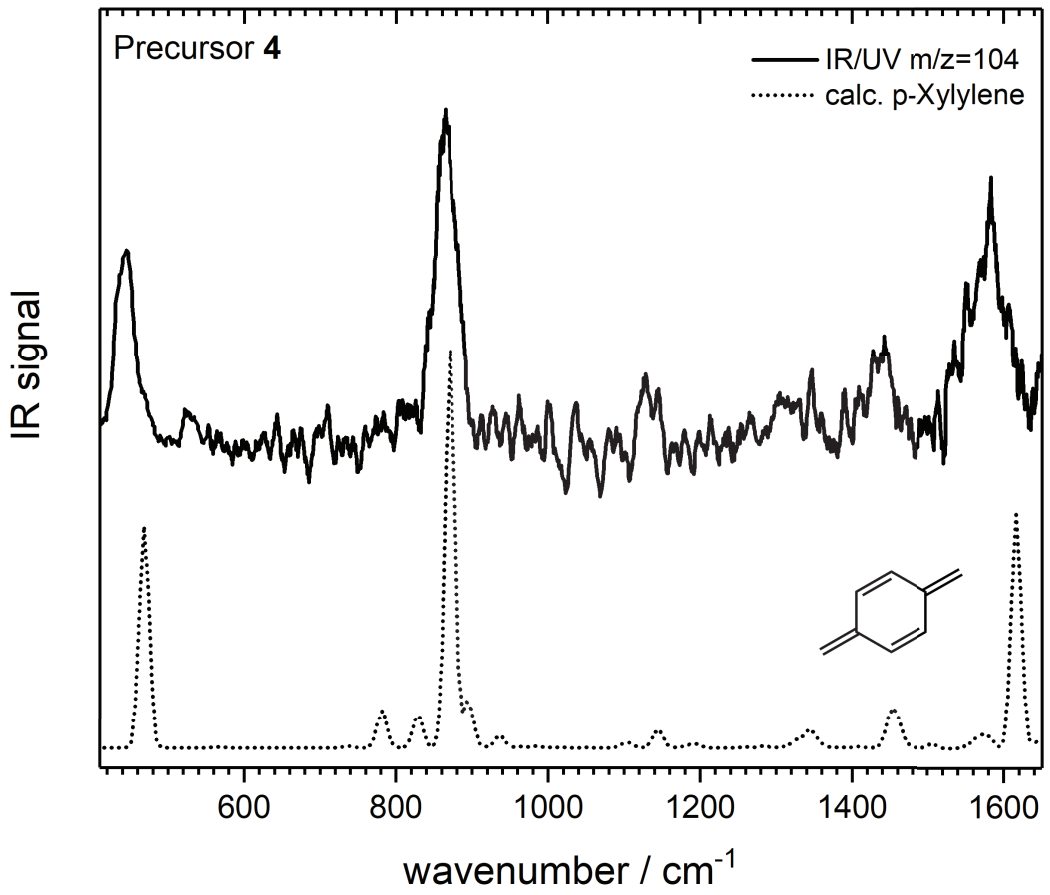

Figure 3.40: The IR/UV spectrum of mass 104 (solid line) from the decomposition of 3-isochromanone in comparison with vibrational calculations of para-xylylene (dotted line).

Although the experimental spectrum is quite noisy, smaller modes at 1128 cm^{-1} and 1443 cm^{-1} can be identified with the help of the DFT simulation. Overall the experimental spectrum is in excellent agreement with the computed vibrational

modes and also matches the IR-spectrum of **3** previously recorded in a rare-gas matrix by Marquardt and coworkers.[291,292] Hence, the carrier of mass 104 can unambiguously be identified as para-xylylene. Here, **6** has proven to be an excellent precursor to produce **3** in a pyrolysis reactor, as no other isomers could be identified in the experimental data. Although not strictly necessary for **3**, the DFT calculations were performed with an anharmonic correction to be consistent with the computed spectra of the other isomers. This, however, did improve the quality of the predicted vibrational modes in terms of energetic position and relative signal intensities.

3.4.3.5 Troubleshooting ortho- and meta-Xylylene

After analyzing the IR/UV data from the decomposition of **4** and **5**, the question arises why it was not possible to identify ortho- and meta-xylylene in the current study, especially because they have been observed in gas-phase experiments previously.[282,294] This probably boils down to two problems: (a) selecting suitable precursors for pyrolysis and (b) problems with the UV excitation of the respective excited states.

Hemberger et al. for example, used in their photoionization study 1,3-bis(iodomethyl)benzene to pyrolytically generate meta-xylylene.[294] In contrast to the bis-bromo compound employed in the current study, the iodine-carbon bond exhibits considerably lower bonding energy which can be cleaved at lower temperatures. Consequently, the pyrolysis reactor can be run at lower temperatures which might reduce undesired isomerization products. 1,3-bis(iodomethyl)benzene was also considered for the study, but the compound's low vapor pressure was insufficient for a pulsed molecular beam experiment and resulted in very low signal intensity.

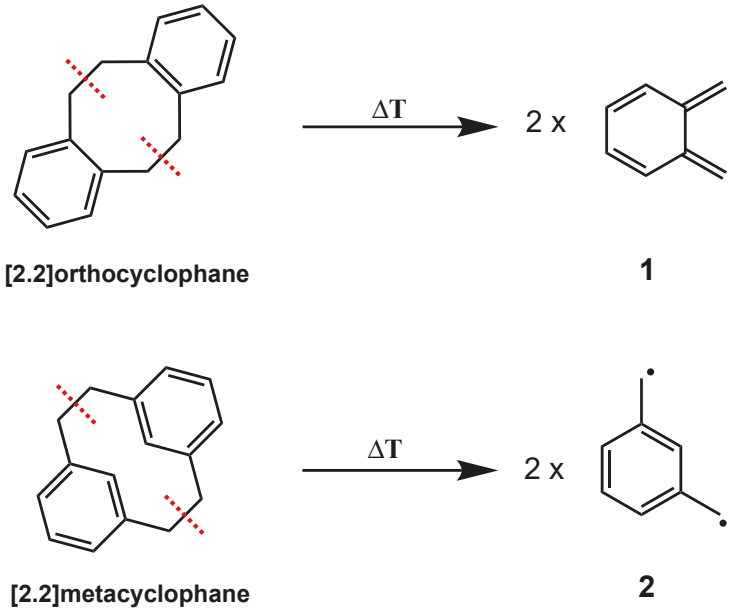

Figure 3.41: Alternative cyclophane precursors for the pyrolytic generation of ortho- and meta-xylylene.

To find a better precursor, it might be beneficial to consider the experiments on para-xylylene. [2.2]paracyclophane turned out to be an excellent precursor to generate **3**, as it is basically the dimer of the desired species. The same approach could be applied to generate the other isomers. [2.2]metacyclophane and [2.2]or-

thocyclophane are the analogous compounds (see Fig. 3.41). Although usually not commercially available, various synthetic routes for both compounds can be found in the literature.[300–303]

On the other hand, the UV ionization of the xylylenes might be another critical factor in detecting those species. In this regard, Mitric and coworkers recently calculated vertical excitation energies and oscillator strengths for relevant molecules in this study (cf. Table 3.6).[148] Experimentally for para-xylylene, a broad UV absorption band from 4.2 to 4.7 eV has been observed for the bright $\pi\pi^*$ state.[281] This transition to a $^1B_{2u}$ features a strong oscillator strength of ≈ 1. In comparison to the computed vertical excitation energy of 4.91 eV (cf. Table 3.6) a redshift by 0.36 eV (TDDFT/B3LYP/6-311++ G**) is expected. Consequently, **3** is efficiently excited at 265 nm (4.68 eV) in the experiment.

For **1**, a bright ($f \approx 0.15$) $\pi\pi^*$ transition into an ^1B state is predicted at 3.87 eV. Also, considering a red-shift correction, this transition lies well below the employed laser wavelength of 266 nm (4.66 eV) and can be considered off-resonant. Other allowed transitions with matching energies were calculated in the range from 5.13 - 5.50 eV. However, these $\pi\pi^*$ and Rydberg-states have considerably lower oscillator strength with $f \approx 0.001$ and $f \approx 0.003$, respectively. On the other hand, the observed isomerization product benzocyclobutene has a bright $\pi\pi^*$ transition at 4.97 eV. Again, considering a slight red-shift to the computed data, this transition matches the utilized UV excitation. Additionally, the BCB transition to the $\pi\pi^*$ possesses an oscillator strength of ≈ 0.017, which is nearly an order of magnitude higher than the comparable transitions for **1**.

The CCSD computations predict several allowed $\pi\pi^*$ and Rydberg transitions for **2** in the range from 3.59-5.21 eV. Experimentally, UV absorption bands from 4.3-4.5 eV (weak) and 5.2-5.6 eV have been reported.[293] The brightest transition into an $^1A_1$ state was computed at 4.97 eV with $f \approx 0.013$ and can be attributed to the lower energy band. For styrene, two $\pi\pi^*$ absorption bands have been observed from 4.3-4.5 eV (weak) and 4.87-5.58 eV (strong).[304–306] The later transition matches the applied UV wavelength substantially better than the transition in **2**. Thus, it can be assumed that the spectral conditions favor a resonant excitation of styrene in contrast to **2**. This, combined with a stronger oscillator strength ($f \approx 0.370$ vs. $f \approx 0.127$), is a sensible explanation for the biased detection of the isomerization product.

Table 3.6: Spectral Parameters of Relevant Species in the Xylylene Experiments. Vertical Excitation Energies ΔH_{vert} and Oscillator Strength f Computed Using EOM-CCSD with aug-cc-pVDZ. Data Compiled by Mitric et al. and taken from Ref.[148]

Spectral Parameters				
	ΔH_{vert}[eV]	f	Symmetry	Character
p-Xylylene (**3**)	3.72	0.000	$^1A_{1g}$	$\pi\pi^*$
	4.91	0.968	$^1B_{2u}$	$\pi\pi^*$
	5.15	0.000	$^1B_{1g}$	$\pi\pi^*$
	5.31	0.002	$^1B_{1u}$	Ry-3s
o-Xylylene (**1**)	3.87	0.153	^1B	$\pi\pi^*$
	5.13	0.001	^1A	Ry-3s
	5.31	0.003	^1B	$\pi\pi^*$
	5.50	0.003	^1A	Ry-3p_z
Benzocyclobutene (**BCB**)	4.97	0.017	$^1A_1$	$\pi\pi^*$
	6.08	0.008	$^1B_1$	Ry-3s
m-Xylylene (**2**)	3.59	0.001	$^3A_1$	$\pi\pi^*$
	3.92	0.001	$^3B_2$	$\pi\pi^*$
	4.44	0.002	$^3A_1$	$\pi\pi^*$
	4.72	0.000	$^3B_1$	Ry-3s
	4.79	0.001	$^3B_2$	$\pi\pi^*$
	4.86	0.009	$^3A_2$	Ry-3p_z
	4.97	0.127	$^3A_1$	$\pi\pi^*$
	5.21	0.000	$^3B_1$	Ry-3p_z
Styrene	4.79	0.007	($^1A'$)	$\pi\pi^*$
	5.50	0.370	($^1A'$)	$\pi\pi^*$
	5.92	0.011	($^1A'$)	Ry-3s

3.4.4 Summary

In this study, the precursors **4**, **5** and **6** were employed to generate the three isomers of xylylene in a resistively heated micro-reactor. The products were detected via IR/UV ion dip spectroscopy, and their gas-phase IR spectrum was recorded in the fingerprint region from 550-1750 cm^{-1}. Identification of the species was conducted with the help of vibrational DFT calculations on a B3LYP/6-311++G** level of theory, and anharmonic corrections were applied to the modes of the xylylene species. The data suggests a neat generation of para-xylylene from **6** under the utilized experimental conditions. **3** was detected at 265 nm and no other isomers contributed to the vibrational spectrum of mass 104.

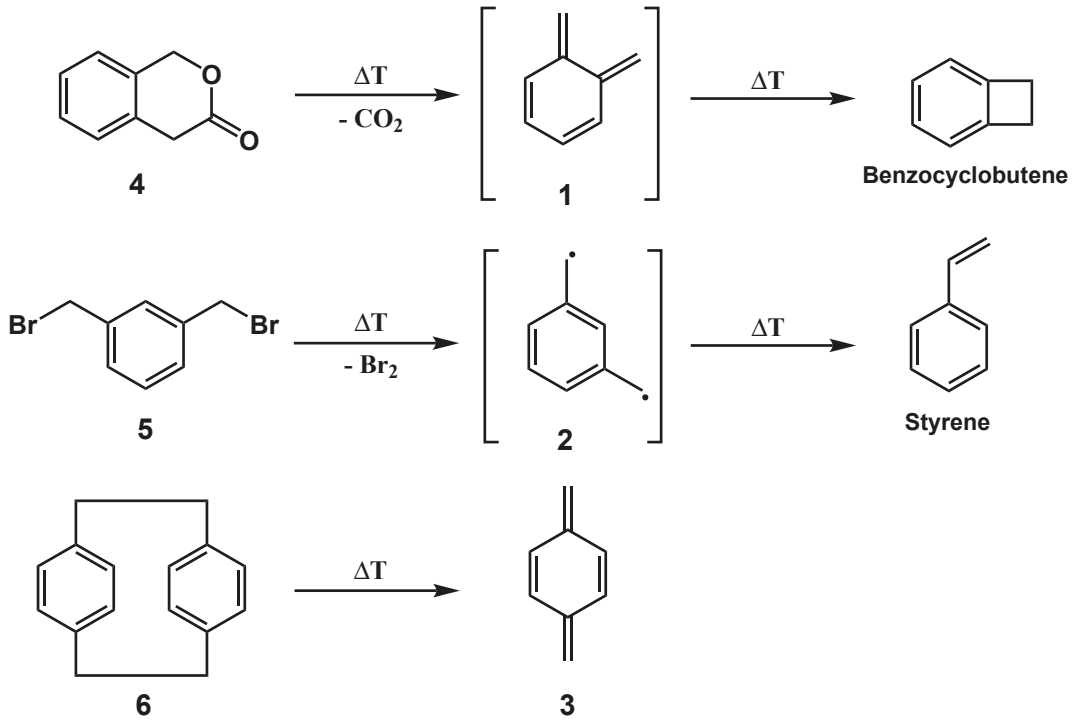

Figure 3.42: Experimental results of the xylylene IR/UV study. Products in brackets were not identified, but might be produced as intermediates. **top**: Decomposition of 3-isochromanone to benzocyclobutene; **center**: Decomposition of 1,3-bisbromoethylbenzene to styrene; **bottom**: Decomposition of [2.2]paracyclophane to para-xylylene.

On the other hand, meta- and ortho-xylylene could not be detected from the decomposition of their respective precursors. Here, isomerization products of the xylylenes were identified as the carrier of m/z = 104. For the meta-xylylene precursor **5** the formation of styrene was observed, and benzocyclobutene was the pyrolysis product of precursor **4** (cf. Fig. 3.42). The lack of identification of **1** and **2** was elaborated on in the troubleshooting section of this chapter. It can be mainly attributed to (a) partial isomerization of the xylylenes due to high pyrolysis temperatures and (b) a preference in the UV excitation of the isomerization products at 266 nm.

3.5 The Pyrolysis of Phthalide: Fulvenallenyl Radicals

3.5.1 Introduction

Fulvenallene and its activated form, the fulvenallenyl radical, have been considered important intermediates in combustion processes. Especially, the formation of many PAHs is suggested to be based on chemistry involving these two species.

Fulvenallene was reported as a product in multiple high-temperature reactions. In particular, the identification of C_7H_6 in the dissociation of toluene[248,266] and benzyl[244,246] implies its importance in the chemistry of high-temperature environments. Hence, numerous theoretical studies have been conducted on this topic, and, these days, fulvenallene is considered the most stable species on the C_7H_6 energy surface.[307–312] Especially, the formation of certain PAHs might be based on fulvenallene and its dissociation products.[313,314] Fulvenallene has been investigated in crossed molecular beams utilizing mass spectrometry[315] and its gas-phase vibrational spectrum in the fingerprint region was obtained by Angell as well as Goulay and coworkers.[316,317] Its ionization energy of IE_{ad} = 8.22 eV was determined in photoionization experiments.[317,318]

The dissociation of fulvenallene is of particular interest, as it produces active species which can undergo further reactions. Theoretical studies suggest that the fulvenallenyl radical could be the major decomposition product of C_7H_6.[309,314] Due to its high degree of delocalization and stability, it is considered relatively long-lived and can consequently contribute to further PAH growth via self reaction mechanisms.[314,318] Said radical is, similar to fulvenallene, to be considered the most stable isomer with C_7H_5 constitution.[319] The UV-induced photodissociation of fulvenallene between 245 - 255 nm was studied by Giegerich and Fischer utilizing velocity-map-imaging.[320] The authors showed that the major reaction channel involves H-loss and the formation of fulvenallenyl. This result is confirmed further by Neumark and coworkers, which found the fulvenallenyl radical as the sole dissociation product of fulvenallene at 248 and 193 nm.[321] Experimental studies on the fulvenallenyl radical itself are relatively scarce. The photodissociation dynamics at 248 and 193 nm were studied by Neumark et al. and showed two channels involving the loss of acetylene or propargyl, respectively.[321] The electronic spectrum of the radical was investigated via anion deposition in a neon matrix. The $A^2B_1 \leftarrow X^2B_1$ transition was identified at 401 nm, and several vibrational bands were observed.[322] The adiabatic ionization energy IE_{ad} = 8.19 eV was determined by synchrotron threshold photoionization experiments.[323] Recently, the IR spec-

trum of fulvenallene pyrolysis products seeded in He droplets has been reported by Douberly et al. for the 3280 - 3340 cm^{-1} region.[318]

In the following study, C_7H_6 and C_7H_5 were pyrolytically generated via the flash pyrolysis of phthalide. The carriers of the molecular beam were then studied using IR/UV double resonance spectroscopy and identified via their IR spectra in comparison with vibrational DFT calculations. The study aimed to measure the fingerprint gas-phase IR spectrum of the fulvenallenyl radical and identify larger PAH products formed during pyrolysis.

3.5.2 Experimental Parameters

A phthalide precursor was placed in a molecular beam source and heated to 186 °C. Phthalide has previously been shown to produce C_7H_6 and C_7H_5 (cf. Fig. 3.43) in a heated chemical flow reactor.[317] The precursor was seeded in 1.5 bar Ar, and the contents were pyrolyzed at 45 W. A solenoid valve generated a pulsed molecular beam which is expanded into the main chamber of a differentially pumped vacuum apparatus. The beam was skimmed upon entering the detection chamber of a TOF-MS, where the free jet was crossed by IR and UV radiation. The UV radiation was provided by a frequency-doubled dye laser producing 255 nm light with an average power of 16 mW at 20 Hz. This ionization follows a [1+1]-REMPI scheme. The IR radiation for the double resonance experiment is generated by a free-electron laser (FELIX). This light source provided scannable IR radiation in the range between 550-1800 cm^{-1} with a step width of 2 cm^{-1} and a repetition rate of 10 Hz. The UV radiation was delayed by 200 ns to optimize depletion. After data acquisition, the spectra were corrected for laser power and the wavelength was calibrated. All spectra in the following study were measured in a single scan and not averaged over multiple measurements. This resulted in a low signal/noise ratio for some mass channels and required heavy digital smoothing.

Table 3.7: Overview of the Experimental Parameters of the Phthalide IR/UV Experiments.

Experimental Parameters	
Parameter	Value
Precursor	$C_8H_6O_2$
UV Wavelength	255 nm
UV Energy	0.8 mJ
UV Delay	200 ns
Ionization Scheme	[1+1]-REMPI
UV Repetition Rate	20 Hz
IR Scan Range	550 - 1800 cm^{-1}
IR Step Width	2 cm^{-1}
IR Repetition Rate	10 Hz
Seeding Gas	Argon
Seeding Pressure	1.5 bar

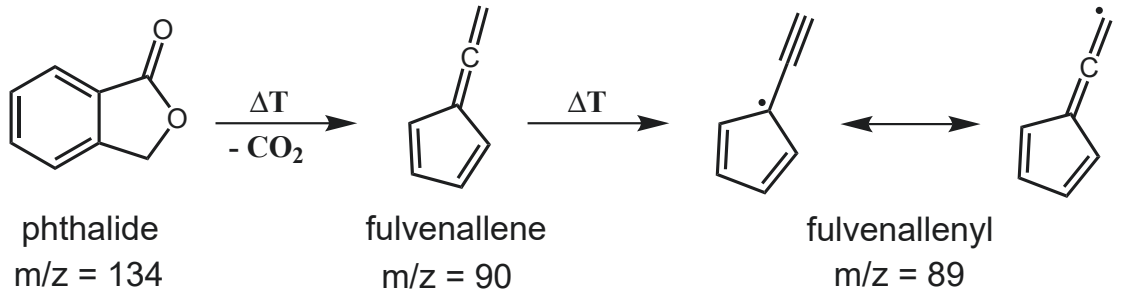

Figure 3.43: The thermal decomposition of phthalide at high temperatures. After the elimination of CO_2 and rearrangements fulvenallene and subsequently the fulvenallenyl radical are produced. Adapted from Ref.[323]

The carriers of the respective masses were finally identified via their IR spectra in comparison with anharmonic DFT calculations at a B3LYP/6-311++G** level of theory.

3.5.3 Results and Discussion

3.5.3.1 Mass Spectrum of the Phthalide Precursor

The mass spectrum of the phthalide precursor after pyrolysis is depicted in Fig. 3.44. It was recorded utilizing a [1+1]-REMPI process at 255 nm and a pyrolysis power of 60 W. The spectrum shows a complete conversion of the precursor as a m/z = 134 signal is absent. Mass signals corresponding to the primary products fulvenallenyl (C_7H_5) and fulvenallene (C_7H_6) are visible at mass 89 and 90 with low to medium signal intensity. A couple of smaller decomposition and DPI products can be observed at lower masses, with mass 78 being the most dominant signal. Furthermore, the spectrum shows various mass signals at higher masses, ranging from low to very strong intensities. The majority of these represent characteristic masses of common PAH products and suggest efficient PAH growth in this experimental environment. Note that the quality of the IR/UV spectra of mass 78 and 90 was insufficient for unambiguous identification and their traces are shown in the Appendix A.7.

3.5.3.2 Mass 89: The Fulvenallenyl Radical

The IR/UV spectrum of m/z = 89 is depicted in Fig. 3.45 (solid line). It shows several distinct vibrational bands in the fingerprint region, which are heavily broadened. As no experimental IR spectrum of fulvenallenyl is available for the fingerprint region, the data is compared to vibrational DFT calculations (dotted line).

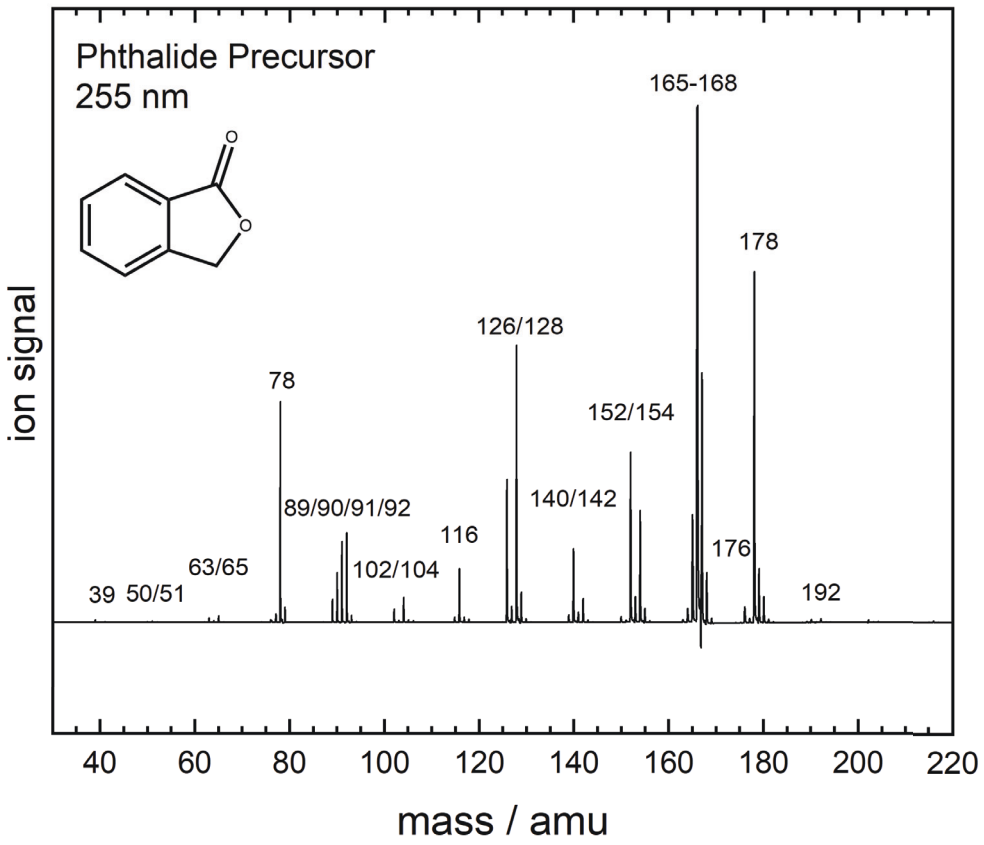

Figure 3.44: Mass spectra of pyrolytically cleaved phthalide measured by 255 nm [1+1]-REMPI at 60 W.

The first vibrational band (**1**) is located at 611 cm^{-1}. It matches the calculated signal at 633 cm^{-1} well and displays transitions into three vibrational modes. The lowest energy vibration is an out-of-plane C-H bending mode of the ethynyl moiety calculated at 589 cm^{-1}, which is visible as a pronounced shoulder on the left side of the transition band. The major peak is formed by a symmetric out-of-plane ring C-H bending mode at 627 cm^{-1} and the in-plane C-H ethynyl bending mode at 641 cm^{-1}, both forming the combined signal peak at 633 cm^{-1}. The next signal can be observed at 730 cm^{-1} (**2**). It corresponds to a single out-of-plane ring C-H bending mode calculated at 740 cm^{-1}. A small peak on the right flank of the signal seems to be due to noise, as no additional vibrational transitions are calculated in this region. In the range from 830 - 960 cm^{-1}, the spectrum shows a broad signal (**3**) of rather low intensity and signal/noise ratio. Here, DFT predicts two modes of low intensity and matching energies: An anti-symmetric out-of-plane ring C-H

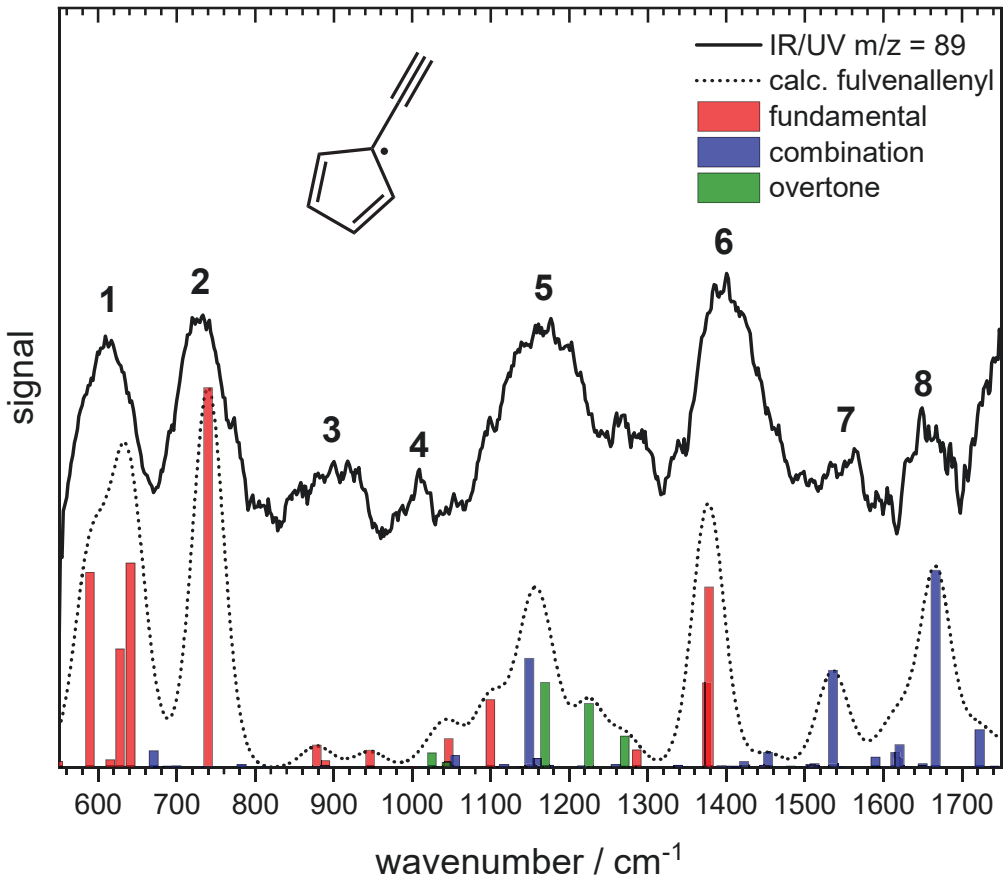

Figure 3.45: IR/UV spectrum of mass 89 (solid line) after thermal decomposition of phthalide. Eight distinct vibrational bands can be identified in the fingerprint region from 550-1750 cm^{-1}. The experimental data are compared to anharmonic DFT calculations of the fulvenallenyl radical (dotted line) for identification.

bending mode at 878 cm^{-1} and a ring CC stretch vibration at 946 cm^{-1}. The next signal (**4**) can be observed at 1008 cm^{-1}. Although the band shows a relatively sharp peak, it corresponds to three distinct vibrational transitions according to the calculations. The overtone of an anti-symmetric ring C-H stretching mode at 1025 cm^{-1}, an anti-symmetric in-plane ring C-H bending mode at 1046 cm^{-1} and the combination band of the just mentioned stretching mode with an ethynyl CC stretching vibration at 1054 cm^{-1}. All three combined form a band at 1042 cm^{-1}, which overestimates the experimental data by 34 cm^{-1}. Over the next couple of hundred wavenumbers, the experimental spectrum shows a single broad IR band (**5**) from 1030-1320 cm^{-1}. The resolution of this band is insufficient for a detailed assignment. Still, the DFT calculations predict several fundamental bands, over-

tones, and combination bands in this area, which seem to form a single signal in the experimental spectrum. **6** at 1393 cm^{-1} is the band with the highest signal intensity in the spectrum. It is formed by two close-lying ring stretching modes at 1375 cm^{-1} and 1378 cm^{-1}, which combine to a signal at 1376 cm^{-1}, slightly underestimating the experimental data. The last two vibrational bands in the spectrum at 1551 cm^{-1} (**7**) and 1655 cm^{-1} (**8**) originate from individual combination bands at 1535 cm^{-1} and 1666 cm^{-1}, respectively. Overall, the experimental spectrum is in good agreement with the vibrational calculations, and the carrier of m/z = 89 can be unambiguously identified as the fulvenallenyl radical. Note that the rising signal at the high energy end of the spectrum is probably not a real signal, as the calculations predict no matching vibration.

Table 3.8: Identified Vibrational Bands of the Fulvenallenyl Radical in Comparison with Calculated Energies. Energies given in cm^{-1}.

Experimental Parameters		
Band	Energy	Transition
1	611	$24_1(589, \delta_{\text{ethynyl,CH,oop}}), 22_1(627, \omega_{\text{ring,CH}}),$ $21_1(641, \delta_{\text{ethynyl,CH,ip}})$
2	730	$19_1(740, \omega_{\text{ring,CH}})$
3	830 - 940	$18_1(878, \tau_{\text{ring,CH}}), 15_1(946, s_{\text{CC,ring}})$
4	1008	$27_2(1025), 13_1(1046, \delta_{\text{CH,ring,ip}})), 27_1 25_1(1054),$
5	1030 - 1320	$12_1(1099,), 27_1 23_1(641), 24_2(1169), 23_2(1224), 21_2(1270),$ $10_1(1285)$
6	1393	$8_1(1375, s_{\text{CC,ring}}), 9_1(1378, s_{\text{CC,ring}})$
7	1551	$27_1 14_1(1535)$
8	1665	$23_1 14_1(1666)$

Vibrational descriptors were applied where suitable, following:
$s = stretch, ip = in-plane, oop = out-of-plane,$
$\delta = deformation, \omega = wagging, \tau = twist$

3.5.3.3 Masses 91, 92 & 104: Benzyl, Toluene and Styrene

Toluene and the benzyl radical are species often identified as carriers of mass 91 and 92 in combustion experiments. In this study, these masses are also observed, and their respective IR/UV spectrum is shown in Fig. 3.46. The IR spectrum of mass 91 (top trace) can be readily identified as benzyl by the two very characteristic out-of-plane wagging modes at 672 cm^{-1} and 752 cm^{-1}. The calculated spectrum overestimates these bands only slightly by approx. 20 cm^{-1}. Above 800 cm^{-1}, the radical exhibits various small vibrational signals, which appear to be more pronounced in the experimental data than the simulated spectrum. Note that the gas-phase IR/UV spectrum of the benzyl radical has previously been measured by Meijer et al. with similar methodology.[245] Likewise, comparing the IR/UV spectrum of m/z = 92 with the calculated spectrum of toluene, the carrier can be identified. All vibrational bands are accounted for in the experimental data and the calculations for toluene. The slight overestimation in calculated wavenumbers is hereby consistent with the benzyl spectrum above.

The origin of benzyl and toluene in the experiment can not be unambiguously assigned. On the one hand, these species could be formed in the decomposition of the phthalide precursor according to Fig. 3.47. After initial detachment of CO_2, the radical and toluene are accessible via consecutive addition of hydrogen. Hence, they are either side products or intermediates in the formation of fulvenallenyl. Both toluene and benzyl have previously been discussed to produce C_7H_6 at suitable conditions.[248,310,319,324]

On the other hand, C_7H_7 and C_7H_8 could be produced via molecule growth from small reactive carbon species. For example, the addition of propargyl (C_3H_3) to C_4 hydrocarbons might be sufficient to produce C_7H_x and are common open-chain decomposition products in many flame studies. Unfortunately, the methodology of the present study is not capable of identifying these small chain molecules for a more accurate assessment of potential growth reactions. Hence, both decomposition from the precursor and formation from small hydrocarbon molecules should be considered for the formation of benzyl and toluene.

The third molecule observed here is displayed in the lower trace of Fig. 3.46. The IR/UV spectrum of mass 104 shows very characteristic signals in the lower energy part of the fingerprint region. The molecule can be readily identified as styrene by three strong bands at 698 cm^{-1} ($\omega_{ring,CH}$), 774 cm^{-1} ($\omega_{ring,CH}$), and 910 cm^{-1} ($\delta_{ethynyl,CH_2,ip}$). Interestingly, the DFT calculations underestimate the vibrational energies noticeably. However, comparing the measured energies of these three bands with other experimental gas-phase spectra of styrene (NIST)[325] shows excellent agreement.

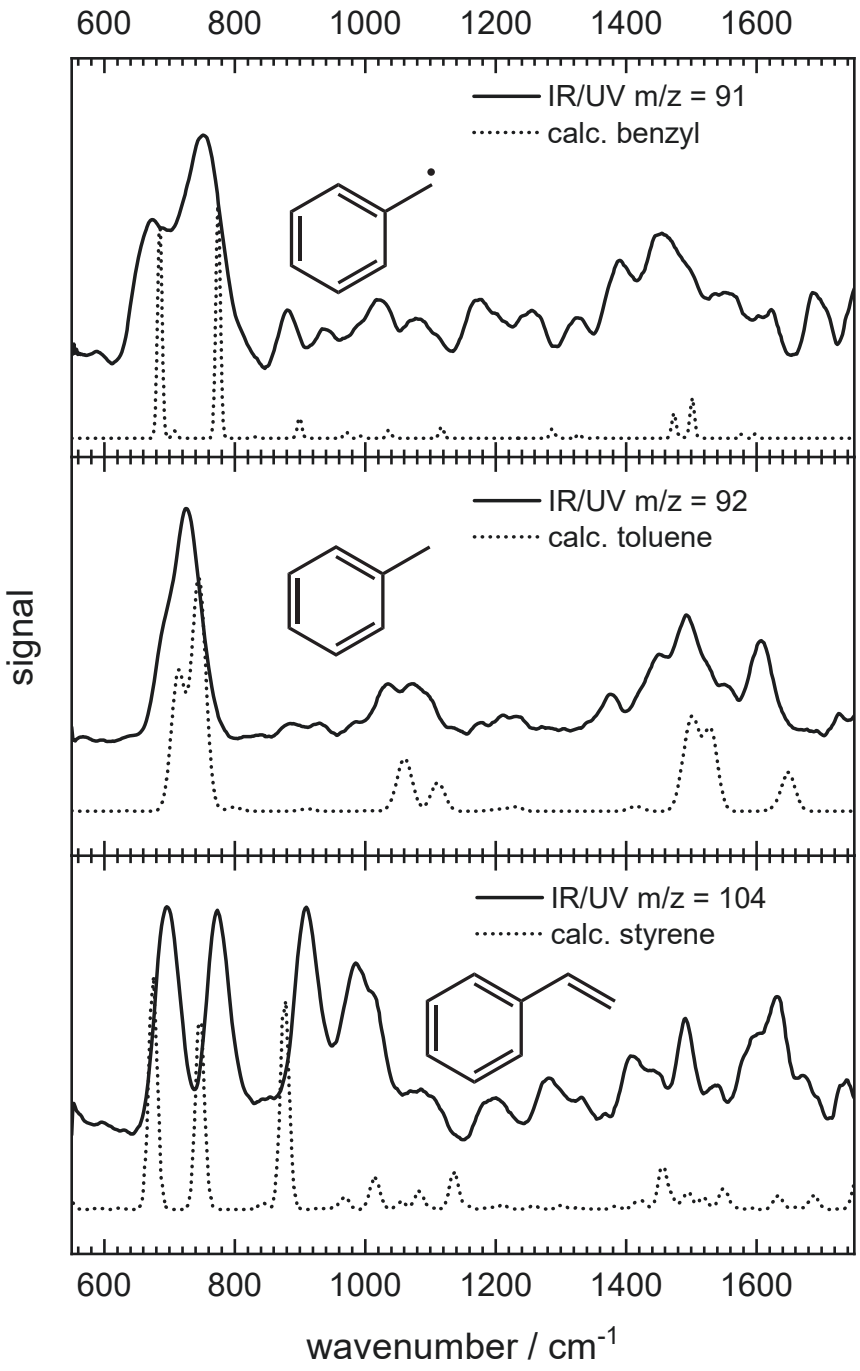

Figure 3.46: Identified benzylic products of the decomposition of phthalide. The respective experimental IR/UV spectra (solid line) are depicted in comparison with DFT simulations (dotted line) in the fingerprint region from 550-1750 cm^{-1}. **top**: IR/UV spectrum of mass 91 in comparison to the benzyl radical; **center**: IR/UV spectrum of mass 92 in comparison to toluene; **bottom**: IR/UV spectrum of mass 104 in comparison to styrene.

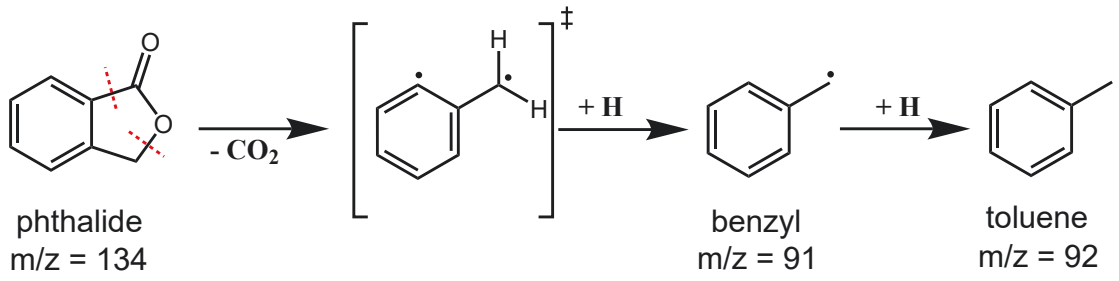

Figure 3.47: Direct formation of the benzyl radical and toluene after elimination of CO_2 from phthalide and consecutive association with hydrogen.

3.5.3.4 Masses 116 & 154: The IR/UV Spectrum of Indene and Biphenyl

The IR/UV spectrum of m/z = 116 is depicted in the upper trace (solid line) of Fig. 3.48. Although the intensity of the mass signal is only medium at best, the spectrum exhibits a good signal/noise ratio, and a large number of vibrational bands can be assigned to the simulated spectrum (dotted line) of indene. The carrier of the mass can be readily identified by five characteristic bands in the fingerprint region. Low energy C-H deformation bands are visible at 720 cm^{-1} and 765 cm^{-1}, in which the first is comprised of two distinct modes which overlap in the experimental spectrum. CC stretching vibrations are observed at 940 cm^{-1} and 1459 cm^{-1}, as well as the CH_2 scissoring mode at 1396 cm^{-1}. Overall, the experimental and calculated energies match very well, and further smaller signals could also be assigned.

There are several possible reaction pathways to how indene can be formed in high-temperature environments. In this case, the formation via the addition reaction of C_7H_7 + C_2H_2, as suggested by Lindstedt et al.[326] and Colket et al.,[327] as well as the addition of acetylene to fulvenallene C_7H_6 + C_2H_2,[328] are most likely, as benzyl has already been identified as a carrier of mass 91 in the experiment and high concentrations of fulvenallene can be assumed. A scheme of these reactions is depicted in Fig. 3.49. After the initial addition of acetylene in **a** to benzyl, a 2-propenylbenzene radical could be formed. Afterward, this radical further undergoes cyclization and re-aromatization to form indene. In **b**, the association of fulvenallene and acetylene results in an activated C_9H_8 species, which subsequently forms indene via several rearrangements and ring-expansion, similar to the rearrangement between fulvene and benzene.[328,329] Hereby, **b** is exothermic by over 100 kcal mol^{-1} and only requires a relatively small activation energy of 27 kcal mol^{-1}.[328] In general, **a** is considered the more important formation pathway for indene, as the activation energy (12-13 kcal mol^{-1}) is significantly lower, and hence

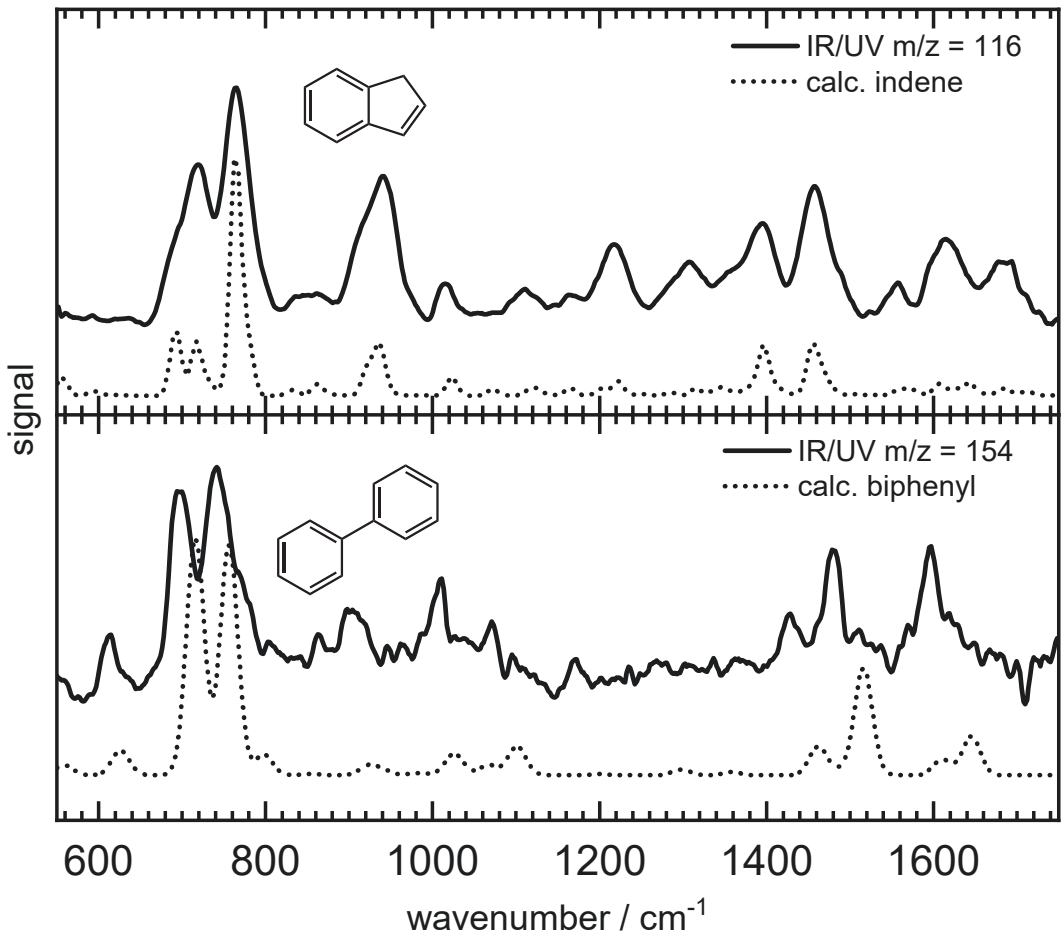

Figure 3.48: The gas-phase infrared spectra of the phthalide decomposition products with m/z=116 and m/z=154. The respective experimental IR/UV spectra (solid line) are depicted in comparison with DFT simulations (dotted line) in the fingerprint region from 550-1750 cm^{-1}. **top**: IR/UV spectrum of mass 116 in comparison to indene; **bottom**: IR/UV spectrum of mass 154 in comparison to biphenyl.

the rate constants are much higher.[330–333] However, da Silva. et al. showed that at elevated temperatures, the fulvenallene + acetylene pathway gains importance and might play an important role in combustion environments, where the concentration of fulvenallene is especially high.[328]

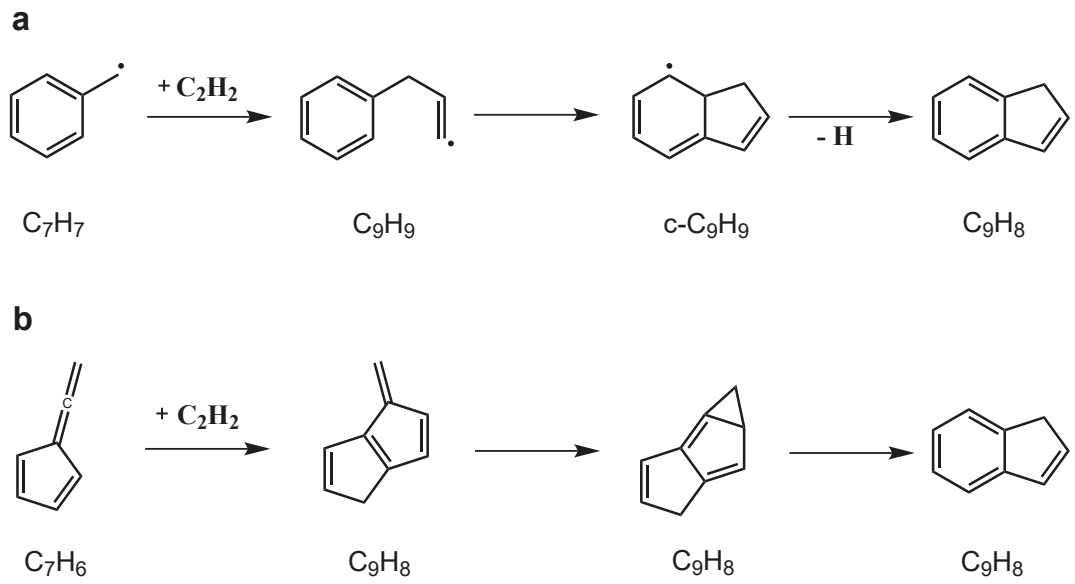

Figure 3.49: Two suggested formation pathways of indene starting from C_7H_x species. **a** formation via the association of benzyl and acetylene and **b** via the association of fulvenallene with acetylene. Educts were either identified in the experiment or assumed present in high concentrations.

The carrier of mass 154 can be identified as biphenyl, as the vibrational fingerprint spectrum (solid line, Fig. 3.48, lower trace) is in good agreement with calculations (dotted line). Especially three C-H wagging modes at 614 cm^{-1}, 697 cm^{-1} and 741 cm^{-1} in the lower energy region, as well as two in-plane C-H deformation modes (1427 cm^{-1} and 1480 cm^{-1}) and a C=C stretch vibration at 1596 cm^{-1}, are characteristic markers for the biphenyl molecule. The overestimation of the vibrational energies is consistent with other calculations in the experiment.

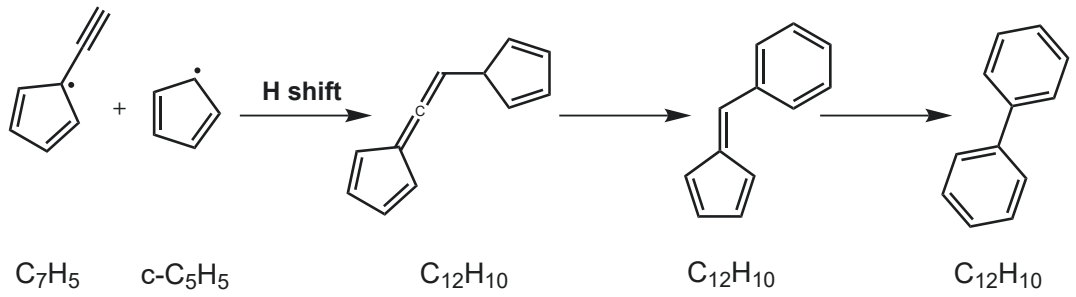

Figure 3.50: Suggested formation pathway of biphenyl in fulvenallene rich environments. The initial allenic intermediate is produced via radical-radical addition of fulvenallenyl and cyclopentadienyl. Subsequent, ring-expansion to six-membered rings then produces the biphenyl product.

Da Silva et al. suggest a compelling formation pathway for biphenyl (cf. Fig. 3.50) in a fulvenallenyl rich environment.[314] Here, fulvenallenyl reacts with cyclopentadienyl to form a molecule with $C_{12}H_{10}$ constitution. The initial allenic addition product undergoes further rearrangement and ring expansion to finally form the biphenyl product. Note that although C_5H_5 is not identified in this study, it is often discussed as an additional decomposition product of fulvenallene or benzyl.[246,311,312,324] The ionization conditions in the current study are probably not suitable for detecting the cyclopentadienyl radical but should be considered present in the experiment.

3.5.3.5 Masses 166 & 168: Non-fused PAH Products Fluorene and Diphenylmethane

The IR/UV spectra of mass 166 (top trace) and 168 (bottom trace) are depicted in Fig. 3.51 in comparison to calculations (dotted line).

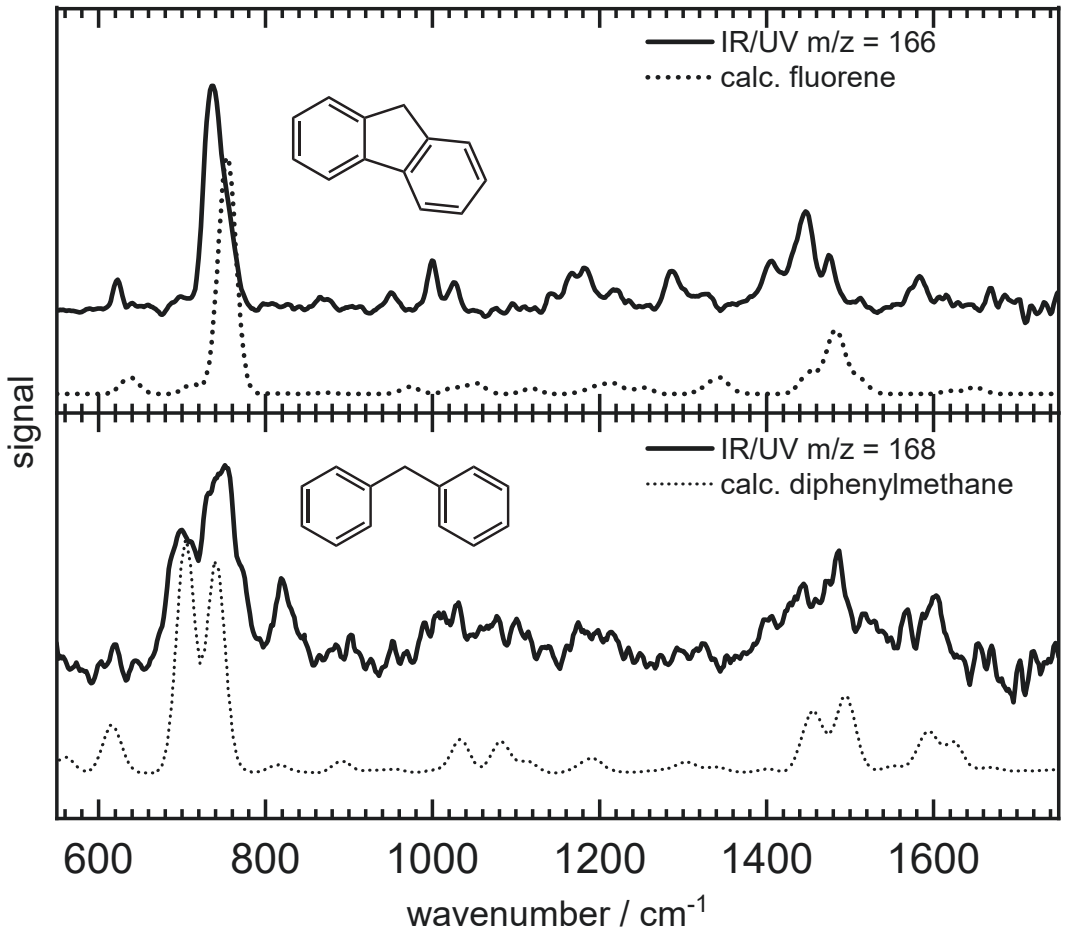

Figure 3.51: The IR/UV spectrum of fluorene and diphenylmethane as identified in the phthalide pyrolysis experiment. The respective experimental IR/UV spectra (solid line) are depicted in comparison with DFT simulations (dotted line) in the fingerprint region from 550-1750 cm^{-1}. **top**: IR/UV spectrum of m/z=166 in comparison to fluorene and **bottom**: IR/UV spectrum of m/z=168 in comparison to diphenylmethane.

The carrier of m/z = 168 can be identified as the common PAH carrier diphenylmethane. Multiple deformation and wagging modes in the sub-1000 cm^{-1} region form four signals at 618 cm^{-1}, 702 cm^{-1}, 751 cm^{-1} and 820 cm^{-1}. The last band is considerably underestimated by the calculation, which predicts several low-intensity

vibrational modes, including an overtone of a low energy ring motion. The underestimation of this specific signal is possibly the reason for the low signal intensity of the band at 834 cm^{-1} in the simulated spectrum. In the central region 1000 cm^{-1} - 1400 cm^{-1} of the fingerprint range, the signal/noise ratio is insufficient for unambiguous assignment to the calculated low-intensity bands. DFT predicts many different vibrational modes at higher energies which form a combined spectrum as seen in the simulation. These vibrations include CC stretching, CH_2 scissoring, CH deformation modes, and some combination bands as well as overtones. A large number of vibrations might be the reason why the experimental spectrum in this region is heavily broadened, and signals are difficult to unambiguously assign. Overall the experimental data show signals at 1443 cm^{-1}, 1487 cm^{-1}, 1569 cm^{-1} and 1603 cm^{-1}, which is in good agreement with the calculations.

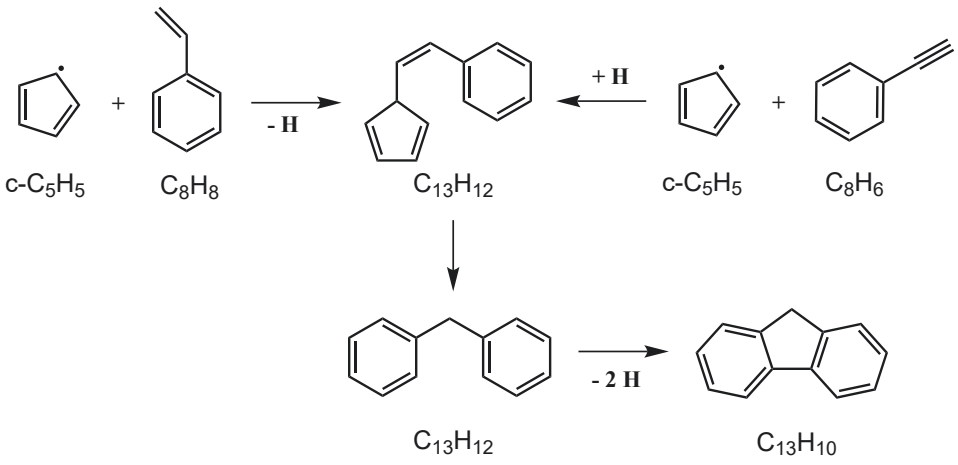

Figure 3.52: Suggested formation of diphenylmethane from the association of cyclopentadienyl and styrene or cyclopentadienyl and phenylacetylene. Further elimination of hydrogen then yields fluorene.

The formation of diphenylmethane might be easily explained by the association of C_7H_7+C_6H_5. However, another potential formation pathway for $C_{13}H_{12}$ in a fulvenallene/fulvenallenyl rich environment is depicted in Fig. 3.52, analogous to the formation of biphenyl suggested by da Silva and coworkers.[314] Here, styrene grows via the addition of cyclopentadienyl, which should be readily available as an additional decomposition product.[246,311,312,324] The initial adduct is formed under H-loss and subsequently undergoes ring-expansion of the cyclopentadiene ring to produce the diphenylmethane product. Similarly, the reaction could also start from phenylacetylene instead of styrene via an analogical pathway.

Diphenylmethane is also likely to produce fluorene (see Fig. 3.52), which is identified as the carrier of mass 166. The corresponding spectrum is depicted in the upper trace of Fig. 3.51. The spectrum is dominated by a large CH wagging band at 736 cm^{-1}. To higher energies, a broadened signal with three distinct peaks at 1406 cm^{-1}, 1447 cm^{-1} and 1476 cm^{-1} is visible corresponding to several deformation modes in this region. The middle area shows several resolved vibrational signals, which can be attributed to low-intensity vibrations in this region. The spectrum exhibits good resolution and matches the DFT calculation well, although a small overestimation in the simulation is visible, which slightly increases with rising energies.

3.5.3.6 Masses 128, 142, 178 & 192: Fused PAH Products

The decomposition of phthalide has shown to produce fused PAH products based on naphthalene and phenanthrene. The corresponding IR/UV spectra of these molecules are displayed in Fig. 3.53 **a** - **d**.

The lightest of these species is observed at m/z = 128 and can be identified as naphthalene. The dominant characteristic wagging signal at 779 cm^{-1} is predicted well in signal intensity and energy by the calculation. Further signals to higher energies are also visible due to a good signal/noise ratio, but the peaks only exhibit small signal intensities, as the simulation also predicts. The formation of naphthalene can be explained by a typical HACA-like C_6H_6+C_4H_2 mechanism or the association of benzyl with C_3H_3. Da Silva et al., however, suggest an additional formation pathway involving fulvenallenyl and a fulvallene intermediate, according to Fig. 3.54 **a**.[314] Additionally, naphthalene as a dimerization product of c-C_5H_5 should also be considered (Fig. 3.54, **b**), according to the reaction pathway proposed by Melius and coworkers.[334] Both pathways have in common that naphthalene is formed via consecutive ring-expansion from two fused five-membered rings. Note that **a** and **b** only show key intermediates, and the proper reaction pathway includes more crucial steps.[334]

Strongly related to naphthalene is the carrier of mass 142, which is depicted in Fig. 3.53 **b**. The spectrum is very noisy and exhibits only one distinct broad signal at 792 cm^{-1}. This is in good agreement with two wagging vibrations of 1-methylnaphthalene, which seem to overlap in the experimental spectrum. Although the calculations (dotted line) predict several other vibrational bands at higher energies, the quality of the upper energy region is insufficient for proper assignment. The experimental data is also compared to the vibrational calculations of 2-methylnaphthalene. At first, the additional wagging vibrations of this isomer, calculated at 738 cm^{-1} and 812 cm^{-1}, are more separated and might explain the heavy broadening of the experimental band, as well as a potential signal peak at 730 cm^{-1}. However, it also predicts a strong signal in the upper energy region from two in-plane deformation bands, which is absent in the experimental spectrum. Hence, the carrier is identified as 1-methylnaphthalene and an influence of the other isomer can not be clearly confirmed.

Mass 178 shows three distinct signals in the lower part of the fingerprint spectrum at 729 cm^{-1}, 803 cm^{-1}, and 860 cm^{-1}. These in-plane C-H deformation bands are characteristic for phenanthrene, which can be identified in comparison with the calculation in **c** of Fig. 3.53. The IR bands are well predicted in energy and relative intensity. Further, smaller signals at higher energies can also be assigned to the simulation. In contrast to naphthalene, the calculation overestimates the ex-

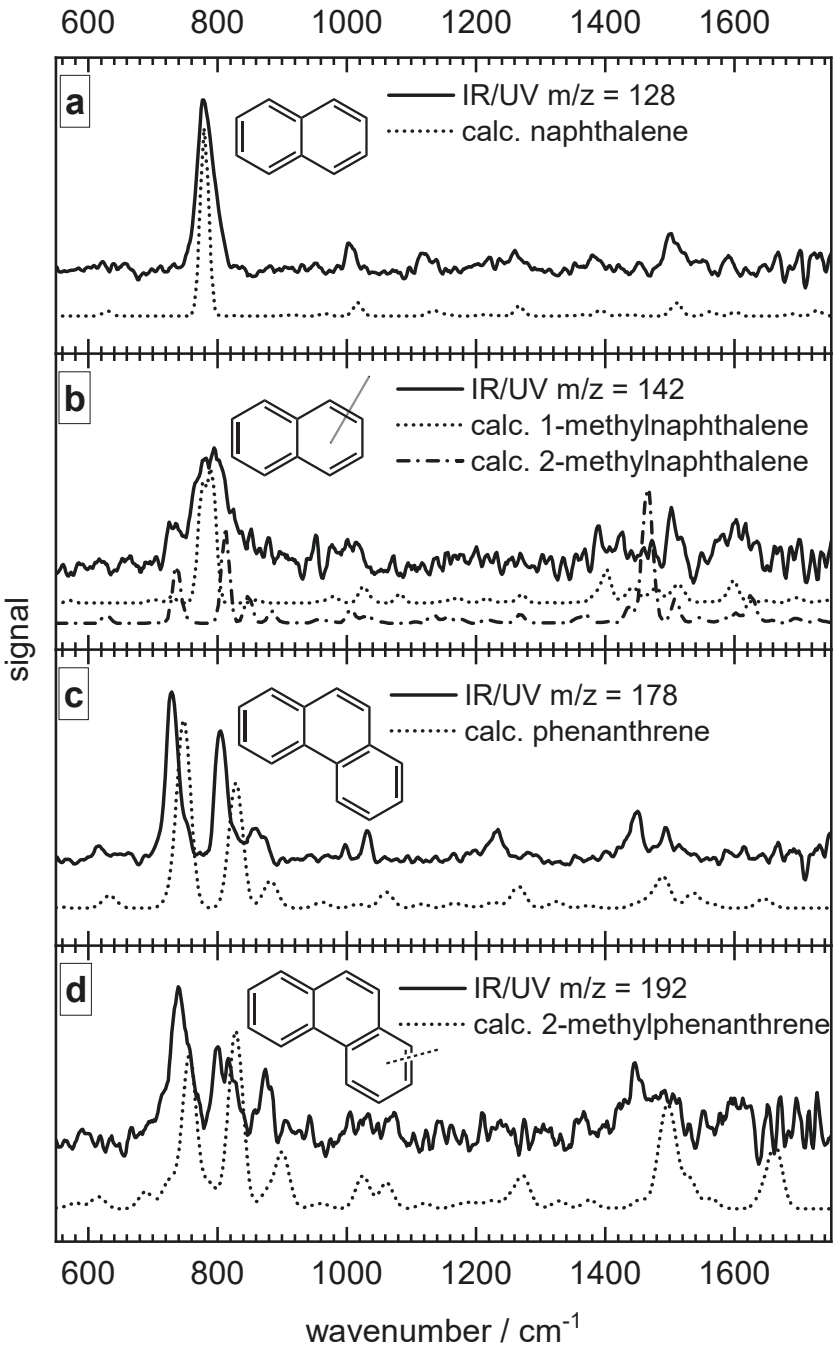

Figure 3.53: The IR/UV spectrum of fused PAH species produced by phthalide. The respective experimental IR/UV spectra (solid line) are depicted in comparison with DFT simulations (dotted line) in the fingerprint region from 550-1750 cm^{-1}. **a**: IR/UV spectrum of m/z=128 in comparison to naphthalene; **b**: IR/UV spectrum of m/z=142 in comparison to 1- and 2-methylnaphthalene; **c**: IR/UV spectrum of m/z=178 in comparison to phenanthrene and **d**: IR/UV spectrum of m/z=192 in comparison to 2-methylphenanthrene.

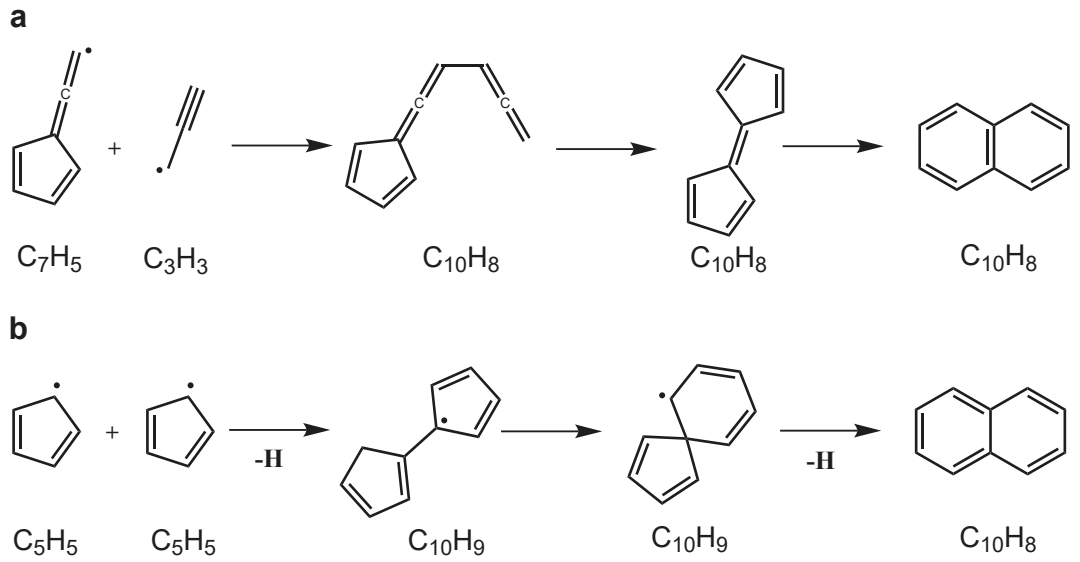

Figure 3.54: Two possible formation pathways for naphthalene. **a** Formation via the addition of propargyl to fulvenallenyl and **b** naphthalene as the product of cyclopentadienyl dimerization.

perimental wavenumbers slightly. Note that anthracene should not be excluded as a partial carrier of mass 178. Although it only has two characteristic vibrational modes in the lower energy region, these are energetically very close to the bands of phenanthrene and exhibit a similar relative signal intensity. Hence, anthracene could not be identifiable in a phenanthrene dominated spectrum.

Phenanthrene is a common product in many combustion studies. Its formation can be described via usual HACA- and PAC-like mechanisms. Similar to the formation of naphthalene, however, da Silva et al. provide an alternative formation pathway for phenanthrene in a C_7H_5 rich environment, according to Fig. 3.55.[314] The dimerization product of two fulvenallenyl radicals cyclizes to form a multicyclic biradical, which subsequently undergoes consecutive ring expansions to form phenanthrene.[314]

Finally, the IR spectrum of the heaviest product is displayed in the bottom trace of Fig. 3.53. Similar to mass 128 and 142, it is most likely produced by methylated phenanthrene. Overall, the spectrum is quite noisy, but three vibrational bands, similar to phenanthrene, can be observed at 740 cm^{-1}, 810 cm^{-1}, and 874 cm^{-1}. Whereas, the second shows a pronounced double peak. Of the four possible methylphenanthrene isomers, the 2-isomer (dotted line) fits the experimental data the best. It correctly predicts the three vibrational bands in the region be-

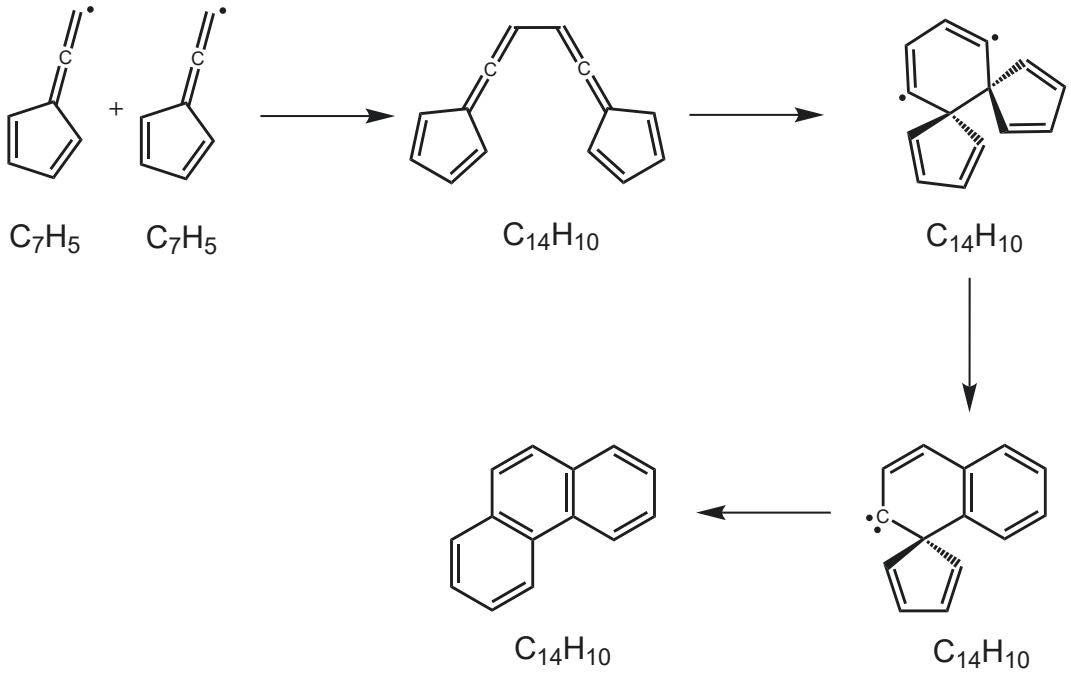

Figure 3.55: Suggested formation of phenanthrene under fulvenallenyl rich conditions. The dimerization if C_7H_5 yields a multi-cyclic biradical intermediate after ring-closing and undergoes consecutive ring-expansion to the observed $C_{14}H_{10}$ product.

tween 700 - 900 cm^{-1} and also a relatively strong vibrational signal in the higher energy region, which might be the origin of a signal at 1446 cm^{-1}. However, due to the quality of the experimental spectrum, potential influences of other isomers should also be considered.

3.5.3.7 Masses 102, 126, 140, 152 & 176: Reaction Products with Terminal Ethynyl Chains

The decomposition of phthalide produced several ethynyl compounds. PAHs with terminal ethynyl side-chains are common high-temperature reaction products observed during combustion or in flame studies.[232] A typical marker of this class of molecules is a particularly strong overtone/combination band around 1200 cm^{-1}. The species identified in this study are depicted in Fig. 3.56 **a**-**e**. In general, the calculated DFT spectra (dotted lines) overestimate the wavenumbers of most experimental bands considerably. Nonetheless, the carriers of mass 102 (**a**), 128 (**b**) and 152 (**d**) can be identified as phenylacetylene, 1,3-diethynylbenzene and 2-ethynylnaphthalene, respectively. The observed bands and assignments of these species are shown in Tab. 3.9.

Mass 140 is depicted in **c** of Fig. 3.56 and corresponds to a carrier with $C_{11}H_8$ constitution. The mass and strong band at 1203 cm^{-1} suggest one of the ethynylindene isomers to be the carrier of this signal. In fact, 4-ethynylindene (dotted line) displays the best agreement between the experimental data and the calculations. However, the differences in the lower energy region and the severe broadening of the band around 779 cm^{-1} might indicate additional isomers, in particular, 1- and 2-ethynylindene. The calculated IR spectra of these two species (see Appendix) also show vibrational bands, which could be in accordance with the observed signals. Moreover, da Silva et al. suggest a formation pathway for these two isomers, which is strongly related to fulvenallenyl rich environments, according to Fig. 3.57.[313] Here, the corresponding radicals are formed in a HACA-like addition of diacetylene to fulvenallenyl. The reaction for both isomers is exothermic by approx. 100 kcal mol^{-1} and would consequently form the closed-shell species by radical hydrogenation. Overall, 4-ethynylindene still provides the best match with the experimental data, but 1- and 2-ethynylindene should certainly be considered as well.

The heaviest species of Fig. 3.56 is depicted in the bottom trace **e**. This mass only showed a small signal in the REMPI mass spectrum, and the IR/UV spectrum is pretty noisy, especially in the upper energy region. The band above 1200 cm^{-1}, again, indicates ethynyl side-chains. This, combined with the mass and the strong signals in the lower energy region, suggests a diethynylnaphthalene carrier for mass 176. Due to many different isomers and the poor quality of the spectrum, a precise identification is not possible. An overview of DFT calculations for different potential candidates is displayed in Appendix A.6, but no simulated spectrum provides a good match for the experimental data.

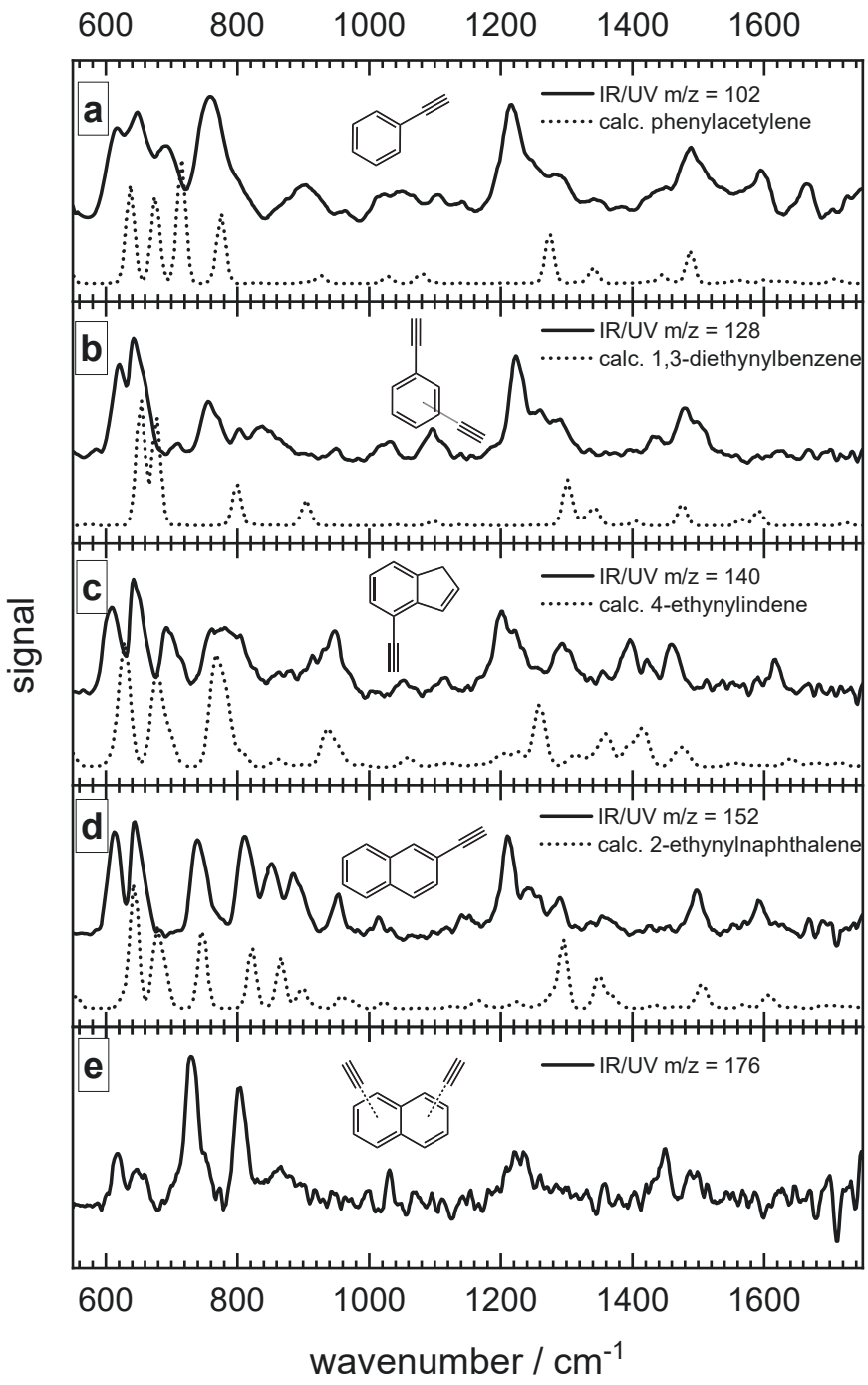

Figure 3.56: All pyrolysis products of phthalide with ethynyl side-chains. The respective experimental IR/UV spectra (solid line) are depicted in comparison with DFT simulations (dotted line) in the fingerprint region from 550-1750 cm^{-1}. **a**: IR/UV spectrum of m/z=102 in comparison to phenylacetylene; **b**: IR/UV spectrum of m/z=128 in comparison to 1,3-diethynylbenzene; **c**: IR/UV spectrum of m/z=140 in comparison to 4-ethynylindene; **d**: IR/UV spectrum of m/z=152 in comparison to 2-ethynylnaphthalene and **e**: IR/UV spectrum of m/z=176.

Table 3.9: Identified Vibrational Bands of Phenylacetylene, 1,3-Diethynylbenzene, and 2-Ethynylnaphthalene in Comparison with Calculated Energies in [cm^{-1}].

Experimental Parameters		
Mass	Energy	Transition
102	615	$28_1(638, \delta_{\text{ethynyl,CH,oop}})$
	648	$27_1(676, \delta_{\text{ethynyl,CH,ip}})$
	694	$26_1(716, \omega_{\text{ring,CH}})$
	759	$25_1(776, \omega_{\text{ring,CH}})$
	902	$22_1(926, \delta_{\text{ring,CH,oop}})$
	1217	$28_2(1276)$
	1288	$27_2(1342)$
	1488	$10_1(1488, \delta_{\text{ring,CH,ip}})$
128	621	$30_1(653, \delta_{\text{ethynyl,CH,oop,sym}})$
	643	$28_1(676, \delta_{\text{ethynyl,CH,ip,anti-sym}})$, $27_1(676, \delta_{\text{ethynyl,CH,ip,sym}})$, $26_1(677, \omega_{\text{ring,CH}})$
	756	$24_1(800, \omega_{\text{ring,CH}})$
	1224	$30_129_1(1301)$
	1262	$28_127_1(1343)$
	1436	$11_1(1476, \delta_{\text{ring,CH,ip}}))$
	1480	$10_1(1565, s_{\text{CC,ring}})$, $9_1(1591, s_{\text{CC,ring}})$
152	614	$41_1(643, \delta_{\text{ethynyl,CH,oop}})$
	644	$39_1(676, \delta_{\text{ethynyl,CH,ip}}\delta_{\text{ring}})$, $38_1(678, \delta_{\text{ethynyl,CH,ip}})$, $53_143_1(689)$
	739	$37_1(747, \omega_{\text{ring,CH}})$
	811	$34_1(822, \delta_{\text{ring,CH,oop}})$
	852	$33_1(866, \delta_{\text{ring,CH,oop}})$
	885	$31_1(899, \delta_{\text{ring,CH,oop}})$
	953	$29_1(956, \delta_{\text{ring,C,ip}})$
	1015	$26_1(1023, s_{\text{CC,ring}}))$
	1211	$41_2(1296), \delta_{\text{ring,CH,ip}}))$
	1290	$38_2(1348)$
	1498	$13_1(1535, s_{\text{CC,ring}})$
	1593	$11_1(1637, s_{\text{CC,ring}})$

Vibrational descriptors were applied where suitable, following:
$s = stretch, ip = in-plane, oop = out-of-plane,$
$\delta = deformation, \omega = wagging, \tau = twist$

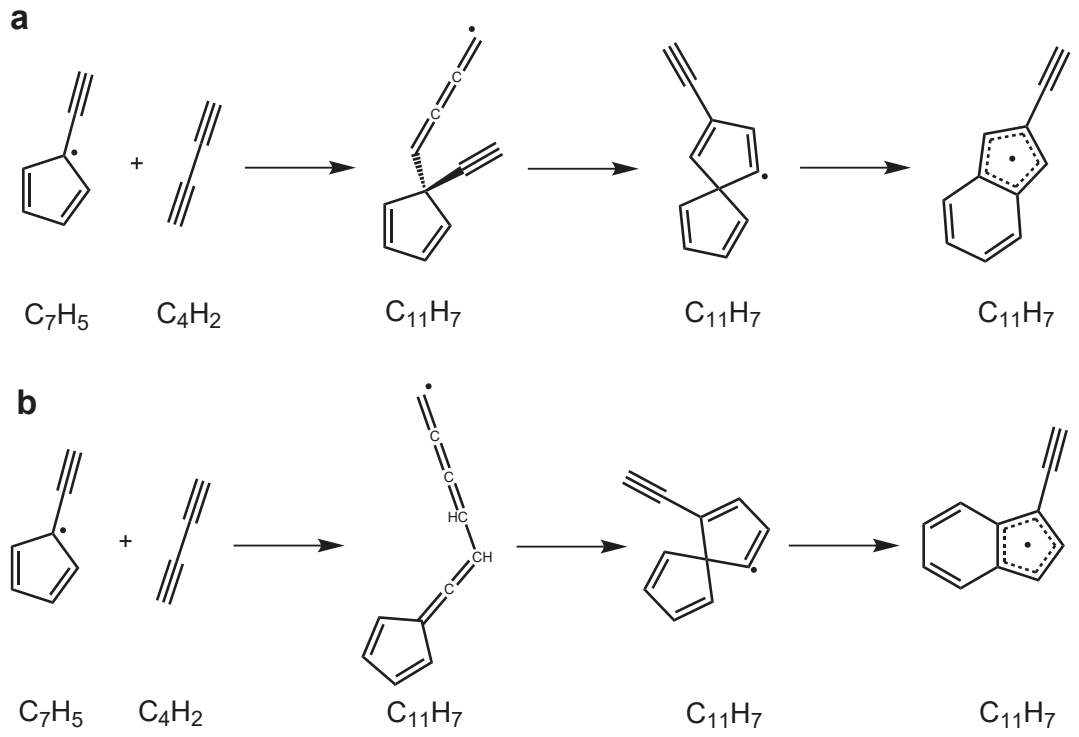

Figure 3.57: Two suggested formation pathways **a** and **b** for the $C_{11}H_7$ radical isomers, where the ethynyl moiety is attached to the five-membered ring in indene.

3.5.4 Summary

The pyrolysis of phthalide has shown to produce a large number of decomposition and secondary reaction products, which were analyzed utilizing IR/UV spectroscopy. The carrier of mass 89 was unambiguously identified as the fulvenallenyl radical (C_7H_5), and the first gas-phase infrared spectrum in the fingerprint region from 550 - 1750 cm^{-1} was recorded. C_7H_5, as well as other decomposition products like fulvenallene (C_7H_6), cyclopentadienyl (C_5H_5), benzyl (C_7H_7) and benzene (C_6H_6), seem to be involved in the growth of numerous heavier species. Note that neither cyclopentadienyl, benzene, nor fulvenallene was directly identified in the present study by their IR/UV spectrum, probably due to unsuitable photon energies. All observed and suggested products are depicted in Fig. 3.58. The molecules which were clearly identified by their respective IR spectrum are displayed in solid boxes. Products that are assumed to be present in the experiment but could not be identified by the utilized methodology or where the IR spectrum was not meaningful enough for an isomeric assignment are displayed in dotted boxes.

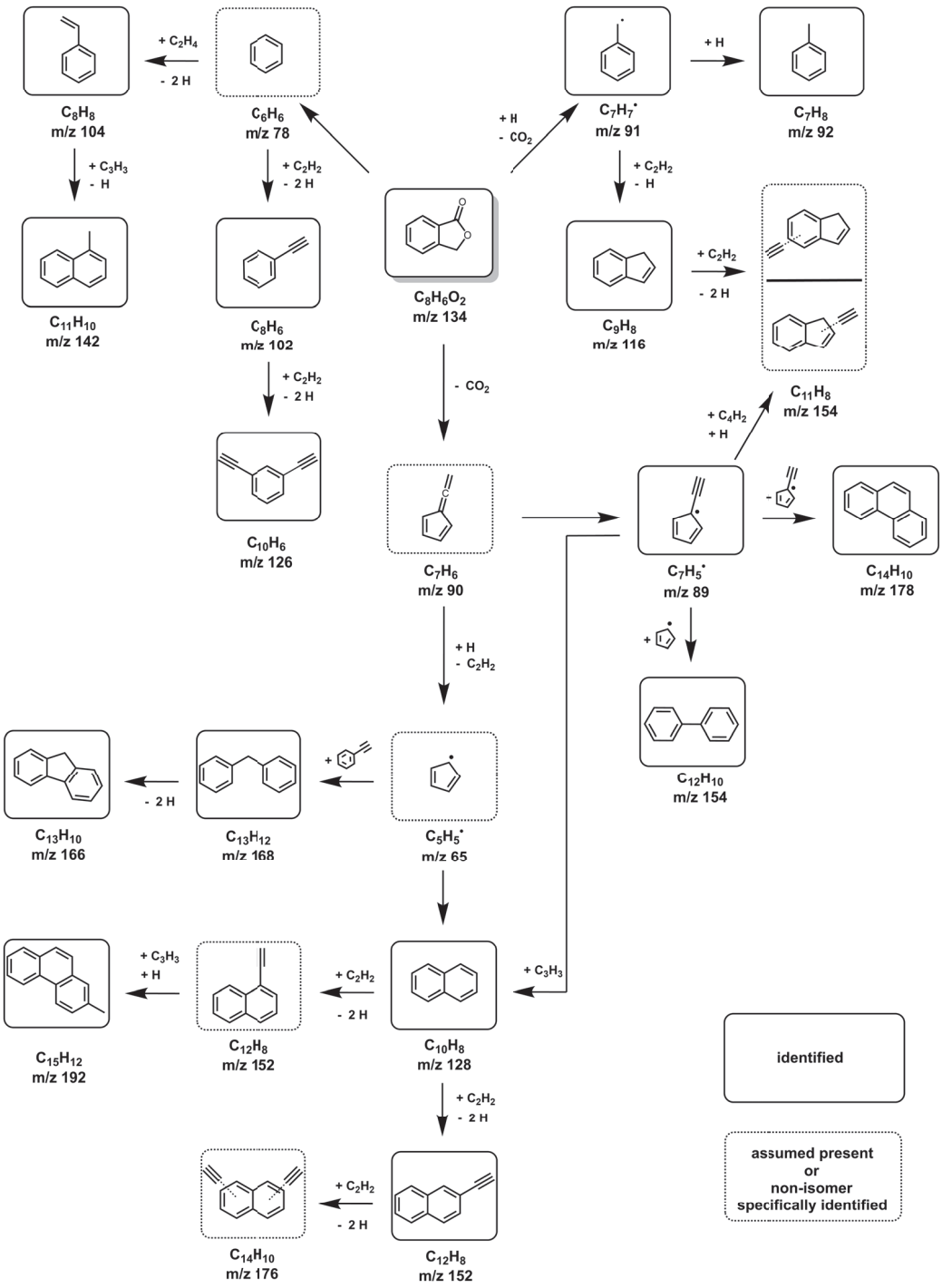

Figure 3.58: Overview of all reaction products of the phthalide pyrolysis. A selection of suggested reactions pathways are depicted and products which were unambiguously identified are displayed in solid boxes. Products which are implied or the specific isomer could not be identified are displayed in dotted boxes.

Many of these products have multiple reaction pathways of formation, including standard HACA- or PAC-like mechanisms. In Fig. 3.58, however, reaction pathways are preferably displayed which involve identifiable species in the experiment or molecules assumed to be present in considerable concentrations.

Overall, the experiment shows the formation of many typical PAHs like indene (C_9H_8), naphthalene ($C_{10}H_8$), phenanthrene ($C_{14}H_{10}$), fluorene ($C_{13}H_{10}$), biphenyl ($C_{12}H_{10}$) or diphenylmethane ($C_{13}H_{12}$). Several of those are formed in a non-HACA like fashion, where the addition product of cyclopentadienyl or fulvenallenyl undergoes ring expansion to form six-membered species.

The identification of the ethynyl compounds phenylacetylene (C_8H_6), diethynylbenzene ($C_{10}H_6$), ethynylnaphthalene ($C_{12}H_8$), diethynylnaphthalene ($C_{14}H_{10}$) and ethynylindene ($C_{11}H_8$) suggest a considerable amount of HACA-like addition reactions of acetylene, which is most likely formed in the decomposition of fulvenallene, phenyl or benzyl.

Taking all this into account, phthalide demonstrated to produce sufficient amounts of the fulvenallenyl radical to acquire its gas-phase fingerprint IR spectrum and be an outstanding precursor for a variety of different hydrocarbons, especially PAHs, where some are produced in non-HACA and PAC like manners.

Chapter 4

Summary

Reactive hydrocarbon species are important in a multitude of different scientific areas. In this thesis, the vibrational spectra of hydrocarbon radicals, biradicals and their reaction product have been studied in a gas-phase environment. The specific molecules investigated here, are of particular importance in the field of combustion- and astrochemistry. They were produced from suitable precursors in a pyrolytically heated micro-reactor and subsequently seeded in an appropriate carrier gas. As methodology, IR/UV ion dip spectroscopy has been utilized, which delivers mass-selected gas-phase IR spectra of all ionizable species detectable in the molecular beam. These, with the help of DFT calculations, allow for determination of the fingerprint IR spectra, identification of mass carriers and formulation of potential reaction mechanisms. All studies have been conducted in collaboration with the group of *Prof. Dr. Anouk. M. Rjis* and the necessary potent IR radiation has been provided by the free-electron laser FELIX. Thus, the IR/UV measurements have been executed at the FELIX Laboratory of the Radboud University in Nijmegen.

The first study presented in this thesis is the investigation of ortho-benzyne in Chapter 3.1. This molecule is of particular interest due to its uncommon electronic structure and its role in high-temperature reactions. Although, the infrared spectrum of o-C_6H_4 was not accessible, a number of reaction products were identified via their fingerprint spectra. Masses in the range from 78 - 228 were assigned to their respective carrier. The identified species include typical PAHs like naphthalene, phenanthrene, up to triphenylene. The identified masses further suggest a PAH growth heavily influenced by diradical 1,4-cycloaddition followed by fragmentation, as well as by classical HACA- and PAC-like mechanisms. These results were augmented by threshold photoionization measurements from Engelbert Reusch, who identified lighter reaction products, which have insufficient IR absorption or unsuitable ionization characteristics to be identified in the IR/UV experiment. An

interesting observation is the identification of m/z = 152. This carrier has been assigned differently by the IR and TPES experiments. Whereas the IR spectrum clearly identifies the species as 2-ethynylnaphthalene, the TPES evidently is in great agreement with biphenylene. This is a good example how different experimental methodologies can benefit from each other to gain a deeper insight into the actual science of a particular system.

Probably, the prime example for an aromatically resonance stabilized radical is benzyl. This radical is of high importance for many combustion studies, as it represents the primary high-temperature decomposition product of toluene. The goal of the study was the identification of the benzyl self reaction products and the results are discussed in Section 3.2. The radical was pyrolytically produced by its respective nitrite precursor. The mass spectrum showed that the benzyl self reaction formed two products with C_{11} and three with C_{14} constitution. All mass peaks were evenly spaced by two mass units, respectively, which suggests a close relation in formation. Indeed, the C_{11} products were identified as diphenylmethane and fluorene, which are simply connected via cyclization. The heaviest product was identified as phenanthrene, which is formed via the cyclization of bibenzyl to 9,10-dihydrophenanthrene and subsequent elimination of hydrogen. This result was quiet interesting as the intermediate of this reaction was often assumed to be stilbene, which was not observed in the study. Hence, the reaction seems to undergo cyclization first before phenanthrene is finally formed via hydrogen elimination.

Expanding the molecular frame of benzyl by an additional methyl group leads to the xylyl radicals and its decomposition product the xylylenes. Also important in combustion research, xylyl radicals represent the preferred decomposition products of xylene, a frequently used anti-knock agent in modern gasoline blends. After further hydrogen elimination the xylyl radicals can then form their respective xylylenes. The results of the xylyl experiments are discussed in Section 3.3. Here the gas-phase vibrational spectrum in the fingerprint region for all three isomers has been recorded for the first time in isolation. Although, all isomers have a very similar structure and symmetry, and consequently similar vibrational bands, the resolution of the experimental data was exceedingly sufficient for a clear assignment. Additionally, the dimerization products of meta- and para-xylyl could also be identified.

A similar approach was taken to determine the fingerprint spectra for the xylylenes. Here, only para-xylylene could be unambiguously identified as the carrier of mass 104. For both ortho- and meta-xylylene precursors, only isomerization products were observed as the carriers of mass 104; benzocyclobutene and styrene, respectively. A possible explanation is elaborated upon in the troubleshooting Sec-

tion 3.4.3.5.

In the final experimental section a study on the decomposition of phthalide is presented. The objective of this experiment was mainly focused around the formation of C_7 species, particularly the fulvenallenyl radical C_7H_5. In fact, the first experimental fingerprint spectrum of isolated C_7H_5 in the gas-phase was measured and is displayed in Fig. 3.45. Furthermore, the experiment demonstrates that the pyrolysis products of phthalide are excellent soot precursors, as many heavier reaction products have been identified. These include typical PAH species like naphthalene and phenanthrene as well as their methylated isomers. A large number of molecules with terminal ethynyl moieties indicate a strong influence of HACA growth in the experimental environment. However, many formation pathways of products have been discussed, which are formed involving experiment specific species, like C_5H_5 and C_7H_5, and often include expansion steps from 5- to 6-membered rings.

Chapter 5

Zusammenfassung

Reaktive Kohlenwasserstoffe spielen eine wichtige Rolle in vielen wissenschaftlichen Bereichen. In der vorliegenden Dissertation wurden die schwingungsspektroskopischen Eigenschaften von Kohlenwasserstoffradikalen, Biradikalen und ihren Reaktionsprodukten in der Gasphase untersucht. Die Spezies, die in den Studien dieser Arbeit untersucht wurden, spielen eine besondere Rolle im Bereich der Verbrennungs- und Astrochemie. Sie wurden aus geeigneten Vorläufern pyrolytisch in einem beheizten Mikroreaktor hergestellt und anschließend mit einem passenden Trägergas in die Gasphase überführt. Als spektroskopische Methode wurde IR/UV Ionen-Dip Spektroskopie verwendet. Diese liefert massenselektive Schwingungsspektren von allen in einem Molekularstrahl ionisierbaren und detektierbaren Spezies. Dies erlaubt es, mit Hilfe von DFT Rechnungen die Schwingungsspektren der isolierten Moleküle zu messen, diese zu identifizieren und auch Rückschlüsse auf die Reaktionsmechanismen zu ziehen. Alle Experimente dieser Thesis wurden in Zusammenarbeit mit der Gruppe von *Prof. Dr. Anouk M. Rijs* durchgeführt. Hierbei wurde als hochbrillante IR-Quelle der Freie-Elektronenlaser *FELIX* der *Radboud University* in Nijmegen verwendet.

Die erste Studie in Kapitel 3.1 beschäftigte sich mit Untersuchungen des ortho-Benzins. Dieses Molekül ist von besonderer Bedeutung aufgrund seiner ungewöhnlichen elektronischen Struktur und seiner Rolle bei Hochtemperaturreaktionen. Obwohl das IR Spektrum des o-C_6H_4 nicht ermittelt werden konnte, war es möglich einige Reaktionsprodukte anhand ihrer Schwingungsspektren zu identifizieren. Massensignale im Bereich von 78 - 228 amu wurden hierbei ihren jeweiligen Molekülen zugeordnet. Hierzu zählen typische PAHs wie Naphthalen, Phenanthren, bis zu Triphenylen. Die identifizierten Spezies legten des Weiteren nahe, dass das PAH Wachstum zum größten Teil durch diradikalische 1,4-Cycloaddition mit anschließender Fragmentierung, sowie HACA und PAC Mechanismen dominiert sein

dürfte. Diese Ergebnisse wurden mit Photoionisationsstudien von Engelbert Reusch vervollständigt, welcher weitere leichtere Reaktionsprodukte identifizieren konnte, die eine unzureichende IR Absorption oder ungeeignete Ionisationseigenschaften aufweisen. Eine besonders interessante Erkenntnis stellt die Identifizierung von Masse 152 dar. Der Träger dieser Masse wurde durch die IR und TPES Experimente unterschiedlich zugeordnet. Hierbei wurde die Masse durch die Schwingungsspektren der IR/UV Experimente als 2-Ethinylnaphthalen identifiziert. Die TPES Spektren jedoch zeigten eine große Übereinstimmung der experimentellen Daten mit Biphenylen. Somit war diese Studie ein hervorragendes Beispiel dafür, wie unterschiedliche Methoden sich gegenseitig ergänzen können, um einen besseren Einblick in ein bestimmtes System zu erhalten.

Benzyl ist womöglich das beste Musterbeispiel für ein aromatisch resonanzstabilisiertes Radikal. Dieses ist von großer Bedeutung in vielen Verbrennungsstudien, da es das primäre hochtemperatur Zerfallsprodukt von Toluol darstellt. Das Ziel dieser Studie war die Identifizierung der Benzyl Selbstreaktionsprodukte und ihre Ergebnisse wurden in Kapitel 3.2 präsentiert. Das Radikal wurde pyrolytisch aus dem jeweiligen Nitritvorläufer hergestellt. Das Massenspektrum zeigte, dass zwei Produkte mit C_{11} und drei Produkte mit C_{14} Zusammensetzung entstanden. Alle Massensignale waren gleichmäßig mit einem Abstand von zwei Masseneinheiten verteilt, was eine enge Beziehung der Spezies im Hinblick auf ihre Bildung nahe legt. So wurden die zwei C_{11} Spezies als Diphenylmethan und Fluoren identifiziert, welche über Zyklisierung miteinander in Verbindung stehen. Das schwerste Produkt im Experiment konnte als Phenanthren identifiziert werden, welches durch die Zyklisierung von Bibenzyl zu 9,10-Dihydrophenantren und anschließender Wasserstoffeliminierung entsteht. Diese Erkenntnis war von besonderer Relevanz, da bisher oft davon ausgegangen wurde, dass das Zwischenprodukt dieser Reaktion Stilben sein müsste; was allerdings in dieser Studie nicht beobachtet wurde. Folglich scheint der erste Schritt dieser Reaktion eine Zyklisierung zu sein und die Wasserstoffeliminierung findet erst im zweiten Schritt statt, wobei Phenanthren gebildet wird.

Wenn Benzyl um eine zusätzliche Methyl-Einheit erweitert wird, erhält man die Gruppe der Xylylradikale und ihrer Zerfallsprodukte, den Xylylenen. Diese Moleküle sind ebenfalls von besonderem Interesse in der Verbrennungsforschung, da Xylylradikale das primäre Hochtemperaturprodukt der Wasserstoffeliminierung von Xylolen sind. Xylyole werden häufig in Kraftstoffen als Anti-Klopfmittel eingesetzt und stellen häufig einen großen Anteil dieser dar. Eine weitere Eliminierung von Wasserstoff liefert anschließend die jeweiligen Xylylene. Die Ergebnisse dieser Experimente wurden in Kapitel 3.3 diskutiert. Hierbei wurde das Gasphasen-IR-Fingerprintspektrum aller Xylyl-Isomere in Isolation zum ersten mal ermittelt. Ob-

wohl alle Isomere eine sehr ähnliche Struktur und Symmetrie aufweisen und die resultieren Schwingungsmoden ebenfalls sehr ähnlich sind, war die Auflösung der experimentellen Daten ausreichend für eine eindeutige Zuordnung. Zusätzlich wurden ebenfalls die Dimerisierungsprodukte von meta- und para-Xylyl beobachtet und identifiziert.

Eine ähnliche Herangehensweise wurde angewandt, um die Schwingungsspektren der Xylylene zu bestimmen. Hierbei konnte jedoch nur das IR-Spektrum von para-Xylylen als Träger der Masse 104 bei der Pyrolyse des jeweiligen Vorläufers eindeutig identifiziert werden. Für beide Vorläufer der ortho- und meta-Xylylen Experimente konnten lediglich Isomerisierungsprodukte als Träger von $m/z = 104$ festgestellt werden: Benzocyclobuten und Stilben. Mögliche Gründe für diese Ergebnisse wurden in Kapitel 3.4.3.5 erläutert.

Im letzten Teil wurden die Arbeiten zur Zersetzung von Phthalid präsentiert. Das Ziel dieser Studie war die Erzeugung und Charakterisierung von C_7 Spezies, insbesondere das Fulvenallenyl Radikal C_7H_5. Hierbei konnte das erste Gasphasen-Fingerprint-IR-Spektrum von isoliertem C_7H_5 ermittelt werden, welches in Fig. 3.45 zu sehen ist. Des Weiteren zeigte die Studie, dass Phthalid ein hervorragender Rußvorläufer ist, da eine große Anzahl weiterer Reaktionsprodukte identifiziert werden konnte. Diese beinhalten typische PAHs wie Naphthalen und Phenanthren, sowie ihre methylierten Isomere. Eine große Vielzahl von Molekülen mit terminalen Ethinylseitenketten deuten auf einen großen Einfluss von HACA ähnlichem PAH Wachstum hin. Hierbei wurden insbesondere Reaktionsmechanismen diskutiert, welche experimentspezifische Reaktionsprodukte, wie C_5H_5 und C_7H_5, beinhalten und oft Ringexpansionen von 5- zu 6-gliedrigen Ringen aufweisen.

Bibliography

[1] Y. Kita and M. Matsugi, Radical Initiators, ser. Wiley Online Books. 2001.

[2] R. J. Young and P. A. Lovell, Introduction to polymers, 2nd ed. London: Chapman & Hall, 1991, vol. 27.

[3] Y. Saeki and T. Emura, Technical progresses for PVC production, *Progress in Polymer Science (Oxford)*, vol. 27, no. 10, pp. 2055–2131, 2002.

[4] L. H. Breimer, Ionizing radiation-induced mutagenesis, *British Journal of Cancer*, vol. 57, no. 1, pp. 6–18, 1988.

[5] B. Halliwell, Reactive oxygen species in living systems: Source, biochemistry, and role in human disease, *The American Journal of Medicine*, vol. 91, no. 3, 1991.

[6] A. Phaniendra, D. B. Jestadi, and L. Periyasamy, Free Radicals: Properties, Sources, Targets, and Their Implication in Various Diseases, *Indian Journal of Clinical Biochemistry*, vol. 30, no. 1, pp. 11–26, 2015.

[7] B. P. Yu, Cellular defenses against damage from reactive oxygen species, *Physiological Reviews*, vol. 74, no. 1, pp. 139–162, 1994.

[8] C. Ufer, H. Kuehn, T. L. Yin, and C. C. Wang, Free Radicals and Embryo Development BT - Systems Biology of Free Radicals and Antioxidants, in, I. Laher, Ed., Berlin, Heidelberg: Springer Berlin Heidelberg, 2014, pp. 537–565.

[9] W. Dröge, Free radicals in the physiological control of cell function, *Physiological reviews*, vol. 82, no. 1, pp. 47–95, 2002.

[10] I. S. Young and J. V. Woodside, Antioxidants in health and disease, *Journal of clinical pathology*, vol. 54, no. 3, pp. 176–186, 2001.

[11] L. A. Pham-Huy, H. He, and C. Pham-Huy, Free radicals, antioxidants in disease and health, *International journal of biomedical science : IJBS*, vol. 4, no. 2, pp. 89–96, 2008.

[12] M. Genestra, Oxyl radicals, redox-sensitive signalling cascades and antioxidants, *Cellular signalling*, vol. 19, no. 9, pp. 1807–1819, 2007.

[13] P. Pacher, J. S. Beckman, and L. Liaudet, Nitric oxide and peroxynitrite in health and disease, *Physiological reviews*, vol. 87, no. 1, pp. 315–424, 2007.

[14] B. Halliwell, Biochemistry of oxidative stress, *Biochemical Society transactions*, vol. 35, no. Pt 5, pp. 1147–1150, 2007.

[15] A. Mardyukov and W. Sander, Matrix isolation and spectroscopic characterization of the phenylperoxy radical and its rearranged products, *Chemistry - A European Journal*, vol. 15, no. 6, pp. 1462–1467, 2009.

[16] A. Snelson, Infrared matrix isolation spectrum of the methyl radical produced by pyrolysis of methyl iodide and dimethyl mercury, *Journal of Physical Chemistry*, vol. 74, no. 3, pp. 537–544, 1970.

[17] S. N. Foner and R. L. Hudson, The detection of atoms and free radicals in flames by mass spectrometric techniques, *The Journal of Chemical Physics*, vol. 21, no. 8, pp. 1374–1382, 1953.

[18] S. Cheskis, I. Derzy, V. A. Lozovsky, A. Kachanov, and D. Romanini, Cavity ring-down spectroscopy of OH radicals in low pressure flame, *Applied Physics B: Lasers and Optics*, vol. 66, no. 3, pp. 377–381, 1998.

[19] A. Matsugi, Thermal Decomposition of Benzyl Radicals: Kinetics and Spectroscopy in a Shock Tube, *Journal of Physical Chemistry A*, vol. 124, no. 5, pp. 824–835, 2020.

[20] A. Fridlyand, P. T. Lynch, R. S. Tranter, and K. Brezinsky, Single pulse shock tube study of allyl radical recombination, *Journal of Physical Chemistry A*, vol. 117, no. 23, pp. 4762–4776, 2013.

[21] H. J. Deyerl, I. Fischer, and P. Chen, Photodissociation dynamics of the allyl radical, *Journal of Chemical Physics*, vol. 110, no. 3, pp. 1450–1462, 1999.

[22] ——, Photodissociation dynamics of the propargyl radical, *Journal of Chemical Physics*, vol. 111, no. 8, pp. 3441–3448, 1999.

[23] Https://ourworldindata.org/, *How much energy does the world consume?*, Nov. 2020.

[24] H. Richter and J. Howard, Formation of polycyclic aromatic hydrocarbons and their growth to soot - a review of chemical reaction pathways, *Progress in Energy and Combustion Science*, vol. 26, pp. 565–608, 2000.

[25] V. Smil, Energy Transitions: Global and National Perspectives, 2nd ed. Praeger, 2017.

[26] Https://www.bp.com/en/global/corporate/energy-economics/statistical-review-of-world-energy.html, *Statistical Review of World Energy*, Nov. 2020.

[27] H. Böhm, D. Hesse, H. Jander, B. Lüers, J. Pietscher, H. G. G. Wagner, and M. Weiss, The influence of pressure and temperature on soot formation in premixed flames, *Symposium (International) on Combustion*, vol. 22, no. 1, pp. 403–411, 1989.

[28] K. Gleason, F. Carbone, and A. Gomez, Pressure and temperature dependence of soot in highly controlled counterflow ethylene diffusion flames, *Proceedings of the Combustion Institute*, vol. 37, no. 2, pp. 2057–2064, 2019.

[29] R. F. Coburn, Mechanisms of carbon monoxide toxicity, *Preventive Medicine*, vol. 8, no. 3, pp. 310–322, 1979.

[30] L. R. Goldbaum, R. G. Ramirez, and K. B. Absalon, What is the mechanism of carbon monoxide toxicity? *Aviation, space, and environmental medicine*, vol. 46, no. 10, pp. 1289–1291, 1975.

[31] D. A. Sarigiannis, S. P. Karakitsios, D. Zikopoulos, S. Nikolaki, and M. Kermenidou, Lung cancer risk from PAHs emitted from biomass combustion, *Environmental Research*, vol. 137, pp. 147–156, 2015.

[32] T. Rengarajan, P. Rajendran, N. Nandakumar, B. Lokeshkumar, P. Rajendran, and I. Nishigaki, Exposure to polycyclic aromatic hydrocarbons with special focus on cancer, *Asian Pacific Journal of Tropical Biomedicine*, vol. 5, no. 3, pp. 182–189, 2015.

[33] B. Moorthy, C. Chu, and D. J. Carlin, Polycyclic Aromatic Hydrocarbons: From Metabolism to Lung Cancer, *Toxicological Sciences*, vol. 145, no. 1, pp. 5–15, 2015.

[34] D. W. Dockery, C. A. 3. Pope, X. Xu, J. D. Spengler, J. H. Ware, M. E. Fay, B. G. J. Ferris, and F. E. Speizer, An association between air pollution and mortality in six U.S. cities, *The New England journal of medicine*, vol. 329, no. 24, pp. 1753–1759, 1993.

[35] T. R. Barfknecht, Toxicology of soot, *Progress in Energy and Combustion Science*, vol. 9, no. 3, pp. 199–237, 1983.

[36] I. Annesi-Maesano, F. Forastiere, N. Kunzli, and B. Brunekref, Particulate matter, science and EU policy, *European Respiratory Journal*, vol. 29, no. 3, 428 LP –431, 2007.

[37] H. Priemus and E. Schutte-Postma, Notes on the Particulate Matter Standards in the European Union and the Netherlands, *International journal of environmental research and public health*, vol. 6, pp. 1155–1173, 2009.

[38] H. Bockhorn, Soot Formation in Combustion, H. Bockhorn, Ed. Springer Verlag, 1994.

[39] M. Frenklach and H. Wang, Detailed modeling of soot particle nucleation and growth, *Symposium (International) on Combustion*, vol. 23, no. 1, pp. 1559–1566, 1991.

[40] H. Wang and M. Frenklach, Calculations of rate coefficients for the chemically activated reactions of acetylene with vinylic and aromatic radicals, *Journal of Physical Chemistry*, vol. 98, no. 44, pp. 11 465–11 489, 1994.

[41] L. Zhao, R. I. Kaiser, W. Lu, B. Xu, M. Ahmed, A. N. Morozov, A. M. Mebel, A. H. Howlader, and S. F. Wnuk, Molecular mass growth through ring expansion in polycyclic aromatic hydrocarbons via radical–radical reactions, *Nature Communications*, vol. 10, no. 1, pp. 1–7, 2019.

[42] A. M. Mebel, A. Landera, and R. I. Kaiser, Formation Mechanisms of Naphthalene and Indene: From the Interstellar Medium to Combustion Flames, *Journal of Physical Chemistry A*, vol. 121, no. 5, pp. 901–926, 2017.

[43] B. Shukla and M. Koshi, Comparative study on the growth mechanisms of PAHs, *Combustion and Flame*, vol. 158, no. 2, pp. 369–375, 2011.

[44] B. Shukla, A. Susa, A. Miyoshi, and M. Koshi, Role of phenyl radicals in the growth of polycyclic aromatic hydrocarbons, *Journal of Physical Chemistry A*, vol. 112, no. 11, pp. 2362–2369, 2008.

[45] B. Shukla and M. Koshi, A highly efficient growth mechanism of polycyclic aromatic hydrocarbons, *Physical Chemistry Chemical Physics*, vol. 12, no. 10, pp. 2427–2437, 2010.

[46] B. Shukla, A. Miyoshi, and M. Koshi, Role of Methyl Radicals in the Growth of PAHs, *Journal of the American Society for Mass Spectrometry*, vol. 21, no. 4, pp. 534–544, 2010.

[47] A. Comandini, S. Abid, and N. Chaumeix, Polycyclic Aromatic Hydrocarbon Growth by Diradical Cycloaddition/Fragmentation, *Journal of Physical Chemistry A*, vol. 121, no. 31, pp. 5921–5931, 2017.

[48] G. L. Dong and K. J. Hüttinger, Consideration of reaction mechanisms leading to pyrolytic carbon of different textures, *Carbon*, vol. 40, no. 14, pp. 2515–2528, 2002.

[49] B. V. Unterreiner, M. Sierka, and R. Ahlrichs, Reaction pathways for growth of polycyclic aromatic hydrocarbons under combustion conditions, a DFT study, *Physical Chemistry Chemical Physics*, vol. 6, no. 18, pp. 4377–4384, 2004.

[50] G. M. Badger, J. K. Donnelly, and T. M. Spotswood, The formation of aromatic hydrocarbons at high temperatures. XXIII. The pyrolysis of anthracene, *Australian Journal of Chemistry*, vol. 17, no. 10, pp. 1147–1156, 1964.

[51] J. Griesheimer and K.-H. Homann, Large molecules, radicals ions, and small soot particles in fuel-rich hydrocarbon flames: Part II. Aromatic radicals and intermediate PAHs in a premixed low-pressure naphthalene/oxygen/argon flame, *Symposium (International) on Combustion*, vol. 27, no. 2, pp. 1753–1759, 1998.

[52] J. Thomas Mckinnon and J. B. Howard, The roles of pah and acetylene in soot nucleation and growth, *Symposium (International) on Combustion*, vol. 24, no. 1, pp. 965–971, 1992.

[53] H. Böhm, H. Jander, and D. Tanke, PAH growth and soot formation in the pyrolysis of acetylene and benzene at high temperatures and pressures: Modeling and experiment, *Symposium (International) on Combustion*, vol. 27, no. 1, pp. 1605–1612, 1998.

[54] M. Mehl, W. J. Pitz, C. K. Westbrook, and H. J. Curran, Kinetic modeling of gasoline surrogate components and mixtures under engine conditions, *Proceedings of the Combustion Institute*, vol. 33, no. 1, pp. 193–200, 2011.

[55] H. Wang and M. Frenklach, A detailed kinetic modeling study of aromatics formation in laminar premixed acetylene and ethylene flames, *Combustion and Flame*, vol. 110, no. 1-2, pp. 173–221, 1997.

[56] S. M. Sarathy, S. Vranckx, K. Yasunaga, M. Mehl, P. Oßwald, W. K. Metcalfe, C. K. Westbrook, W. J. Pitz, K. Kohse-Höinghaus, R. X. Fernandes, and H. J. Curran, A comprehensive chemical kinetic combustion model for the four butanol isomers, *Combustion and Flame*, vol. 159, no. 6, pp. 2028–2055, 2012.

[57] Z. A. Mansurov, Soot Formation in Combustion Processes (Review), *Combustion, Explosion and Shock Waves*, vol. 41, no. 6, p. 727, 2005.

[58] K. Ravindra, R. Sokhi, and R. Van Grieken, Atmospheric polycyclic aromatic hydrocarbons: Source attribution, emission factors and regulation, *Atmospheric Environment*, vol. 42, no. 13, pp. 2895–2921, 2008.

[59] H. Shen, Y. Huang, R. Wang, D. Zhu, W. Li, G. Shen, B. Wang, Y. Zhang, Y. Chen, Y. Lu, H. Chen, T. Li, K. Sun, B. Li, W. Liu, J. Liu, and S. Tao, Global atmospheric emissions of polycyclic aromatic hydrocarbons from 1960 to 2008 and future predictions, *Environmental Science and Technology*, vol. 47, no. 12, pp. 6415–6424, 2013.

[60] E. Hussar, S. Richards, Z.-Q. Lin, R. P. Dixon, and K. A. Johnson, Human Health Risk Assessment of 16 Priority Polycyclic Aromatic Hydrocarbons in Soils of Chattanooga, Tennessee, USA, *Water, Air, & Soil Pollution*, vol. 223, no. 9, pp. 5535–5548, 2012.

[61] T. Kameda, Atmospheric chemistry of polycyclic aromatic hydrocarbons and related compounds, *Journal of Health Science*, vol. 57, no. 6, pp. 504–511, 2011.

[62] B. Zielinska, J. Arey, R. Atkinson, and A. M. Winer, The nitroarenes of molecular weight 247 in ambient particulate samples collected in southern california, *Atmospheric Environment (1967)*, vol. 23, no. 1, pp. 223–229, 1989.

[63] O. Cvrčková and M. Ciganek, Photostability of Polycyclic Aromatic Hydrocarbons (PAHs) and Nitrated Polycyclic Aromatic Hydrocarbons (NPAHs) in dichloromethane and isooctane solutions, *Polycyclic Aromatic Compounds*, vol. 25, no. 2, pp. 141–156, 2005.

[64] J. Sasaki, S. M. Aschmann, E. S. Kwok, R. Atkinson, and J. Arey, Products of the gas-phase OH and NO3 radical-initiated reactions of naphthalene, *Environmental Science and Technology*, vol. 31, no. 11, pp. 3173–3179, 1998.

[65] R. Atkinson and J. Arey, Atmospheric chemistry of gas-phase polycyclic aromatic hydrocarbons: Formation of atmospheric mutagens, *Environmental Health Perspectives*, vol. 102, no. SUPPL. 4, pp. 117–126, 1994.

[66] K. R. Darnall, A. C. Lloyd, A. M. Winer, and J. N. Pitts, Reactivity Scale for Atmospheric Hydrocarbons Based on Reaction with Hydroxyl Radical, *Environmental Science and Technology*, vol. 10, no. 7, pp. 692–696, 1976.

[67] J. Ringuet, A. Albinet, E. Leoz-Garziandia, H. Budzinski, and E. Villenave, Reactivity of polycyclic aromatic compounds (PAHs, NPAHs and OPAHs) adsorbed on natural aerosol particles exposed to atmospheric oxidants, *Atmospheric Environment*, vol. 61, no. x, pp. 15–22, 2012.

[68] W. A. J. van Pul, F. de Leeuw, J. A. van Jaarsveld, M. A. van der Gaag, and C. J. Sliggers, The potential for long-range transboundary atmospheric transport, *Chemosphere*, vol. 37, no. 1, pp. 113–141, 1998.

[69] F. Wania and D. MacKay, Peer Reviewed: Tracking the Distribution of Persistent Organic Pollutants, *Environmental Science & Technology*, vol. 30, no. 9, 390A–396A, 1996.

[70] K. H. Kim, S. A. Jahan, E. Kabir, and R. J. Brown, A review of airborne polycyclic aromatic hydrocarbons (PAHs) and their human health effects, *Environment International*, vol. 60, pp. 71–80, 2013.

[71] Y. Zhong and L. Zhu, Distribution, input pathway and soil-air exchange of polycyclic aromatic hydrocarbons in Banshan Industry Park, China, *Science of the Total Environment*, vol. 444, pp. 177–182, 2013.

[72] G. J. Hodgkinson, Interstellar chemistry, *Journal of the British Astronomical Association*, vol. 89, pp. 331–355, 1979.

[73] Http://www.spitzer.caltech.edu/images/1645-ssc2006-16a1-Orion-in-the-Infrared, *Orion in the Infrared*, Nov. 2020.

[74] P. Swings and L. Rosenfeld, Notes considerations regarding interstellar molecules, *ApJ*, vol. 86, pp. 483–486, 1932.

[75] A. McKellar, Evidence for the molecular origin of some hitherto unidentified interstellar lines, *Astronomical Society of the Pacific*, no. 52, pp. 187–192, 1940.

[76] S. Iglesias-Groth, A. Manchado, R. Rebolo, J. I. González Hernández, D. A. García-Hernández, and D. L. Lambert, A search for interstellar anthracene towards the Perseus anomalous microwave emission region, *Monthly Notices of the Royal Astronomical Society*, vol. 407, no. 4, pp. 2157–2165, 2010.

[77] R. Gredel, Y. Carpentier, G. Rouillé, M. Steglich, F. Huisken, and T. Henning, Abundances of PAHs in the ISM: Confronting observations with experimental results, *Astronomy and Astrophysics*, vol. 530, pp. 1–15, 2011.

[78] C. Joblin, A. Leger, and P. Martin, Contribution of polycyclic aromatic hydrocarbon molecules to the interstellar extinction curve, *The Astrophysical Journal*, vol. 393, p. L79, 1992.

[79] G. Rouillé, M. Steglich, Y. Carpentier, C. Jäger, F. Huisken, T. Henning, R. Czerwonka, G. Theumer, C. Börger, I. Bauer, and H. J. Knölker, On the relevance of polyynyl-substituted polycyclic aromatic hydrocarbons to astrophysics, *Astrophysical Journal*, vol. 752, no. 1, 2012.

[80] G. H. Herbig, The diffuse interstellar bands, *Annual Review of Astronomy and Astrophysics*, vol. 33, no. 1, pp. 19–73, 1995.

[81] E. K. Campbell, M. Holz, D. Gerlich, and J. P. Maier, Laboratory confirmation of C60+ as the carrier of two diffuse interstellar bands, *Nature*, vol. 523, no. 7560, pp. 322–323, 2015.

[82] C. W. Bauschlicher, C. Boersma, A. Ricca, A. L. Mattioda, J. Cami, E. Peeters, F. Sánchez De Armas, G. P. Saborido, D. M. Hudgins, and L. J. Allamandola, The NASA Ames polycyclic aromatic hydrocarbon infrared spectroscopic database: The computed spectra, *Astrophysical Journal, Supplement Series*, vol. 189, no. 2, pp. 341–351, 2010.

[83] A. G. Tielens, Interstellar polycyclic aromatic hydrocarbon molecules, *Annual Review of Astronomy and Astrophysics*, vol. 46, pp. 289–337, 2008.

[84] J. Puget, A New Component Of The Interstellar Matter: Small Grains And Large Aromatic Molecules, *Annual Review of Astronomy and Astrophysics*, vol. 27, no. 1, pp. 161–198, 1989.

[85] L. J. Allamandola, A. G. G. M. Tielens, and J. R. Barker, Interstellar Polycyclic Aromatic Hydrocarbons: The Infrared Emission Bands, the Excita-

tion/Emission Mechanism, and the Astrophysical Implications, *The Astrophysical Journal Supplement Series*, vol. 71, p. 733, 1989.

[86] L. Verstraete, The role of PAHs in the physics of the interstellar medium, *EAS Publications Series*, vol. 46, pp. 415–426, 2011.

[87] A. M. Röder, Excited-State Dynamics in Open-Shell Molecules, PhD Thesis, 2017.

[88] W. Demtröder and W. Demtröder, Laser Spectroscopy in Molecular Beams, *Laser Spectroscopy 2*, pp. 183–224, 2015.

[89] T. E. Wall, Preparation of cold molecules for high-precision measurements, *Journal of Physics B: Atomic, Molecular and Optical Physics*, vol. 49, no. 24, 2016.

[90] W. R. Gentry and C. F. Giese, High-precision skimmers for supersonic molecular beams, *Review of Scientific Instruments*, vol. 46, no. 1, p. 104, 1975.

[91] S. D. Eder, A. Salvador Palau, T. Kaltenbacher, G. Bracco, and B. Holst, Velocity distributions in microskimmer supersonic expansion helium beams: High precision measurements and modeling, *Review of Scientific Instruments*, vol. 89, no. 11, 2018.

[92] G. A. Bird, Transition regime behavior of supersonic beam skimmers, *Physics of Fluids*, vol. 19, no. 10, pp. 1486–1491, 1976.

[93] J. Liu, E. J. Salumbides, U. Hollenstein, J. C. Koelemeij, K. S. Eikema, W. Ubachs, and F. Merkt, Determination of the ionization and dissociation energies of the hydrogen molecule, *Journal of Chemical Physics*, vol. 130, no. 17, 2009.

[94] J. Liu, D. Sprecher, C. Jungen, W. Ubachs, and F. Merkt, Determination of the ionization and dissociation energies of the deuterium molecule (D2), *Journal of Chemical Physics*, vol. 132, no. 15, 2010.

[95] W. Ubachs, J. C. J. Koelemeij, K. S. E. Eikema, and E. J. Salumbides, Physics beyond the Standard Model from hydrogen spectroscopy, *Journal of Molecular Spectroscopy*, vol. 320, pp. 1–12, 2016.

[96] P. J. Chantry, Doppler Broadening in Beam Experiments, *The Journal of Chemical Physics*, vol. 55, no. 6, pp. 2746–2759, Sep. 1971.

[97] T. E. Gough, R. E. Miller, and G. Scoles, Sub-Doppler resolution infrared spectroscopy of supersonic molecular beams of nitric oxide, *Journal of Molecular Spectroscopy*, vol. 72, no. 1, pp. 124–127, 1978.

[98] L. Belau, K. R. Wilson, S. R. Leone, and M. Ahmed, Vacuum ultraviolet (VUV) photoionization of small water clusters, *Journal of Physical Chemistry A*, vol. 111, no. 40, pp. 10 075–10 083, 2007.

[99] C. Desfrançois, S. Carles, and J. P. Schermann, Weakly bound clusters of biological interest, *Chemical Reviews*, vol. 100, no. 11, pp. 3943–3962, 2000.

[100] G. Berden, W. L. Meerts, M. Schmitt, and K. Kleinermanns, High resolution UV spectroscopy of phenol and the hydrogen bonded phenol-water cluster, *Journal of Chemical Physics*, vol. 104, no. 3, pp. 972–982, 1996.

[101] L. F. Roncaratti, L. Belpassi, D. Cappelletti, F. Pirani, and F. Tarantelli, Molecular-beam scattering experiments and theoretical calculations probing charge transfer in weakly bound complexes of water, *Journal of Physical Chemistry A*, vol. 113, no. 52, pp. 15 223–15 232, 2009.

[102] K. Luria, W. Christen, and U. Even, Generation and propagation of intense supersonic beams, *Journal of Physical Chemistry A*, vol. 115, no. 25, pp. 7362–7367, 2011.

[103] U. Even, Pulsed Supersonic Beams from High Pressure Source : Simulation Results and Experimental Measurements, vol. 2014, no. Section 3, 2014.

[104] M. R. Tarbutt, J. J. Hudson, B. E. Sauer, E. A. Hinds, V. A. Ryzhov, V. L. Ryabov, and V. F. Ezhov, A jet beam source of cold YbF radicals, *Journal of Physics B: Atomic, Molecular and Optical Physics*, vol. 35, no. 24, pp. 5013–5022, 2002.

[105] H. L. Bethlem, G. Berden, and G. Meijer, Decelerating neutral dipolar molecules, *Physical Review Letters*, vol. 83, no. 8, pp. 1558–1561, 1999.

[106] S. Y. Van De Meerakker, N. Vanhaecke, and G. Meijer, Stark deceleration and trapping of oh radicals, *Annual Review of Physical Chemistry*, vol. 57, pp. 159–190, 2006.

[107] E. Narevicius, A. Libson, C. G. Parthey, I. Chavez, J. Narevicius, U. Even, and M. G. Raizen, Stopping supersonic beams with a series of pulsed electromagnetic coils: An atomic coilgun, *Physical Review Letters*, vol. 100, no. 9, pp. 18–21, 2008.

[108] ——, Stopping supersonic oxygen with a series of pulsed electromagnetic coils: A molecular coilgun, *Physical Review A - Atomic, Molecular, and Optical Physics*, vol. 77, no. 5, pp. 1–4, 2008.

[109] S. A. Meek, H. L. Bethlem, H. Conrad, and G. Meijer, Trapping molecules on a chip in traveling potential wells, *Physical Review Letters*, vol. 100, no. 15, pp. 18–21, 2008.

[110] R. Fulton, A. I. Bishop, M. N. Shneider, and P. F. Barker, Controlling the motion of cold molecules with deep periodic optical potentials, *Nature Physics*, vol. 2, no. 7, pp. 465–468, 2006.

[111] M. Schnell and G. Meijer, Cold molecules: Preparation, applications, and challenges, *Angewandte Chemie - International Edition*, vol. 48, no. 33, pp. 6010–6031, 2009.

[112] D. Mani, T. Fischer, R. Schwan, A. Dey, B. Redlich, A. F. Van Der Meer, G. Schwaab, and M. Havenith, A helium nanodroplet setup for mid and far-infrared spectroscopy using pulsed-free-electron lasers: Vibrational spectra of propargyl alcohol, *RSC Advances*, vol. 7, no. 86, pp. 54 318–54 325, 2017.

[113] S. Grebenev, M. Hartmann, A. Lindinger, N. Pörtner, B. Sartakov, J. P. Toennies, and A. F. Vilesov, Spectroscopy of molecules in helium droplets, *Physica B: Condensed Matter*, vol. 280, no. 1, pp. 65–72, 2000.

[114] V. E. Bondybey, A. M. Smith, and J. Agreiter, New developments in matrix isolation spectroscopy, *Chemical Reviews*, vol. 96, no. 6, pp. 2113–2134, 1996.

[115] N. Singhal, M. Kumar, P. K. Kanaujia, and J. S. Virdi, MALDI-TOF mass spectrometry: An emerging technology for microbial identification and diagnosis, *Frontiers in Microbiology*, vol. 6, no. AUG, pp. 1–16, 2015.

[116] W. B. Dunn, S. Overy, and W. P. Quick, Evaluation of automated electrospray-TOF mass spectrometry for metabolic fingerprinting of the plant metabolome, *Metabolomics*, vol. 1, no. 2, pp. 137–148, 2005.

[117] C. Mullen, M. J. Coggiola, and H. Oser, Femtosecond Laser Photoionization Time-of-Flight Mass Spectrometry of Nitro-aromatic Explosives and Explosives Related Compounds, *Journal of the American Society for Mass Spectrometry*, vol. 20, no. 3, pp. 419–429, 2009.

[118] S. Potapov, E. Izrailov, V. Vergizova, M. Voronov, S. Suprunovich, M. Slyadnev, and A. Ganeev, Pulsed glow discharge in thin-walled metallic hollow

cathode. Analytical possibilities in atomic and mass spectrometry, *Journal of Analytical Atomic Spectrometry*, vol. 18, no. 6, pp. 564–571, 2003.

[119] S. Shimma, Y. Sugiura, T. Hayasaka, N. Zaima, M. Matsumoto, and M. Setou, Mass imaging and identification of biomolecules with MALDI-QIT-TOF-based system, *Analytical Chemistry*, vol. 80, no. 3, pp. 878–885, 2008.

[120] B. A. Mamyrin, Time-of-flight mass spectrometry (concepts, achievements, and prospects), *International Journal of Mass Spectrometry*, vol. 206, no. 3, pp. 251–266, 2001.

[121] U. Boesl, Time-of-flight mass spectrometry: Introduction to the basics, *Mass Spectrometry Reviews*, vol. 36, no. 1, pp. 86–109, 2017.

[122] D. S. Cornett, M. Peschke, K. LaiHing, P. Y. Cheng, K. F. Willey, and M. A. Duncan, Reflectron time-of-flight mass spectrometer for laser photodissociation, *Review of Scientific Instruments*, vol. 63, no. 4, pp. 2177–2186, 1992.

[123] B. Mamyrin, V. Karataev, D. Shmikk, and V. Zagulin, The mass-reflectron, a new nonmagnetic time-of-flight mass spectrometer with high resolution, *Soviet Journal of Experimental and Theoretical Physics*, vol. 37, no. 1, p. 45, 1973.

[124] M. Koch, D. R. Cohn, R. M. Patrick, M. P. Schuetze, L. Bromberg, D. Reilly, K. Hadidi, P. Thomas, and P. Falkos, Electron Beam Atmospheric Pressure Cold Plasma Decomposition of Cariion Tetrachloride and Trichloroethylene, *Environmental Science and Technology*, vol. 29, no. 12, pp. 2946–2952, 1995.

[125] B. M. Penetrante, M. C. Hsiao, B. T. Merritt, G. E. Vogtlin, and P. H. Wallman, Comparison of Electrical Discharge Techniques for Nonthermal Plasma Processing of NO in N2, *IEEE Transactions on Plasma Science*, vol. 23, no. 4, pp. 679–687, 1995.

[126] M. J. Travers, W. Chen, J. U. Grabow, M. C. McCarthy, and P. Thaddeus, Microwave spectra of the methylpolyynes CH3(CC)4H and CH3(CC)5H, *Journal of Molecular Spectroscopy*, vol. 192, no. 1, pp. 12–16, 1998.

[127] M. C. McCarthy, W. Chen, M. J. Travers, and P. Thaddeus, Microwave Spectra of 11 Polyyne Carbon Chains, *The Astrophysical Journal Supplement Series*, vol. 129, no. 2, pp. 611–623, 2000.

[128] T. Motylewski and H. Linnartz, Cavity ring down spectroscopy on radicals in a supersonic slit nozzle discharge, *Review of Scientific Instruments*, vol. 70, no. 2, pp. 1305–1312, 1999.

[129] M. C. Van Beek and J. J. Ter Meulen, An intense pulsed electrical discharge source for OH molecular beams, *Chemical Physics Letters*, vol. 337, no. 4-6, pp. 237–242, 2001.

[130] A. K. Lemmens, D. B. Rap, J. M. Thunnissen, B. Willemsen, and A. M. Rijs, Polycyclic aromatic hydrocarbon formation chemistry in a plasma jet revealed by IR-UV action spectroscopy, *Nature Communications*, vol. 11, no. 1, pp. 1–7, 2020.

[131] R. G. Manning, E. R. Grant, J. C. Merrill, N. J. Parks, and J. W. Root, Hydrogen abstraction by fluorine atoms under conditions of thermal initiation: Hydrocarbons and fluorinated hydrocarbons, *International Journal of Chemical Kinetics*, vol. 7, no. 1, pp. 39–44, 1975.

[132] G. Lebras, N. I. Butkovskaya, and V. L. Talrose, Reactoin of F Atoms with CH2Cl2 by Modulated Beam Mass Spectrometry, *Chemical Physics*, vol. 50, pp. 63–69, 1980.

[133] S. E. Bradforth, D. W. Arnold, R. B. Metz, A. Weaver, and D. M. Neumark, Spectroscopy of the transition state: Hydrogen abstraction reactions of fluorine, *Journal of Physical Chemistry*, vol. 95, no. 21, pp. 8066–8078, 1991.

[134] C. E. Kolb and M. Kaufman, Molecular beam analysis investigation of the reaction between atomic fluorine and carbon tetrachloride, *The Journal of Physical Chemistry*, vol. 76, no. 7, pp. 947–953, 1972.

[135] K. A. Peterson and T. H. Dunning, Benchmark calculations with correlated molecular wave functions. VII. Binding energy and structure of the HF dimer, *The Journal of Chemical Physics*, vol. 102, no. 5, pp. 2032–2041, 1995.

[136] D. Schleier, A. Humeniuk, E. Reusch, F. Holzmeier, D. Nunez-Reyes, C. Alcaraz, G. A. Garcia, J. C. Loison, I. Fischer, and R. Mitric, Diborene: Generation and Photoelectron Spectroscopy of an Inorganic Biradical, *Journal of Physical Chemistry Letters*, vol. 9, no. 20, pp. 5921–5925, 2018.

[137] C. Alcaraz, I. Fischer, and D. Schroeder, ChemInform Abstract: Radical Chemistry in the Gas Phase, *ChemInform*, vol. 43, no. 37, no–no, 2012.

[138] J. J. Russell, J. A. Seetula, R. S. Timonen, D. Gutman, and D. F. Nava, Kinetics and Thermochemistry of the t-C4H9Radical. Study of the Equilib-

rium t-C4H9+ HBr i-C4H10+ Br, *Journal of the American Chemical Society*, vol. 110, no. 10, pp. 3084–3091, 1988.

[139] I. R. Slagle, J. Y. Park, M. C. Heaven, and D. Gutman, Kinetics of Polyatomic Free Radicals Produced by Laser Photolysis. 3. Reaction of Vinyl Radicals with Molecular Oxygen, *Journal of the American Chemical Society*, vol. 106, no. 16, pp. 4356–4361, 1984.

[140] I. R. Slagle and D. Gutman, Kinetics of Polyatomic Free Radicals Produced by Laser Photolysis. 5. Study of the Equilibrium CH3 + O2 CH3O2 between 421 and 538 °C, *Journal of the American Chemical Society*, vol. 107, no. 19, pp. 5342–5347, 1985.

[141] C. Wentrup, Flash Vacuum Pyrolysis: Techniques and Reactions, *Angewandte Chemie - International Edition*, vol. 56, no. 47, pp. 14 808–14 835, 2017.

[142] K. Prozument, G. Barratt Park, R. G. Shaver, A. K. Vasiliou, J. M. Oldham, D. E. David, J. S. Muenter, J. F. Stanton, A. G. Suits, G. Barney Ellison, and R. W. Field, Chirped-pulse millimeter-wave spectroscopy for dynamics and kinetics studies of pyrolysis reactions, *Physical Chemistry Chemical Physics*, vol. 16, no. 30, pp. 15 739–15 751, 2014.

[143] R. Li, J. C. Wu, J. L. Chang, and Y. T. Chen, Vibronic spectra of the allyl radical at 6-8 eV with resonance-enhanced multiphoton ionization technique, *Science in China, Series B: Chemistry*, vol. 44, no. 4, pp. 360–365, 2001.

[144] P. Chen, S. D. Colson, W. A. Chupka, and J. A. Berson, Flash pyrolytic production of rotationally cold free radicals in a supersonic jet. Resonant multiphoton spectrum of the 3p2A2 ← X2A2 origin band of CH3, *The Journal of Physical Chemistry*, vol. 90, no. 11, pp. 2319–2321, 1986.

[145] G. Maier, H. P. Reisenauer, and H. Pacl, C2H2Si Isomers: Generation by Pulsed Flash Pyrolysis and Matrix-Spectroscopic Identification, *Angewandte Chemie International Edition in English*, vol. 33, no. 12, pp. 1248–1250, 1994.

[146] M. Zierhut, B. Noller, T. Schultz, and I. Fischer, Excited-state decay of hydrocarbon radicals, investigated by femtosecond time-resolved photoionization: Ethyl, propargyl, and benzyl, *Journal of Chemical Physics*, vol. 122, no. 9, 2005.

[147] D. W. Kohn, H. Clauberg, and P. Chen, Flash pyrolysis nozzle for generation of radicals in a supersonic jet expansion, *Rev. Sci. Instrum.*, vol. 63, no. 8, pp. 4003–4005, 1992.

[148] F. Hirsch, K. Pachner, I. Fischer, K. Issler, J. Petersen, R. Mitric, S. Bakels, and A. M. Rijs, Do Xylylenes Isomerize in Pyrolysis? *ChemPhysChem*, vol. 21, no. 14, pp. 1515–1518, 2020.

[149] P. Hemberger, M. Steinbauer, M. Schneider, I. Fischer, M. Johnson, A. Bodi, and T. Gerber, Photoionization of three isomers of the C9H7 radical, *Journal of Physical Chemistry A*, vol. 114, no. 14, pp. 4698–4703, 2010.

[150] J. Giegerich, Velocity-Map-Imaging Studien an reaktiven Intermediaten: Fulvenallen, C3H2 Isomere und Alkylradikale, PhD Thesis, Universität Würzburg, 2015.

[151] J. Giegerich, J. Petersen, and R. Mitric, Photodissociation dynamics of propargylene, HCCCH †, vol. 1, no. C, pp. 6294–6302, 2014.

[152] A. Chrostowska, G. Pfister-Guillouzo, F. Gracian, and C. Wentrup, Pitfalls in the Photoelectron Spectroscopic Investigations of Benzyne. Photoelectron Spectrum of Cyclopentadienylideneketene, *Aust. J. Chem.*, vol. 63, pp. 1084–1090, 2010.

[153] L. Hanley and R. Zimmermann, Light and molecular ions: The emergence of vacuum UV single-photon ionization in MS, *Analytical Chemistry*, vol. 81, no. 11, pp. 4174–4182, 2009.

[154] P. Constantinidis, Schwingungsspektroskopische Untersuchung reaktiver Moleküle und ihrer Hochtemperatur-Reaktionsprodukte, PhD Thesis, Universität Würzburg, 2018.

[155] P. Constantinidis, H. C. Schmitt, I. Fischer, B. Yan, and A. M. Rijs, Formation of polycyclic aromatic hydrocarbons from bimolecular reactions of phenyl radicals at high temperatures, *Physical Chemistry Chemical Physics*, vol. 17, no. 43, pp. 29 064–29 071, 2015.

[156] C. A. Taatjes, D. L. Osborn, T. M. Selby, G. Meloni, H. Fan, and S. T. Pratt, Absolute photoionization cross-section of the methyl radical, *Journal of Physical Chemistry A*, vol. 112, no. 39, pp. 9336–9343, 2008.

[157] T. Adam and R. Zimmermann, Determination of single photon ionization cross sections for quantitative analysis of complex organic mixtures, *Analytical and Bioanalytical Chemistry*, vol. 389, no. 6, pp. 1941–1951, 2007.

[158] G. Malloci, G. Mulas, and C. Joblin, Electronic absorption spectra of PAHs up to vacuum UV, *Astronomy & Astrophysics*, vol. 426, no. 1, pp. 105–117, 2004.

[159] H. Xu and S. T. Pratt, Photodissociation of anisole and absolute photoionization cross-section of the phenoxy radical, *Journal of Physical Chemistry A*, vol. 117, no. 46, pp. 12 075–12 081, 2013.

[160] T. A. Cool, J. Wang, K. Nakajima, C. A. Taatjes, and A. Mcllroy, Photoionization cross sections for reaction intermediates in hydrocarbon combustion, *International Journal of Mass Spectrometry*, vol. 247, no. 1, pp. 18–27, 2005.

[161] B. Yang, J. Wang, T. A. Cool, N. Hansen, S. Skeen, and D. L. Osborn, Absolute photoionization cross-sections of some combustion intermediates, *International Journal of Mass Spectrometry*, vol. 309, pp. 118–128, 2012.

[162] J. D. Savee, S. Soorkia, O. Welz, T. M. Selby, C. A. Taatjes, and D. L. Osborn, Absolute photoionization cross-section of the propargyl radical, *Journal of Chemical Physics*, vol. 136, no. 13, 2012.

[163] J. C. Loison, Absolute photoionization cross section of the methyl radical, *Journal of Physical Chemistry A*, vol. 114, no. 23, pp. 6515–6520, 2010.

[164] B. V. King, M. J. Pellin, J. F. Moore, I. V. Veryovkin, M. R. Savina, and C. E. Tripa, Estimation of useful yield in surface analysis using single photon ionisation, *Applied Surface Science*, vol. 203-204, pp. 244–247, 2003.

[165] N. P. Lockyer and J. C. Vickerman, Single photon ionisation mass spectrometry using laser-generated vacuum ultraviolet photons, *Laser Chemistry*, vol. 17, no. 3, pp. 139–159, 1997.

[166] G. Bjorklund, Effects of focusing on third-order nonlinear processes in isotropic media, *IEEE Journal of Quantum Electronics*, vol. 11, no. 6, pp. 287–296, 1975.

[167] A. C. Sinnock and B. L. Smith, Refractive indices of the condensed inert gases, *Physical Review*, vol. 181, no. 3, pp. 1297–1307, 1969.

[168] M. Tarazkar, D. A. Romanov, and R. J. Levis, High-order nonlinear refractive indices for He, Ne, Kr, and Xe atoms, *Physical Review A - Atomic, Molecular, and Optical Physics*, vol. 90, no. 6, pp. 1–10, 2014.

[169] P. J. Leonard, Refractive indices, Verdet constants, and Polarizabilities of the inert gases, *Atomic Data and Nuclear Data Tables*, vol. 14, no. 1, pp. 21–37, 1974.

[170] R. Mahon, T. McIlrath, V. Myerscough, and D. Koopman, Third-harmonic generation in argon, krypton, and xenon: Bandwidth limitations in the vicinity of Lyman-α, *IEEE Journal of Quantum Electronics*, vol. 15, no. 6, pp. 444–451, 1979.

[171] D. J. Butcher, Vacuum ultraviolet radiation for single-photoionization mass spectrometry: A review, *Microchemical Journal*, vol. 62, no. 3, pp. 354–362, 1999.

[172] T. Imasaka, A. Hamachi, T. Okuno, T. Imasaka, and Y. Kida, Resonant and nonresonant multiphoton ionization processes in the mass spectrometry of explosives, *Analytical Chemistry*, vol. 87, no. 5, pp. 3027–3031, 2015.

[173] W. Demtröder, Laserspektroskopie: Grundlagen und Techniken. Springer Berlin Heidelberg, 2007.

[174] H. Kouno and T. Imasaka, The efficiencies of resonant and nonresonant multiphoton ionization in the femtosecond region, *Analyst*, vol. 141, no. 18, pp. 5274–5280, 2016.

[175] U. Boesl, A. Bornschlegl, C. Logé, and K. Titze, Resonance-enhanced multiphoton ionization with circularly polarized light: Chiral carbonyls, *Analytical and Bioanalytical Chemistry*, vol. 405, no. 22, pp. 6913–6924, 2013.

[176] U. Boesl, Multiphoton excitation and mass-selective ion detection for neutral and ion spectroscopy, *Journal of Physical Chemistry*, vol. 95, no. 8, pp. 2949–2962, 1991.

[177] D. S. Zakheim and P. M. Johnson, Rate equation modelling of molecular multiphoton ionization dynamics, *Chemical Physics*, vol. 46, no. 3, pp. 263–272, 1980.

[178] L. J. Butler and D. M. Neumark, Photodissociation dynamics, *Journal of Physical Chemistry*, vol. 100, no. 31, pp. 12 801–12 816, 1996.

[179] O. P. Haefliger and R. Zenobi, Laser Mass Spectrometric Analysis of Polycyclic Aromatic Hydrocarbons with Wide Wavelength Range Laser Multiphoton Ionization Spectroscopy, *Analytical Chemistry*, vol. 70, no. 13, pp. 2660–2665, 1998.

[180] A. Li, T. Uchimura, H. Tsukatani, and T. Imasaka, Trace analysis of polycyclic aromatic hydrocarbons using gas chromatography-mass spectrometry based on nanosecond multiphoton ionization, *Analytical Sciences*, vol. 26, no. 8, pp. 841–846, 2010.

[181] Y. Hu, J. Guan, and E. R. Bernstein, Mass-selected IR-VUV (118 nm) spectroscopic studies of radicals, aliphatic molecules, and their clusters, *Mass Spectrometry Reviews*, vol. 32, no. 6, pp. 484–501, 2013.

[182] A. P. Milce, D. E. Heard, R. E. Miller, and B. J. Orr, Rovibrational spectroscopy of the C2H2-Ar van der Waals complex, using a fluorescence depletion infrared-ultraviolet double resonance technique, *Chemical Physics Letters*, vol. 250, no. 1, pp. 95–103, 1996.

[183] B. Fehrensen, M. Hippler, and M. Quack, Isotopomer-selective overtone spectroscopy by ionization detected IR + UV double resonance of jet-cooled aniline, *Chemical Physics Letters*, vol. 298, no. 4-6, pp. 320–328, 1998.

[184] E. C. Stanca-Kaposta and J. P. Simons, High-resolution Infrared – Ultraviolet (IR – UV) Double-resonance Spectroscopy of Biological Molecules, in *Handbook of High-resolution Spectroscopy*, M. Quack and F. Merkt, Eds., 2011.

[185] K. H. Fischer, P. Hemberger, I. Fischer, and A. M. Rijs, Infrared Spectra of Reactive Species Generated by Flash Pyrolysis in a Free Jet, *ChemPhysChem.*, vol. 11, pp. 3228–3230, 2010.

[186] A. M. Rijs, M. Kabeláč, A. Abo-Riziq, P. Hobza, and M. S. De Vries, Isolated gramicidin peptides probed by IR spectroscopy, *ChemPhysChem*, vol. 12, no. 10, pp. 1816–1821, 2011.

[187] G. C. Van Zundert, S. Jaeqx, G. Berden, J. M. Bakker, K. Kleinermanns, J. Oomens, and A. M. Rijs, IR spectroscopy of isolated neutral and protonated adenine and 9-methyladenine, *ChemPhysChem*, vol. 12, no. 10, pp. 1921–1927, 2011.

[188] I. León, E. J. Cocinero, A. M. Rijs, J. Millán, E. Alonso, A. Lesarri, and J. A. Fernández, Formation of water polyhedrons in propofol-water clusters, *Physical Chemistry Chemical Physics*, vol. 15, no. 2, pp. 568–575, 2013.

[189] D. J. Bakker, A. Dey, D. P. Tabor, Q. Ong, J. Mahé, M. P. Gaigeot, E. L. Sibert, and A. M. Rijs, Fingerprints of inter- and intramolecular hydrogen bonding in saligenin-water clusters revealed by mid- and far-infrared spec-

troscopy, *Physical Chemistry Chemical Physics*, vol. 19, no. 31, pp. 20 343–20 356, 2017.

[190] A. M. Rijs and J. Oomens, IR Spectroscopic Techniques to Study Isolated Biomolecules, *Top. Curr. Chem.*, vol. 364, pp. 1–42, 2015.

[191] M. J. Frisch, G. W. Trucks, H. B. Schlegel, G. E. Scuseria, M. A. Robb, J. R. Cheeseman, G. Scalmani, V. Barone, G. A. Petersson, H. Nakatsuji, X. Li, M. Caricato, A. V. Marenich, J. Bloino, B. G. Janesko, R. Gomperts, B. Mennucci, H. P. Hratchian, J. V. Ortiz, A. F. Izmaylov, J. L. Sonnenberg, Williams, F. Ding, F. Lipparini, F. Egidi, J. Goings, B. Peng, A. Petrone, T. Henderson, D. Ranasinghe, V. G. Zakrzewski, J. Gao, N. Rega, G. Zheng, W. Liang, M. Hada, M. Ehara, K. Toyota, R. Fukuda, J. Hasegawa, M. Ishida, T. Nakajima, Y. Honda, O. Kitao, H. Nakai, T. Vreven, K. Throssell, J. A. Montgomery Jr., J. E. Peralta, F. Ogliaro, M. J. Bearpark, J. J. Heyd, E. N. Brothers, K. N. Kudin, V. N. Staroverov, T. A. Keith, R. Kobayashi, J. Normand, K. Raghavachari, A. P. Rendell, J. C. Burant, S. S. Iyengar, J. Tomasi, M. Cossi, J. M. Millam, M. Klene, C. Adamo, R. Cammi, J. W. Ochterski, R. L. Martin, K. Morokuma, O. Farkas, J. B. Foresman, and D. J. Fox, Gaussian 16 Rev. B.01. Wallingford, CT, 2016.

[192] J. M. Madey, Stimulated emission of bremsstrahlung in a periodic magnetic field, *Journal of Applied Physics*, vol. 42, no. 5, pp. 1906–1913, 1971.

[193] L. R. Elias, W. M. Fairbank, J. M. Madey, H. A. Schwettman, and T. I. Smith, Observation of stimulated emission of radiation by relativistic electrons in a spatially periodic transverse magnetic field, *Physical Review Letters*, vol. 36, no. 13, pp. 717–720, 1976.

[194] D. A. G. Deacon, L. R. Elias, J. M. J. Madey, G. J. Ramian, H. A. Schwettman, and T. I. Smith, First Operation of a Free-Electron Laser, *Phys. Rev. Lett.*, vol. 38, no. 16, pp. 892–894, 1977.

[195] P. Schmüser, M. Dohlus, and J. Rossbach, Ultraviolet and Soft X-Ray Free-Electron Lasers: Introduction to Physical Principles, Experimental Results, Technological Challenges, 1st. Springer Publishing Company, Incorporated, 2008.

[196] T. Shintake, Review of the worldwide SASE FEL development, in *2007 IEEE Particle Accelerator Conference (PAC)*, 2007, pp. 89–93.

[197] J. P. Berthet, F. Glotin, J. M. Ortega, and W. Salah, Beam adaptation at the infrared FEL CLIO, *EPAC 2006 - Contributions to the Proceedings*, pp. 56–58, 2006.

[198] J. M. Klopf, M. Helm, S. C. Kehr, U. Lehnert, P. Michell, A. Pashkin, H. Schneider, W. Seide, S. Winnerl, and S. Zvyagin, FELBE-Upgrades and Status of the IRlTHz FEL User Facility at HZDR, *International Conference on Infrared, Millimeter, and Terahertz Waves, IRMMW-THz*, pp. 9–10, 2018.

[199] W. J. Van Der Zande, R. T. Jongma, L. Van Der Meer, and B. Redlich, FELIX facility: Free electron laser light sources from 0.2 to 75 THz, *International Conference on Infrared, Millimeter, and Terahertz Waves, IRMMW-THz*, pp. 3–4, 2013.

[200] A. Aksoy, Kaya, Karsli, B. Koç, and F. Elçim, Current status of free electron laser @ tarla, *Proceedings of the 39th International Free-Electron Laser Conference, FEL 2019*, pp. 102–105, 2019.

[201] M. Svandrlik, E. Allaria, F. Bencivenga, C. Callegari, F. Capotondi, D. Castronovo, P. Cinquegrana, I. Cudin, M. Dal Forno, M. B. Danailov, G. D'auria, R. De Monte, G. De Ninno, A. Demidovich, S. Di Mitri, B. Diviacco, A. Fabris, R. Fabris, W. M. Fawley, M. Ferianis, E. Ferrari, P. Finetti, L. Froehlich, P. F. Radivo, G. Gaio, L. Giannessi, M. Kiskinova, G. Loda, M. Lonza, N. Mahne, C. Masciovecchio, F. Parmigiani, G. Penco, O. Plekan, M. Predonzani, E. Principi, L. Raimondi, F. Rossi, L. Rumiz, C. Scafuri, C. Serpico, P. Sigalotti, S. Spampinati, C. Spezzani, L. Sturari, C. Svetina, M. Trovo', A. Vascotto, M. Veronese, R. Visintini, D. Zangrando, M. Zangrando, B. Mahieu, and P. Craievich, Fermi seeded FEL progress report, *IPAC 2013: Proceedings of the 4th International Particle Accelerator Conference*, pp. 1182–1184, 2013.

[202] S. Schreiber, B. Faatz, J. Feldhaus, K. Honkavaara, and R. Treusch, FEL user facility FLASH, *IPAC 2010 - 1st International Particle Accelerator Conference*, pp. 2149–2151, 2010.

[203] M. Scholz, FEL Performance Achieved at the European XFEL, *9th International Particle Accelerator Conference*, pp. 29–33, 2018.

[204] F. Curbis, S. Werin, M. Eriksson, and P. Johnsson, Towards an X-ray FEL at the MAX IV laboratory, *Proceedings of the 36th International Free Electron Laser Conference, FEL 2014*, pp. 549–552, 2014.

[205] V. Schlott, V. Arsov, M. Baldinger, R. Baldinger, G. Bonderer, M. Dehler, R. Ditter, D. Engeler, S. Hunziker, R. Ischebeck, M. Kaiser, B. Keil, W. Koprek, R. Kramert, F. Marcellini, G. Orlandi, C. O. Loch, P. Pollet, M. Roggli, M. Rohrer, A. Romann, M. Stadler, and D. Treyer, Overview and Status of SWISSFEL Diagnostics, *Proceedings of IBIC2015*, pp. 12–16, 2015.

[206] K. Szamota-Leandersson, R. Nietubyc, P. Czuma, P. Krawczyk, J. Krzywinski, J. Sekutowicz, M. Staszczak, J. Szewinski, W. Bal, J. Poznanski, A. Bartnik, H. Fiedorowicz, K. Janulewicz, and N. Palka, Polfel - New facility in Poland, *Proceedings of the 39th International Free-Electron Laser Conference, FEL 2019*, pp. 746–748, 2019.

[207] G. S. Edwards, R. H. Austin, F. E. Carroll, M. L. Copeland, M. E. Couprie, W. E. Gabella, R. F. Huglund, B. A. Hooper, M. S. Hutson, E. D. Jansen, K. M. Joos, D. P. Kiehart, I. Lindau, J. Miao, H. S. Pratisto, J. H. Shen, Y. Tokutake, A. F. Van der Meer, and A. Xie, Free-electron-laser-based biophysical and biomedical instrumentation, *Review of Scientific Instruments*, vol. 74, no. 7, pp. 3207–3245, 2003.

[208] R. Whitney, D. Douglas, and G. Neil, Airborne megawatt class free-electron laser for defense and security, in *Proc.SPIE*, vol. 5792, 2005.

[209] D. Oepts, A. F. G. Vandermeer, and P. W. Vanamersfoort, The Free-Electron-Laser User Facility FELIX, *Infrared Phys. Technol.*, vol. 36, no. 1, pp. 297–308, 1995.

[210] P. Phase and R. Condition, Ponderomotive Phase and Resonance Condition, pp. 1–45, 2018.

[211] B. D. Patterson and R. Abela, Novel opportunities for time-resolved absorption spectroscopy at the X-ray free electron laser, *Phys. Chem. Chem. Phys.*, vol. 12, no. 21, pp. 5647–5652, 2010.

[212] FELIX-Operating-Principle, Https://www.ru.nl/felix/about-felix/about-felix/fel-operating-principle/, Sep. 2020.

[213] R. Warmuth, 1,2-Didehydrobenzol: Ein gespanntes Alkin oder ein Cumulen? — NMR-spektroskopische Charakterisierung in einem molekularen Container, *Angewandte Chemie*, vol. 109, no. 12, pp. 1406–1409, 1997.

[214] H. H. Wenk, M. Winkler, and W. Sander, 100 Jahre Didehydroaromaten, *Angewandte Chemie*, vol. 115, no. 5, pp. 518–546, 2003.

[215] H. Pellissier and M. Santelli, The use of arynes in organic synthesis, *Tetrahedron*, no. 59, pp. 701–730, 2003.

[216] O. L. Chapman, K. Mattes, C. L. Mcintosh, J. Pacansky, G. V. Calder, and G. Orr, Benzyne, *Journal of the American Chemical Society*, vol. 95, no. 18, pp. 6134–6135, 1973.

[217] I. R. Dunkin and J. G. MacDonald, Matrix photolysis of unsaturated cyclic anhydrides and the infrared spectrum of tetradeuteriobenzyne, *Journal of the Chemical Society, Chemical Communications*, no. 17, pp. 772–773, 1979.

[218] C. Wentrup, R. Blanch, H. Briehl, and G. Gross, Benzyne, Cyclohexyne, and 3-Azacyclohexyne and the Problem of Cycloalkyne versus Cycloalkylideneketene Genesis, *Journal of the American Chemical Society*, vol. 110, no. 6, pp. 1874–1880, 1988.

[219] J. G. Radziszewski, B. A. Hess, and R. Zahradnik, Infrared Spectrum of o-Benzyne: Experiment and Theory, *Journal of the American Chemical Society*, vol. 114, no. 1, pp. 52–57, 1992.

[220] S. G. Kukolich, M. C. McCarthy, and P. Thaddeus, Molecular Structure of o-Benzyne from Microwave Measurements, *J. Phys. Chem. A*, vol. 108, no. 14, pp. 2645–2651, 2004.

[221] E. G. Robertson, P. D. Godfrey, and D. McNaughton, The microwave spectrum of o-benzyne measured in a novel Stark modulated spectrometer for transient molecules, *Journal of Molecular Spectroscopy*, vol. 217, no. 1, pp. 123–126, 2003.

[222] X. Zhang and P. Chen, Photoelectron Spectrum of o-Benzyne. Ionization Potentials as a Measure of Singlet-Triplet Gaps, *Journal of the American Chemical Society*, vol. 114, no. 8, pp. 3147–3148, 1992.

[223] P. G. Wenthold, R. R. Squires, and W. C. Lineberger, Ultraviolet Photoelectron Spectroscopy of the o-, m-, and p-Benzyne Negative Ions. Electron Affinities and Singlet-Triplet Splittings for o-, m-, and p-Benzyne, *J. Am. Chem. Soc.*, vol. 120, pp. 5279–5290, 1998.

[224] F. Zhang, D. Parker, Y. S. Kim, R. I. Kaiser, and A. M. Mebel, On the Formation of ortho-Benzyne (o-C6H4) under Single-Collision Conditions and its Role in Interstellar Chemistry, *Ap.J.*, vol. 728, p. 141, 2011.

[225] X. Zhang, A. T. MacCarone, M. R. Nimlos, S. Kato, V. M. Bierbaum, G. B. Ellison, B. Ruscic, A. C. Simmonett, W. D. Allen, and H. F. Schaefer,

Unimolecular thermal fragmentation of ortho-benzyne, *Journal of Chemical Physics*, vol. 126, no. 4, 2007.

[226] C. Xu, M. Braun-Unkhoff, C. Naumann, and P. Frank, A shock tube investigation of H atom production from the thermal dissociation of ortho-benzyne radicals, *Proceedings of the Combustion Institute*, vol. 31, no. 1, pp. 231–239, 2007.

[227] J. Cernicharo, A. M. Heras, A. G. G. M. Tielens, J. R. Pardo, F. Herpin, M. Guélin, and L. B. F. M. Waters, Infrared Space Observatory's Discovery of C4H2, C6H2, and Benzene in CRL 618, *The Astrophysical Journal*, vol. 546, no. 2, pp. L123–L126, 2001.

[228] S. L. W. Weaver, A. J. Remijan, R. J. McMahon, and B. J. McCall, A Search for ortho-benzyne (o-C6H4) in CRL 618, *ApJ*, vol. 671, no. 2, pp. L153–L156, 2007.

[229] F. Hirsch, E. Reusch, P. Constantinidis, I. Fischer, S. Bakels, A. M. Rijs, and P. Hemberger, Self-Reaction of Ortho-Benzyne at High Temperatures Investigated by Infrared and Photoelectron Spectroscopy, *J. Phys. Chem. A*, vol. 122, no. 49, pp. 9563–9571, 2018.

[230] A. Comandini and K. Brezinsky, Theoretical study of the formation of naphthalene from the radical/π-bond addition between single-ring aromatic hydrocarbons, *Journal of Physical Chemistry A*, vol. 115, no. 22, pp. 5547–5559, 2011.

[231] R. Nyquist and W. Potts, Infrared absorptions characteristic of the terminal acetylenic group (-CC-H), *Spectrochimica Acta*, vol. 16, no. 4, pp. 419–427, 1960.

[232] P. Constantinidis, F. Hirsch, I. Fischer, A. Dey, and A. Rijs, Products of the Propargyl Self-Reaction at High Temperatures Investigated by IR/UV Ion Dip Spectroscopy, *Journal of Physical Chemistry A*, vol. 121, no. 1, 2017.

[233] J. Evans and R. Nyquist, The vibrational spectra and vibrational assignments of the propargyl halides, *Spectrochimica Acta*, vol. 19, no. 7, pp. 1153–1163, 1963.

[234] G. Friedrichs, E. Goos, J. Gripp, H. Nicken, J.-B. Schönborn, H. Vogel, and F. Temps, The Products of the Reactions of o-Benzyne with Ethene, Propene, and Acetylene: A Combined Mass Spectrometric and Quantum Chemical Study. *Z. Phys. Chem.*, vol. 223, pp. 387–407, 2009.

[235] M. E. Schafer and R. S. Berry, The Dimerization of Gaseous Benzyne, *Journal of the American Chemical Society*, vol. 87, no. 20, pp. 4497–4501, 1965.

[236] C. Wentrup, The Benzyne Story, *Aust. J. Chem.*, vol. 63, pp. 979–986, 2010.

[237] T. W. Schmidt, The electronic spectroscopy of resonancestabilised hydrocarbon radicals, *Int. Rev. Phys. Chem.*, vol. 35, no. 2, pp. 209–242, 2016.

[238] G. Kalghatgi, R. Head, J. Chang, Y. Viollet, H. Babiker, and A. Amer, An Alternative Method Based on Toluene/n-Heptane Surrogate Fuels for Rating the Anti-Knock Quality of Practical Gasolines, *SAE International Journal of Fuels and Lubricants*, vol. 7, no. 3, pp. 663–672, 2014.

[239] G. Kalghatgi, H. Babiker, and J. Badra, A Simple Method to Predict Knock Using Toluene, N-Heptane and Iso-Octane Blends (TPRF) as Gasoline Surrogates, *SAE International Journal of Engines*, vol. 8, no. 2, pp. 505–519, 2015.

[240] F. Hirsch, P. Constantinidis, I. Fischer, S. Bakels, and A. M. Rijs, Dimerization of the Benzyl Radical in a High-Temperature Pyrolysis Reactor Investigated by IR/UV Ion Dip Spectroscopy, *Chemistry - A European Journal*, vol. 24, no. 30, pp. 7647–7652, 2018.

[241] M. Margraf, B. Noller, C. Schroter, T. Schultz, and I. Fischer, Time- and frequency-resolved photoionization of the C (2)A(2) state of the benzyl radical, C7H7, *Journal of Chemical Physics*, vol. 133, no. 7, 2010.

[242] A. Röder, A. Humeniuk, J. Giegerich, I. Fischer, L. Poisson, and R. Mitrić, Femtosecond Time-Resolved Photoelectron Spectroscopy of the Benzyl Radical, *Phys. Chem. Chem. Phys.*, vol. 19, no. 19, pp. 12 365–12 374, 2017.

[243] J. D. Savee, J. Zador, P. Hemberger, B. Sztaray, A. Bodi, and D. L. Osborn, Threshold photoelectron spectrum of the benzyl radical, *Molecular Physics*, vol. 113, no. 15-16, pp. 2217–2227, 2015.

[244] G. T. Buckingham, T. K. Ormond, J. P. Porterfield, P. Hemberger, O. Kostko, M. Ahmed, D. J. Robichaud, M. R. Nimlos, J. W. Daily, and G. Barney Ellison, The thermal decomposition of the benzyl radical in a heated micro-reactor. I. Experimental findings, *Journal of Chemical Physics*, vol. 142, no. 4, 2015.

[245] R. G. Satink, G. Meijer, and G. Von Helden, Infrared Spectroscopy of Neutral C7H7 Isomers: Benzyl and Tropyl, *Journal of the American Chemical Society*, vol. 125, no. 51, pp. 15 714–15 715, 2003.

[246] M. Shapero, N. C. Cole-Filipiak, C. Haibach-Morris, and D. M. Neumark, Benzyl Radical Photodissociation Dynamics at 248 nm, *Journal of Physical Chemistry A*, vol. 119, no. 50, pp. 12 349–12 356, 2015.

[247] Y. Song, X. F. Zheng, M. Lucas, and J. S. Zhang, Ultraviolet photodissociation dynamics of the benzyl radical, *Physical Chemistry Chemical Physics*, vol. 13, no. 18, pp. 8296–8305, 2011.

[248] Y. Li, L. Zhang, Z. Tian, T. Yuan, J. Wang, B. Yang, and F. Qi, Experimental Study of a Fuel-Rich Premixed Toluene Flame at Low Pressure, *Energy & Fuels*, vol. 23, no. 3, pp. 1473–1485, 2009.

[249] B. Shukla, A. Susa, A. Miyoshi, and M. Koshi, In Situ direct sampling mass spectrometric study on formation of polycyclic aromatic hydrocarbons in toluene pyrolysis, *Journal of Physical Chemistry A*, vol. 111, no. 34, pp. 8308–8324, 2007.

[250] P. M. Ivanov, The torsional energy profile of 1,2-diphenylethane: An ab initio study, *Journal of Molecular Structure*, vol. 415, no. 1-2, pp. 179–186, 1997.

[251] C. Latouche and V. Barone, Computational chemistry meets experiments for explaining the behavior of bibenzyl: A thermochemical and spectroscopic (infrared, Raman, and NMR) investigation, *Journal of Chemical Theory and Computation*, vol. 10, no. 12, pp. 5586–5592, 2014.

[252] S. Sinha and A. Raj, Polycyclic aromatic hydrocarbon (PAH) formation from benzyl radicals: A reaction kinetics study, *Phys. Chem. Chem. Phys.*, vol. 18, no. 11, pp. 8120–8131, 2016.

[253] K. Luther, K. Oum, K. Sekiguchi, and J. Troe, Recombination of benzyl radicals: Dependence on the bath gas, temperature, and pressure, *Physical Chemistry Chemical Physics*, vol. 6, no. 16, pp. 4133–4141, 2004.

[254] A. A. Boyd, B. Noziere, and R. Lesclaux, Kinetics and Thermochemistry of the Reversible Combination Reactions of the Allyl and Benzyl Radicals with NO, *The Journal of Physical Chemistry*, vol. 99, no. 27, pp. 10 815–10 823, 1995.

[255] D. C. Astholz, J. Durant, and J. Troe, Thermal decomposition of toluene and of benzyl radicals in shock waves, *Symposium (International) on Combustion*, vol. 18, no. 1, pp. 885–892, 1981.

[256] A. Matsugi and A. Miyoshi, Kinetics of the self-reactions of benzyl and o-xylyl radicals studied by cavity ring-down spectroscopy, *Chemical Physics Letters*, vol. 521, pp. 26–30, 2012.

[257] R. D. Burkhart, Absolute rate constants for the bimolecular reaction of radical pairs in solution. Benzyl and pentyl radicals, *Journal of the American Chemical Society*, vol. 90, no. 2, pp. 273–277, 1968.

[258] H. Hippler and J. Troe, Thermodynamic properties of benzyl radicals: Enthalpy of formation from toluene, benzyl iodide, and dibenzyl dissociation equilibria, *The Journal of Physical Chemistry*, vol. 94, no. 9, pp. 3803–3806, 1990.

[259] J. Jones, G. B. Bacskay, and J. C. Mackie, Decomposition of the Benzyl Radical: Quantum Chemical and Experimental (Shock Tube) Investigations of Reaction Pathways, *The Journal of Physical Chemistry A*, vol. 101, no. 38, pp. 7105–7113, 1997.

[260] W. Mueller-Markgraf and J. Troe, Thermal decomposition of benzyl iodide and of benzyl radicals in shock waves, *The Journal of Physical Chemistry*, vol. 92, no. 17, pp. 4899–4905, 1988.

[261] Y. Li, J. Cai, L. Zhang, T. Yuan, K. Zhang, and F. Qi, Investigation on chemical structures of premixed toluene flames at low pressure, *Proceedings of the Combustion Institute*, vol. 33, no. 1, pp. 593–600, 2011.

[262] M. Tenenbein, Leaded Gasoline Abuse: The Role of Tetraethyl Lead, *Hum. Exp. Toxicol.*, no. 16, pp. 217–222, 1997.

[263] M. P. Walsh, The Global Experience with Lead in Gasoline and the Lessons we Should Apply to the Use of MMT, *Am J Ind Med*, vol. 50, no. 11, pp. 853–860, 2007.

[264] V. Simon, M. Baer, L. Torres, S. Olivier, M. Meybeck, and J. P. Della Massa, The Impact of Reduction in the Benzene Limit Value in Gasoline on Airborne Benzene, Toluene and Xylenes Levels, *Sci. Total Environ.*, vol. 334-335, pp. 177–183, 2004.

[265] M. Talibi, P. Hellier, and N. Ladommatos, Impact of Increasing Methyl Branches in Aromatic Hydrocarbons on Diesel Engine Combustion and Emissions, *Fuel*, vol. 216, pp. 579–588, 2018.

[266] T. C. Zhang, L. D. Zhang, X. Hong, K. W. Zhang, F. Qi, C. K. Law, T. H. Ye, P. H. Zhao, and Y. L. Chen, An experimental and theoretical study

of toluene pyrolysis with tunable synchrotron VUV photoionization and molecular-beam mass spectrometry, *Comb. Flame*, vol. 156, no. 11, pp. 2071–2083, 2009.

[267] R. Bounaceur, I. Da Costa, R. Fournet, F. Billaud, and F. Battin-Leclerc, Experimental and Modeling Study of the Oxidation of Toluene, *Int. J. Chem. Kinet.*, vol. 37, no. 1, pp. 25–49, 2005.

[268] G. Porter and E. Strachan, The Electronic Spectra of Benzyl, *Spectrochim. Acta*, vol. 12, no. 4, pp. 299–304, 1958.

[269] L. Grajcar and S. Leach, Analyse du Spectre d'Emission du Radical Benzyle et de Certains Isotoped Deuteres, *J. Chim. Phys.*, vol. 61, no. 11-2, pp. 1523–1530, 1964.

[270] G. C. Eiden and J. C. Weisshaar, Adiabatic ionization potential of benzyl radical by two-color resonant two-photon ionization, *J. Phys. Chem.*, vol. 95, no. 16, pp. 6194–6197, 1991.

[271] G. C. Eiden, F. Weinhold, and J. C. Weisshaar, Photoelectron spectroscopy of free radicals with cm-1 resolution: The benzyl cation, *J. Chem. Phys.*, vol. 95, no. 11, pp. 8665–8668, 1991.

[272] M. Fukushima and K. Obi, Dispersed Fluorescence Spectra from SIngle Vibronic Levels of the Benzyl Radical Observed in a Pulsed Discharge Jet, *Chem. Phys. Lett.*, vol. 242, no. 4-5, pp. 443–448, 1995.

[273] M. Steglich, G. Knopp, and P. Hemberger, How the Methyl Group Position Influences the Ultrafast Deactivation in Aromatic Radicals, *Phys Chem Chem Phys*, vol. 21, no. 2, pp. 581–588, 2019.

[274] C. Cossart-Magos, D. Cossart, and S. Leach, Rotational Contour Analysis of the Electronic Origin Band in the Emission Spectrum of the Orthoxylyl Radical at 4683 A, *Chem. Phys.*, vol. 1, pp. 306–312, 1973.

[275] T.-Y. D. Li, X.-Q. Tan, T. M. Cerny, J. M. Williamson, D. W. Cullin, and T. A. Miller, High-Resolution Fluorescence Excitation Spectra of Jet-Cooled Benzyl and p-Methylbenzyl Radicals, *Chem. Phys.*, vol. 167, pp. 203–214, 1992.

[276] J. I. Selco and P. G. Carrick, Jet-cooled Emission Spectra of Xylyl Radicals, *J. Molec. Spectrosc.*, vol. 173, pp. 277–295, 1995.

[277] M. H. Suh, S. K. Lee, and T. A. Miller, Vibronic Emission Spectrum of p-Xylyl Radical, *J Mol Spectrosc*, vol. 194, no. 2, pp. 211–218, 1999.

[278] L. S. Choi and S. K. Lee, Analysis of Rotionally Colled Vibronic Emission Spectra of m-Xylyl Radical, *Bull. Korean Chem. Soc.*, vol. 17, no. 8, p. 749, 1996.

[279] ——, Visible Emission Spectra of o-Xylyl Radical, *Bull. Korean Chem. Soc.*, vol. 16, no. 3, p. 281, 1995.

[280] T.-Y. D. Lin and T. A. Miller, Measurement of Methyl Torsional Barriers in the Ground and Excited States of the o-,m-,and p-Methylbenzyl Radicals, *J. Phys. Chem.*, vol. 94, pp. 3554–3559, 1990.

[281] P. Hemberger, A. J. Trevitt, T. Gerber, E. Ross, and G. da Silva, Isomer-specific product detection of gas-phase xylyl radical rearrangement and decomposition using VUV synchrotron photoionization, *Journal of Physical Chemistry A*, vol. 118, no. 20, pp. 3593–3604, 2014.

[282] P. Hemberger, A. J. Trevitt, E. Ross, and G. da Silva, Direct observation of para-xylylene as the decomposition product of the meta-xylyl radical using VUV synchrotron radiation, *Journal of Physical Chemistry Letters*, vol. 4, no. 15, pp. 2546–2550, 2013.

[283] M. Steglich, A. Bodi, J. P. Maier, and P. Hemberger, Probing Different Spin States in Xylyl Radicals and Ions, *Phys. Chem. Chem. Phys.*, vol. 20, no. 10, pp. 7180–7189, 2018.

[284] K. Pachner, M. Steglich, P. Hemberger, and I. Fischer, Photodissociation Dynamics of the Ortho- and Para-Xylyl Radicals, *J Chem Phys*, vol. 147, no. 8, p. 84 303, 2017.

[285] F. Hirsch, M. Flock, I. Fischer, S. Bakels, and A. M. Rijs, The Gas-Phase Infrared Spectra of Xylyl Radicals, *Journal of Physical Chemistry A*, vol. 123, no. 44, pp. 9573–9578, 2019.

[286] N. J. Reilly, G. da Silva, C. M. Wilcox, Z. Ge, D. L. Kokkin, T. P. Troy, K. Nauta, S. H. Kable, M. C. McCarthy, and T. W. Schmidt, Interconversion of Methyltropyl and Xylyl Radicals: A Pathway Unavailable to the Benzyl–Tropyl Rearrangement, *The Journal of Physical Chemistry A*, vol. 122, no. 5, pp. 1261–1269, 2018.

[287] T. Stuyver, B. Chen, T. Zeng, P. Geerlings, F. De Proft, and R. Hoffmann, Do Diradicals Behave Like Radicals? *Chemical Reviews*, vol. 119, no. 21, pp. 11 291–11 351, 2019.

[288] M. Abe, Diradicals, *Chemical Reviews*, vol. 113, no. 9, pp. 7011–7088, 2013.

[289] G. da Silva, E. E. Moore, and J. W. Bozzelli, Decomposition of Methylbenzyl Radicals in the Pyrolysis and Oxidation of Xylenes, *J Phys Chem A*, vol. 113, no. 38, pp. 10 264–10 278, 2009.

[290] G. da Silva and J. W. Bozzelli, On the reactivity of methylbenzenes, *Combustion and Flame*, vol. 157, no. 11, pp. 2175–2183, 2010.

[291] R. Marquardt, W. Sander, T. Laue, and H. Hopf, 1,4-dicarbonyl-2,5-cyclohexadiene, *Liebigs Annalen*, vol. 1995, no. 9, pp. 1643–1648, 1995.

[292] ——, Photochemistry of [2.2]Paracyclophan-enes — a Matrix-Isolation Study, *Liebigs Annalen*, vol. 1996, no. 12, pp. 2039–2043, 1996.

[293] P. Neuhaus, D. Grote, and W. Sander, Matrix Isolation, Spectroscopic Characterization, and Photoisomerization of m-Xylylene, *Journal of the American Chemical Society*, vol. 130, no. 10, pp. 2993–3000, 2008.

[294] M. Steglich, V. B. Custodis, A. J. Trevitt, G. da Silva, A. Bodi, and P. Hemberger, Photoelectron Spectrum and Energetics of the meta-Xylylene Diradical, *Journal of the American Chemical Society*, vol. 139, no. 41, pp. 14 348–14 351, 2017.

[295] A. Röder, J. Petersen, K. Issler, I. Fischer, R. Mitrić, and L. Poisson, Exploring the Excited-State Dynamics of Hydrocarbon Radicals, Biradicals, and Carbenes Using Time-Resolved Photoelectron Spectroscopy and Field-Induced Surface Hopping Simulations, *The Journal of Physical Chemistry A*, vol. 123, no. 50, pp. 10 643–10 662, 2019.

[296] A. K. Lemmens, D. B. Rap, J. M. M. Thunnissen, C. J. Mackie, A. Candian, A. G. G. M. Tielens, A. M. Rijs, and W. J. Buma, Anharmonicity in the mid-infrared spectra of polycyclic aromatic hydrocarbons: Molecular beam spectroscopy and calculations, *A&A*, vol. 628, 2019.

[297] D. Gregory, R. A. Jackson, and P. J. Bennett, Mechanisms for the formation of exhaust hydrocarbons in a single cylinder spark-ignition engine, fueled with deuterium-labeled ortho-, meta- and para-xylene, *Combustion and Flame*, vol. 118, no. 3, pp. 459–468, 1999.

[298] O. L. Chapman, U. p. E. Tsou, and J. W. Johnson, Thermal Isomerization of Benzocyclobutene, *Journal of the American Chemical Society*, vol. 109, no. 2, pp. 553–559, 1987.

[299] O. L. Chapman, J. W. Johnson, R. J. McMahon, and P. R. West, Rearrangements of the isomeric tolylmethylenes, *Journal of the American Chemical Society*, vol. 110, no. 2, pp. 501–509, 1988.

[300] F. Vögtle, Cyclophan-Chemie, 1st ed. Vieweg+Teubner Verlag, 1990.

[301] H. H. Gleiter and Rolf, Modern Cyclophane Chemistry. Wiley-VCH, 2004.

[302] S. Kotha, M. E. Shirbhate, and G. T. Waghule, Selected synthetic strategies to cyclophanes, *Beilstein Journal of Organic Chemistry*, vol. 11, pp. 1274–1331, 2015.

[303] V. Bökelheide and R. W. Griffin, Synthesis of [2.2]Metacyclophanes, *Journal of Organic Chemistry*, vol. 34, no. 6, pp. 1960–1961, 1969.

[304] J. A. Syage, F. Al Adel, and A. H. Zewail, Jet-cooled styrene: Spectra and isomerization, *Chemical Physics Letters*, vol. 103, no. 1, pp. 15–22, 1983.

[305] D. G. Leopold, R. J. Hemley, V. Vaida, and J. L. Roebber, Direct absorption spectra of higher excited states of jet-cooled monosubstituted benzenes: Phenylacetylene, styrene, benzaldehyde, and acetophenone, *The Journal of Chemical Physics*, vol. 75, no. 10, pp. 4758–4769, 1981.

[306] M. de Groot and W. J. Buma, Vibronic spectra of the lower excited singlet states of styrene: A Time Dependent Density Functional Theory study, *Chemical Physics Letters*, vol. 435, no. 4, pp. 224–229, 2007.

[307] M. W. Wong and C. Wentrup, Interconversions of Phenylcarbene, Cycloheptatetraene, Fulvenallene, and Benzocyclopropene. A Theoretical Study of the C7H6 Energy Surface, *The Journal of Organic Chemistry*, vol. 61, no. 20, pp. 7022–7029, 1996.

[308] D. Polino, A. Famulari, and C. Cavallotti, Analysis of the Reactivity on the C7H6 Potential Energy Surface, *The Journal of Physical Chemistry A*, vol. 115, no. 27, pp. 7928–7936, 2011.

[309] D. Polino and C. Cavallotti, Fulvenallene Decomposition Kinetics, *The Journal of Physical Chemistry A*, vol. 115, no. 37, pp. 10 281–10 289, 2011.

[310] C. Cavallotti, M. Derudi, and R. Rota, On the mechanism of decomposition of the benzyl radical, *Proceedings of the Combustion Institute*, vol. 32 I, no. 1, pp. 115–121, 2009.

[311] G. da Silva, J. A. Cole, and J. W. Bozzelli, Thermal decomposition of the benzyl radical to fulvenallene (C 7H 6) + H, *Journal of Physical Chemistry A*, vol. 113, no. 21, pp. 6111–6120, 2009.

[312] M. Derudi, D. Polino, and C. Cavallotti, Toluene and benzyl decomposition mechanisms: Elementary reactions and kinetic simulations, *Physical Chemistry Chemical Physics*, vol. 13, no. 48, pp. 21 308–21 318, 2011.

[313] G. da Silva and A. J. Trevitt, Chemically activated reactions on the C7H5 energy surface: Propargyl plus diacetylene, i-C5H3 + acetylene, and n-C5H3 + acetylene, *Phys. Chem. Chem. Phys.*, vol. 13, no. 19, pp. 8940–8952, 2011.

[314] G. da Silva and J. W. Bozzelli, The C7H5 fulvenallenyl radical as a combustion intermediate: Potential new pathways to two- and three-ring PAHs, *Journal of Physical Chemistry A*, vol. 113, no. 44, pp. 12 045–12 048, 2009.

[315] C. He, A. M. Thomas, G. R. Galimova, A. N. Morozov, A. M. Mebel, and R. I. Kaiser, Gas-Phase Formation of Fulvenallene (C7H6) via the Jahn-Teller Distorted Tropyl (C7H7) Radical Intermediate under Single-Collision Conditions, *Journal of the American Chemical Society*, vol. 142, no. 6, pp. 3205–3213, 2020.

[316] J. Thapa, M. Spencer, N. G. Akhmedov, and F. Goulay, Kinetics of the OH Radical Reaction with Fulvenallene from 298 to 450 K, *Journal of Physical Chemistry Letters*, vol. 6, no. 24, pp. 4997–5001, 2015.

[317] C. Angell, The vapor-phase infrared spectrum and structure of fulvenallene, *Journal of Molecular Structure*, vol. 10, no. 2, pp. 265–273, 1971.

[318] A. R. Brown, J. T. Brice, P. R. Franke, and G. E. Douberly, Infrared Spectrum of Fulvenallene and Fulvenallenyl in Helium Droplets, *Journal of Physical Chemistry A*, vol. 123, no. 17, pp. 3782–3792, 2019.

[319] G. da Silva, Reaction of benzene with atomic carbon: Pathways to fulvenallene and the fulvenallenyl radical in extraterrestrial atmospheres and the interstellar medium, *Journal of Physical Chemistry A*, vol. 118, no. 22, pp. 3967–3972, 2014.

[320] J. Giegerich and I. Fischer, Photodissociation dynamics of fulvenallene, C7H6, *Physical Chemistry Chemical Physics*, vol. 15, no. 31, pp. 13 162–13 168, 2013.

[321] I. A. Ramphal, M. Shapero, C. Haibach-Morris, and D. M. Neumark, Photodissociation dynamics of fulvenallene and the fulvenallenyl radical at 248 and 193 nm, *Physical Chemistry Chemical Physics*, vol. 19, no. 43, pp. 29 305–29 314, 2017.

[322] A. Chakraborty, J. Fulara, and J. P. Maier, The Electronic Spectrum of the Fulvenallenyl Radical, *Angewandte Chemie - International Edition*, vol. 55, no. 1, pp. 228–231, 2016.

[323] M. Steinbauer, P. Hemberger, I. Fischer, and A. Bodi, Photoionization of C7H6 and C7H5: Observation of the fulvenallenyl radical, *ChemPhysChem*, vol. 12, pp. 1795–1797, 2011.

[324] G. da Silva, J. A. Cole, and J. W. Bozzelli, Kinetics of the cyclopentadienyl + Acetylene, fulvenallene + H, and 1-Ethynylcyclopentadiene + H reactions, *Journal of Physical Chemistry A*, vol. 114, no. 6, pp. 2275–2283, 2010.

[325] P. Linstrom and W. Mallard, NIST Chemistry WebBook, NIST Standard Reference Database Number 69. Gaithersburg MD: National Institute of Standards and Technology, 2021.

[326] P. Lindstedt, L. Maurice, and M. Meyer, Thermodynamic and kinetic issues in the formation and oxidation of aromatic species, *Faraday Discussions*, vol. 119, pp. 409–432, 2001.

[327] M. B. Colket, R. J. Hall, and M. D. Smooke, Mechanistic Models of Soot Formation, *UTCR Report*, pp. 1–14, 1994.

[328] G. da Silva and J. W. Bozzelli, Indene Formation from Alkylated Aromatics: Kinetics and Products of the Fulvenallene + Acetylene Reaction, *The Journal of Physical Chemistry A*, vol. 113, no. 31, pp. 8971–8978, 2009.

[329] L. K. Madden, A. M. Mebel, M. C. Lin, and C. F. Melius, Theoretical study of the thermal isomerization of fulvene to benzene, *Journal of Physical Organic Chemistry*, vol. 9, no. 12, pp. 801–810, 1996.

[330] V. V. Kislov and A. M. Mebel, The Formation of Naphthalene, Azulene, and Fulvalene from Cyclic C5 Species in Combustion: An Ab Initio/RRKM Study of 9-H-Fulvalenyl (C5H5C5H4) Radical Rearrangements, *The Journal of Physical Chemistry A*, vol. 111, no. 38, pp. 9532–9543, 2007.

[331] N. Marinov, W. Pitz, C. Westbrook, A. Lutz, A. Vincitore, and S. Senkan, Chemical kinetic modeling of a methane opposed-flow diffusion flame and comparison to experiments, *Twenty-Seventh Sysposium (International) on Combustion Volume One*, vol. 27, no. 1, pp. 605–613, 1998.

[332] R. Sivaramakrishnan, R. S. Tranter, and K. Brezinsky, High Pressure Pyrolysis of Toluene. 1. Experiments and Modeling of Toluene Decomposition, *The Journal of Physical Chemistry A*, vol. 110, no. 30, pp. 9388–9399, 2006.

[333] L. Vereecken and J. Peeters, Reactions of chemically activated C9H9 species II: The reaction of phenyl radicals with allene and cyclopropene, and of benzyl radicals with acetylene, *Phys. Chem. Chem. Phys.*, vol. 5, no. 13, pp. 2807–2817, 2003.

[334] C. F. Melius, M. E. Colvin, N. M. Marinov, W. J. Pit, and S. M. Senkan, Reaction mechanisms in aromatic hydrocarbon formation involving the C5H5 cyclopentadienyl moiety, *Symposium (International) on Combustion*, vol. 26, no. 1, pp. 685–692, 1996.

List of Tables

List of Figures

Chapter A

Appendix

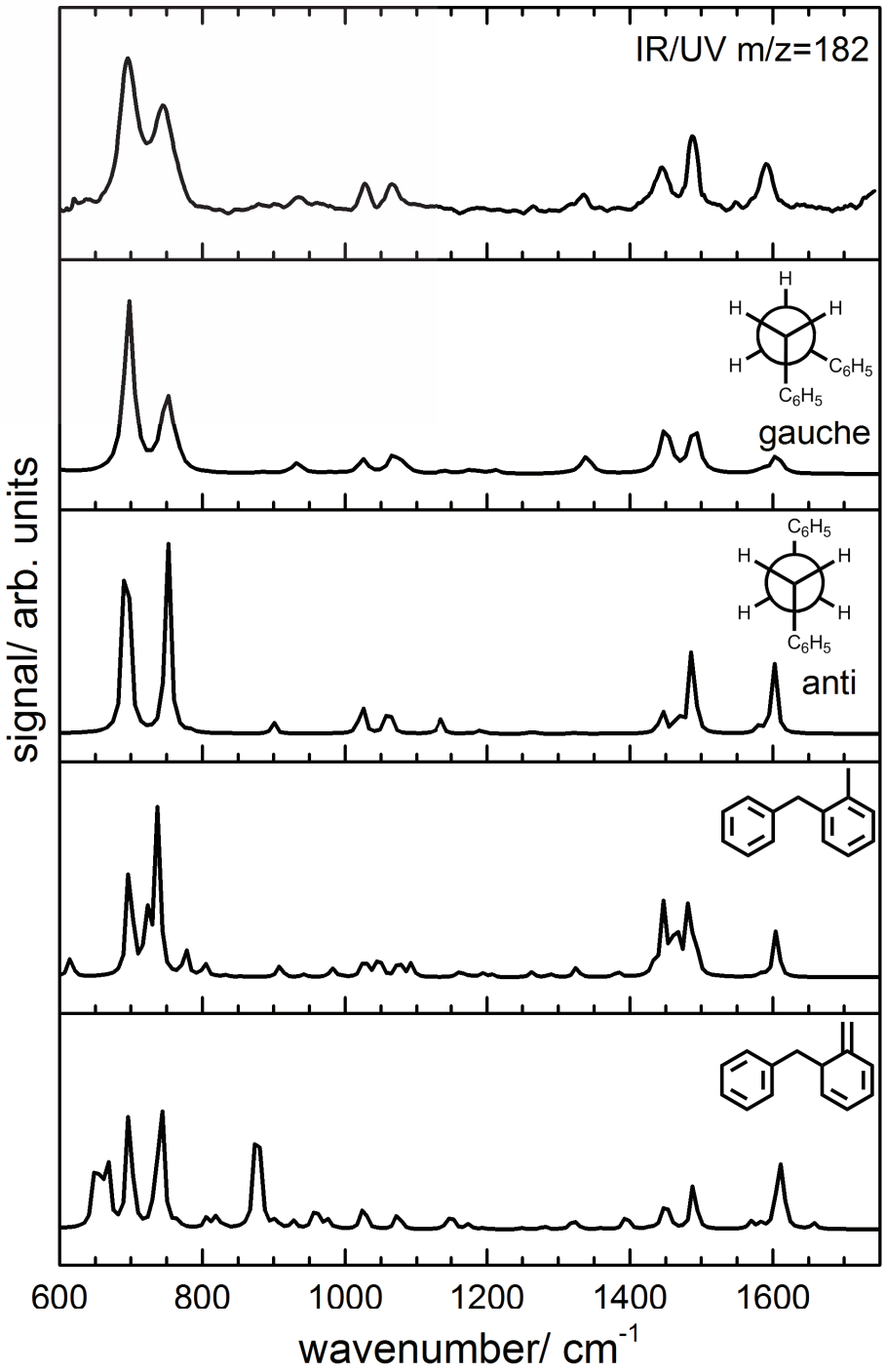

Figure A.1: Additional DFT calculations for m/z=182 from the benzyl experiments I.

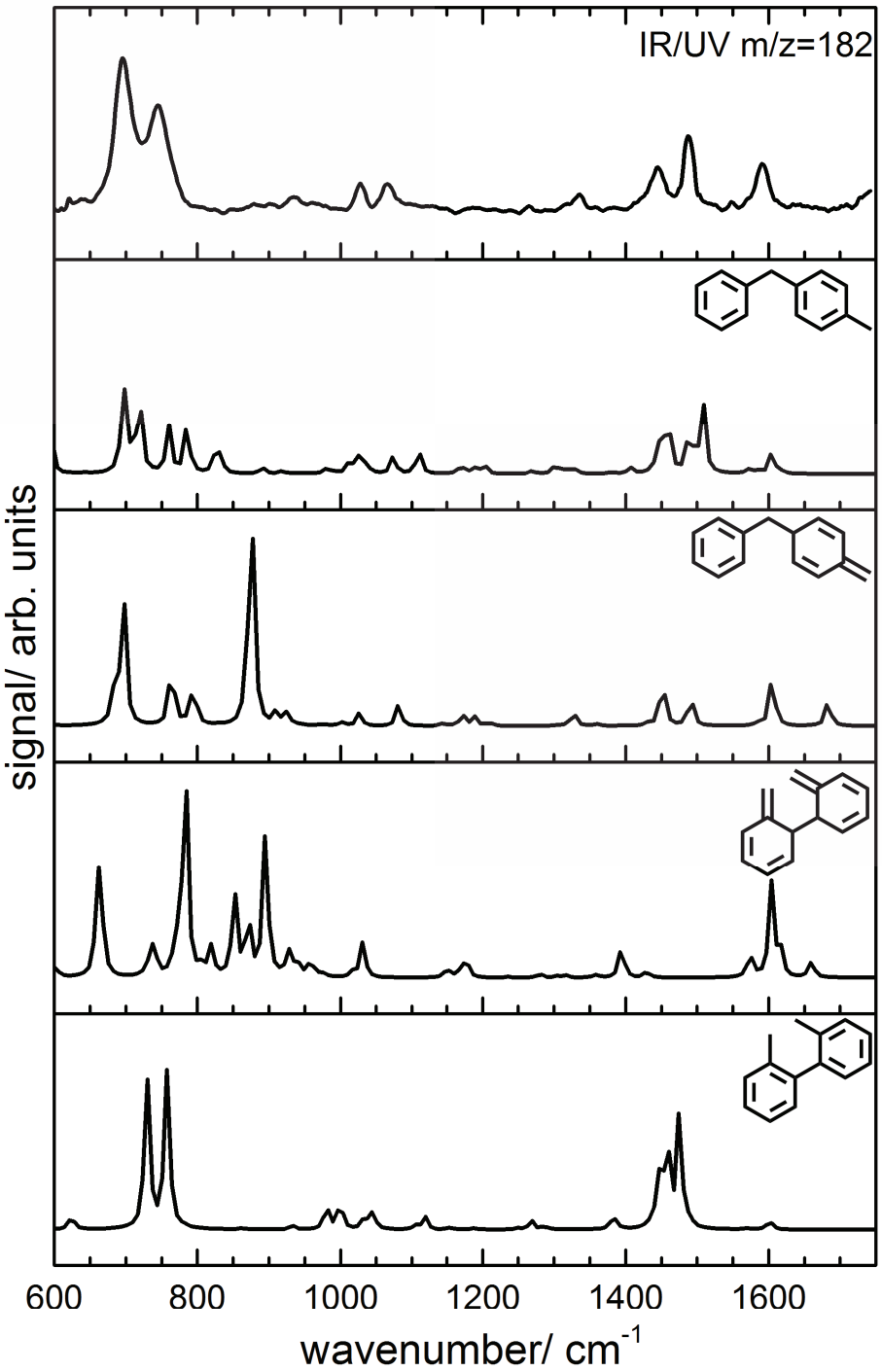

Figure A.2: Additional DFT calculations for m/z=182 from the benzyl experiments II.

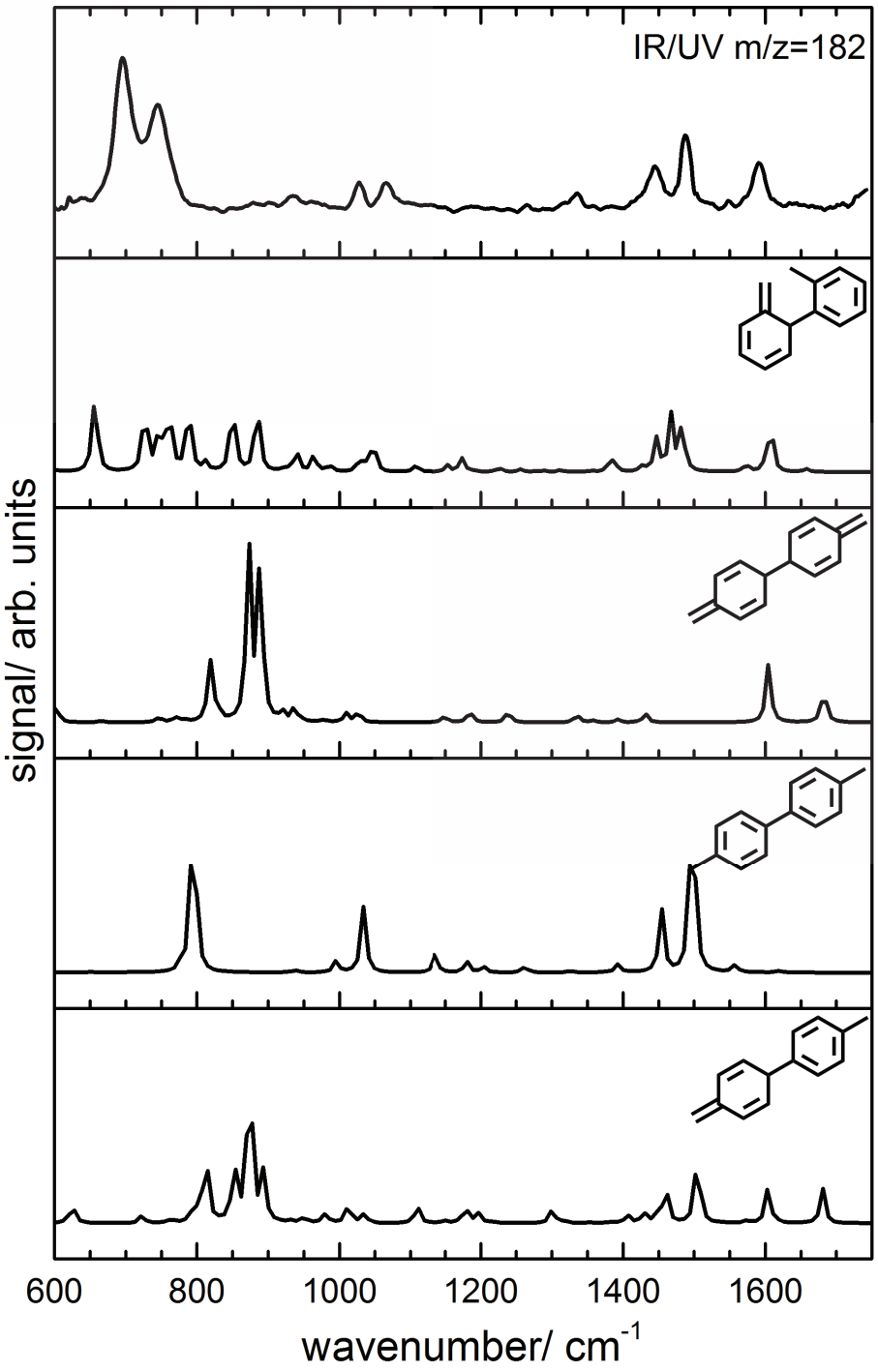

Figure A.3: Additional DFT calculations for m/z=182 from the benzyl experiments III.

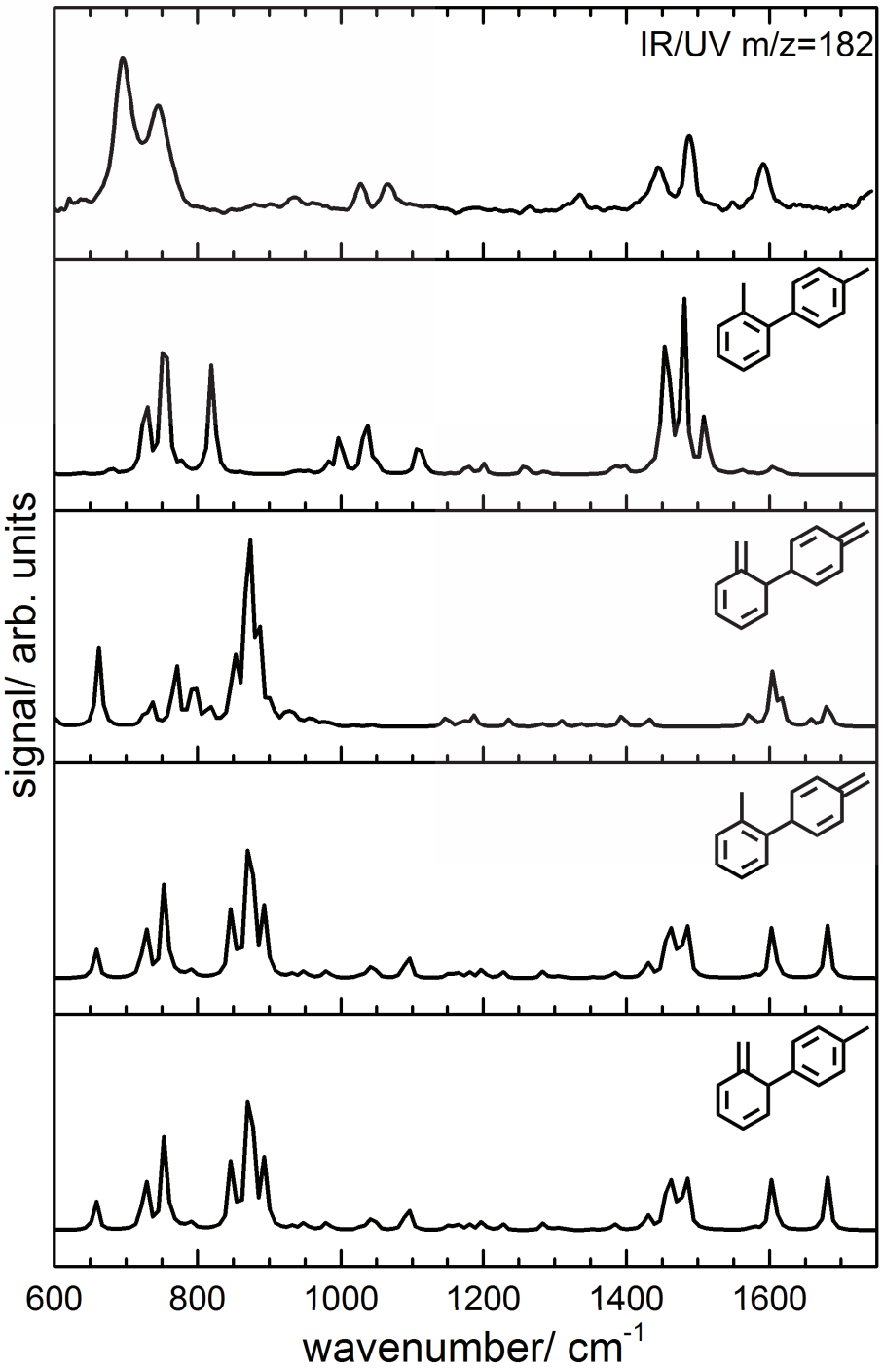

Figure A.4: Additional DFT calculations for m/z=182 from the benzyl experiments IV.

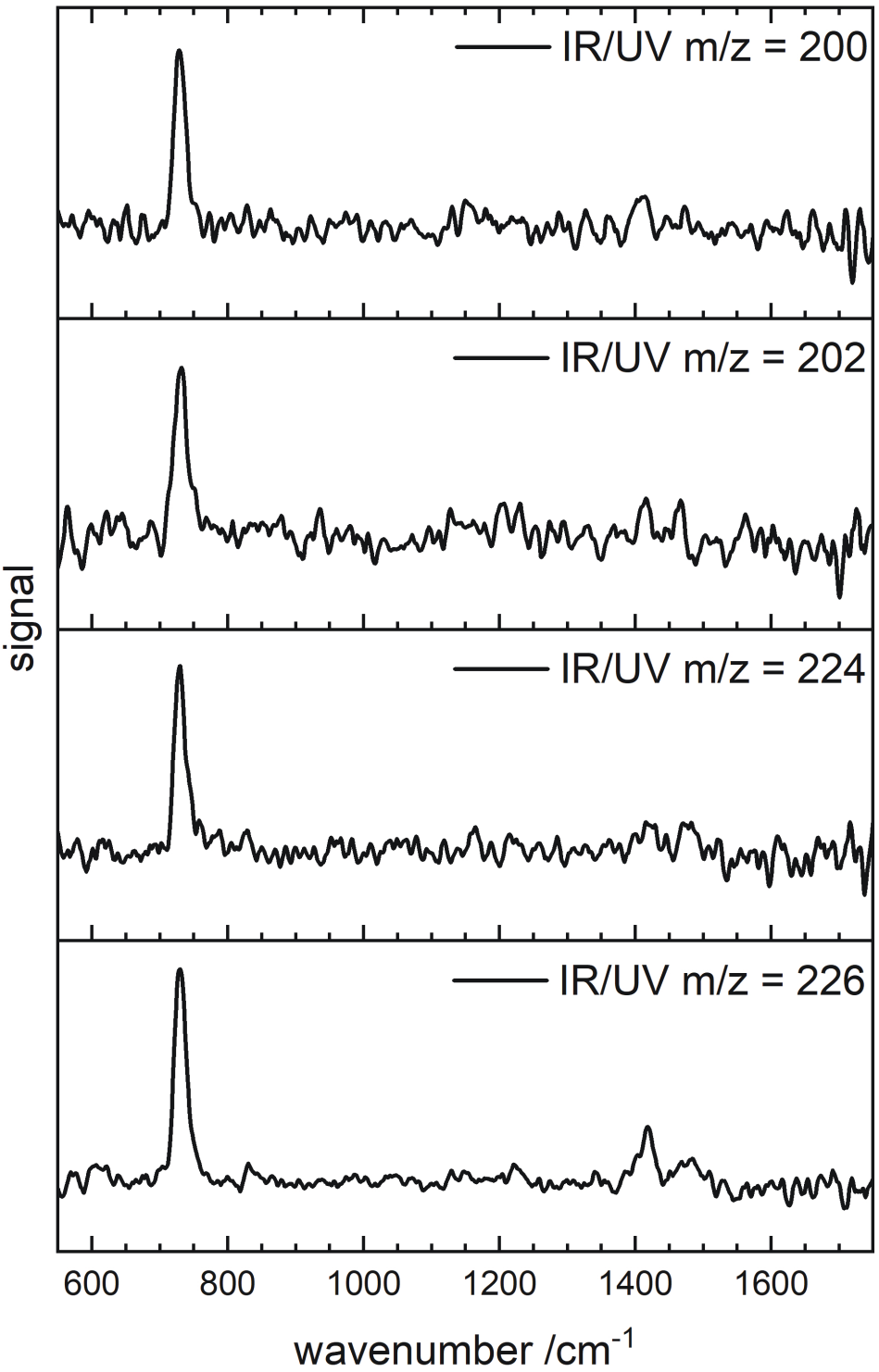

Figure A.5: IR/UV signals from DPI in the ortho-benzyne experiments. All show an identical IR/UV spectrum from the parent molecule m/z=228.

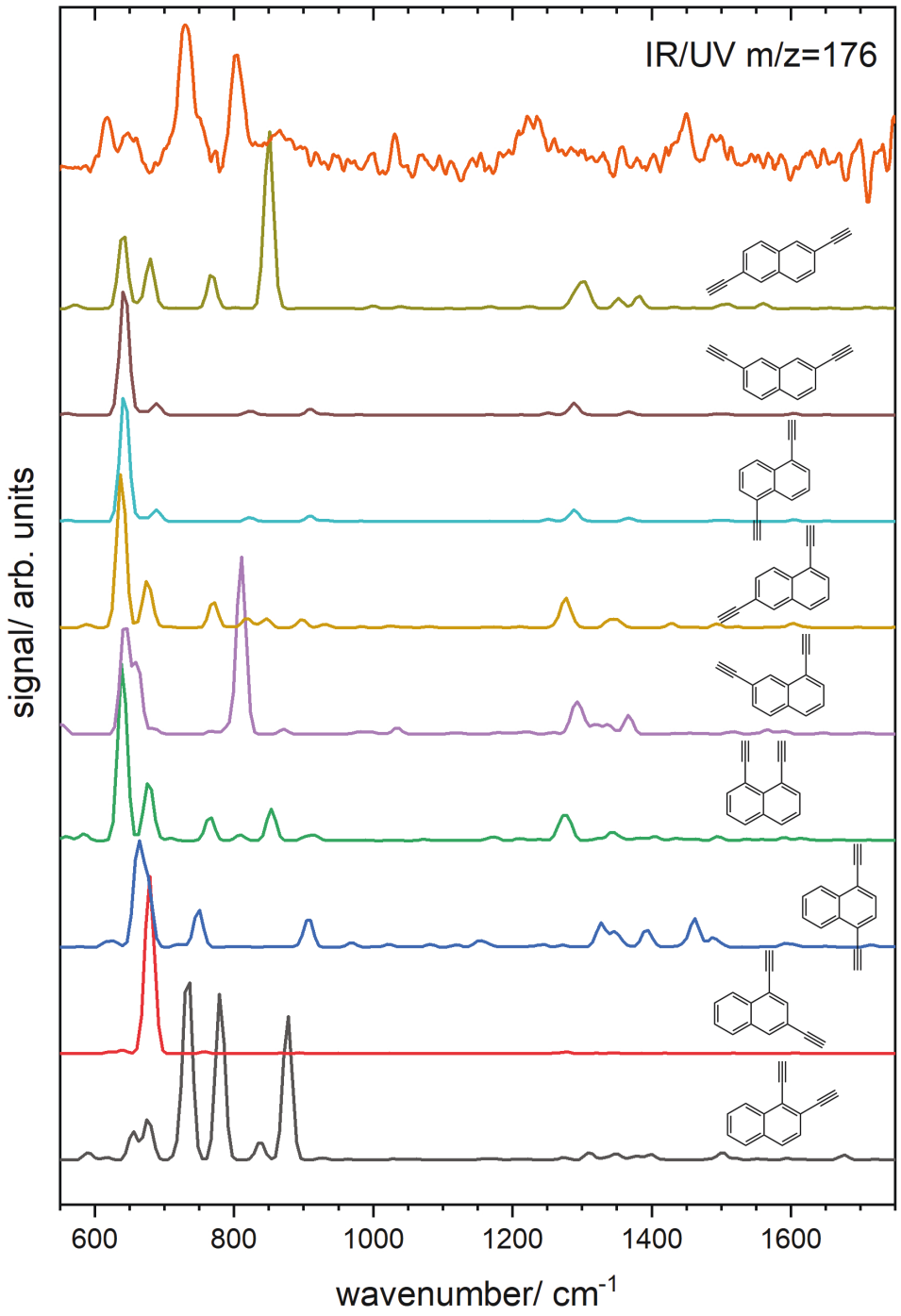

Figure A.6: Possible candidates for mass 176 from the decomposition of phthalide. No simulated spectrum is a good match with the experimental data.

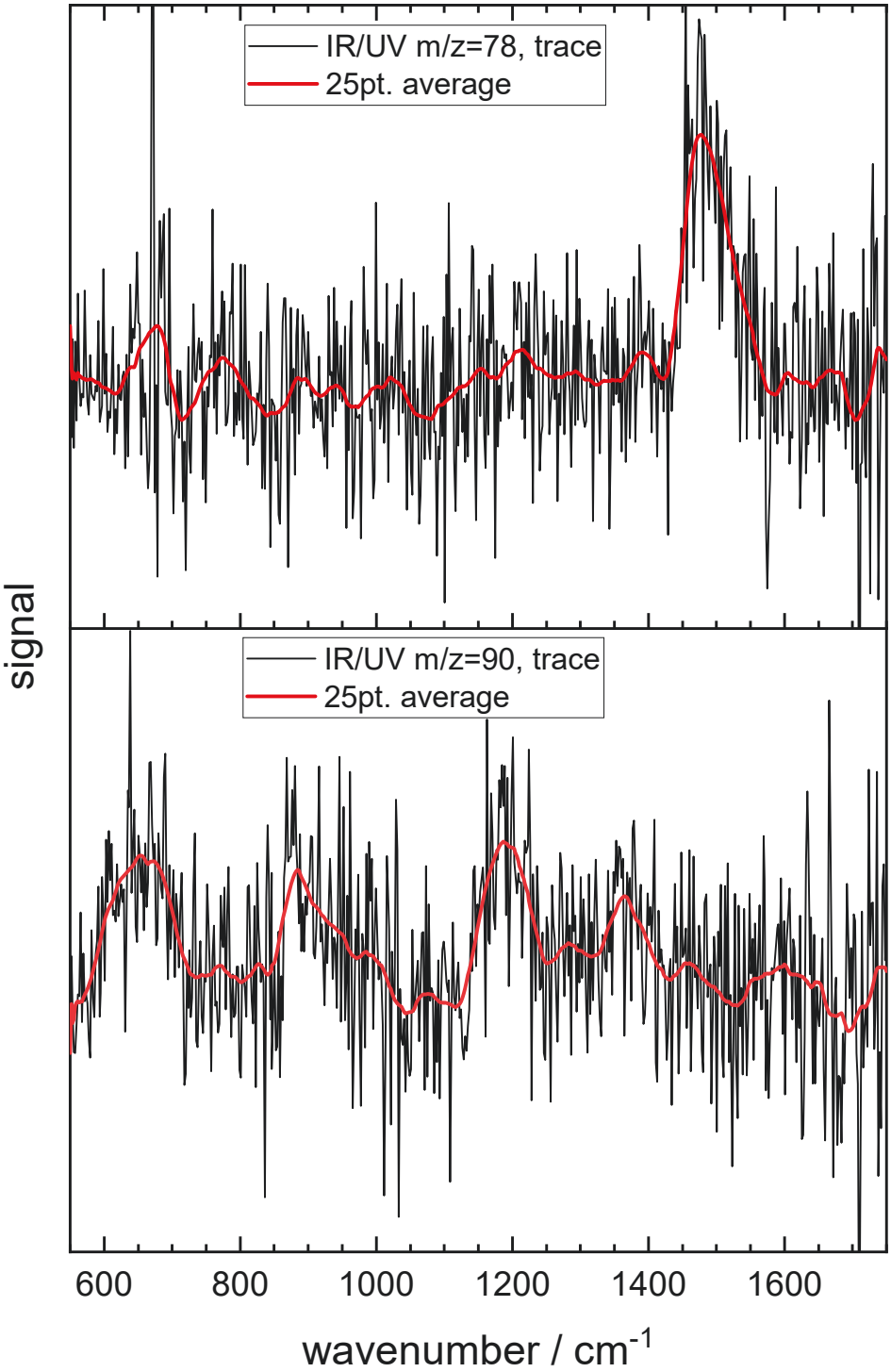

Figure A.7: IR/UV traces of mass 78 and 90 from the pyrolysis of phthalide.

Danksagung

Zu aller erst möchte ich mich bei meinem Doktorvater *Prof. Dr. Ingo Fischer* für die hervorragende Betreuung über die letzten Jahre bedanken. Danke für das tolle Projekt, dem ich mich widmen durfte, dafür dass du immer ein offenes Ohr hattest und dafür, dass du mir die Freiheiten eingeräumt hast, dass ich mich auch um andere wissenschaftliche Projekte kümmern durfte. Danke Ingo!

Des Weiteren möchte ich mich bei meinen Kooperationspartnern in den Niederlanden bedanken. Besonders *Prof. Dr. Anouk Rijs*, die mich über die Jahre stets hervorragend bei FELIX empfangen und unterstützt hat. Ebenso *Dr. Daniel Bakker* und *Sjors Bakels* mit denen die langen Messzeiten nie langweilig wurden.

Bei meinem Vorgänger *Dr. Phillip Constantinidis* möchte ich mich dafür bedanken, dass er mich stets unterstützt hat und geduldig mit mir war, wenn ich Fragen hatte.

Vielen Dank an *Prof. Dr. Animesh Ojha*, mit dem ich mich einige Sommer der Welt der Graphene Quantum Dots gewidmet habe.

Meinem Bürokollegen *Dr. Jens Giegerich* danke ich für die Einführung in den Arbeitskreis, die stets gute Atmosphäre und die vielen anderen Dinge, die wie über die Jahre getan haben. Meiner anderen Bürokollegin, *Dr. Anja Röder*, danke ich für stets interessante Gespräche, aussichtslose Schachpartien und die tolle Zeit in Paris.

Dr. Kai Pachner danke ich für die vielen Aktivitäten, die besonders dem leiblichen Wohl sorgten.

Vielen Dank an *Marco Flock* für den ganzen Unsinn, den wir über die Jahre getrieben haben, das leistungsgerechte tägliche Kickertraining und die tolle Zeit in Edinburgh.

Besonderer Dank gilt auch *Dr. Hans-Christian Schmitt* für die schöne Zeit in Paris und als eine Person, auf die man sich immer verlassen kann.

Meinem Weggefährten *Engelbert Reusch* danke ich für seinen besonderen Sinn für Humor, seine bodenständige Art und die Versorgung mit zuckerhaltigen Aufputschmitteln.

Ich danke *Domenik Schleier* für seine stets offene Art und seinen guten Geschmack für amerikanischen Sportarten.

Ein besonderes Dankeschön an *Isabella Wagner* dafür, dass sie Rudi nicht auf mich gehetzt hat.

Tobias Preitschopf danke ich für die schöne letzte Messzeit in Nijmegen und dafür, dass ich meine wissenschaftlichen Arbeiten in gute Hände übergeben konnte.

Marius Gerlach, *Christian Matthaei* und *Floriane Sturm* danke ich für den frischen Wind, den die drei in die Arbeitsgruppe gebracht haben.

Ein besonderer Dank gilt *Dr. Roland Colditz*, der mich stets am Mittagstisch mit den aktuellsten Informationen versorgt hat.

Den vielen Alt-Doktoranten des AK Fischers wie *Dr. Kathrin Fischer*, *Dr. Fabian Holzmeier*, *Dr. Melanie Lang* und *Dr. Michael Steinbauer* danke ich für die tolle Aufnahme in den AK in den Anfangszeiten. Besonders auch *Dr. Thiemo Gerbich* und *Dr. Jörg-Viktor Herterich* für die Einführung in die hohe Kunst des Kickerns.

Meinen Freunden aus dem AK Brixner *Dr. Simon Draeger* und *Heiko Hildenbrandt* danke ich für die stets unterhaltsame Zeit im Demo-Praktikum und allen außeruniversitären Aktivitäten.

Meinen zahlreichen Kooperationspartnern besonders *Dr. Benjamin Hupp*, *Prof. Dr. Andreas Steffen*, *Jaqueline Ramler*, *Prof. Dr. Crispin Lichtenberg* und *Dr. Klaus Eckstein* danke ich für die tolle und stets unkomplizierte Zusammenarbeit.

Ein besonderer Dank gilt auch den zahlreichen Mitarbeitern aus den Werkstätten des IPTC und FELIX Laboratory, die mit ihren fachlichen Kompetenzen die ganzen Experimente und Studien erst möglich gemacht haben.

Nicht zuletzt geht mein größter Dank an meine Familie, die mich stets während meines Studiums und meiner Promotion unterstützt und mir den Rücken freigehalten hat. Vielen Dank!